Experimental characterization and modelling of electromagnetic waves generated by seismoelectric conversion at porous media interfaces.

Victor Martins Gomes

Tuesday 28th May, 2024

École doctorale des Sciences Exactes et leurs Applications (ED 211)

Université de Pau et des Pays de l'Adour

THÈSE

pour l'obtention du grade de

DOCTEUR de Université de Pau et des Pays de l'Adour

Spécialité: "Géophysique"

à présenter et à soutenir publiquement par

Victor MARTINS GOMES

le 5 décembre 2022

Caractérisation expérimentale et modélisations des ondes électromagnétiques générées par conversion sismoéléctrique aux interfaces des milieux poreux

Experimental characterization and modelling of electromagnetic waves generated by seismoelectric conversion at porous media interfaces

Daniel BRITO	Professeur, Université de Pau et des Pays de l'Adour	Directeur
Hélène BARUCQ	Directrice de recherce, Inria Bordeaux Sub-Ouest	Co-Directrice
Jury de thèse:		
Laurence JOUNIAUX	Directrice de recherche, Institut de Physique du Globe de Strasbourg	Rapporteure
Damien JOUGNOT	Chargé de recherche, CNRS-Sorbonne Université	Rapporteur
Michel DIETRICH	Directeur de recherche, Université Grenoble Alpes	Examinateur
Clarisse BORDES	Maîtresse de conférences, Université de Pau et des Pays de l'Adour	Examinatrice
Christina MORENCY	Chargée de recherche, Lawrence Livermore National Laboratory	Examinatrice
Martin TYGEL	Professeur, Universidade Estadual de Campinas	Examinateur

Laboratoire des Fluides Complexes et leurs Réservoirs (LFCR)

Abstract

Inside fluid-bearing porous media, mechanical disturbances created by traveling seismic waves entail the conversion of seismic into electromagnetic (EM) energy. Two forms of conversion, electrokinetic in nature, have been continually investigated in the context of subsurface exploration: the first consists of a wavefield strictly bounded to the seismic wave, therefore referred as coseismic fields, while the other only happens when the physical properties change, ergo at geological interfaces, and it radiates independently of the seismic waves, with EM-velocities (usually bigger than 1E6 m/s). Due to the sensitivity of the latter to lithology changes, in special variation in the pore-fluid, it is pertinent to near-surface investigation as a complement to reflection seismic, much like controlled-source electromagnetics. Because of that, there is a continuous effort to develop and promote an indirect geophysical procedure based on these electrokinetic conversions, the seismoelectric method. However, obstacles coming from the number of parameters involved (≥ 15) and the lack of a comprehensive understanding of these phenomena delays a widespread use of seismoelectrics: currently there are two main theoretical descriptions, but thus far, none validated in a proper quantitative manner. As a contribution to the existing knowledge about seismic-to-EM conversions, this thesis proposes an easily reproducible experimental setup, capable of measuring both conversions at the same time, with satisfactory signal-to-noise ratio. This setup allows the reproduction of diverse geological settings, including porous layers filled with different fluids, a peculiarity with respect to previous experiments designed to study the same subject. In parallel, an existing numerical code, built upon the most frequently used set of seismo-EM governing equations, was properly adapted to model the experiment, hence opening the path to comparisons between theory and laboratory measurements. As a consequence, a series of measurements in both homogeneous and layered media were conducted, as well as their corresponding numerical modeling. Simulations showed that even though amplitude disagreements exist, overall the theoretical predictions successfully agree with experimental data. Additionally, by studying, experimentally and numerically, the effects of layer thinning on the interface response, it was observed that a boosting of the measured signals happens when the layer has a thick-

ness equal to half the P-wavelength in this layer (P, as usual, refers to compression waves). At last, the effect of fluid conductivity on interface-generated EM waves was investigated. It was noticed that, in the experiment realized, amplitudes decrease with increasing conductivity, whereas the ratio between interface response and co-seismic amplitudes increase. Also, comparison with numerical simulations confirmed again that theory succeeds in providing a fair representation of experiments.

Résumé

Des perturbations mécaniques créées par le déplacement d'ondes sismiques dans le milieux poroeux entraînent la conversion d'énergie sismique en énergie électromagnétique (EM). Deux formes de conversion, de nature électrocinétique, ont été continuellement étudiées dans le cadre de l'exploration du sous-sol: la première est un champ d'onde strictement lié à l'onde sismique, par conséquent appelé champ cosismique, tandis que l'autre ne se produit que lors du changement de propriétés physiques aux interfaces géologiques, avec la géneration d'un rayonnement d'ondes EM dont les vitesses sont classiquement supérieures à 1E6 m/s, très largement audessus des vitesses sismiques. En raison de la sensibilité de cette dernière conversion aux changements de lithologie, en particulier à la variation du fluide interstitiel, il est pertinent d'étudier ses effets en complement d'etudes sismiques ou électromagnetiques de proche surface par example. Par conséquent, il existe un effort continu pour développer et promouvoir une approche géophysique indirecte, basée sur ces conversions électrocinétiques, la méthode sismoélectrique. Cependant, des obstacles provenant du nombre de paramètres physiques impliqués dans la modélisation des effets (≥ 15) et un manque de compréhension globale sur ces phénomènes, diffèrent pour l'instant une utilisation généralisée de la sismoélectrique: il existe actuellement deux descriptions théoriques principales, mais à ce jour, aucune validée d'une manière quantitative appropriée. En tant que contribution aux connaissances existantes sur les conversions sismo-EM, cette thèse propose un montage expérimental adaptée aux mesures simultanées des deux conversions électrocinétiques, avec un rapport signal-sur-bruit satisfaisant. Cette configuration expérimentale permet la reproduction de divers milieux géologiques, y compris des couches poreuses baignants dans différents fluides, une particularité par rapport aux expériences précédentes conçues pour étudier le même sujet. En parallèle, un code numérique déjà existant, construit en se basant sur la théorie sismo-EM la plus fréquemment utilisée, a été adapté pour modéliser l'expérience, ouvrant ainsi la voie à des comparaisons entre théorie et mesures de laboratoire. Par conséquent, une série de mesures dans des milieux homogènes et stratifiés ont été menées, ainsi qu'une modélisation numérique correspondante. Les simulations ont montré que même s'il existe des désaccords

d'amplitude, dans l'ensemble, les prédictions théoriques sont en accord avec les données expérimentales. De plus, en étudiant à la fois expérimentalement et numériquement les effets de l'amincissement de la couche sur la réponse de l'interface, il a été observé qu'une amplification des signaux mesurés se produit lorsque la couche a une épaisseur égale à la moitié de la longueur des ondes de compression P. Enfin, l'effet de la conductivité du fluide sur les ondes électromagnétiques générées par l'interface a été étudié. Il a été remarqué que, dans l'expérience réalisée, les amplitudes diminuent avec l'augmentation de la conductivité, tandis que le rapport entre la réponse interfaciale et les amplitudes cosismiques augmente. De plus, la comparaison avec des simulations numériques a confirmé, à nouveau, que la théorie réussit à fournir une représentation juste des expériences.

Acknowledgments

First of all I would like to express my gratitude to my supervisors Daniel BRITO and Hélène BARUCQ for guiding me through this adventure. Your advice, patience, and support were an invaluable contribution that helped me until the end. I extend my thanks to Clarisse BORDES and Stéphane GARAMBOIS who also helped me, guided me, and advised me, being always available to share their knowledge on seismoelectrics.

My deepest thanks to Laurence JOUNIAUX and Damien JOUGNOT for accepting to report on my thesis; their comments were helpful and very informative. I also thanks the other members of my jury: Michel DIETRICH, Christina MORENCY, and Martin TYGEL; your comments and our discussion were enlightening and enjoyable, contrarily to what one would expect from a thesis defense.

I am also grateful to Eric NORMANDIN and Patrick PLOURABOUÉ for the help when developing the preamplifier for my experiment. Additionally, I need to mention Bertrand FASENTIEUX since without his help cutting the rock samples, most of my results would not exist. I also appreciate the help of Joseph DIAZ regarding the distilled water.

Thanks to all the members of the CGR group as well as the Magique3D team, in special Julien DIAZ. I am grateful for all the discussions, advises, and good times.

I also need to thanks all my friends whose support and friendship were essential to ensure I would arrive here today, specially during the sanitary crisis we went through.

My family also needs all my gratitude, staying apart for so long is hard, even though necessary. Thus, a special thanks to my mother, my father, and my sister for their understanding and support. Not being able to see them was the hardest part.

Finally, I am grateful to Ellen for bearing me during all the hard times created by the thesis, and for being incredibly supporting and patient throughout this journey. I am really fortunate to have you with me during all this time.

Contents

Abstract **iii**

Résumé **v**

1 A General Introduction **1**

1.1 Introduction 1

1.2 State-of-art on seismoelectric conversions at interfaces in porous media 1

1.2.1 Laboratory experiments 2

1.2.2 Numerical modelling 11

1.3 Motivation and goals 13

1.4 Thesis outline 14

2 Theoretical framework **17**

2.1 Physical parameters of porous media 17

2.1.1 Geometrical and transport parameters 17

2.1.2 Mechanical parameters 23

2.1.3 Electromagnetic parameters 28

2.2 Electrokinetic phenomena at the pore scale 32

2.2.1 The electric double layer 33

2.2.2 Electric potential in the diffuse layer 34

2.2.3 Streaming potential coefficient 36

2.3 Governing equations of seismoelectromagnetic phenomena 38

2.3.1 Pride's electrokinetic formulation 39

2.3.2 Revil's formulation 54

3 Numerical framework **55**

3.1 Governing equations in layered media 55

3.2 The wave-vector in uniform media 58

3.3 Reflection and transmission matrices 60

3.4 Upper and lower bounds of the media 61

3.5 A stratified media 63

3.6 Vertical components of E and H . . . 65
3.7 Back to time and cartesian coordinates . . . 66
3.8 Electric potential . . . 67
3.8.1 2, 3 and 5-electrodes configurations . . . 68
3.9 Reciprocity tests . . . 69

4 Experimental framework 79
4.1 Sand . . . 81
4.2 Sandstones . . . 82
4.3 Pore-fluid water . . . 83
4.4 Plastic container . . . 84
4.5 Source . . . 84
4.6 Laser vibrometer (displacement receiver) . . . 88
4.7 Electric data receiver . . . 92
4.7.1 Difference between acquisitions with oscilloscope probes and preamplifiers . . . 94
4.7.2 Placement of the reference electrode . . . 103
4.7.3 Electrode characteristics . . . 106
4.8 Acquisition procedure . . . 112
4.8.1 Preparation . . . 112
4.8.2 Stabilization time . . . 113
4.8.3 Oscilloscope parameters . . . 114
4.8.4 Operational details of acquisition . . . 115
4.9 Varying the conductivity . . . 116
4.10 Towards automation . . . 118

5 Quantitative comparison between laboratory and numerical data in ligth of electrokinetic theory 125
5.1 Summary . . . 125
5.2 Introduction . . . 126
5.3 Theoretical basis . . . 128
5.4 Experimental setup . . . 130
5.4.1 The porous media . . . 130
5.4.2 Seismic source . . . 132
5.4.3 Seismic measurements description . . . 133
5.4.4 Seismoelectric measurements description . . . 134

5.5 Numerical modelling tool . . . 135
5.5.1 A brief description . . . 135
5.5.2 Extension of the existing numerical code . . . 136
5.5.3 Particularities of the numerical modelling of the experiments . 137
5.6 Seismoelectrics in a homogeneous medium . . . 138
5.6.1 Experimental data . . . 138
5.6.2 Comparison between experiments and theory . . . 144
5.7 Seismoelectrics in a layered medium . . . 152
5.7.1 Experimental data . . . 152
5.7.2 Numerical modelling . . . 156
5.7.3 Interpreting the interface response . . . 159
5.8 Conclusions . . . 165
5.9 Complementary studies . . . 166
5.9.1 Modelling with different parameters for the sand . . . 167
5.9.2 Experiments parallel to layer . . . 170

6 Experimental and numerical study on the effect of layer thickness and constrasts of fluid conductivity upon the EM interface response 173
6.1 Effect of thickness . . . 173
6.1.1 Layer thickness, thin beds and seismic waves . . . 174
6.1.2 Experimental and numerical methodology . . . 176
6.1.3 Results and discussion . . . 177
6.2 Effect of fluid conductivity . . . 185
6.2.1 Methodological aspects of experiments and numerical simulations . . . 185
6.2.2 Experimental results and discussions . . . 187
6.2.3 Comparing experiments and theory . . . 193
6.2.4 Sensitivity study of σ_f . . . 201
6.3 Partial conclusions . . . 209

7 Summary, conclusions, and perspectives 211
7.1 Summary . . . 211
7.2 Main results and conclusions . . . 212
7.3 Perspectives . . . 214
7.3.1 Regarding experiments . . . 214
7.3.2 Regarding theoretical predictions . . . 215

Bibliography **217**

Appendices **229**

A Calculation of plane wave slowness 229

A.1 Longitudinal waves 229

A.2 Transversal wave 230

B Deriving the system of equations used by Garambois (1999) 232

C Example of python routine used to control acquisition 237

D Interpreting the interface response using a dipole-based model 252

1 A General Introduction

1.1 Introduction

Seismic wave propagation in a fluid-filled porous media creates electromagnetic (EM) disturbances through a physical process referred in the literature as seismoelectric conversion. Two EM fields result from this conversion, one accompanying the seismic wave in the form of a transient electric field and the other generated at interfaces and independently propagating away from its originating point, with a diffusive behavior characteristic to the near-field region of EM fields (detected by receivers at distances smaller than a wavelength from the interface). The latter has an arguably high potential of application in near-surface exploration, possibly comparable to other indirect EM methods. However there is still a long way to go before a thorough quantitative understanding of the conversion phenomena at interfaces is achieved. Pursuing this goal, the present study intends to become a valuable addition to the overall comprehension of the cited conversion process, by providing a comparison between laboratory experiments and numerical data, modeled using the widely accepted theory of Pride (1994).

1.2 State-of-art on seismoelectric conversions at interfaces in porous media

Reseach on seismoelectric and its reciprocal electroseismic phenomena, electrokinetic in nature, remounts to the 1930's (Blau and Louis, 1936; Thompson, 1936) however oriented laboratory studies only started around 1960 with the works of M. S. Antziferov in 1958 and 1962 and the study of E. I. Parkhomenko in 1962, even thought a likewise phenomenon had already been observed by S. Mauschly in 1918 (as cited in Parkhomenko, 1971). Theoretical attempts to establish governing physical relations were firstly made in Frenkel (1944), departing from Ivanov's field observations (Ivanov, 1939; Ivanov, 1940), and later in Neev and Yeatts (1989). Nonetheless it was Pride (1994), complemented by Pride and Haartsen (1996) and

Haartsen and Pride (1997), that really attained it through coupling of Biot's theory and Maxwell's electromagnetic formulation by flux-force relations.

Following Pride's electrokinetic theory, research has been mainly directed towards two effects of seismic-to-electromagnetic conversion. For a propagating compressional wave, the first effect is an (coseismic) electric field whose support is strictly binded to that of the seismic wave (Pride and Haartsen, 1996); the second has its origins linked to the discontinuities of electrical and/or mechanical properties across interfaces, existing as an EM-disturbance moving at much higher speeds than that of the generating seismic wave (Haartsen and Pride, 1997). Both have already been extensively studied experimentally (e.g., Zhu et al., 1994; Bordes et al., 2008; Zhu et al., 2008; Schakel et al., 2011a).

Given the focus of this work, mainly laboratory studies and numerical developments will be reviewed in what follows.

1.2.1 Laboratory experiments

Reported laboratory experiments devoted to the observation of interfacial seismoelectric responses have begun with the works Haartsen et al. (1995) and Zhu and Toksöz (1996), where EM-waves were generated by a compressional transducer at the interface between fluid-saturated lucite sandstone and man-made sandy porous medium. Zhu et al. (1999) and Zhu et al. (2000) complemented the previous works, extending the knowledge about seismoelectric and electroseismic conversions, in the kilohertz range, using cylindrical and layered models; additionally, the latter attempted to compare experimental data with theoretical calculations, as previously done in Haartsen et al. (1995), employing the methodology described in Haartsen (1995) and Haartsen and Pride (1997).

Furthermore Zhu and Toksöz (2003a) simulated crosshole measurements with a water-filled fracture between source and receiver boreholes to study how fracture aperture relates with the amplitude of the seismoelectric signal created at interfaces. They have also shown the feasibility of inferring the geometrical parameters of an inclined fracture, considering that the propagation velocity from source to fracture is known (see figure 1.1). Using the same borehole model, Zhu and Toksöz (2003b) investigated the effect of varying the saturant conductivity in the measured seismoelectric signals. By analyzing the EM wave-fields created at two interfaces, they defined two conductivity regions: (I) corresponds to amplitudes increasing proportionally to conductivity, suggesting the solid-grain surface does not yet contain

enough adsorbed ions, and (II) refers to a region where an inverse proportionality is observed, implying that for this range of fluid conductivity the Gouy-Chapman-Stern model (Gouy, 1910; Chapman, 1913; Stern, 1924) is valid and, consequently, so is Pride's theory. Chen and Mu (2005) observed a similar conductivity behavior using uniform fine quartz sand, saturated with various concentrations of NaCl. Moreover, they experimented with layered models (either a saturated sand, a NaCl solution or oil), examining the relation between the signal's amplitude and the source-receiver offset, and eventually showing that the EM-waves are sensitive to oil-saltwater interfaces (figure 1.2), typically encountered in petroleum reservoirs.

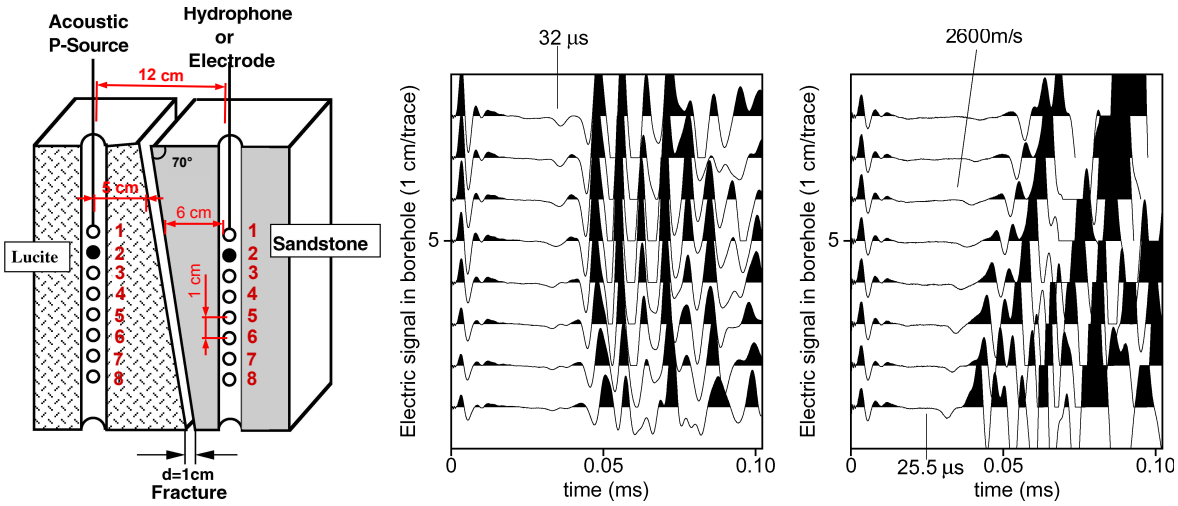

Figure 1.1: Seismoelectric acquisition with a cross-hole geometry containing an inclined, water saturated fracture, separating a Lucite block from a sandstone block, both also saturated (a). In (b) the source is fixed at position 2 in the Lucite borehole and the electrode moves from position 1 until 8 in the sandstone borehole. (c) shows the data acquired by keeping the electrode at position 2 and moving the source from 1 until 8. Amplitudes were normalized by 14 μV. From the data, a dip angle of 69.2^o was estimated for the fracture and the distance from position 1 of the source to the fracture was estimated as 4.9 cm, both values close to the real ones. Figure adapted from Zhu and Toksöz 2003a.

Zhu and Toksöz (2005) also recorded EM-wave with the above mentioned fractured borehole model. Besides that they were able to register the magnetic field induced by the Stoneley wave propagating along the fracture through a Hall-effect magnetic sensor which wasn't, however, sensitive to the converted wave. Block and Harris (2006) measured the effect of electrolyte concentration in the seismoelectric response, using an ultrasonic pulse in a column-shaped experiment, composed of loose-glass micro-spheres and unconsolidated medium-grain sand; results were

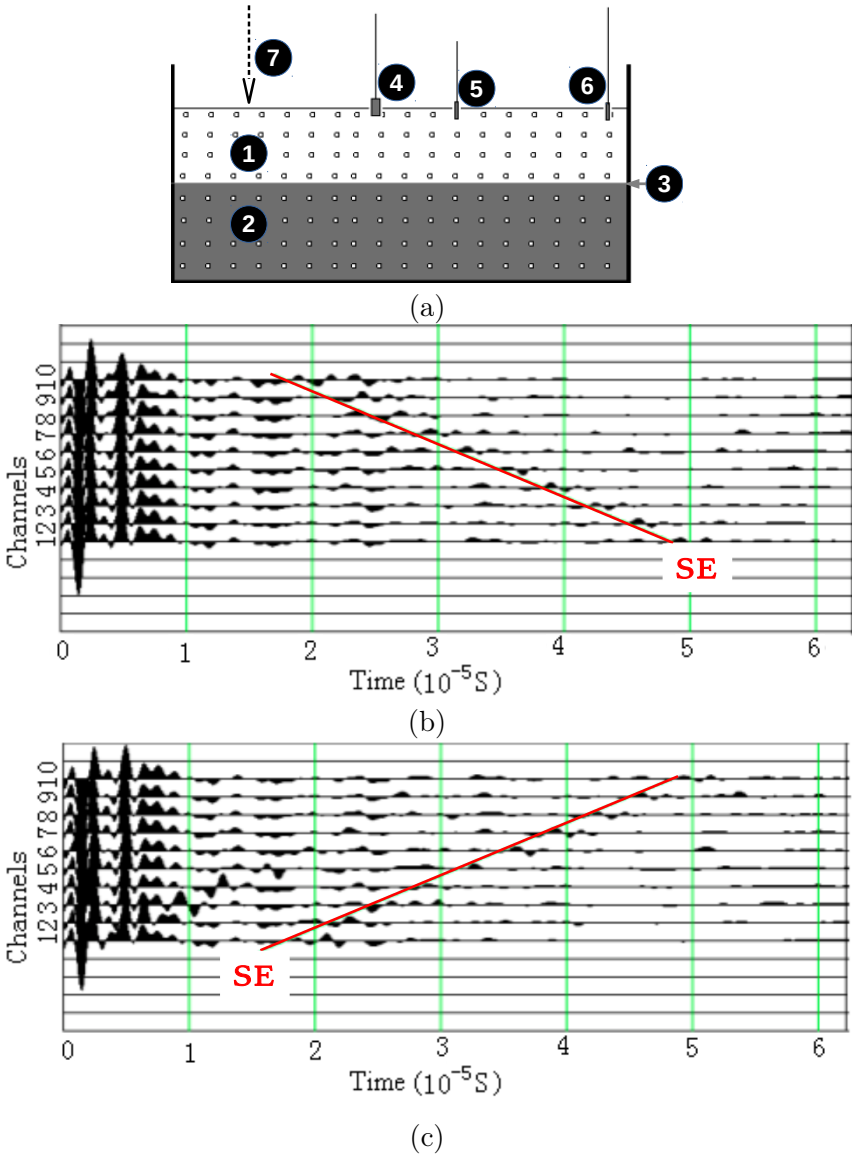

Figure 1.2: Experimental set-up for seismoelectric acquisition in (a): 1 - sand saturated with a NaCl solution (C=0.3%), 2 - lubricating oil-saturated sand layer, 3 - impervious poly (chloroethene) membrane (0.01 mm), 4 - acoustic source, 5 - receiving electrode, 6 - reference electrode and 7 - source's moving direction. The electrodes are kept at the same position while the source can move up or down. (b) shows the data acquired by gradually moving the source 1 cm downwards and (c) when moving it 2 cm upwards. SE in red highlights the measured seismoelectric signal. Adapted from Chen and Mu 2005.

subsequently contrasted with theoretical predictions. Their conclusions about fluid conductivity were essentially the same as earlier works. Liu et al. (2008) showed ultrasonic P-waves can created EM waves when traversing the interface between frozen and unfrozen media, thus confirming the existence of a double-layer at this

boundary. Zhu et al. (2008) performed seismoelectric and electroseismic measurements in the frequency range 15–150kHz using rock samples (a sandstone and a granite) immersed in a water tank (see figure 1.3a, 1.3d). Using the measurements, the respective coupling coefficients were calculated and afterwards they were qualitatively compared to the theoretical results, considering a closed-capillary model. Even though the experimental results and the predictions from theory did not agree, the authors argued they showed similar trends in the frequency domain (figure 1.3), what led them to hypothesize that a relationship between pore-size and frequency-coupling coefficients might exist. In the end, their results showed the energy of the interface response (seismic to electric and vice-versa) increases with permeability and porosity.

The works Charara et al. (2009), Schakel and Smeulders (2009), Schakel and Smeulders (2010a) and Schakel et al. (2011c) (the last two extended in Schakel et al. (2011b), Schakel et al. (2011a) and Schakel et al. (2012)) focused on cross-checking numerical solutions of Pride's equations against experiments in water-filled tanks with rock samples of various kinds (i.e., Fontainebleu and Berea sandstones and sintered glass), agreeing altogether about the validity of Pride's electrokinetic theory in describing seismoelectric/electroseismic phenomena. Schakel et al. (2011b) showed how their numerical and experimental data agreed in terms of travel times, waveform, polarity and spatial amplitude decay. Nonetheless they point a scaling issue when matching the data, which they attribute to the difficulty of correctly estimating variations in pore fluid conductivity and the zeta potential. With a similar approach, Schakel et al. (2011a) focused on analyzing the interfacial EM-wave amplitude variation as a function of conductivity, representing an addition to early works (above cited). An increase in discrepancy between theory and experiments with decreasing conductivity was also reported, which they concluded could be related to surface conductivity phenomena, unrelated to those covered by Pride's electrokinetic theory (see figure 1.4). The work Schakel et al. (2012) complements the previous by exploring EM signals generated by porous samples thinner than the wavelength. As before, both pressure and EM wave-fields agreed well with predictions, except for an amplitude dissimilarity in the latter, which they approximately corrected by changing the surface conductance, pore-fluid conductivity and the zeta potential.

At the same period Holzhauer and Yaramanci (2011) sought a laboratory setup capable of enhancing both coseismic and interface-generated EM signals, measured in a column model composed of sorted and saturated glass beads (350–500) μm and

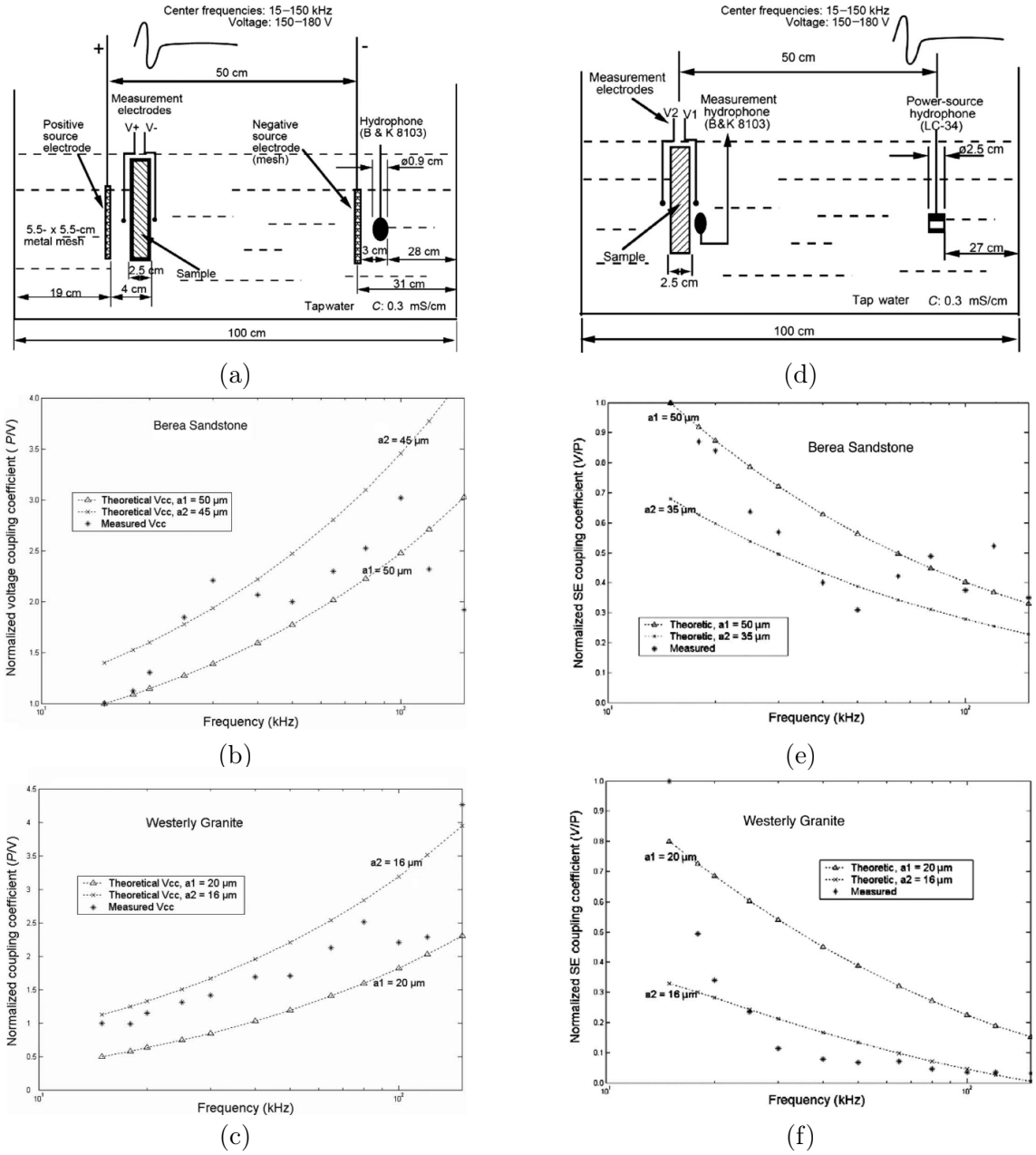

Figure 1.3: Configuration of electroseismic (a) and seismoelectric (d) measurements. (b) and (c) show the normalized electroseismic coupling coefficient when the sample is, respectively, a Berea Sandstone and a Westerly Granite as well as the normalized theoretical values considering the capillary radii of 50 μm (a1) and 45 μm (a2) in (b) and of 20 μm (a1) and 16μm (a2) in (c). The corresponding seismoelectric coefficients, calculated using the same rock samples, are shown in (e), considering the radii 50 μm (a1) and 35 μm (a2), and (f), considering the radii 20 μm (a1) and 16 μm (a2). Adapted from Zhu et al. 2008.

submerged in a 10^{-2} S/m electrolyte. It was noted that shielding of the source and

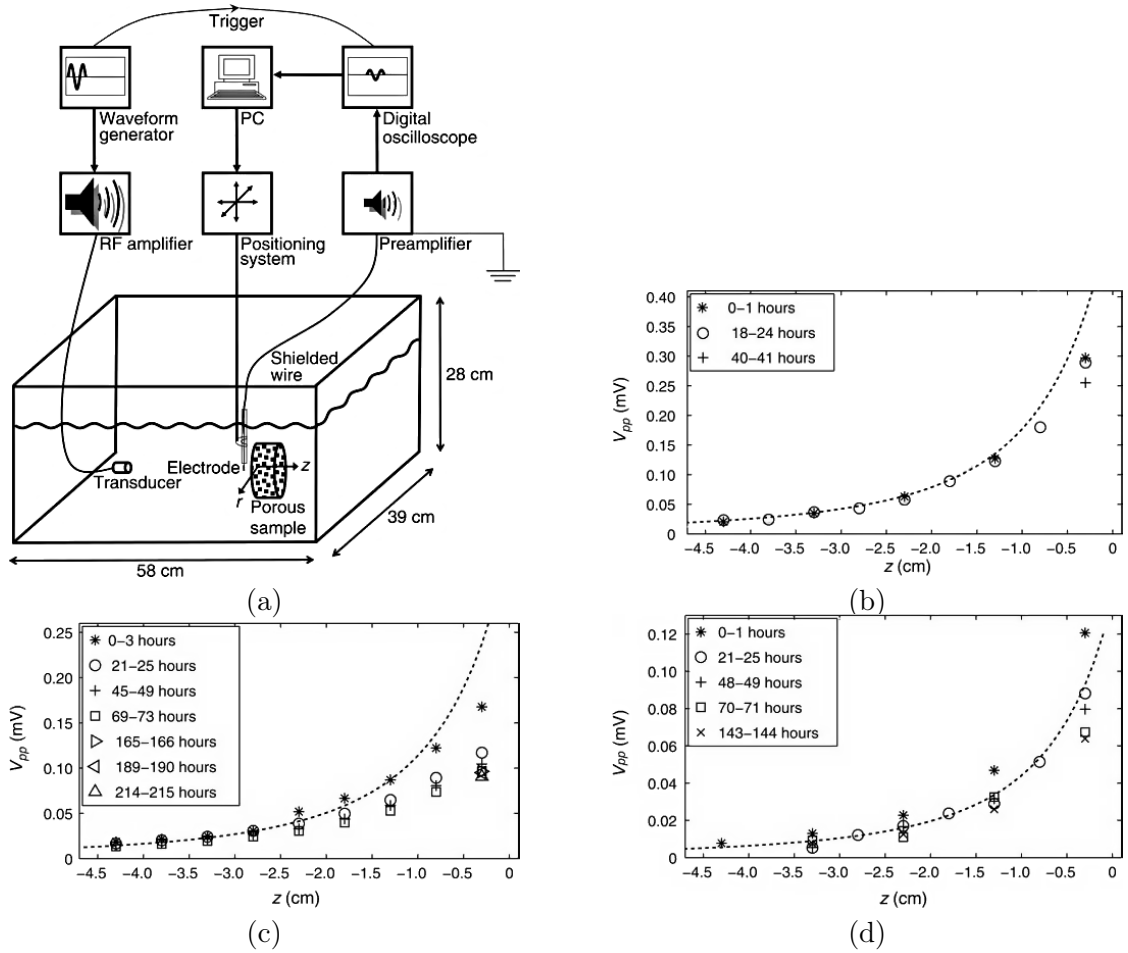

Figure 1.4: Experimental set-up for measuring seismoelectric signals inside a water-tank (a).The z-axis increases to the right and the center of the rock sample is the origin of the coordinate system. In (b), (c) and (d) the measured (symbols) and modelled (dashed lines) electric potential's peak-to-peak amplitudes are shown. The fluid conductivities considered (in S/m) are: 1.20E-2 (b), 1.27E-3 (c) and 1.01E-1 (d). Measurements were repeated several times to test repeatability of results. From (b), (c) and (d) one sees the fit of the modelled data gets better with increasing conductivity. Adapted from Schakel et al. 2011a.

proper grounding of the system lead to substantial improvement, even though optimization of other parameters were also discussed. Following up Zhu et al. (2008), Zhu and Nafi Toksöz (2013) experimentally determined DC streaming potential (low frequency range) and high-frequency seismoelectric (10–120 kHz) coupling coefficients (defined as ratio between amplitudes of interface response and pressure wavefields) for a sample of Berea sandstone with permeability close to 450 mD saturated with, and immersed in, NaCl solutions whose fluid conductivity is in the range: 12–350 mS/m. The inverse proportionality relation of seismic-to-electric energy con-

version and pore-fluid conductivity, as well as frequency, predicted by theory was confirmed. Moreover the authors argued that for the lowest measured frequency (15 kHz) the seismoelectric coupling coefficient is close to the DC coefficient; however lower frequencies were not studied in a seismoelectric context due to intrinsic limitations of the experiment.

Focusing in the EM-waves generated at fluid-solid and solid-solid interfaces, Smeulders et al. (2014) used the same experimental setup as Schakel et al. (2011a) to simulate the monitoring of a moving oil-water contact (inside porous glass samples), and a scenario where a fluid slab (a thin plastic container) superpose a saturated porous medium (a Fontainebleu sandstone sample). Authors concluded from the first case that the EM response created at the interface between water and a water-satured porous medium is stronger than that created at the boundary between water and an oil-satured medium. Furthermore, they noticed that measurements are sensitive enough to oil displacements, that application to identification of oil-filled fractures can be envisaged. The second case complemented their observations, by showing that a contact between water and water-saturated sandstone leads to a more pronounced EM signal than a contact between oil and water-saturated sandstone. Zhu et al. (2016) (continuing the work Zhu and Toksöz (2014)) analysed seismoelectric coupling (associated with the EM interface response) using an experimental setup identical to their earlier work (above cited). For that, the employed Berea sandstone samples with different permeabilities, and a synthetic quartz-sand sample with anisotropic permeability. An increase of seismoelectric amplitudes linked to permeability was confirmed from experimental data, and measurements agreed with theoretical predictions.

Most of the recent laboratory studies, focused on the EM interface response, is led by a group in the China University of Petroleum. Peng et al. (2016a) and Peng et al. (2016b) treat the development of an experimental setup to measure seismoelectric signals, largely similar to the ones already discussed. By moving the rock sample away from the acoustic source and the measurement electrodes, conclusions about the interfacial EM-wave attenuation were made. Moreover, the impact of permeability on the interface response amplitude was explored and the inferred relations are in accordance with those of previous studies. Peng et al. (2018b) adapt the previous experimental configuration to investigate electroseismic phenomena. With that, both the electroseismic signal, generated at the interface, and the pressure field electrically induced (near the electrode) were observed; amid all other points

discussed, comparison of their frequency analysis indicated that those signals are not related and that the former has a closer behavior to the source signature, thus confirming its electroseismic origin. Concurrently Peng et al. (2017) inspected in detail the seismoelectric response of wedge and cavity models, discussing amplitude and polarity features and pointing the main aspects of recorded events. Using the wedge model, the enhancement of EM-wave signal, already reported in numerical studies (Haartsen and Pride, 1997; Grobbe and Slob, 2016), was experimentally confirmed (see figure 1.5); with the cavity model and the evaluation of polarity and amplitude changes across interfaces, authors suggest the application to seismoelectric borehole data, when receiver depth varies, possibly leading to improvement in interpretation of structures and horizons.

Innovative results are shown in Peng et al. (2018a) (a work recently extended in Peng et al. (2020)) through investigation of seismoelectric conversion in shales. It is discussed that even though porosity and permeability of shales are smaller than sandstones, the seismoeletric coefficient of both rock types can be close in magnitude, a possible reason being bigger zeta potentials and mineral specific surface areas associated with shales. Going further, the authors experimentally demonstrate that the presence of illite (whose specific surface area is very high) in the interface will considerably increase seismoelectric conversion. At last, a seismoelectric anisotropic parameter is defined under the hypothesis that coupling coefficients for shales could retain information about anisotropy; indeed consistency (by an almost linear relation) with P and S-wave anisotropic parameters (Thomsen, 1986) was seen. At the same time, Peng et al. (2018c) and Peng et al. (2019) considered the effects of permeability, porosity and frequency on the coupling coefficient, comparing experimental data with numerical modeling by employing a micro-capillary model for media. It was shown that the energy of seismoelectric signals increases with porosity (at least for the considered range), whereas for permeability a complex relationship exists. Additionally, the authors observe that the interface response should be more sensitive to variations in low permeability rock samples, suggesting a potential application to tight gas and tight oil reservoirs, which in general possess low permeability values.

Finally, Wang et al. (2020) designed an experiment seeking a correspondence with offshore seismoelectric acquisitions. For that a synthetic rock (made of epoxy-glued sand grains) was laid on top of a Berea sandstone inside a water tank. Both the coseismic waves inside the synthetic rock and the EM signal created at the fluid-rock

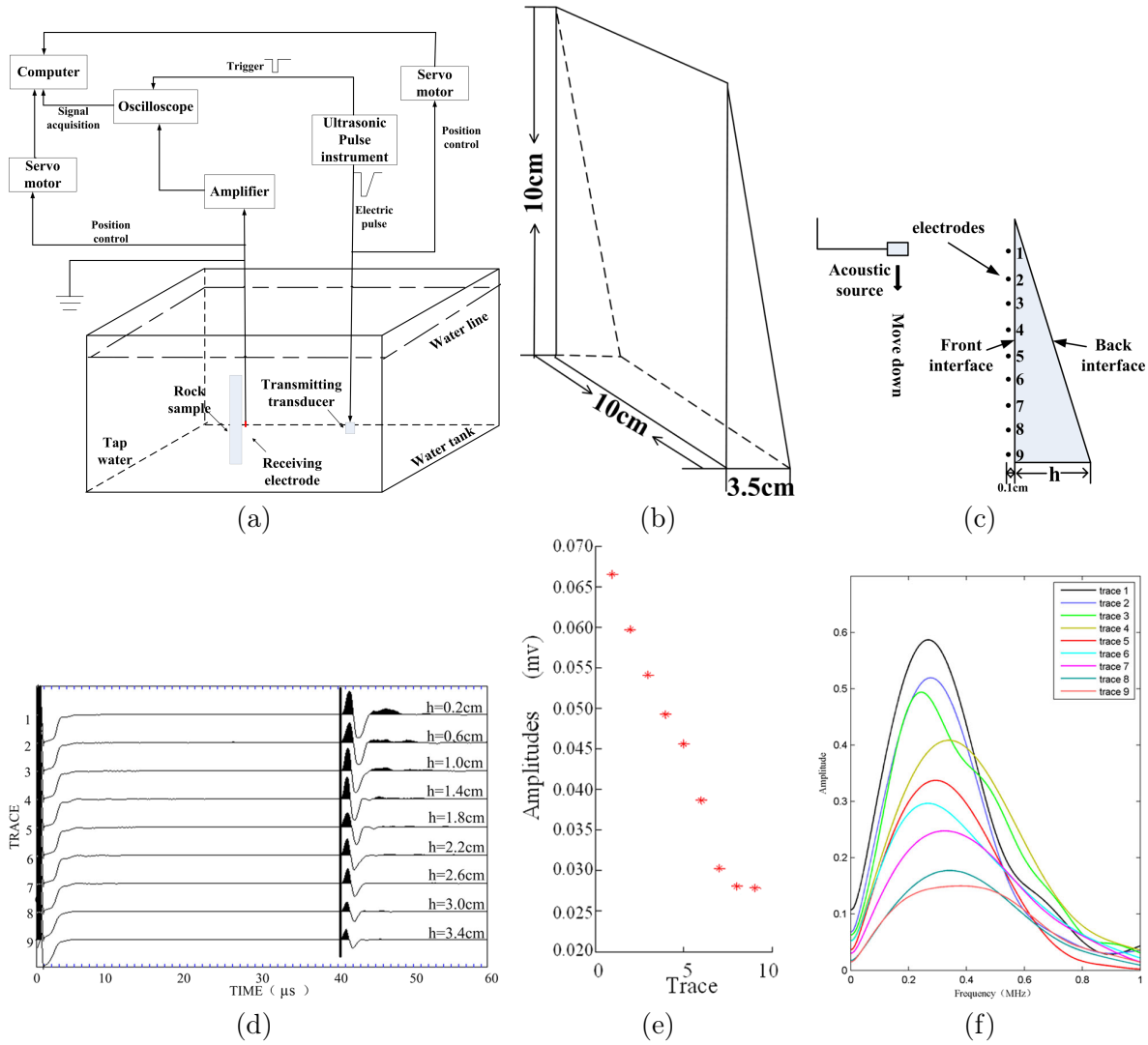

Figure 1.5: Schematic of the experimental apparatus for seismoelectric measurements (a). Dimensions of the wedge model are shown in (b) while a depiction of how measurements were realized is shown in (c). The interfacial EM response measured by electrodes, considering different wedge thicknesses (h), and an input signal whose wavelength (λ) is about 0.9 cm, is displayed in (d). (e) shows the peak-to-peak amplitude of the signals in (d), as a function of h, and (f) displays the amplitude spectra of the signals in (d). One can notice from these results how the amplitudes increase when the wedge thickness goes from $\approx 3\lambda$ to $\approx \lambda/5$. Adapted from Peng et al. 2017.

interface were sucessfully detected, nevertheless the interface response created in the boundary of both porous media could not be measured.

1.2.2 Numerical modelling

Numerical modelling of seismo-electromagnetic phenomena in geophysics has possibly begun with research on seismomagnetic waves/anomalies generated by earthquakes (see: Stacey, 1964; Hao et al., 1982; Johnston, 2002) and whose nature can not only be hyphotesized as electrokinetic, like the work Mikhailenko (1991) concerned with the simulation of the co-seismic magnetic field in an elastic Earth model, which was later extended and detailed in Mikhailenko and Soboleva (1996) and Mikhailenko and Soboleva (1997). The first numerical simulation based on Pride's equations, thus focused only on seismo-electromagnetic phenomena of electrokinetic origin, was shown in Haartsen and Pride (1994) with further detailing in Haartsen (1995) and Haartsen and Pride (1997). It considers seismic and electromagnetic point sources in stratified porous media and employs the global matrix method, introduced by Chin et al. (1984) as an extension of the Thomson-Haskell's technique (Thomson, 1950; Haskell, 1953), to solve for the macroscopic EM and poroelastic wavefields.

Garambois (1999) proposes a slight modification to the previous method. Computation of wavefields uses an extension of the generalized reflection and transmission matrix method Kennett and Kerry (1979) which allows the evaluation of partial solutions, an straightfoward access to reflection and transmission coefficients making it easy to increase or reduce them by a desired factor, and guarantees more numerical stability particularly at high frequencies. This same work was later published in Garambois and Dietrich (2002). Concomitantly, Hu and Wang (2000) formulated the expressions for the seismic and the electric fields in a fluid-filled borehole as well as in its adjacent homogeneous porous formations, and numerically simulated the wavefields generated by a point pressure source. Considering that the coseismic and the EM interface-generated fields have no impact on the acoustic field (i.e., no electro-seismic phenomena) Hu and Liu (2002) simplified Pride's equations allowing the seismic wavefields to be separately calculated before computing the electric fields generated, in order to study the validity of the departing assumption. Moreover, Ranada Shaw (2005) and Ranada Shaw et al. (2006) simulated well-to-well and vertical seismoelectric surveys with a numerical code quite similar to Garambois (1999).

Focusing in electroseismic prospecting White and Zhou (2006) followed the same steps as Garambois and Dietrich (2002) but using the formalism introduced in Ursin (1983) to compute reflection and transmission matrices; more recently, Gonçalves

(2019) followed the same idea to develope an alike numerical methodology, but generalized to seismoelectric and electroseismic problems. Hu et al. (2007), also studying electroseismic conversions, simulated EM and acoustic fields generated by a vertical dipole in a borehole while comparing two approaches: (1) using the full set of Pride's equations, and (2) supposing that the converted acoustic field has a negligible influence on the propagating EM fields, what simplifies the computation of a solution by decoupling Maxwell's and Biot's equations. Cui et al. (2007) and later Cui et al. (2011) modeled non-axisymmetric seismoelectric fields generated by eccentric sources in boreholes, with the wavefields computed in a manner similar to Schmitt and Bouchon (1985). Schakel and Smeulders (2008) and Schakel and Smeulders (2010b) and Schakel (2011) derived electrokinetic reflexion and transmission coefficients controlling seismic-to-electromagnetic and electromagnetic-to-seimic conversions in a fluid/porous-medium interface. These coefficients were later used for full-waveform simulation of experimental setups seeking a validation of numerical codes and their theoretical support (Schakel et al., 2011c; Schakel et al., 2011b; Schakel et al., 2012).

Through extension of the methodology presented in Chen (1993) and Chen (1999) to compute seismograms, Ren et al. (2010) proposed a numerical strategy to model coupled seismo-EM wave propagation in porous layered media. Later it was employed by Ren et al. (2012) in the study of the coseismic EM fields generated by finite faulting in porous media, where it was shown that instead of a point source, a combination of sources distributed along the fault, should be used to simulate near-field arrivals. The authors also showed that both the ruptures' starting position and its speed can affect the generated coseismic fields. Following the previous work, Ren et al. (2016a) derives reflexion and transmission coefficients for a solid-porous interface in order to study evanescent seismo-EM waves generated at these kind of boundaries. Ren et al. (2016b) extended the latter with a sensitivity study of the seismo-EM (evanescent and interfacial) fields, with a focus on application to earthquake seismology. More recently, Ren et al. (2018) performed a throughout quantitative study of the mentioned evanescent wavefield in which a mathematical expression for its amplitude decay was proposed. At last, Zheng et al. (2021) extended the numerical solution of Ren et al. (2010) to allow the placement of receivers and source in the same depth (or in very similar depths), using the method presented in Zhang et al. (2001).

All the above works explored semi-analytical solutions of Pride's electrokinetic theory (Pride, 1994). In that context, the methodology developed by Grobbe (2015) and Grobbe (2016) is noteworthy and leads to essentially the same results as that of Garambois (1999).

Lastly, even though they are not explicitly presented, approximate methods have also been employed to model seismoelectric phenomena in more complex geological settings. With that purpose the methods of finite-difference (Haines and Pride, 2006; Guan and Hu, 2008; Venzeler and Priimenko, 2009; Ji et al., 2022; Wang et al., 2021), finite-element (Zyserman et al., 2010; Zyserman et al., 2020), spectral-element (Morency et al., 2021), and discontinuous Garlekin (Meyer, 2021), have been employed.

1.3 Motivation and goals

Despite the efforts of the geophysical community to encourage the development of the seismoelectric method to explore the subsurface, there are still a couple of challenges to beat before the utopical future, where seismoelectrics is routinely used as an indirect methodology of near-surface exploration, becomes a reality. As reviewed in the previous section, after Thompson (1936) drew attention to the potential of seismoelectric phenomena in exploration geophysics, the governing equations of Pride (1994) were a turning point that opened the way to numerical studies of all phenomena involved. From 1994 until the present, through field, laboratory, and numerical studies, knowledge grew considerably and Grobbe et al. (2020) summarizes and discusses the current state of this research field.

Looking to help expand the understanding of seismoelectric phenomena, in this work a laboratory experiment was set in place and all measurement will be compared with numerical simulations, based on the theory of Pride (1994), using a numerical code conceived initially by Garambois and Dietrich (2002), adapted by Dietrich et al. (2018) to include the solution for the electric potential, and here to properly model the experimental set-up.

To my knowledge, in spite of a significant number of laboratory studies on the present subject (listed chronologically in the previous section), most either deals with the coseismic or the EM interface response individually. Moreover, in the laboratory, the interface response is seldom studied in the context of porous-to-porous media interfaces; fluid-to-porous media is the setting most often adopted, possibly due to

the fact it is easy to create in the laboratory (i.e., it is a simple matter of inserting a rock sample inside a water tank). The few laboratory studies that do look at porous-to-porous media configurations, fail to measure with precision the coseismic and the interface response at the same time. With that in mind, the present study will present an experiment that attained such objective and now can be used as a reference to reproduce different geological settings.

In a way, the present experimental research is a continuation of earlier efforts from Barrière et al. (2012), Bordes et al. (2015), Holzhauer et al. (2017), and Devi et al. (2018), all realized in the same research facility and using essentially the same sand as the porous medium. What distinguishes the present work from the preceding, is the fact EM interface responses will also be measured and studied. As in Holzhauer et al. (2017), the effect of fluid conductivity on seismoelectric wavefields will be investigated, but the influence of layer thickness on the interface response will be evaluated as well, in order to address the problem of how thin-layers change the amplitude of interface response, as done in Peng et al. (2017).

At last, following earlier comparisons between Pride's theory (Pride, 1994) and laboratory experiments (e.g., Block and Harris, 2006; Bordes et al., 2008; Zhu et al., 2016; Devi et al., 2018), the same will be done here using analytic solutions and numerical simulations to evaluate in a quantitative manner, the effectiveness of said theory in modeling seismic and seismoelectric waves in the experiment. Validating Pride's theory to the present experiments may open the path to explore and numerically simulate more complex situations in the future, like fluids with different viscosities, or temperature variations, what can eventually be used to reproduce real-world geological settings like geothermal and oil reservoirs, or aquifers.

1.4 Thesis outline

In chapter 2 of this thesis, most of the theoretical basis will be presented. At first, I will introduce all physical parameters, directly and indicrectly, affecting seismic-to-electromagnetic phenomena. After that, I will present the concepts underlying electrokinetic phenomena, at the boundary between solid grain and pore-fluid. Finally, in the last section, 2.3, the theory of Pride (1994) will be the subject, and I will discuss about its main characteristics.

After detailing the theory, chapter 3 explains, in a detailed manner, the numerical approach of Garambois and Dietrich (2002), and the adaptations performed as well.

In the end of the chapter, reciprocity tests confirm the implementation contains no error and can be employed to numerically simulate the experiments.

The experimental setup and all experiment-related topics will be presented in chapter 4. The equipments in the electric and seismic acquisition chain are discussed, and the choice of every significant parameter justified. Additionally, trials to improve the experimental setup that failed will also be treated.

Having detailed all the background needed for this study, in chapter 5 I will present two experiments, the first wiht an homogeneous medium and the second a layered medium. The measurements will be compared with numerical simulations in a quantitative way, and in the end I will focus on the interface response and how it is created when a P-wave reaches an interface.

Chapter 6 focuses on the EM interface response, studying how it can be affected when either the thickness of the layer or the fluid conductivity varies. In the end, chapter 7, I summarize the results, list all main conclusions, and discuss some perspective research that could complement this thesis.

2 Theoretical framework

2.1 Physical parameters of porous media

A porous medium is an assemblage of solid grains, the rock matrix, arranged in such a way that voids will exist in-between the grains, constituting the pore space (see Figure 2.1). The porous region will contain fluid, gas, or a combination of both, depending on the geological processes behind the rock genesis.

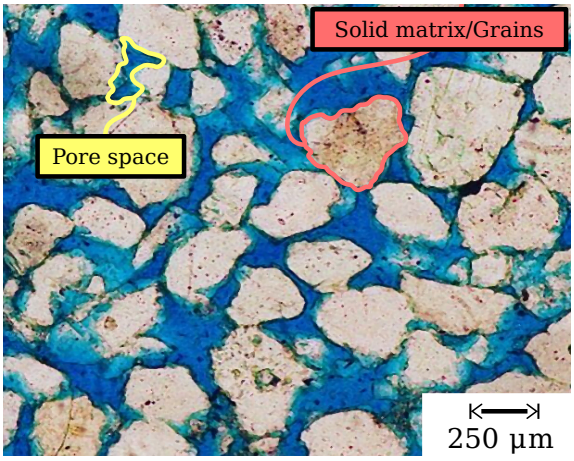

Figure 2.1: Depiction of microscopic view of a porous medium. Solid grains and pores are highlighted.

In this section these media will be discussed in terms of the physical properties characterizing both the solid and liquid/gas phases. The parameters discussed will allow for a physical description of any material classified as porous. They will be used in the subsequent sections as controlling parameters in the propagation of mechanical and electromagnetic disturbances in such porous materials.

2.1.1 Geometrical and transport parameters

Different pore connectivity models exist to describe the permeability of porous media (e.g., Katz and Thompson, 1986; Pape et al., 1999; Afagwu et al., 2021), most of them consist of theoretically-derived relations that were empirically adjusted to

describe a specific rock-type. The most widespread is the capillary tube model, or Kozeny-Carman model (Carman, 1956), in which a porous rock sample is subdivided into elementary volumes (with side-length L) containing a capillary tube of length l and radius r, and whose volume is analogous to the pore volume. Figure 2.2 illustrates this model.

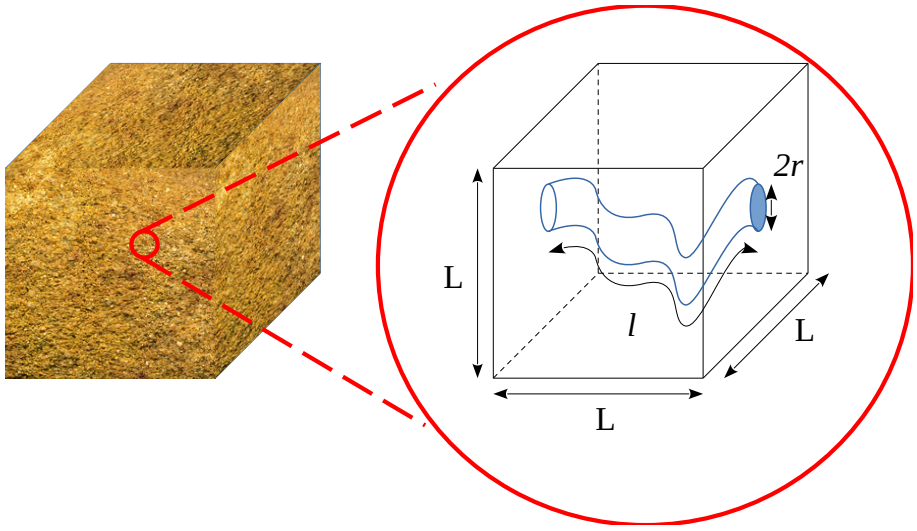

Figure 2.2: Depiction of the capillary model.

Though simplistic, this model can ease the understanding of the physical properties introduced in the rest of this section.

Porosity

In a rock, porosity quantifies the amount of void space (pores, fractures, cracks and vugs) in relation to the bulk volume. Auxiliary terms are employed when distinguishing between different kinds of porosity (see Schön (2015)), but for fluid flow/storage purposes the effective porosity, referring to interconnected pore space, is of main interested. It is defined as the volume ratio:

$$\phi = \frac{\text{pore volume}}{\text{bulk volume}}, \tag{2.1}$$

thus dimensionless.

The fraction of porous space for clastic rocks (of interest in this thesis) depends primarily on the grain's shape, diameter and distribution. Secondarily it will also depend on mechanical processes, like compaction and fracturing, and geochemical

processes, like grain dissolution and mineral precipitation. It can be seen that for the capillary model (Figure 2.2) the porosity can be expressed as: $\phi = (\pi r^2 l)/\mathrm{L}^3$.

To measure the effective porosity of a rock, a direct method consists of a comparison between the mass of a sample when it is dry (m_{dry}) and after saturation (m_{wet}). Considering V_{total} the volume of a sample, the following relation applies:

$$\phi = \frac{m_{wet} - m_{dry}}{\rho_f V_{total}}, \tag{2.2}$$

where ρ_f is the density of the saturating fluid. Whilst simple, the drawback of this method is that full saturation can not easily be attained by imbibition in ambient pressure and temperature. A possible solution is to depressurise the sample while it is immersed.

Viscous characteristic length

This parameter, Λ, was initially introduced in Johnson et al. (1987) as a weighted pore-surface to pore-volume ratio with the weigth depending on the local fluid velocity, and thus favoring pore throaths. A simpler interpretation of Λ comes when considering the capillary tube model, for which Johnson et al. (1987) showed that $\Lambda = r$, i.e., the capillary radius in figure 2.2. At last, the measurement of this parameter is usually based on the attenuation of high-frequency (considering Biot's theory) sound waves, see Leclaire et al. (1996).

Tortuosity

In the capillary tube model (Figure 2.2), the tortuosity expresses the deviation of the actual pore channel from a rigth cylinder, therefore it is related to the geometrical properties of the pore channel and the porosity. From its definition one can write:

$$\alpha_\infty = \frac{l}{\mathrm{L}} \geq 1. \tag{2.3}$$

To account for the tortuosity of pore channels, as defined above, in a wave propagation context, Biot (1956b) introduced a sinuosity factor and Stoll and Bryan (1970) a structure constant, both directly related to α_∞. Using physical relations developed in Biot (1956a) and considering a granular medium, with ellipsoid-shaped grains, Berryman (1980) found a relation between the tortuosity, the porosity and

a grain-dependent parameter r_B (with $0 \leq r_B \leq 1$, and $r_B = 0.5$ for spherical grains).

In real porous media, where the pore channels are irregular, theoretical predictions may fail. For that reason it is best to determine it experimentally (Stoll and Bryan, 1970). With this purpose, two experimental procedures to measure tortuosity are compared in Johnson et al. (1982), using fused-glass beads (177-210 μm diameter) to produce porous media of different porosities.

Formation factor

Another important geometrical factor, frequently considered in well-log interpretation, is the formation resistivity factor F. Its physical meaning was formally proposed by Archie (1942) as a ratio between the bulk resistivity of the porous medium ($1/\sigma$), and the resisitivity of the pore fluid ($1/\sigma_w$). Additionally, the following empirical relationship was indicated:

$$\mathsf{F} = \phi^{-m_c}. \tag{2.4}$$

It was established considering clean water-saturated sand formations, however it is often applied to other rock types, with proper adaptation (examples in Schön, 2015). Due to its important role in petrophysics, the term Archie's law is conveniently used, even though Equation 2.4 only holds when the solid phase of the porous medium is insulating; implying the absence of shale.

The exponent m_c, in Archie's work, was about 1.3 for unconsolidated sands while for consolidated sandstones it varied between 1.8 and 2. These observations are probably the reason m_c is, at times, called cementation exponent. Using samples with different sand compositions: quartz grains, glass spheres, shale particles, thin shell fragments, and combinations of both; Jackson et al. (1978) concluded that m_c depends strongly on the shape of grains, namely their sphericity, with values ranging from 1.2 for perfect spheroids and 1.9 for flattened spheroids[1]. Additionally, values between 1.4 and 1.6 were observed for natural (quartz) marine sands, what agrees with the observations of Archie (1942), and thus reinforces the validity of Equation 2.4.

[1] Formally an oblate or prolate spheroid.

A second equation, important because it implies a link between electrical and hydraulic properties, is:

$$\mathsf{F} = \alpha_\infty/\phi. \tag{2.5}$$

From this definition, the tortuosity is assumed numerically equivalent to the pore-geometry parameter affecting the pore fluid conduction in porous media (i.e., the resistivity).

To arrive at equation 2.5, Wyllie and Rose (1950) considered the capillary channel model and I will briefly recapitulate their reasoning for completness. Let's initially consider the highlighted volume in Figure 2.2 contains only the pore fluid, thus neither the solid nor the pore channel exist. If we connect a battery to this volume, with poles placed at opposed faces, the resistance across the sample will be:

$$R_1 = \frac{\mathrm{L}}{\sigma_w \mathrm{L}^2}.$$

Now, if we account for the fluid-filled cappilary channel, with constant cross sectional area, inside an insulating solid, the sample resistance becomes:

$$R_2 = \frac{l}{\sigma_w \phi \mathrm{L}^2}.$$

R_1 and R_2 are, respectively, the pore fluid and the porous medium resistances. By definition $\mathsf{F} = R_2/R_1$, thus:

$$\mathsf{F} = \frac{l/\mathrm{L}}{\phi} = \frac{\alpha_\infty}{\phi};$$

where Equation 2.3 was used.

While the formulation above lacks in physical details, Wyllie and Rose (1950) showed substantial agreement between experimental results and Equation 2.5 for clean porous media. Finally, Brown (1980) derived the cited relation using the differential equations governing the fluid flow inside the pore channels for the capillary model (see reference for details), thus linking Equation 2.5 to a widely accepted physical basis.

Fluid dynamic viscosity

This pore fluid property describes the shear forces within a moving fluid, thus it characterizes the easiness with which a fluid can flow. It can be thought of as the ratio between shear stresses and the spatial variation of shear strain inside a (fluid) volume (Feynman et al., 1963). Its units are $[\text{Pa} \cdot \text{s}]$ and, in here, the letter η will refer to this parameter.

Non-ideal fluids ($\eta > 0$) can be classified according to their homogeneity during flow. When significant density variation occurs a fluid is said compressible, while if the density remains constant it is an incompressible fluid.

Additionally, regarding the ratio between shear stresses and shear strain rate, fluids can be defined as Newtonian or non-Newtonian. For the first group, the ratio (η) is constant whereas for the second, it will show a dependency on the stress magnitude. Throughout this thesis, I consider the fluids incompressible and Newtonian.

Considering a porous medium, if the fluid is compressible a bulk viscosity, or second viscosity coefficient (Feynman et al., 1963), will change the fluid bulk modulus (defined in section 2.1.2) and, consequently, the velocity of propagation of P-waves. Pride et al. (1992) analyze the influence of the bulk viscosity in the context of poroelastodynamics, pointing that at certain cases it may have a significant contribution to attenuation.

Finally, in the context of the electrokinetic phenomena studied, Pride and Morgan (1991) describe a resistance to flow, of electrical nature, that happens when specific conditions are met, as an "apparent viscosity enhancement". This fact is neglected in Pride (1994), when the author develops the governing equations for seismoelectric phenomena, which this thesis uses as a reference.

Intrinsic permeability

When considering steady laminar fluid flow[2] inside the pores of a general porous medium, Darcy's law (see Schön (2015) for details) relates the average fluid flow ($\mathbf{v}$) to the pressure (p) gradient by:

[2] A steady flow is such that at every point inside the fluid, the velocity remains constant (Feynman et al., 1963). Laminar flow, as the term implies, means an orderly layering of fluid particles following smooth traveling paths.

$$\phi \mathbf{v} = \frac{k_0}{\eta}(-\nabla p). \tag{2.6}$$

The fraction in the right side expresses the resistance of the medium (fluid + solid frame) to fluid flow. Since η is the dynamic viscosity of the fluid, it accounts for the flow resistance within the fluid. Therefore k_0, the intrinsic permeability, accounts for flow resistance due to the geometrical characteristics of the pore channel (pore size and interconnection). This property is often expressed in Darcy units (1 Darcy $\simeq 10^{-12}$ m^2), even though it has the physical unit of area. A collection of permeability relations and models, considering different rock types, can be found in Schön (2015).

Finally, there is an important equation, relating all the geometrical parameters discussed above. It is defined as (Pride, 1994; Pride, 2005):

$$m \equiv \frac{\phi \Lambda^2}{\alpha_\infty k_0} = \frac{\Lambda^2}{k_0 \mathsf{F}}. \tag{2.7}$$

It comes from the model for dynamic permeability (a property discussed further along in this chapter) proposed by Johnson et al. (1987) and its value is usually between 4 and 8 (Pride, 1994) for a variety of porous media, as long as clean formations are considered. As a matter of fact, Sheng and Zhou (1988) and Charlaix et al. (1988) show numerical and experimental results suggesting m does not vary much under microstructural variations. Complementarily, Pride (2005) comments that for unconsolidated sediments and clean sandstones $m = 8$ is a satisfactory assumption; it is the value found when considering the simple capillary tube model (Johnson et al., 1987; Schön, 2015).

2.1.2 Mechanical parameters

Bulk density

For two-phase porous media, the bulk density ρ is simply the sum of each phase's density. Considering a medium whose solid frame has a density ρ_s, and that within its pores there is a fluid with density ρ_f:

$$\rho = \phi \rho_f + (1 - \phi)\rho_s. \tag{2.8}$$

Elastic moduli

An elastic material has the ability to return to its original state after the forces deforming it cease. The elasticity of most solid materials will hold as long the applied forces do not reach a cap. Hooke's law[3] describes the relation between the applied forces and the deformations produced in elastic bodies.

For homogeneous isotropic media, Hooke's law relates the displacements $\mathbf{u}$ and the stresses τ through the equation (Pride et al., 1992):

$$\tau_\xi = K_\xi \nabla \cdot \mathbf{u}_\xi \mathbf{I} + G_\xi(\nabla \mathbf{u}_\xi + \nabla \mathbf{u}_\xi^T - \frac{2}{3}\nabla \cdot \mathbf{u}_\xi \mathbf{I}); \tag{2.9}$$

where I is the identity matrix, $\nabla \cdot \mathbf{u}_\xi$ refers to volumetric strain and $\nabla \mathbf{u}_\xi$ to shear strain. Additionally, in case multi-phase media is considered, the subscript ξ will refer to the phase.

The constants K_ξ and G_ξ are the bulk and shear modulus, respectively[4]. The first is the ratio between hydrostatic stress and volumetric strain, while the second is the ratio between shear stress and strain. They have units of pressure (Pa), are intrinsic to a material, and will dictate its elastic behaviour (i.e., the velocity of mechanical wave propagation).

It is worth remarking that in the case of fluids and gases $G_{\xi=\text{f or g}} = -i\omega\eta$, where η is the (shear) viscosity discussed afterwards. In geophysical applications, most times $K_{\text{f or g}} >> |-i\omega\eta|$, therefore the second term in Equation 2.9 can be neglected; or to put simply: applied stresses in the fluid/gas phase will incur only volumetric strain (Pride et al., 1992).

Poroelastic incompressibilities

Because this thesis considers porous media, incompressibility moduli, conceptually equivalent to K_s, K_f, and K_g (defined above), expressing the poroelastic behaviour of the solid rock frame, the pore fluid, and the bulk rock, need to be defined.

Considering a porous rock sample subject to a constant confining pressure p_c, Pride (2005) defines the drained and the undrained bulk moduli (K_fr and K_G, re-

[3] See Feynman et al. (1963) for a derivation from first principles (applied force $\propto$ change in volume).

[4] Please, refer to Schön (2015) for examples of values considering different rock types.

spectively), as well as the undrained fluid-pressure to confining-pressure ratio B as:

$$K_{\mathrm{fr}} = -\left.\frac{p_c + \delta p_c}{\nabla \cdot \mathbf{u}_s}\right|_{\delta p_f = 0}, \tag{2.10a}$$

$$K_{\mathrm{G}} = -\left.\frac{p_c + \delta p_c}{\nabla \cdot \mathbf{u}_s}\right|_{\nabla \cdot \mathbf{w} = 0}, \tag{2.10b}$$

$$B = \left.\frac{p_f + \delta p_f}{p_c + \delta p_c}\right|_{\nabla \cdot \mathbf{w} = 0}. \tag{2.10c}$$

These relations were defined from a laboratory perspective, which I will also consider here. From Equation 2.10a, K_{fr} is inversely proportional to the volumetric change, of the sample, $(\nabla \cdot \mathbf{u}_s)$ that takes place when a variation in the confining pressure (δp_c) occurs. Measurements happen under the condition that pore fluid pressure is constant $(\delta p_f = 0)$, thus either the pores are empty or fluid/gas is allowed to flow inside the sample. In subsection 2.1.2, theoretical formulations for this modulus will be discussed.

Regarding the undrained modulus, it is measured from the sample's volumetric change when p_c varies, and no fluid flow happens $(\nabla \cdot \mathbf{w} = 0$[5]$)$. That means the sample is isolated in a way that fluid can neither enter nor leave the rock. In agreement with the litterature, K_{G} will be designated as Gassmann modulus, after Gassmann (1951)[6].

Under the condition $\nabla \cdot \mathbf{w} = 0$, fluid will be constrained inside the pores. Therefore an increase in p_c induces an increase in p_f, which will be controlled by B, or Skempton's coefficient, referring to Skempton (1954) where B first appeared. Even though it does not appear in the equations governing seismic wave propagation in porous media (Equations 2.42a, 2.42b, and 2.42c), the derivation of Biot-Gassmann relations, discussed in the next sub-section, depends on B (Pride, 2005).

Finally, it is primordial to state that, for all moduli treated in this chapter, the porous material of interest is macroscopic homogeneous and isotropic. Additionally, fluid viscosity is small enough to be disregarded such that the shear modulus will not depend on the fluid.

[5] $\mathbf{w}$ is defined in equation 2.39.

[6] An exact translation to english is available in "On Elasticity of Porous Media by F. Gassmann, Zürich, 1951" (2013).

Biot-Gassmann relations

When a compressional wave disturbs a (biphasic) porous media, its velocity depends on the undrained bulk modulus, since both solid and fluid/gas play a role. The value of K_{G} is usually obtained from laboratory considering a well known fluid/gas. Nevertheless, the fluids filling the pores of naturally occurring porous rocks may not be known beforehand, in the context of indirect subsurface investigation. For that purpose a convenient equation exists (Gassmann, 1951):

$$K_{\mathrm{G}} = K_{\mathrm{s}}\left(\frac{K_{\mathrm{fr}} + \mathfrak{Q}}{K_{\mathrm{s}} + \mathfrak{Q}}\right) \qquad \text{with} \qquad \mathfrak{Q} = K_{\mathrm{f}}\frac{K_{\mathrm{s}} - K_{\mathrm{fr}}}{\phi(K_{\mathrm{s}} - K_{\mathrm{f}})}. \tag{2.11}$$

Considering the shear modulus of the saturated rock is equivalent to the frame shear modulus[7], using velocity measurements when a known fluid saturates a sample and Equation 2.11, it is possible to predict the mechanical behaviour of the rock sample for other fluid or a combination of fluids (Schön, 2015).

Other forms of K_{G} exist, following the algebraic manipulation of Equation 2.11 (Pride, 2005; Schön, 2015). For convenience I will adopt the expression of Pride (1994):

$$K_{\mathrm{G}} = \frac{K_{\mathrm{fr}} + \phi K_{\mathrm{f}} + (1+\phi)K_{\mathrm{s}}\mathfrak{Q}}{1 + \mathfrak{Q}} \qquad \text{with} \qquad \mathfrak{Q} = \frac{K_{\mathrm{f}}}{\phi K_{\mathrm{fr}}^2}[(1-\phi)K_{\mathrm{s}} - K_{\mathrm{fr}}]. \tag{2.12}$$

Biot (1962b) introduced two additional incompressibilities, directly related to changes in pore fluid pressure:

$$M = -\frac{p_f + \delta p_f}{\nabla \cdot \mathbf{w}}\bigg|_{\nabla\cdot\mathbf{u}_s=0}, \tag{2.13a}$$

$$C = -\frac{p_f + \delta p_f}{\nabla \cdot \mathbf{u}_s}\bigg|_{\delta\cdot\mathbf{w}=0}. \tag{2.13b}$$

For a rock sample, M relates an increase/decrease of fluid/gas to changes in the pressure inside the pores, considering the sample volume does not vary. Conceptually, C is dependent on K_{G} and B; it relates variations in pore fluid pressure to changes in the sample volume, with the constraint of no fluid flow. From Equations 2.13b, 2.10b, and 2.10c, $C = BK_{\mathrm{G}}$.

[7] $G_{\mathrm{f}} \simeq 0 \implies G = G_{\mathrm{fr}}$, where G equals to the shear modulus of the porous medium (solid+fluid/gas).

From Pride (1994) M and C will be expressed as a function of the previously discussed moduli:

$$M = \frac{K_\mathrm{f} + K_\mathrm{s}\mathfrak{Q}}{1+\mathfrak{Q}}, \tag{2.14a}$$

$$C = \frac{K_\mathrm{f}}{\phi(1+\mathfrak{Q})}. \tag{2.14b}$$

At last, the stiffness tensor (introduced in Biot (1962b)), governing the velocity of compressional (P) waves, is defined, as usual, as:

$$H = K_\mathrm{G} + 4G_\mathrm{fr}/3. \tag{2.15}$$

Theoretical models for K_fr and G_fr

Even though frame bulk and shear moduli can be obtained from laboratory measurements, it is useful to have a supporting theoretical model, in case experimental values are not available. Most models will relate K_fr and G_fr to physical parameters that are more accessible experimentally, like wave velocity and porosity (for examples refer to Schön, 2015).

For both consolidated and unconsolidated rocks, I will consider the models presented in Pride (2005). For the first case a model depending on the degree of consolidation between the grains was proposed, while for the second case the model is based on Walton (1987), and media is idealized as a random packing of identical spheres.

When dealing with consolidated media, the frame moduli expressions are as follows:

$$K_\mathrm{fr} = K_\mathrm{s}\frac{1-\phi}{1+c\phi} \quad \text{and} \quad G_\mathrm{fr} = G_\mathrm{s}\frac{1-\phi}{1+1.5c\phi}. \tag{2.16}$$

Parameter c is the consolidation parameter, inversely proportional to the degree of consolidation. Pride (2005) suggests values between 2 and 20 for consolidated sandstones, but it is advised to adjust it using seismic velocities.

For unconsolidated media, the model considers that an increase in the effective pressure ($p_{eff} = p_c - p_f$) leads to more grain-to-grain contacts (n_o). Expressions are:

$$K_\mathrm{fr} = \frac{1}{6}\left[\frac{4(1-\phi)^2 n_o^2 p_o}{\pi^4 C_s^2}\right]^{1/3} \frac{(p_{eff}/p_o)^{1/2}}{\left[1+(16\frac{p_{eff}}{9p_o})^4\right]^{1/24}} \quad \text{and} \quad G_\mathrm{fr} = 3\frac{K_\mathrm{fr}}{5}. \tag{2.17}$$

The parameter p_o represents a limiting pressure. Beyond this value, the maximum number of grain-to-grain contacts will have already been achieved. Moreover, C_s is a compliance parameter (inverse of incompressibilities) defined by:

$$C_{\mathrm{s}} = \frac{1}{4\pi}\left(\frac{1}{G_{\mathrm{s}}} + \frac{1}{K_{\mathrm{s}} + G_{\mathrm{s}}/3}\right). \tag{2.18}$$

As a reference, Pride (2005) suggests the values: $8 < n_o < 11$, and $p_o = 18$ MPa, for random sand packs. These two values, together with p_{eff}, are the free parameters of the model; they need adjusting to match the measured seismic velocities.

2.1.3 Electromagnetic parameters

Fluid molarity and conductivity

Electric conductivity is an intrinsic property of a material that indicates its propensity to allow flow of electric charges. Complementarily, molarity refers to the amount of chemical species in a solution. In the case of electrolytes, conductivity will be a function of molarity.

Despite a lack of information about the exact chemical constituents of the pore fluid used during this thesis, for practical purposes it will be considered a binary symmetric (NaCl) water-based electrolyte. The fluid used during experiments will be detailed in chapter 4.

Under the mentioned constraint three theoretical models, relating fluid conductivity σ_{f} [S/m] and molarity $\mathtt{M}_{\mathrm{f}}$ [mol/L], will be presented, with two of them accounting for the influence of temperature. The first is a simple equation relating σ_{f} to the individual conductivities of each l-species ion within the fluid:

$$\sigma_{\mathrm{f}} = \sum_{l=1}^{L} (ez_l)^2 b_l \mathcal{N}_l, \quad \text{with} \quad \mathcal{N}_l = \mathtt{M}_{\mathrm{f}} \mathcal{N}_{\mathrm{A}},$$

with e the elementary charge, z_l the valence of each ionic specimen, b_l the corresponding mobility (velocity per unit force), $\mathcal{N}_A$ is Avogrado's number, and $\mathcal{N}_l$ the ionic density. Because there are only two types of ions to be accounted for (L = 2, $z_1 = -z_2$, and $\mathcal{N}_1 = \mathcal{N}_2$), the previous equation can be simplified to:

$$\sigma_{\mathrm{f}} = (ez_1)^2 \mathtt{M}_{\mathrm{f}} \mathcal{N}_{\mathrm{A}} (b_1 + b_2). \tag{2.19}$$

A second equation, proposed by Sen and Goode (1992)[8], and empirically derived as a function of molality [mol/Kg] (molality=molarity because I consider water) and temperature T (in Celsius), is:

$$\sigma_{\mathrm{f}} = (5.6 + 0.27T - 0.00015T^2)\mathtt{M}_{\mathrm{f}} - \left(\frac{2.36 + 0.099T}{1 + 0.214\sqrt{\mathtt{M}_{\mathrm{f}}}}\right)\mathtt{M}_f^{3/2}. \tag{2.20}$$

The third relation, as the previous, expresses σ_{f} as a function of temperature and molarity (Bigelow 1992, as cited in Schön 2015):

$$\sigma_{\mathrm{f}} = \left(0.0123 + \frac{3467.5}{58443\mathtt{M}_{\mathrm{f}}^{0.955}}\frac{81.77}{1.8T + 38.77}\right)^{-1}. \tag{2.21}$$

Figure 2.3 compares all three equations. An increase of conductivity with temperature is evident for both models accounting for this parameter. Additionally, the third equation leads to sligthly higher conductivities (for a fixed molarity) than the second equation. Considering $\mathtt{M}_{\mathrm{f}} = 1\mathrm{E}-3$ mol/L, in Figure 2.3a the first model is sufficiently close to the second for temperatures between 13 and 15 °C, while in Figure 2.3b the first and third model superpose when temperatures are between 6.5 and 7.5 °C.

In general the increase in σ_{f} due to temperature is proportional to molarity. Again, for $\mathtt{M}_{\mathrm{f}} = 1\mathrm{E}-3$ mol/L, a 2 °C variation in model 2 leads to a change of about 6% in σ_{f}; in model 3 the same temperature fluctuation will create a $\simeq 7\%$ change in the value of σ_{f}. This observation may be important to field applications but, as will be seen in Chapter 4, it will play a minor role here, since temperatures were kept constant and the condition $\mathtt{M}_{\mathrm{f}} < 1\mathrm{E}-3$ mol/L was satisfied, most of the times.

Permittivity

A material's (absolute) permittivity ϵ_ξ [F/m] characterizes its electric polarizability. It means that, for a rock (dielectric) sample subject to an external electric field, electric dipoles will appear due to the displacement of electrons as well as ions (Wachter and Hoeber, 2006), what will result in an electric displacement field taking place. The ratio between external and displacement fields defines ϵ_ξ; the constitutive relation in Equation 2.37 expresses this concept.

[8] An erratum to this paper exists ("To: "Influence of temperature on electrical conductivity of shaly sands" by P. N. Sen and P. A. Goode (January 1992 GEOPHYSICS, p. 89–96)" 1992). It concerns the equation presented here. Therefore it is advisable to check it.

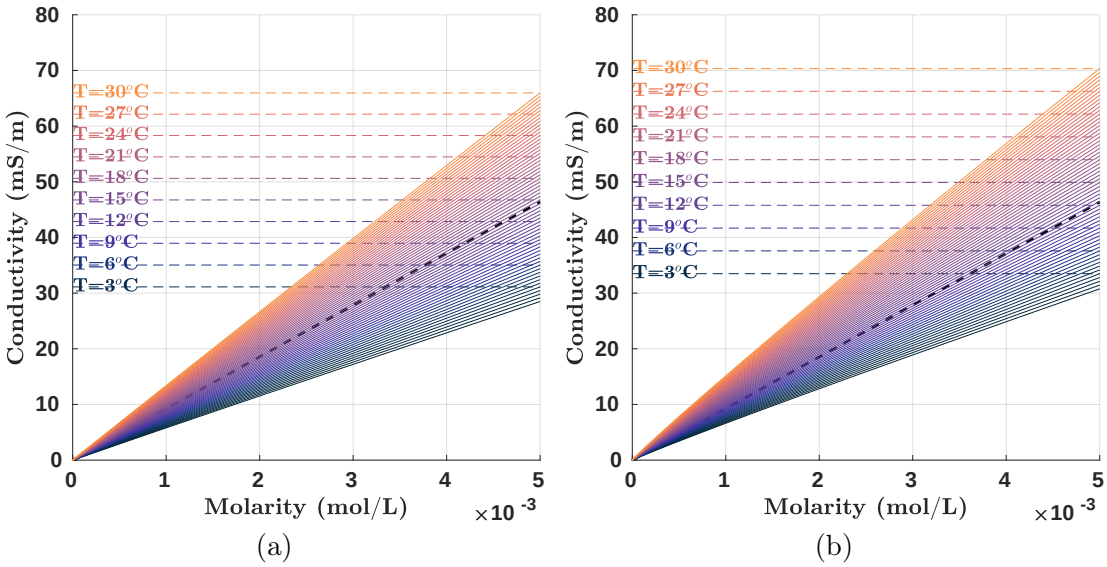

Figure 2.3: Comparison of equations for fluid conductivity. In both figures the black line represents Equation 2.19. (a) compares the latter with Equation 2.20 and (b) with Equation 2.21.

The dielectric constant κ_ξ, or relative permittivity, is a value relative to the vacuum permittivity ϵ_0: $\kappa_\xi = \epsilon_\xi/\epsilon_0$. It is convenient to use the normalized value, κ_ξ, to avoid the manipulation of numbers close to the negative twelfth power of ten.

In lossy dielectrics, ϵ_ξ is a complex number whose imaginary part contributes to attenuation (of electromagnetic waves). The frequency dependent expression is (Wachter and Hoeber, 2006):

$$\epsilon(\omega)_\xi = \epsilon_\xi + i\sigma(\omega)_\xi/\omega.$$

Considering porous media, for the frequency-dependent conductivity of the solid grains (defined later, in equation 2.51) it is safe to affirm $\sigma(\omega)_\mathrm{s} \ll 1$. This way, $\epsilon(\omega)_\mathrm{s}{=}\epsilon_\mathrm{s}$ is a valid assumption. This is not applicable to the fluid phase since $\sigma(\omega)_\mathrm{f} \gg \sigma(\omega)_\mathrm{s}$, and depending on the molarity of the electrolyte, the factor $\sigma(\omega)_\mathrm{f}/\omega$ may have a considerable value.

From now onwards the terms permittivity and dielectric constant will only refer to the real part, without distinction of phase. The frequency-dependent value will show up again later with another definition.

Regarding the values of κ_ξ, Figure 2.4 shows a global picture of the values considered (at radio frequencies and ambient temperature) for the most significant rock constituents, from a near-surface exploration perspective.

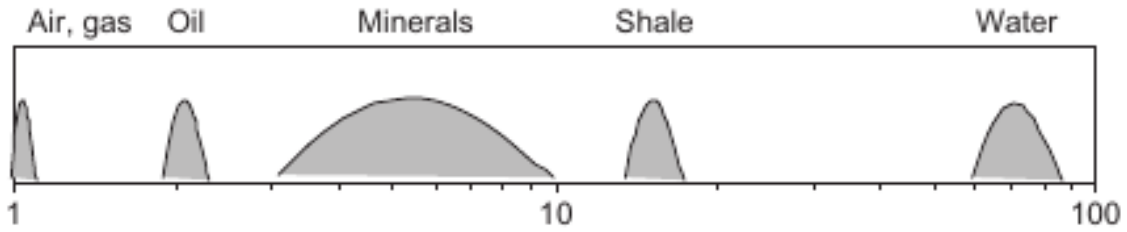

Figure 2.4: Approximate range of the dielectric constant considering some key rock components. Extracted from Schön (2015).

As for σ_f, κ_f will have a dependency on $\mathtt{M}_f$ and temperature. Both Schön (2015) and Holzhauer (2015), based on the same empirical equation, note that molarity does not play a big role on the values of κ_f. An increase in temperature, on the other side, tends to reduce the dielectric constant considerably; in the model studied by these authors, a change in temperature from 15 to 40 °C leads to a 10 % reduction in the value of κ_f.

When dealing with the solid, κ_s is frequently considered a constant, in the case of quartz a value around 4. Nevertheless, it will also depend on the temperature. Stuart (1955) and Gubkin et al. (1986) observe, from experimental data in the [20 –400] °C range, that there's a limiting temperature separating two zones. First, for temperatures below the threshold κ_s remains practically unchanged. Above the limit there is a sharp rise. The temperature at which the trend changes also increased with the frequency, its value was about 200 and 250 °C for 4 and 90 kHz, respectively.

Magnetic permeability

This property (designated here as μ) controls a material's response (its magnetic induction) to external magnetic fields. It is directly related to the concept of diamagnetic materials, those able to create contraposing magnetic fields in response to applied ones. For minerals commonly ocurring in soil and rocks, this property's value is sufficiently close to the magnetic permeability of vacuum, μ_0 [$VsA^{-1}m^{-1}$] (Schön, 2015). Therefore, μ_0 is often assumed to be the value of a rock's magnetic permeability.

Fluids are no exception to the rule and play only a minor role in the bulk magnetic permeability of a porous rock (see Schön (2015) for examples), such that using μ_0 is an adequate choice, as long as paramagnetic and ferromagnetic minerals (e.g., hematite and magnetite) are not present.

Additionally, Ali and Potter (2012) show experimentally that μ, for pure diamagnetic materials, like quartz and water, does not depend on temperature. This may change if quantities of paramagnetic materials, even in small proportions, compose the rock.

2.2 Electrokinetic phenomena at the pore scale

Among other seismic to electromagnetic conversion phenomena[9], those of electrokinetic origin are the focus of this thesis. In a fluid-filled porous medium, it will arise when the charges, contained within the electrolyte filling its pores, move in response to propagating mechanical waves.

In the case of compressional waves, the difference of pressure in a wavelength creates zones with more or less concentration of ions. It is the movement of these ions, in-between compressed and dilated regions, that creates a streaming current. The latter leads to a local electric field and, consequently, a potential difference (streaming potential) in a half-wavelength. Additonally a conduction current will oppose the streaming one, restoring the electro-neutrality.

Shear waves can also generate streaming currents following the movement of ions in a porous medium. Associated with these currents, a magnetic field will appear, as well as a weak electric field, induced by the latter. Though small in magnitude and often disregarded, this phenomenon has already been confirmed experimentally by Bordes et al. (2006).

In a similar manner, an electromagnetic wave will create an electroosmotic flow; that means the electrolyte will have a relative movement with respect to the rock matrix. In turn, an electroseismic wavefield will appear. This effect is the reciprocal of the aforementioned streaming potential, but it will not be explored in this thesis.

[9] Piezomagnetic effects linked to earthquakes are often discussed in seismology (Stacey, 1964; Johnston, 2002).

2.2.1 The electric double layer

When an electrolyte fills the pores of a rock, the initially neutral solid surface will chemically adsorb anions. Consequently, a region that contains mainly counterions will materialize nearby every grain's surface. This ionic structure is the electric double layer, and it constitutes the physical system that converts, by electrokinetic means, mechanical into electrical energy.

Despite the plurality of double layer models, the one proposed by Stern (1924) is frequently used (see Bockris and Reddy, 1970, sec. 7.4). It considers a double layer subdivided in two. The region closer to the solid surface is the Stern layer, in which ions are practically immobile. The second is the diffuse layer, where the position of each ion will be controlled by the forces of attraction (to the adsorbed layer) and diffusion (to the neutral solution). A particular modification of this model is generally accepted, it was formulated by Grahame (1947) and proposes to split the Stern layer in two. The first, known as inner Helmholtz plane (IHP), contains only adsorbed anions, while the second, or outer Helmholtz plane (OHP), contains cations bound to the solid/anion plane by van der Waals and electrostatic forces (Pride and Morgan, 1991).

Figure 2.5 depicts the Stern-Grahame electric double layer model. When relative solid-to-electrolyte movement takes place, the shear, or slipping, plane is the name of the boundary that separates the outer and the inner parts of the diffuse layer. While the latter has ions more firmly bounded to the Stern layer's ions, the outer part will move with the flow. Even though there is a lot of uncertainty about the shear plane location, it is generally accepted that the ionic distribution in the outer diffuse layer will follow the Poisson-Boltzman equation (Davis and Kent, 1990), and the electric potential at the shear plane is the ζ potential. I will discuss this parameter, characteristic to a double-layer, in the next subsection.

The local conductivity, as a function of the distance from the solid surface, also appears in Figure 2.5, considering a case where surface conductivity σ_s is greater than the fluid conductivity. σ_s refers to electrical conduction inside the double layer, and its value has contributions from both the Stern and the diffuse layer, the first being the most significant (Revil and Glover, 1998; Leroy and Revil, 2004). For quartz-based rocks this value is usually neglected when $\sigma_f > 1$ mS/m. Conversely, if clay minerals are present or ionic concentrations are small, σ_s should be accounted for (Jouniaux and Zyserman, 2016). As a matter of fact this parameter will play an important part in my numerical simulations.

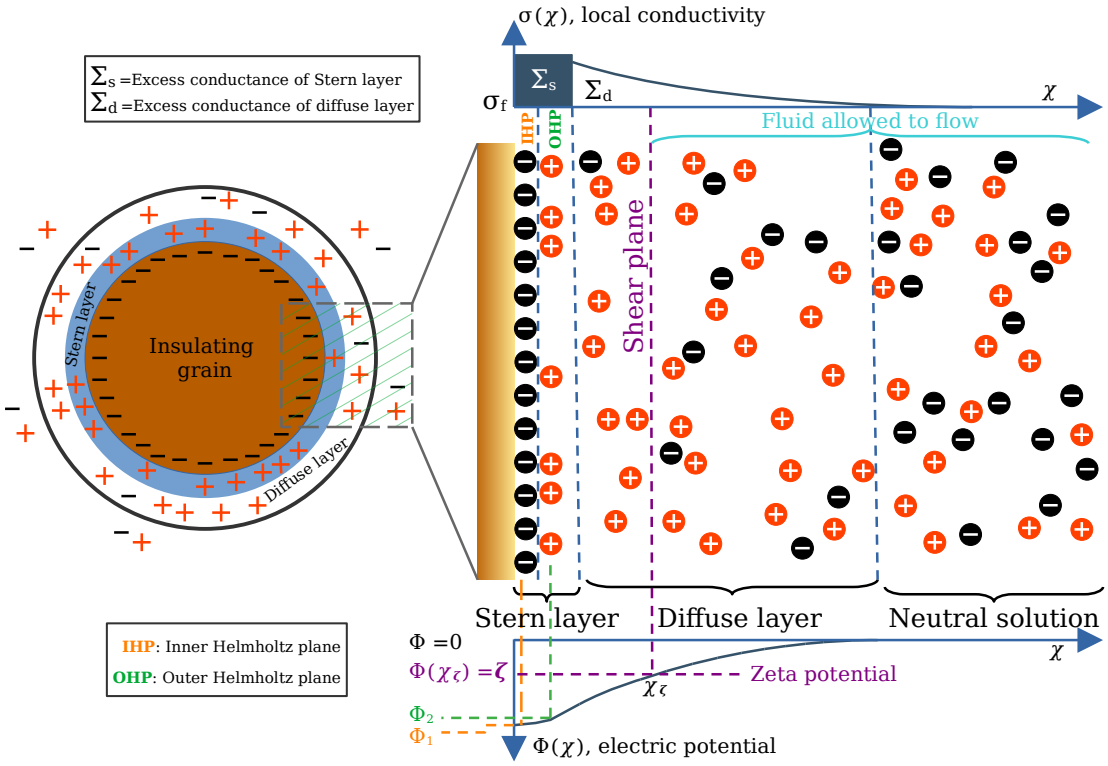

Figure 2.5: Conceptual model of the electric double layer making up the boundary between the solid rock grains and the pore electrolyte (conceived after Revil and Florsch (2010) and Glover and Jackson (2010)). Every positive and negative symbol corresponds, respectively, to cations and anions. Three main regions exist, depending on the density of ions and on their capacity to move. Both the electric potential and the local conductivity vary with distance χ from the grain's surface. With increasing χ, Φ tends towards zero, and $\sigma(\chi)$ decreases until σ_f.

2.2.2 Electric potential in the diffuse layer

As discussed above, a part of the liquid phase inside the pores will be strongly attached to the solid grains, by both chemical and electrostatic forces. Therefore, when fluid flows, a slipping plane will appear separating the fluid molecules bound to the solid phase and those moving independently. Every porous medium has a characteristic electric potential at this boundary, ζ.

Considering the potential $\Phi(\chi)$ as a function of distance χ from the solid surface (see Figure 2.5), in the diffuse layer it will follow Poisson's equation (for electrostat-

ics), with the charge density expressed using a Boltzmann distribution (Pride, 1994; Jouniaux and Ishido, 2012):

$$\nabla^2\Phi = -\sum_{l=1}^{L} \frac{ez_l\mathcal{N}_l}{\epsilon_\mathrm{f}} \exp\left(-\frac{ez_l}{k_B T}\Phi\right).$$

All variables in this equation were introduced in the previous section, except for k_B which refers to Boltzmann constant.

Considering $|ez_l\zeta/k_\mathrm{B}T| \ll 2$, the Debye-Hückel approximation (Pride and Morgan, 1991; Pride, 1994) allows the solution:

$$\Phi = \zeta\exp(-(\chi-\chi_\zeta)/d_\mathrm{Db}), \quad \text{with} \quad d_\mathrm{Db}^{-2} = \sum_{l=1}^{L} \frac{e^2 z_i^2 \mathcal{N}_l}{\epsilon_\mathrm{f} k_\mathrm{B} T}. \tag{2.22}$$

χ_ζ is the distance of the slipping plane from the solid surface and d_Db is the Debye length, the approximate thickness of the diffuse layer. The validity of this solution is the subject of the appendix A of Pride (1994).

From equation 2.22 it is clear the potential decays exponentially away from the slipping plane, and that the diffuse layer thickness is inversely proportional to the electrolyte's molarity. Moreover, the value of Φ at the slipping plane, ζ, has a direct influence in the electrokinetic coupling (as will be seen in the next section), therefore it is primordial to understand how ζ varies in different physical conditions and which properties of the porous medium will impact it the most.

A dependence of ζ on PH, temperature, rock and fluid composition was experimentally confirmed by multiple studies (e.g., Ishido and Mizutani, 1981; Lorne et al., 1999a; Revil et al., 1999a; Guichet et al., 2006; Walker and Glover, 2018). Therefore, given a specific physical parameter, an empirical equation can be found, in the litterature, to describe how ζ depends on it. As an example, Pride and Morgan (1991) considers the situation where the porous medium, at T = 25 °C and PH = 7, is a quartz-based rock whose pores are filled with an NaCl or KCl electrolyte. They derive a relation between ζ and $\mathtt{M}_\mathrm{f}$, considering the range $[10^{-7}, 10^{-1}]$ mol/L:

$$\zeta = 0.008 + 0.026\log_{10}\mathtt{M}_\mathrm{f}. \tag{2.23}$$

This equation is a fair approximation for clean rocks and I will use it in the numerical simulations.

It is worthy to remark that Revil et al. (1999a) came up with a theoretical equation similar to 2.23, but accounting for PH and temperature dependence. They also considered the effect of surface conductance Σ_s. Their formula can be conveniently written as:

$$\zeta = b(T)\log_{10}\mathtt{M}_f + c(T, PH, \Sigma_s). \tag{2.24}$$

The expressions for coefficients b and c above can be found in the original work. Whereas this equation is valid when the mineral is quartz, Revil et al. (1999b), complementarily, proposed an empirical relation for clay dominated porous media.

Furthermore, Guichet et al. (2003) found for quartz-rich sand (with a 300 μm mean diameter), M_f in the range [10 - 25] mS/m, room temperature (19.8 – 27.4 °C), and PH between 7.3 and 8.7, the following relation:

$$\zeta = -0.0146\log\sigma_f - 0.0854. \tag{2.25}$$

The behaviour of ζ predicted by this equation is in disagreement with other results reported in the litterature (e.g., Walker and Glover, 2018). However, anomalous values of ζ have been reported more than once (Ishido and Mizutani, 1981; Guichet et al., 2006; Li et al., 2018), often related with the presence of specific ions in the pore fluid. Therefore the validity of Equation 2.25 will depend on the characteristics of the pore fluid in the medium.

2.2.3 Streaming potential coefficient

In thermodynamic systems, the interaction between simultaneous irreversible transport processes was described by Onsager (1931a) and Onsager (1931b) using the linear relation:

$$\mathcal{J}_i = \sum_j L_{ij}\mathcal{X}_j, \tag{2.26}$$

which relates the applied forces $\mathcal{X}_j$ to the fluxes $\mathcal{J}_i$ created, using a coupling coefficient L_{ij}.

When electrokinetic phenomena are implied, the force applied can either be a pressure gradient ∇p or a voltage difference $\nabla\Phi$. Therefore, considering constant

temperature and a homogeneous ionic distribution in the fluid, the electric current density $\mathbf{J}$ [A/m^2] and the flow velocity $\mathbf{v}$ [m/s] respect the expressions:

$$\mathbf{J} = \sigma_{\mathrm{B}}(-\nabla\Phi) - L_{m0}\nabla p; \tag{2.27a}$$

$$\mathbf{v} = \frac{k_0}{\eta}(-\nabla p) - L_{e0}\nabla\Phi. \tag{2.27b}$$

σ_{B} is the bulk conductivity, accounting for fluid and surface conductivity, L_{e0} characterizes the fluid flow generated by electric forces, and L_{m0} the electric currents due to mechanical forces. Moreover, Onsager's reciprocity relations imply $L_{m0} = L_{e0}$ [A/(Pa · m)].

Disregarding the terms representing coupling of forces in Equations 2.27, the first of them (2.27a) is Ohm's law while the second (2.27b) is Darcy's law (discussed in 2.1.1).

Considering a porous medium, creating a gradient of pressure will lead to fluid flow that drags the excess ions near the slipping plane, and as a consequence, a streaming current density $\mathbf{J_s}$ will take place. The charge imbalance generated by the latter creates a potential gradient that itself will induce a conduction current density $\mathbf{J_c}$, in order to ensure the electrolyte neutrality. When the system reaches the equilibrium, no electric current should exist and Equation 2.27a can be written as:

$$\frac{\nabla\Phi}{\nabla p} = -\frac{L_{m0}}{\sigma_{\mathrm{B}}} = C_{ek}; \tag{2.28}$$

which is the accepted definition of the streaming potential coefficient C_{ek}[V · Pa].

The Helmholtz-Smoluchowski equation (Overbeek, 1952) details the relation between C_{ek}, ζ and pore fluid properties for the capillary model (Figure 2.2), considering that only the fluid conductivity σ_{f} influences the conduction currents (i.e., σ_{B} = σ_{f}). The expression is:

$$C_{ek} = \frac{\epsilon_{\mathrm{f}}\zeta}{\eta\sigma_{\mathrm{f}}}. \tag{2.29}$$

Surface conductivity σ_{s} may be accounted for in C_{ek} by substituting σ_{f} with an effective conductivity σ_{eff} in the pore fluid (Jouniaux et al., 2000). In the litterature, σ_{eff} is usually expressed as a function of pore-geometry parameters (Overbeek, 1952;

Ishido and Mizutani, 1981; Johnson et al., 1986; Morgan et al., 1989). The following equation generalizes the existing relations for porous media:

$$\sigma_{\text{eff}} = \sigma_{\text{f}}\left(1 + \frac{2\Sigma_{\text{s}}}{\Lambda\sigma_f}\right), \tag{2.30}$$

which is only valid for $2\Sigma_{\text{s}}/\Lambda \ll \sigma_{\text{f}}$ (Johnson et al., 1986).

Based on Revil et al. (1999b), Guichet et al. (2003) and Guichet et al. (2006) propose:

$$\sigma_{\text{eff}} = \sigma_{\text{f}}[1 + m_c(\mathtt{F} - 1)\sigma_{\text{s}}/\sigma_{\text{f}}], \tag{2.31}$$

considering the high-salinity domain $\sigma_{\text{f}} \geq 5(m_c - 1)\sigma_{\text{s}}$, full saturation, and σ_{s} estimated from the ratio of $2\Sigma_{\text{s}}$ and the mean grain radius of the porous medium.

At last, outside the high-salinity domain (as defined above) Revil and Glover (1998) propose a relation accounting also for the behaviour of the ions in the pore fluid. The importance of discussing about σ_{s} will become evident when analysing the results of this thesis.

2.3 Governing equations of seismoelectromagnetic phenomena

A two-phase (solid and fluid electrolyte) porous grain assemblage, whose phases are continuously distributed in a macroscopic region (i.e., dimensions much greater than those of grains), leads to coupled mechanical and electromagnetic (EM) fields in the presence of a disturbance. The corresponding microscopically driven mechanism (of coupling) is the interaction between adsorbed excess charge in the grains' surface and mobile ions in the fluid (as described in the previous section).

The theory of poroelasticity for fluid (compressible viscous) saturated porous solids, describing combined solid and fluid average motion in response to a propagating stress wave, is conventionally credited to Biot (1956a), Biot (1956b), Biot (1962a), and Biot (1962b), even though there are other works devoted to the same problem (Kosten and Zwikker, 1941; Frenkel, 1944; Pride et al., 1992)[10]. Assuming a thin electric double layer (Stern, 1924; Bockris and Reddy, 1970) in the surface of every grain, and applying an averaging theorem (Slattery, 1967; Whitaker, 1969)

[10]Pride and Garambois (2005) compare equations obtained in Biot (1956a) and Biot (1956b) to the developments of Frenkel (1944). Authors conclude the latter contributed as much as Biot's to deduction of poroelasticity equations, and suggest the reference *Frenkel-Biot* equations is as appropriate as the currently employed term: *Biot equations*.

to the microscopic Maxwell's and Biot's equations, Pride (1994) establishes a complete electrokinetic theory for the integrated acoustic and electromagnetic fields in saturated porous media.

Considering a homogeneous isotropic whole space, and departing from the mentioned theory, Pride and Haartsen (1996) solved the governing equations in the case of plane waves and point-sources, inferring the existence of two longitudinal waves (fast and slow P-waves) and two transverse (shear and EM-wave); besides deriving the boundary conditions holding at an interface between two distinct porous media. In complement, Block and Harris (2006) and Schakel and Smeulders (2010b) studied the specific solutions for a fluid-porous medium interface, and Warden et al. (2013) described and adaptation for partial saturation.

2.3.1 Pride's electrokinetic formulation

Premises for validity and limitations

The foundations of the hereafter discussed theory were built under a set of limiting conditions. Knowledge about these is primordial to determine which systems can be modeled by the considered formulation. As in Bordes (2005), Warden et al. (2012) and Holzhauer (2015) the main assumptions are listed:

- All disturbances are linear, meaning they obey the superposition principle.
- The saturant is an ideal electrolyte, meaning freely moving ions (i.e., roughly satisfied by considering concentrations smaller than 1 mol/L).
- Medium as well as the porous solid frame/matrix are isotropic and full saturation takes place.
- Disturbance-induced diffusion (currents related to Lorentz forces) are neglected, what reciprocally implies satisfaction of: (1) solid's dielectric constant is considerably small in relation to the fluid's; and (2) thickness of the double layer is significantly smaller than the grain's radius of curvature ($d \ll \Lambda$), allowing for a planar representation of this layer on the surface of grains.
- Wavelengths must be greater than grain size.
- Grains are randomly oriented such that the volumetric average polarization will be zero, thus suggesting piezoelectric effects won't exist.
- Adsorbed surface-charge density is uniform, implying no free charge can be induced in the grains' surface and, consequently, no chemical reactions capable of invalidating these suppositions.

- Before the disturbance no steady currents or static magnetic fields will exist (static-equilibrium).
- Magnetic susceptibilities of fluid and solid are presumed negligible, therefore disconsidering media whose composition includes iron, nickel or cobalt.
- Solid grains are electrically insulating, thus the conductivity of the media will depend solely on the fluid.

Additionally, from poroelasticity three more postulations should be mentioned. First, inter-grain friction isn't accounted for (only fluid-solid interaction), which to some extent is related to the second: nonexistence of thermomechanical coupling[11]. Lastly, the interstitial fluid is viscous, monophasic and Newtonian.

For the class of water-saturated quartz-dominated sediments and sedimentary rocks on which rely this work, Pride (1994) states that all above-cited premises will be valid.

From pore and grain to macro-scales

The surface S_w separating the adsorbed layer from the diffuse one is taken by Pride as the boundary between solid and fluid phases. However, due to the adsorbed (Stern) layer's minor thickness it is impracticable to study it separately, hence its physical properties are comprised in the boundary conditions at S_w, i.e., uniform surface-charge density and no-slip flow condition (Day, 1990).

As a first step in obtaining macroscopic equations, Pride defined, for both fluid and solid phases, the Maxwell equations along with the corresponding mechanical expressions governing pore-scale phenomena, and analysed the respective boundary conditions at S_w. Subsequently, a homogenization procedure, relying on an averaging theorem introduced in Slattery (1967), was used to determine the final equations (i.e., through a volume average of the microscopic equations). The volume over which the averaging occurs (V_A) has mesoscopic dimensions, meaning it is between the minimum grain size and the wavelength of the existing disturbance. Throughout it physical properties are assumed constant for all phases and macroscopic properties (e.g., porosity) are supposed to smoothly vary inside the porous medium.

[11] A thermoelastic formulation of fluid-filled porous media, accounting for heat transport through porous fluid flow and differential expansion for fluid phase and solid frame, is discussed in Kurashige (1989).

For the ξth phase of a porous medium, occupying a volume V_ξ inside V_A, the volumetric average of a microscopic field $\mathbf{a}_\xi$ is represented by:

$$\langle \mathbf{a}_\xi \rangle = \frac{1}{V_A} \int_{V_\xi} \mathbf{a}_\xi dV. \tag{2.32}$$

Once gradients of functions are quite common in differential equations describing physical phenomena, Slattery's theorem, which relates the gradient of an average to the average of a gradient is quite handy when dealing with averaged fields; it is written as:

$$\langle \nabla \mathbf{a}_\xi \rangle = \nabla \langle \mathbf{a}_\xi \rangle + \frac{1}{V_A} \int_{S_w} \mathbf{n}_\xi \mathbf{a}_\xi dS, \tag{2.33}$$

where $\mathbf{n}_\xi$ is the normal to S_w and is oriented from fluid to solid, thus implying $\mathbf{n}_{fluid}$ and $\mathbf{n}_{solid}$ have opposed directions. Besides Slattery (1967), derivation of this theorem can also be found in Whitaker (1969) and Pride et al. (1992).

Electromagnetic equations

Pride's theory rely on the full set of Maxwell equations. For a $e^{-\imath\omega t}$ time dependence:

$$\nabla \times \mathbf{E} = \imath\omega \mathbf{B}; \tag{2.34a}$$

$$\nabla \times \mathbf{H} = -\imath\omega \mathbf{D} + \mathbf{J}; \tag{2.34b}$$

$$\nabla \cdot \mathbf{D} = \rho_{free} \equiv \phi \sum_l \mathrm{e} z_l \overline{n_l}; \tag{2.34c}$$

$$\nabla \cdot \mathbf{B} = 0; \tag{2.34d}$$

considering $\imath^2 = \sqrt{-1}$.

The first rule (2.34a), commonly referred as Faraday's law or more generally Maxwell-Faraday equation, describes the existence of a spatially varying electric field ($\mathbf{E}$) as consequence of a time variation of the magnetic flux density ($\mathbf{B}$). As shown in Feynman et al. (1963), even though only the temporal change of the $\mathbf{B}$ field is evidenced in equation 2.34a, time-varying modifications of the reference region (when $\mathbf{B}$ is kept constant) are also implied to create electric fields. The fourth expression (2.34d), Gauss' law for magnetism, translates the fact that a magnetic mono-pole, in analogy to electric charges, does not exist. In other words, through a closed surface the magnetic flux in is equal the one out, such that for a representation

by lines of the vector field, either lines close around themselves or they have an infinite extension, never diverging/converging from/to a point.

Before going to the other equations, two auxiliary fields: the electric displacement $\mathbf{D}$ and the magnetic $\mathbf{H}$, as well as constitutive relations between them and fields $\mathbf{E}$ and $\mathbf{B}$, will be briefly discussed. Usually, definition of $\mathbf{D}$ and $\mathbf{H}$ are:

$$\mathbf{D} = \epsilon_0 \mathbf{E} + \mathbf{P}; \tag{2.35a}$$

$$\mathbf{H} = \frac{1}{\mu_0}\mathbf{B} - \mathbf{M}; \tag{2.35b}$$

where polarization ($\mathbf{P}$) and magnetization ($\mathbf{M}$) phenomena are accounted for. Such phenomena are induced by bound charges (ρ_{bound}) and currents ($\mathbf{J}_{bound}$) which in turn are linked to external or applied fields (e.g., $\mathbf{E}$ and $\mathbf{B}$).

The relation between polarization and $\mathbf{E}$, as for magnetization and $\mathbf{B}$, might be quite complex, depending mainly on the medium's microscopic structure, therefore its definition is found using a quantum mechanics and quantum statistics approach (Wachter and Hoeber, 2006). However, making phenomenologically-lead approximations, quite simpler formulas can be established. For linear isotropic media composed of dielectric and diamagnetic materials[12] (comprising those materials that Pride's equations account for) one has:

$$\mathbf{P} = \epsilon_0 \chi_e \mathbf{E}; \tag{2.36a}$$

$$\mathbf{M} = \chi_m \mathbf{H}; \tag{2.36b}$$

with χ_e and χ_m the respective electric and magnetic susceptibilities (i.e., the specific constants controlling both the degree of magnetization and of polarization). Constitutive relations follow from direct substitution of 2.36a and 2.36b into 2.35a and 2.35b:

$$\begin{cases} \mathbf{D} = \epsilon \mathbf{E}, & \epsilon = \epsilon_0(1 + \chi_e) \text{ or } \epsilon = \epsilon_0 \kappa; \\ \mathbf{B} = \mu \mathbf{H}, & \mu = \mu_0(1 + \chi_m). \end{cases} \tag{2.37}$$

Regarding the constants above (2.37), subscript 0 refers to free space (vacuum) values, ϵ is the permittivity, μ is the magnetic permeability and κ is the dielectric constant or relative permittivity (i.e., $\kappa = \epsilon/\epsilon_0$). From the previous assumptions (section 2.3.1), μ is believed to be as insignificantly small as to allow the presumption

[12] Distinction between materials in terms of electric and magnetic behaviour can be found in Feynman et al. (1963) or Griffiths (1999).

$\mu \approx \mu_0$. Pride (1994) employed a model to permittivity which considers it as a function of porosity (ϕ), tortuosity (α_∞) and both relative permittivity of fluid electrolyte and solid grains (κ_ξ, $\xi = \mathrm{f}$ or s):

$$\epsilon = \epsilon_0 \left[\frac{\phi}{\alpha_\infty} (\kappa_\mathrm{f} - \kappa_\mathrm{s}) + \kappa_\mathrm{s} \right]. \tag{2.38}$$

Going back to the initial set of equations, 2.34b, known as Maxwell-Ampère's law, depicts the reverse phenomenon of 2.34a, namely, that a time-changing electric field will produce a magnetic field. The last equality, 2.34c, is customarily designated as Gauss' law and says that a charge accumulation is responsible for an electric field. In what concerns the electrokinetic theory here discussed, ρ_{free} is the locally induced charge density due to a perturbation in the porous media, which in turn is given by the integral contribution of all ions in the saturating fluid electrolyte (right side of 2.34c, where e is the elementary charge, z_l the valence and $\overline{n_l}$ the volumetric density of each l ionic species).

Mechanical equations

Biot's formulation (Biot, 1956a; Biot, 1956b) to poroelastodynamics uses a heuristic approach, assuming that continuum mechanics can be directly translated to macroscopic quantities and microscopic (pore-scale) properties are negligible (Bourbié et al., 1987; Carcione, 2007). Pride et al. (1992) follow a more rigorous procedure to deduce the macroscopic equations of motion (Garambois, 1999; Carcione, 2007), starting from first principles and arriving at a generalization of Biot's theory. It is this last work that Pride (1994) considers.

To arrive at the final expressions, Pride et al. (1992) defined the relative-displacement between solid ($\mathbf{u}_\mathrm{s}$) and fluid ($\mathbf{u}_\mathrm{f}$):

$$\mathbf{w} = \phi(\mathbf{u}_\mathrm{f} - \mathbf{u}_\mathrm{s}); \tag{2.39}$$

the macroscopic (bulk) density:

$$\rho_\mathrm{B} = \phi\rho_\mathrm{f} + (1 - \phi)\rho_\mathrm{s}; \tag{2.40}$$

and the macroscopic stress tensor, combining fluid (τ_f) and solid (τ_s) stresses, and applied uniformly to all the faces of a cubic porous material's sample:

$$\tau_\mathrm{B} = \phi\tau_\mathrm{f} + (1-\phi)\tau_\mathrm{s}. \tag{2.41}$$

The final macroscopic laws of motion are thus written:

$$\nabla \cdot \tau_\mathrm{B} = -\omega^2(\rho_\mathrm{B}\mathbf{u}_\mathrm{s} + \rho_\mathrm{f}\mathbf{w}); \tag{2.42a}$$

$$\tau_B = (K_G\nabla \cdot \mathbf{u}_\mathrm{s} + C\nabla \cdot \mathbf{w})\mathbf{I} + G_\mathrm{fr}(\nabla\mathbf{u}_\mathrm{s} + \nabla\mathbf{u}_\mathrm{s}^T - \frac{2}{3}\nabla \cdot \mathbf{u}_\mathrm{s}\mathbf{I}); \tag{2.42b}$$

$$-p = C\nabla \cdot \mathbf{u}_\mathrm{s} + M\nabla \cdot \mathbf{w}; \tag{2.42c}$$

detailing the coupling between stress, strain and fluid/interstitial pressure (eqs. 2.42b and 2.42c) and the dynamic behaviour of the force balance on the bulk porous material (eq. 2.42a). $\mathbf{I}$, as standard, is the identity matrix. G, K_G, C and M are the four elastic parameters controlling isotropic poroelasticity. They were previously defined in section 2.1.2.

Transport equations

Flux-force relations elucidating the dynamic interaction between electric and mechanical fields were obtained in Pride (1994) through evaluation of the integrals defining the conduction current $\mathbf{J_c}$, the streaming current $\mathbf{J_s}$, and the relative fluid flow $\mathbf{v}$; which compose the definitions of total current density $\mathbf{J}$ and filtration (Darcy) velocity $\dot{\mathbf{w}}$:

$$\mathbf{J} \equiv \phi(\mathbf{J_c} + \mathbf{J_s}); \tag{2.43a}$$

$$\dot{\mathbf{w}} \equiv \phi\mathbf{v}. \tag{2.43b}$$

Following the propagation of a wave, streaming currents arise from electrofiltration (i.e., the movement of the double layer's counter-ions driven by fluid-pressure gradients) while conduction currents are linked to the localized electric field created by the accumulation of counter-ions in low fluid-pressure regions, and their depletion in high fluid-pressure regions (Pride and Haartsen, 1996). The relative fluid flow, from the time derivative of eq. 2.39, is the fluid's velocity relative to that of

the frame. Additionally, $\mathbf{J_s}$ and $\mathbf{v}$ account for both mechanically- and electrically-induced fields:

$$\mathbf{J_s} = \mathbf{J}_{\mathbf{s}m} + \mathbf{J}_{\mathbf{s}e} \text{ and } \mathbf{v} = \mathbf{v}_m + \mathbf{v}_e. \tag{2.44}$$

Final equations have the form:

$$\mathbf{J} = \sigma(\omega)\mathbf{E} + L_m(\omega)(-\nabla p + \omega^2 \rho_f \mathbf{u}_\mathrm{s}); \tag{2.45a}$$

$$-\imath\omega\mathbf{w} = L_e(\omega)\mathbf{E} + \frac{k(\omega)}{\eta}(-\nabla p + \omega^2 \rho_f \mathbf{u}_\mathrm{s}); \tag{2.45b}$$

where L_m and L_e are, respectively, the electrokinetic coupling coefficient, accounting for mechanical to electric conversions, and the electroosmotic coefficient responsible for the reciprocal electric to mechanical energy conversions. In the right side of 2.45a, the first term is Ohm's law that refers to the conduction current. The last term of equation 2.45b is the generalized Darcy's law considering single phase fluids.

These equations (2.45) are somewhat the frequency dependent version of Equations 2.27, and again Onsager's reciprocity relations imply $L_m(\omega) = L_e(\omega)$.

Coupling coefficients

The frequency-dependent coefficients in Equations 2.45 will be detailed below, but before going further, the concept of transition frequency ω_t needs introduction. Regarding Biot's theory, it appears as a threshold that marks the transition from low-frequency viscous flow to high-frequency inertial flow. It will depend on pore-geometry and fluid properties of the medium (Pride, 1994):

$$\omega_t = \frac{\phi}{\alpha_\infty k_0}\frac{\eta}{\rho_\mathrm{f}}. \tag{2.46}$$

Since ρ_f is the pore fluid/gas density, it is implied that ω_t depends on saturation. Additionally, if a rock is fully saturated with water, only the pore-geometry will influence the value of ω_t.

In order to define the dynamic permeability $k(\omega)$ and the dynamic electrokinetic coupling coefficient $L(\omega) \equiv L_m(\omega) = L_e(\omega)$, Pride (1994) adopts the procedure followed by Johnson et al. (1987)[13]. For $k(\omega)$, the following definition holds:

$$k(\omega) = k_0 \left[\left(1 - \imath \frac{4}{m} \frac{\omega}{\omega_t} \right)^{1/2} - \imath \frac{\omega}{\omega_t} \right]^{-1}. \tag{2.47}$$

The dynamic permeability depends not only on its static approximation (k_0) and on the porous structure, but also on the fluid filling the pores, through m (Equation 2.7) and ω_t.

Probably, the most important coefficient, derived by Pride (1994), was $L(\omega)$. It represents all coupling between Biot's and Maxwell's equations. As $k(\omega)$, its expression depends on the low-frequency approximation $L_0 \equiv L_{m0} = L_{e0}$ (see subsection 2.2.3), fluid characteristics, pore structure, and the thickness of the double layer:

$$L(\omega) = L_0 \left[1 - i \frac{\omega}{\omega_t} \frac{m}{4} \left(1 - 2 \frac{\tilde{d}}{\Lambda} \right)^2 \left(1 - i^{3/2} \tilde{d} \sqrt{\frac{\omega \rho_f}{\eta}} \right)^2 \right]^{-1/2}. \tag{2.48}$$

In Equation 2.48 $\tilde{d}$ is often approximated by the Debye length d_{Db}, given by Equation 2.22. It will also be the case here, however, for completness, it is important to present the correct definition (based on the terminology of subsection 2.2.2):

$$\tilde{d} = \int_0^D \frac{\Phi(\chi)}{\zeta} d\chi. \tag{2.49}$$

D is a distance from the slipping plane after which the excess ions, in the double layer, become insignificant. Pride (1994) points out that it is usually a few Debye lengths, thus it implicates $\tilde{d} \leq d_{\mathrm{Db}}$. Under the thin double layer assumption, taking $\tilde{d} = d_{\mathrm{Db}}$ in the calculation of $L(\omega)$ will lead only to a minor, almost insignificant, uncertainty.

Pride (1994) disregards the effects of surface conductivity in the coupling coefficients such that the definition of L_0 is:

$$L_0 = -\frac{\phi}{\alpha_\infty} \frac{\epsilon_0 \kappa_f \zeta}{\eta} \left(1 - 2 \frac{\tilde{d}}{\Lambda} \right) = -C_{ek} \sigma_B \left(1 - 2 \frac{\tilde{d}}{\Lambda} \right), \tag{2.50}$$

[13] A general discussion about the procedure of Johnson et al. (1987) as well as the validity of $k(\omega)$, can be found in Pride et al. (1993).

where the Helmholtz-Smoluchowski equation (2.29), and the relation $\sigma_{\mathrm{B}} = \sigma_{\mathrm{f}}\mathbf{F}$ (Jouniaux et al., 2000), were used to hint at the similarity between Equations 2.28 and 2.50. The terms inside the parentheses is a correction whose validity only holds for thin double layers.

The last coefficient to discuss is the conductivity $\sigma(\omega)$. Besides the electrolyte conductivity, its definition also accounts for the excess conductance induced at the double layer by electromigration and electroosmotic effects, Σ_{em} and Σ_{os}, respectively. The final expression is:

$$\sigma(\omega) = \sigma_{\mathrm{B}}\left[1 + \frac{2}{\sigma_{\mathrm{f}}\Lambda}[\Sigma_{\mathrm{em}} + \Sigma_{\mathrm{os}}(\omega)]\right], \tag{2.51}$$

where the conductances, considering binary symmetric electrolytes (e.g., NaCl), have the following expressions:

$$\Sigma_{\mathrm{em}} = 4d(ez_1)^2 b_1 \mathcal{N}_1 \left[\cosh\left(\frac{ez_1\zeta}{2k_{\mathrm{B}}T}\right) - 1\right], \tag{2.52a}$$

$$\begin{aligned} \Sigma_{\mathrm{os}}(\omega) &= \frac{(\epsilon_0\kappa_{\mathrm{f}})^2\zeta^2}{2d\eta}\mathcal{P}\left(1 - 2\frac{i^{3/2}}{\mathcal{P}}\frac{d}{\delta_v}\right)^{-1}, \\ \text{with} \quad \mathcal{P} &= \frac{16k_{\mathrm{B}}Td^2\mathcal{N}_1}{\epsilon_0\kappa_{\mathrm{f}}\zeta^2}\left[\cosh\left(\frac{ez_1\zeta}{2k_{\mathrm{B}}T}\right) - 1\right]. \end{aligned} \tag{2.52b}$$

The only dependence of $\sigma(\omega)$ on frequency comes from the viscous skin depth $\delta_v = \sqrt{\eta/\rho_{\mathrm{f}}\omega}$ in Σ_{os}, which controls the transition from viscous to inertial flow, induced by electrical forces.

Plane wave analysis

In order to gain more insigth into the governing equations previously discussed, and derive some relations from the wavefields dictated by them, I will look for the plane wave solution in a homogeneous isotropic medium in the absence of sources. The results I seek are essentially the same that Pride and Haartsen (1996) report, and I will follow the steps described in Meyer (2021).

As a starting point I will rewrite the first-order equations (in the frequency domain) as Haartsen and Pride (1997), accounting for current-density sources $\mathbf{C}$,

magnetic-current sources $\mathbf{M}$, and body-force densities acting on the fluid ($\mathbf{f}$) and on the bulk material ($\mathbf{F}$):

$$\nabla \times \mathbf{E} = \imath\omega\mathbf{B} - \mathbf{M}, \tag{2.53a}$$
$$\nabla \times \mathbf{H} = -\imath\omega\mathbf{D} + \mathbf{J} + \mathbf{C}, \tag{2.53b}$$
$$\mathbf{D} = \epsilon\mathbf{E}, \tag{2.53c}$$
$$\mathbf{B} = \mu\mathbf{H}, \tag{2.53d}$$
$$\nabla \cdot \tau_{\mathrm{B}} = -\omega^2(\rho_{\mathrm{B}}\mathbf{u}_{\mathrm{s}} + \rho_{\mathrm{f}}\mathbf{w}) + \mathbf{F}, \tag{2.53e}$$
$$\tau_B = (K_G\nabla \cdot \mathbf{u}_{\mathrm{s}} + C\nabla \cdot \mathbf{w})\mathbf{I} + G_{\mathrm{fr}}(\nabla\mathbf{u}_{\mathrm{s}} + \nabla\mathbf{u}_{\mathrm{s}}^T - \frac{2}{3}\nabla \cdot \mathbf{u}_{\mathrm{s}}\mathbf{I}), \tag{2.53f}$$
$$-p = C\nabla \cdot \mathbf{u}_{\mathrm{s}} + M\nabla \cdot \mathbf{w}, \tag{2.53g}$$
$$\mathbf{J} = \sigma(\omega)\mathbf{E} + L_m(\omega)(-\nabla p + \omega^2\rho_f\mathbf{u}_{\mathrm{s}} + \mathbf{f}), \tag{2.53h}$$
$$-\imath\omega\mathbf{w} = L_e(\omega)\mathbf{E} + \frac{k(\omega)}{\eta}(-\nabla p + \omega^2\rho_f\mathbf{u}_{\mathrm{s}} + \mathbf{f}). \tag{2.53i}$$

This system of 9 equations can be reformulated into a more compact form, expressing only the dependence on $\mathbf{u}$, $\mathbf{w}$, and $\mathbf{E}$. The steps to arrive at this new system will be detailed below. For convenience, from here onwards, G_{fr} will be simply written as G.

At first we apply the divergence operator to 2.53f and find:

$$\nabla \cdot \tau_{\mathrm{B}} = H\nabla(\nabla \cdot \mathbf{u}) - G\nabla \times (\nabla \times \mathbf{u}) + C\nabla(\nabla \cdot \mathbf{w}),$$

where Equation 2.15 and the property $\nabla^2\mathbf{u} = \nabla(\nabla\cdot\mathbf{u}) - \nabla\times(\nabla\times\mathbf{u})$ were employed. Now it is just a matter of inserting this result in Equation 2.53e:

$$\omega^2\rho_{\mathrm{B}}\mathbf{u} + H\nabla(\nabla \cdot \mathbf{u}) - G\nabla \times (\nabla \times \mathbf{u}) + C\nabla(\nabla \cdot \mathbf{w}) = \mathbf{F}. \tag{2.54}$$

This is the first relation.

To arrive at the second equation we apply the gradient operator to 2.53g, after which we get:

$$-\nabla p = C\nabla\nabla \cdot \mathbf{u} + M\nabla\nabla \cdot \mathbf{w}. \tag{2.55}$$

Inserting this result in 2.53i we find the second relation:

$$-\omega^2\rho_{\mathrm{f}}\mathbf{u} - C\nabla\nabla \cdot \mathbf{u} - \omega^2\tilde{\rho}\mathbf{w} - M\nabla\nabla \cdot \mathbf{w} + \imath\omega\tilde{\rho}L(\omega)\mathbf{E} = \mathbf{f}, \tag{2.56}$$

where the effective density of the pore-fluid, defined as:

$$\tilde{\rho}(\omega) = \frac{\imath}{\omega}\frac{\eta}{k(\omega)}, \tag{2.57}$$

was used.

For the last equation, more steps are needed. Subtituting 2.53d into 2.53a and 2.53c into 2.53b and combining the results with 2.53h, the following intermediate relation can be found:

$$\nabla \times \nabla \times \mathbf{E} - \omega^2\mu\epsilon\mathbf{E} - \imath\omega\mu\sigma(\omega)\mathbf{E} - \imath\omega\mu L(\omega)(-\nabla p + \omega^2\rho_{\mathrm{f}}\mathbf{u} + \mathbf{f}) = \imath\omega\mu\mathbf{C} - \nabla \times \mathbf{M}.$$

Finally, inserting 2.55 and 2.56 in the previous result, the final equation follows:

$$\nabla \times \nabla \times \mathbf{E} - \omega^2\mu\tilde{\epsilon}\mathbf{E} + \imath\omega^3\mu L(\omega)\tilde{\rho}\mathbf{w} = \imath\omega\mu\mathbf{C} - \nabla \times \mathbf{M}, \tag{2.58}$$

where the effective electrical permittivity,

$$\tilde{\epsilon}(\omega) = \epsilon + \frac{\imath}{\omega}\sigma(\omega) - \tilde{\rho}(\omega)L^2(\omega), \tag{2.59}$$

was introduced.

Analysing how harmonic plane waves will behave with Pride's model allows one to define important relations connecting the three wavefields: $\mathbf{u}$, $\mathbf{w}$, and $\mathbf{E}$. Besides that, it is possible to access the complex slowness, and consequently the velocity of propagation and the related attenuation, for each wavemode. The general form of vectorial harmonic plane waves in cartesian coordinates is:

$$\boldsymbol{\Psi}(x, y, z, \omega) = \Psi_0 \exp(\imath\mathbf{k}\cdot\mathbf{X})\hat{\boldsymbol{\Psi}}, \quad \text{with} \quad \mathbf{k} = \omega \mathrm{s}(\omega)\hat{\mathbf{k}}. \tag{2.60}$$

Ψ_0 is the magnitude, $\mathbf{k}$ is the wave vector (dictating the direction of propagation), $\mathbf{X}$ refers to the cartesian basis vectors, and $\hat{\mathbf{k}}$ and $\hat{\boldsymbol{\Phi}}$ are unit vectors pointing at the direction of propagation, and the direction of oscillation (i.e., the polarization). Figure 2.6 illustrates a plane wave propagating.

Representing $\mathbf{u}$, $\mathbf{w}$, and $\mathbf{E}$ as plane waves, and accounting for their individual polarization (i.e., $\hat{\boldsymbol{\Psi}} = \hat{\mathbf{u}}, \hat{\mathbf{w}},$ and $\hat{\mathbf{E}}$), one finds:

$$\mathbf{u} = \mathrm{u}_0 \exp(\imath\mathbf{k}\cdot\mathbf{X})\hat{\mathbf{u}}, \quad \mathbf{w} = \mathrm{w}_0 \exp(\imath\mathbf{k}\cdot\mathbf{X})\hat{\mathbf{w}}, \quad \text{and} \quad \mathbf{E} = \mathrm{E}_0 \exp(\imath\mathbf{k}\cdot\mathbf{X})\hat{\mathbf{E}}.$$

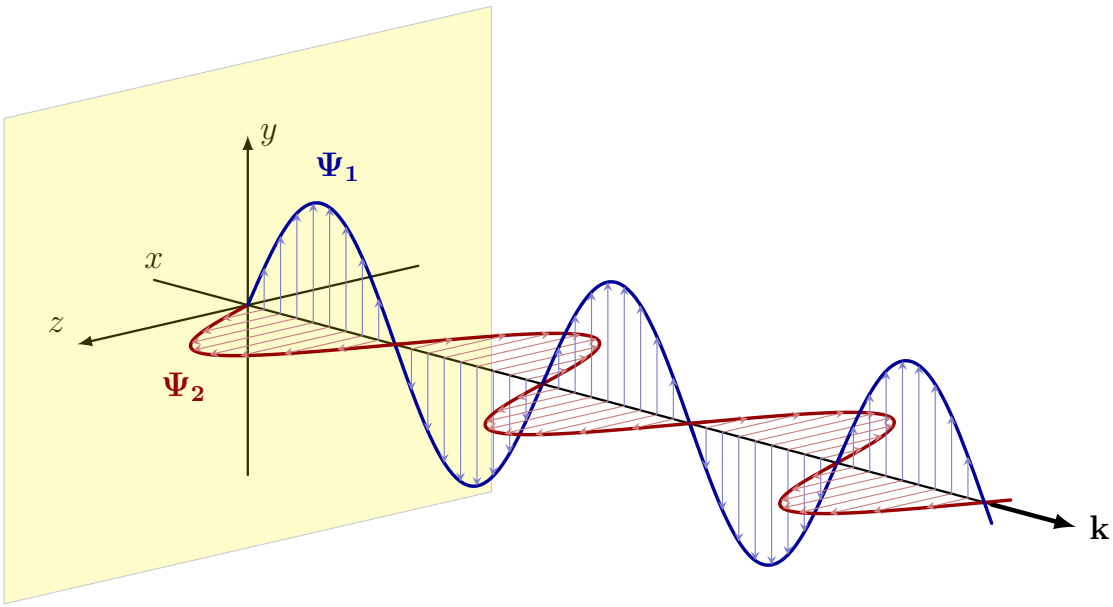

Figure 2.6: Harmonic plane wave propagation with direction given by the wave vector $\mathbf{k}$. Two orthogonal wavefields are represented, $\mathbf{\Psi_1}$ and $\mathbf{\Psi_2}$.

Now we remove all source terms and insert the plane wave forms in the equations highlighted above (2.54, 2.56, and 2.58). The following system of equations, which I will conveniently represent in matrix form, can be found:

$$\begin{bmatrix} -\mathbf{k}(H-G)(\hat{\mathbf{u}}\cdot\mathbf{k}) + \hat{\mathbf{u}}(\omega^2\rho_{\mathrm{B}} - G|\mathbf{k}|^2) & \omega^2\rho_{\mathrm{f}}\hat{\mathbf{w}} - C(\hat{\mathbf{w}}\cdot\mathbf{k})\mathbf{k} & 0 \\ -\omega^2\rho_{\mathrm{f}}\hat{\mathbf{u}} + C(\hat{\mathbf{u}}\cdot\mathbf{k})\mathbf{k} & -\omega^2\tilde{\rho}\hat{\mathbf{w}} + M(\hat{\mathbf{w}}\cdot\mathbf{k})\mathbf{k} & \imath\omega\tilde{\rho}L(\omega)\hat{\mathbf{E}} \\ 0 & \imath\omega^3\mu L(\omega)\tilde{\rho}\hat{\mathbf{w}} & |\mathbf{k}|^2\hat{\mathbf{E}} - (\hat{\mathbf{E}}\cdot\mathbf{k})\mathbf{k} - \omega^2\mu\tilde{\epsilon}\hat{\mathbf{E}} \end{bmatrix} \begin{bmatrix} \mathrm{u}_0 \\ \mathrm{w}_0 \\ \mathrm{E}_0 \end{bmatrix} = 0. \tag{2.61}$$

In the system defined above (2.61), four types of waves will exist. The longitudinal ones are: P, for the fast compressional, and B (referring to Biot) for slow compressional. Complementarily, the transversely polarized are: S for shear waves, and EM for electromagnetic waves. I will proceed with the solution of 2.61 for each wavemode below.

- Longitudinal modes

For this case, waves are polarized in the direction of motion, thus $\mathbf{k}$ and $\mathbf{\Psi}$ are collinear: $\mathbf{\Psi} = \mathfrak{b}\mathbf{k}$, and $\mathbf{\Psi} \cdot \mathbf{k} = \mathfrak{b}|\mathbf{k}|^2$. Inserting these relations in Equation 2.61 and using the definition of $\mathbf{k}$, we get:

$$\begin{bmatrix} -(H-G)\mathfrak{b}\mathbf{k}\omega^2 \mathrm{s}(\omega)^2 - \\ \mathfrak{b}\mathbf{k}G\omega^2\mathrm{s}(\omega)^2 + \mathfrak{b}\mathbf{k}\omega^2\rho_{\mathrm{B}} & \omega^2\rho_{\mathrm{f}}\mathfrak{b}\mathbf{k} - \mathfrak{b}\mathbf{k}\omega^2\mathrm{s}(\omega)^2 C & 0 \\ -\omega^2\rho_{\mathrm{f}}\mathfrak{b}\mathbf{k} + \mathfrak{b}\mathbf{k}\omega^2\mathrm{s}(\omega)^2 C & -\omega^2\tilde{\rho}\mathfrak{b}\mathbf{k} + \mathfrak{b}\mathbf{k}\omega^2\mathrm{s}(\omega)^2 M & \imath\omega\tilde{\rho}L(\omega)\mathfrak{b}\mathbf{k} \\ 0 & \imath\omega^3\mu L(\omega)\tilde{\rho}\mathfrak{b}\mathbf{k} & -\omega^2\mu\tilde{\epsilon}\mathfrak{b}\mathbf{k} \end{bmatrix} \begin{bmatrix} \mathrm{u}_0 \\ \mathrm{w}_0 \\ \mathrm{E}_0 \end{bmatrix} = 0. \tag{2.62}$$

The final system appears after division by $\omega^2\mathfrak{b}\mathbf{k}$:

$$\begin{bmatrix} -H\mathrm{s}(\omega)^2 + \rho_{\mathrm{B}} & \rho_{\mathrm{f}} - \mathrm{s}(\omega)^2 C & 0 \\ -\rho_{\mathrm{f}} + \mathrm{s}(\omega)^2 C & -\tilde{\rho} + \mathrm{s}(\omega)^2 M & \imath\frac{\tilde{\rho}}{\omega}L(\omega) \\ 0 & \imath\omega\mu L(\omega)\tilde{\rho} & -\mu\tilde{\epsilon} \end{bmatrix} \begin{bmatrix} \mathrm{u}_0 \\ \mathrm{w}_0 \\ \mathrm{E}_0 \end{bmatrix} = 0. \tag{2.63}$$

Non-trivial solutions of 2.63 will only exist if the determinant of the matrix is zero. After calculating the determinant admitting it vanishes, P and B wave slowness can be found (check Appendix A):

$$2s^2_{\xi=\mathrm{P,B}} = -\gamma \pm \sqrt{\gamma^2 - 4\frac{\tilde{\rho}\rho(1+\tilde{\rho}L(\omega)^2/\tilde{\epsilon}) - \rho_{\mathrm{f}}^2}{\Delta}}; \tag{2.64}$$

with $\Delta = HM - C^2$. The positive sign will be used for the B waves while the negative applies for P waves, reminding that B waves are slower than P waves. Finally, for convenience I used the parameter γ:

$$\gamma = \frac{-M\rho + H\tilde{\rho}(-1 - \tilde{\rho}L^2/\tilde{\epsilon}) + 2\rho_f C}{\Delta}. \tag{2.65}$$

Relations between the three considered wavefields can be obtained after solving 2.63. As function of the solid displacement amplitude:

$$\mathrm{w}_0 = \frac{(\rho_\mathrm{B} - Hs^2)}{(Cs^2 - \rho_\mathrm{f})}\mathrm{u}_0, \tag{2.66a}$$

$$\mathrm{E}_0 = \frac{\imath\omega\tilde{\rho}L(\omega)}{\tilde{\epsilon}}\frac{(\rho_\mathrm{B} - Hs^2)}{(Cs^2 - \rho_\mathrm{f})}\mathrm{u}_0. \tag{2.66b}$$

Equation 2.66b is often used in the context of seismoelectric studies, once it relates seismic displacements with coseismic wavefields. In the litterature the term seismoelectric transfer function is repeatedly used (Garambois and Dietrich, 2001; Bordes et al., 2015).

- Tranverse modes

  Propagation of transversely polarized waves imply solid displacement, relative flow, and electric fields perpendicularly oriented in relation to $\mathbf{k}$. Therefore $\mathbf{k}\cdot\hat{\mathbf{u}} = \mathbf{k}\cdot\hat{\mathbf{w}} = \mathbf{k}\cdot\hat{\mathbf{E}} = 0$, while $\hat{\mathbf{u}} = \hat{\mathbf{w}} = \hat{\mathbf{E}}$. Applying this condition to 2.61, using the definition of $\mathbf{k}$, and dividing the outcome by the wave polarization and by ω^2:

$$\begin{bmatrix} \rho_\mathrm{B} - G\mathrm{s}(\omega)^2 & \rho_\mathrm{f} & 0 \\ -\rho_\mathrm{f} & -\tilde{\rho} & \imath\frac{\tilde{\rho}}{\omega}L(\omega) \\ 0 & \imath\omega\mu L(\omega)\tilde{\rho} & \mathrm{s}(\omega)^2 - \mu\tilde{\epsilon} \end{bmatrix} \begin{bmatrix} \mathrm{u}_0 \\ \mathrm{w}_0 \\ \mathrm{E}_0 \end{bmatrix} = 0. \tag{2.67}$$

Again, setting the deteminant to zero leads to two complex slowness, for the shear and electromagnetic waves:

$$2s^2_{\xi=\mathrm{S,EM}} = \frac{\rho_\mathrm{t}}{G} + \mu\tilde{\epsilon}\left(1 + \frac{\tilde{\rho}L(\omega)^2}{\tilde{\epsilon}}\right) \pm \left\{\left[\frac{\rho_\mathrm{t}}{G} + \mu\tilde{\epsilon}\left(1 + \frac{\tilde{\rho}L(\omega)^2}{\tilde{\epsilon}}\right)\right]^2 - 4\frac{\mu}{G}\left(\tilde{\epsilon}\rho_\mathrm{t} + \rho_\mathrm{B}\tilde{\rho}L(\omega)^2\right)\right\}^{1/2}. \tag{2.68}$$

In order to reduce the complexity of this expression, I used the complex density, as defined in Pride and Haartsen (1996):

$$\rho_\mathrm{t} = \rho_\mathrm{B} - \frac{\rho_\mathrm{f}^2}{\tilde{\rho}}. \tag{2.69}$$

In Equation 2.68, the positive symbol is used for shear waves and the negative for EM waves (such convention for the symbols comes from the studying of the case when $L(\omega) = 0$). Depending on which cartesian axis is parallel to the wave polarization, we can distinguish between SH-TE and SV-TM modes. Considering the propagation suggested by Figure 2.6, if the waves are polarized along the y-axis, we have SH-TE, whereas if the polarization is parallel to the z-axis we have SV-TM, hinting at the existence of a magnetic wave whose polarization is orthogonal to the other waves.

At this point, the relations between the amplitudes of the waves are missing. The procedure to arrive at them is exactly the same as for longitudinal waves, and the following expressions can be found:

$$\mathrm{w}_0 = \frac{(Gs^2 - \rho_\mathrm{B})}{\rho_\mathrm{f}}\mathrm{u}_0, \tag{2.70a}$$

$$\mathrm{E}_0 = -\frac{\imath\omega\mu\tilde{\rho}L(\omega)}{(s^2 - \mu\tilde{\epsilon})}\frac{(Gs^2 - \rho_\mathrm{B})}{\rho_\mathrm{f}}\mathrm{u}_0. \tag{2.70b}$$

- Phase velocity and attenuation

  The velocity of propagation is the inverse of the slowness, thus the speed (real phase velocity) with which a wave propagates is:

  $$v_\xi = 1/\mathrm{Re}\{s_\xi\}, \tag{2.71}$$

  with ξ the subscript indicating the wave type ($\xi = \mathrm{P}, \mathrm{B}, \mathrm{SV}, \mathrm{SH}, \mathrm{TE}, \mathrm{TM}$).

  At last, in what regards the intrinsic attenuation, it will be defined as in Biot's theory. Therefore it will only account for frictional heating losses generated by applying pressure gradients into a viscous fluid (see Holzhauer (2015) for a more complete discussion about attenuation in poroelastic media). The intrinsic attenuation of each ξ wave kind is directly proportional to the imaginary part of the slowness, through the relation:

  $$\alpha_\xi = \omega Im\{s_\xi\}. \tag{2.72}$$

  The frequency dependence translates the fact that the higher the frequency, the more attenuation phenomena will affect wave propagation.

2.3.2 Revil's formulation

Alternatively to the model introduced by Pride (1994), and explained above, Revil and Mahardika (2013) and Jardani and Revil (2015) propose another set of governing equations based on the concept of effective charge density dragged by the flow inside the pores. Without going into details, I will point out that this new model for the electrokinetic phenomena, occurring in porous media, represents a significant improvement in the sense it allows one to account for a larger variety of geological scenarios.

The model considers both saturated and unsaturated conditions. Besides, it naturally accounts for surface conductivity, thus being able to model media whose solid-phase composition is not just quartz. Additionally, while Pride's formulation treats only the cases where a thin-layer can be assumed, Revil and Mahardika (2013) also consider thick double layers, i.e., the thickness of the double layer is comparable to the pore radius such that all ions in the double layer will be dragged by flow, with no dependence on frequency.

Finally, even though I will not explore this alternative model, it is conceivable to compare it with the experiments realized during this thesis since it can represent more complex rocks, which is the case of one of the sandstones used, discussed in section 4.2.

3 Numerical framework

For the numerical solution of Pride's equations, considering different source-receiver configurations and diverse geological models, this thesis relies on the numerical code initially presented by Garambois (1999). It adapts the semi-analytical approach developed by Kennett and Kerry (1979), to simulate the coupled seismic and electromagnetic disturbances generated by point forces in isotropic fluid saturated porous media, with vertical layering and azimuthal symmetry.

Due to the acquisition geometry of the experimental setup, explained in the next chapter, to access the components of the electromagnetic wavefields oriented along the z-axis, their dependence on other components were deduced from the system of equations solved by Garambois' code. Additionally, the extension proposed in Dietrich et al. (2018) was also incorporated in the code to be consistent with what is actually measured experimentally (i.e., absolute potentials).

In what follows I will explain the original numerical code, the additional components calculated, and in the end I will show reciprocity tests used to validate the final code.

3.1 Governing equations in layered media

Considering stratified media composed of homogeneous porous layers, the governing equations (Eqs. 2.53i) can be rewritten as a system of 12 equations highlighting the vertical derivative of seismic and electromagnetic fields. The development to arrive at this new system is detailed in Appendix B. These 12 relations represent two independent sub-systems, analogous to the SV-TM and SH-TE, discussed in the previous chapter. These two systems are:

- PSVTM: Coupling the longitudinal P and B waves, the shear wave polarized along the vertical plane (SV), and EM waves whose magnetic field is transversely polarized (TM).
- SHTE: Coupling horizontally polarized shear waves (SH) with EM waves whose electric fields also have a transverse polarization (TE).

For completeness, the sub-systems derived in Appendix B will be re-written below. A cartesian coordinate system is used so far, thus the sub-scripts V and H will imply the relations: $\psi_{\mathrm{V}} = \partial_{\mathrm{x}}\psi_{\mathrm{x}} + \partial_{\mathrm{y}}\psi_{\mathrm{y}}$, and $\psi_{\mathrm{H}} = \partial_{\mathrm{x}}\psi_{\mathrm{y}} - \partial_{\mathrm{y}}\psi_{\mathrm{x}}$. Additionally ∇^2_{h} will refer to the horizontal components of the Laplacian.

PSVTM:

$$\frac{\partial}{\partial \mathrm{z}} u_{\mathrm{V}} = -\nabla^2_{\mathrm{h}} u_{\mathrm{z}} + \frac{\tau_{\mathrm{V}}}{G}, \tag{3.1a}$$

$$\frac{\partial}{\partial \mathrm{z}} u_{\mathrm{z}} = \left(2G\frac{M}{\Delta} - 1\right) u_{\mathrm{V}} + \frac{M}{\Delta}\tau_{zz} + \frac{C}{\Delta}p, \tag{3.1b}$$

$$\frac{\partial}{\partial \mathrm{z}} w_{\mathrm{z}} = \left(\frac{\rho_{\mathrm{f}}}{\tilde{\rho}} - 2G\frac{C}{\Delta}\right) u_{\mathrm{V}} - \frac{C}{\Delta}\tau_{zz} - \left(\frac{H}{\Delta} + \frac{\nabla^2_{\mathrm{h}}}{\tilde{\rho}\omega^2}\right) p + \frac{L}{\imath\omega} E_{\mathrm{V}} + \frac{1}{\tilde{\rho}\omega^2} f_{\mathrm{V}}, \tag{3.1c}$$

$$\begin{aligned}\frac{\partial}{\partial \mathrm{z}} \tau_{\mathrm{V}} = &-\left[\omega^2\left(\rho_{\mathrm{B}} - \frac{\rho_{\mathrm{f}}^2}{\tilde{\rho}}\right) + 2G\left(2 - 2G\frac{M}{\Delta}\right)\nabla^2_{\mathrm{h}}\right] u_{\mathrm{V}} - \left(1 - 2G\frac{M}{\Delta}\right)\nabla^2_{\mathrm{h}}\tau_{\mathrm{zz}} \\ &- \left(\frac{\rho_{\mathrm{f}}}{\tilde{\rho}} - 2G\frac{C}{\Delta}\right)\nabla^2_{\mathrm{h}} p - \imath\omega\rho_{\mathrm{f}} L E_{\mathrm{V}} - F_{\mathrm{V}} + \frac{\rho_{\mathrm{f}}}{\tilde{\rho}} f_{\mathrm{V}},\end{aligned} \tag{3.1d}$$

$$\frac{\partial}{\partial \mathrm{z}} \tau_{\mathrm{zz}} = -\omega^2[\rho_{\mathrm{B}} u_{\mathrm{z}} + \rho_{\mathrm{f}} w_{\mathrm{z}}] - \tau_{\mathrm{V}} - F_{\mathrm{z}}, \tag{3.1e}$$

$$\frac{\partial}{\partial \mathrm{z}}(-p) = -\omega^2\rho_{\mathrm{f}} u_{\mathrm{z}} - \omega^2\tilde{\rho}\left(1 + \frac{\tilde{\rho}L^2}{\tilde{\epsilon}}\right) w_{\mathrm{z}} - \frac{\tilde{\rho}L}{\tilde{\epsilon}} H_{\mathrm{H}} + \frac{\tilde{\rho}L}{\tilde{\epsilon}} C_{\mathrm{z}} - f_{\mathrm{z}}, \tag{3.1f}$$

$$\frac{\partial}{\partial \mathrm{z}} H_{\mathrm{H}} = -\rho_{\mathrm{f}}\omega^2 L u_{\mathrm{V}} - L\nabla^2_{\mathrm{h}}(-p) + \imath\omega\tilde{\epsilon}\left(1 + \frac{\tilde{\rho}L^2}{\tilde{\epsilon}}\right) E_{\mathrm{V}} - L f_{\mathrm{V}} - C_{\mathrm{V}}, \tag{3.1g}$$

$$\frac{\partial}{\partial \mathrm{z}} E_{\mathrm{V}} = \imath\omega\frac{\tilde{\rho}L}{\tilde{\epsilon}}\nabla^2_{\mathrm{h}} w_{\mathrm{z}} + \imath\omega\mu\left(1 + \frac{1}{\mu\tilde{\epsilon}\omega^2}\nabla^2_{\mathrm{h}}\right) H_{\mathrm{H}} - \frac{\imath}{\omega\tilde{\epsilon}}\nabla^2_{\mathrm{h}} C_{\mathrm{z}} - M_{\mathrm{H}}. \tag{3.1h}$$

SHTE:

$$\frac{\partial}{\partial \mathrm{z}} u_{\mathrm{H}} = \frac{\tau_{\mathrm{H}}}{G}, \tag{3.2a}$$

$$\frac{\partial}{\partial \mathrm{z}} \tau_{\mathrm{H}} = -\left[\omega^2\left(\rho_{\mathrm{B}} - \frac{\rho_{\mathrm{f}}^2}{\tilde{\rho}}\right) + G\nabla^2_{\mathrm{h}}\right] u_{\mathrm{H}} - \imath\omega\rho_{\mathrm{f}} L E_{\mathrm{H}} - F_{\mathrm{H}} + \frac{\rho_{\mathrm{f}}}{\tilde{\rho}} f_{\mathrm{H}}, \tag{3.2b}$$

$$\frac{\partial}{\partial \mathrm{z}} H_{\mathrm{V}} = \rho_{\mathrm{f}}\omega^2 L u_{\mathrm{H}} - \imath\omega\tilde{\epsilon}\left(1 + \frac{\tilde{\rho}L^2}{\tilde{\epsilon}} + \frac{1}{\mu\tilde{\epsilon}\omega^2}\nabla^2_{\mathrm{h}}\right) E_{\mathrm{H}} + L f_{\mathrm{H}} + C_{\mathrm{H}} + \frac{1}{\imath\mu\omega}\nabla^2_{\mathrm{h}} M_{\mathrm{z}}, \tag{3.2c}$$

$$\frac{\partial}{\partial \mathrm{z}} E_{\mathrm{H}} = -\imath\mu\omega H_{\mathrm{V}} + M_{\mathrm{V}}. \tag{3.2d}$$

To be consistent with the numerical code cylindrical coordinates will be used, notice, however, that both PSVTM and SHTE systems will remain unchanged after this coordinate conversion. Since lateral homogeneity is considered, this conversion allows one to get rid of ${\nabla_\mathrm{h}}^2$ by applying a n-th order Hankel transform over the radial component r and a Fourier transform over the angular θ. For any ψ function with a $e^{-\imath\omega t}$ time dependency, this Hankel-Fourier transformation can be formally expressed as:

$$\mathcal{HF}\{\psi(r,\theta,z,\omega)\} = \hat{\psi}(\mathbf{k},n,z,\omega) = \frac{1}{2\pi}\int_0^\infty r\mathcal{J}_n(\mathbf{k}r)dr\int_{-\pi}^{\pi}\psi(r,\theta,z,\omega)e^{-\imath n\theta}d\theta, \tag{3.3}$$

where $\mathbf{k}$ is the horizontal wavenumber and $\mathcal{J}_n$ is the n-th order Bessel function of the first kind. The following property follows from this transformation: $\mathcal{HF}\nabla_\mathrm{h}^2\psi = -\mathbf{k}^2\hat{\psi}$.

Complementarily, to ensure dimensional homogeneity the following normalizations will be used in all equations:

$$\hat{\psi}_1 = \frac{\hat{\psi}_\mathrm{V}}{\imath\mathbf{k}}, \quad \text{and} \quad \hat{\psi}_2 = \frac{\hat{\psi}_\mathrm{H}}{\imath\mathbf{k}}. \tag{3.4}$$

These are necessary due to the horizontal derivation implied by the sub-scripts V and H.

Both systems can be written using vectorial notation as:

$$\frac{\partial}{\partial \mathrm{z}}\mathbf{B} = \mathbf{A}\mathbf{B} + \mathbf{S}, \tag{3.5}$$

where the depth-dependent wavefields are:

$$\begin{aligned}\mathbf{B}^{\mathrm{PSVTM}} &= [\hat{u}_1, \hat{u}_\mathrm{z}, \hat{w}_\mathrm{z}, \hat{\tau}_1, \hat{\tau}_\mathrm{zz}, -\hat{p}, \hat{H}_2, \hat{E}_1]^\mathrm{T},\\ \mathbf{B}^{\mathrm{SHTE}} &= [\hat{u}_2, \hat{\tau}_2, \hat{H}_1, \hat{E}_2]^\mathrm{T};\end{aligned} \tag{3.6}$$

The vectors of forces $\mathbf{S}$ are:

$$\begin{aligned}\mathbf{S}^{\mathrm{PSVTM}} &= [0, 0, \frac{\imath\mathbf{k}}{\tilde{\rho}\omega^2}\hat{f}_1, -\hat{F}_1 + \frac{\rho_\mathrm{f}}{\tilde{\rho}}\hat{f}_1, -\hat{F}_\mathrm{z}, -\hat{f}_\mathrm{z} + \frac{\tilde{\rho}L}{\tilde{\epsilon}}\hat{C}_\mathrm{z}, -L\hat{f}_1 - \hat{C}_1, \frac{\mathbf{k}}{\omega\tilde{\epsilon}}\hat{C}_\mathrm{z} - \hat{M}_2]^\mathrm{T},\\ \mathbf{S}^{\mathrm{SHTE}} &= [0, \frac{\rho_\mathrm{f}}{\tilde{\rho}}\hat{f}_2 - \hat{F}_2, L\hat{f}_2 + \hat{C}_2 + \frac{\mathbf{k}}{\imath\mu\omega}\hat{M}_\mathrm{z}, \hat{M}_1]^\mathrm{T}.\end{aligned} \tag{3.7}$$

It is important to note that all azimuthal variation comes from these two vectors and is a consequence of the nature of forces applied.

At last, the coupling matrices depend on the physical parameters at a given depth, thus each layer has an associated **A** matrix. For the PSVTM system the coupling matrix is:

$$\mathbf{A}^{\mathrm{PSVTM}} = \begin{bmatrix} 0 & -\imath\mathbf{k} & 0 & \frac{1}{G} \\ \imath\mathbf{k}(2G\frac{M}{\Delta}-1) & 0 & 0 & 0 \\ \imath\mathbf{k}(\frac{\rho_{\mathrm{f}}}{\tilde{\rho}}-2G\frac{C}{\Delta}) & 0 & 0 & 0 \\ -[\omega^2\rho_{\mathrm{t}}-2G\mathbf{k}^2(2-2G\frac{M}{\Delta})] & 0 & 0 & 0 \\ 0 & -\omega^2\rho_{\mathrm{B}} & -\omega^2\rho_{\mathrm{f}} & 0 \\ 0 & -\omega^2\rho_{\mathrm{f}} & -\omega\tilde{\rho}(1+\frac{\tilde{\rho}L^2}{\tilde{\epsilon}}) & 0 \\ -\rho_{\mathrm{f}}\omega^2 L & 0 & 0 & 0 \\ 0 & 0 & -\omega\mathbf{k}\frac{\tilde{\rho}L}{\tilde{\epsilon}} & 0 \end{bmatrix} \begin{bmatrix} 0 & 0 & 0 & 0 \\ \frac{M}{\Delta} & -\frac{C}{\Delta} & 0 & 0 \\ -\frac{C}{\Delta} & (\frac{H}{\Delta}-\frac{\mathbf{k}^2}{\tilde{\rho}\omega^2}) & 0 & \frac{L}{\imath\omega} \\ -\imath\mathbf{k}(1-2G\frac{M}{\Delta}) & \imath\mathbf{k}(\frac{\rho_{\mathrm{f}}}{\tilde{\rho}}-2G\frac{C}{\Delta}) & 0 & -\imath\omega\rho_{\mathrm{f}}L \\ -\imath\mathbf{k} & 0 & 0 & 0 \\ 0 & 0 & -\imath\mathbf{k}\frac{\tilde{\rho}L}{\tilde{\epsilon}} & 0 \\ 0 & -\imath\mathbf{k}L & 0 & \imath\omega\tilde{\epsilon}(1+\frac{\tilde{\rho}L^2}{\tilde{\epsilon}}) \\ 0 & 0 & \imath\omega\mu(1-\frac{\mathbf{k}^2}{\mu\tilde{\epsilon}\omega^2}) & 0 \end{bmatrix}. \tag{3.8}$$

And for the SHTE system:

$$\mathbf{A}^{\mathrm{SHTE}} = \begin{bmatrix} 0 & \frac{1}{G} & 0 & 0 \\ -\omega^2\rho_{\mathrm{t}}+G\mathbf{k}^2 & 0 & 0 & -\imath\omega\rho_{\mathrm{f}}L \\ \rho_{\mathrm{f}}\omega^2 L & 0 & 0 & -\imath\omega\tilde{\epsilon}(1+\frac{\tilde{\rho}L^2}{\tilde{\epsilon}}-\frac{\mathbf{k}^2}{\mu\tilde{\epsilon}\omega^2}) \\ 0 & 0 & -\imath\mu\omega & 0 \end{bmatrix}. \tag{3.9}$$

3.2 The wave-vector in uniform media

Inside a homogeneous medium, the wavefields forming **B** at a reference depth z_0 (say the depth at which a point source exists) can be decomposed into upgowing (U) and downgoing (D) components. This can be done by defining a wave-vector $\mathbf{V} = [V_{\mathrm{U}}^{\xi}, V_{\mathrm{D}}^{\xi}]^{\mathrm{T}}$ that contains the complex amplitudes of all wavetypes, and a matrix

$\mathbf{D}$ whose columns are the eigenvectors of $\mathbf{A}$. It follows that the displacement-stress-EM vector can be written as:

$$\mathbf{B} = \mathbf{D}\mathbf{V}. \tag{3.10}$$

As cited in the previous section, there will exist 4 wavetypes (ξ = P, B, SV, and TM) in the PSVTM case and 2 (ξ = SH, and TE) in the SHTE, that means $\mathbf{V}^{\mathrm{PSVTM}}$ will have 8 elements and $\mathbf{V}^{\mathrm{SHTE}}$ will contain 4. Concurrently, $\mathbf{D}^{\mathrm{PSVTM}}$ is an 8x8 matrix and $\mathbf{D}^{\mathrm{SHTE}}$ a 4x4 matrix.

The elements of $\mathbf{D}$, namely the eigenvectors of $\mathbf{A}$, were derived by Haartsen and Pride (1997) for both PSVTM and SHTE systems. Additionally, Garambois (1999) proposed the following block matrix representations:

$$\mathbf{D}^{\mathrm{PSVTM}} = \begin{bmatrix} \mathbf{m}_{\mathrm{U}(3\times4)} & \mathbf{m}_{\mathrm{D}(3\times4)} \\ \mathbf{n}_{\mathrm{U}(3\times4)} & \mathbf{n}_{\mathrm{D}(3\times4)} \\ \mathbf{hp}_{\mathrm{U}(1\times4)} & \mathbf{hp}_{\mathrm{D}(1\times4)} \\ \mathbf{ep}_{\mathrm{U}(1\times4)} & \mathbf{ep}_{\mathrm{D}(1\times4)} \end{bmatrix} \quad \text{and} \quad \mathbf{D}^{\mathrm{SHTE}} = \begin{bmatrix} \mathbf{ms}_{\mathrm{U}(1\times2)} & \mathbf{ms}_{\mathrm{D}(1\times2)} \\ \mathbf{ns}_{\mathrm{U}(1\times2)} & \mathbf{ns}_{\mathrm{D}(1\times2)} \\ \mathbf{hs}_{\mathrm{U}(1\times2)} & \mathbf{hs}_{\mathrm{D}(1\times2)} \\ \mathbf{es}_{\mathrm{U}(1\times2)} & \mathbf{es}_{\mathrm{D}(1\times2)} \end{bmatrix}. \tag{3.11}$$

Sub-matrices $\mathbf{m}_{\mathrm{U}}$, $\mathbf{m}_{\mathrm{D}}$, $\mathbf{ms}_{\mathrm{U}}$, and $\mathbf{ms}_{\mathrm{D}}$ transform the complex amplitudes of waves propagating upwards and downwards into displacements, while $\mathbf{n}_{\mathrm{U}}$, $\mathbf{n}_{\mathrm{D}}$, $\mathbf{ns}_{\mathrm{U}}$, and $\mathbf{ns}_{\mathrm{D}}$ will transform these amplitudes into stresses and pressure (in the PSVTM case). Matrices $\mathbf{hp}_{\mathrm{U}}$, $\mathbf{hp}_{\mathrm{D}}$, $\mathbf{hs}_{\mathrm{U}}$, and $\mathbf{hs}_{\mathrm{D}}$ concern the transformations into magnetic fields, and the remaining matrices, $\mathbf{ep}_{\mathrm{U}}$, $\mathbf{ep}_{\mathrm{D}}$, $\mathbf{es}_{\mathrm{U}}$, and $\mathbf{es}_{\mathrm{D}}$, the transformations into electric fields.

The wave-vectors, corresponding to different depths inside a layer, are connected using a matrix $\mathbf{Q}$ termed wave-propagator (Kennett and Kerry, 1979) that depends on the depths analysed. Using the depth of reference z_0, $\mathbf{V}$ will be expressed as:

$$\mathbf{V}(z) = \mathbf{Q}(z, z_0)\mathbf{V}(z_0) = \exp[\imath\omega\mathbf{\Lambda}(z - z_0)]\mathbf{V}(z_0), \tag{3.12}$$

where $\imath\omega\mathbf{\Lambda}$ is a diagonal matrix whose elements are the eigenvalues of $\mathbf{A}$.

Finally, the wavefields at different depths inside a homogeneous layer respect the relation:

$$\mathbf{B}(z) = \mathbf{D}\mathbf{Q}(z, z_0)\mathbf{D}^{-1}\mathbf{B}(z_0). \tag{3.13}$$

This decomposition of $\mathbf{B}$ will prove covenient when dealing with an interface, a case discussed in the next section.

3.3 Reflection and transmission matrices

When two homogeneous layers have one or more different physical properties, at the interface welding these two half-spaces, the boundary conditions dictate a continuity of seismic and electromagnetic wavefields. Considering an interface at a depth z_I, such condition entails:

$$\mathbf{B}(z_I-) = \mathbf{B}(z_I+), \tag{3.14}$$

where the signs - and + designate, respectively, the region above and below z_I. Notice the z-axis points downwards, in the sense z increases with depth.

The complex amplitudes of each wave-type, when a wave impinges at an interface, are controlled by the reflection and transmission coefficients, which describe the change in $\mathbf{V}$ due to a variation in physical properties. To find these coefficients, the definition 3.10 enters 3.14 and, as in Kennett and Kerry (1979), the following relation takes shape:

$$\mathbf{V}(z_I-) = \mathbf{D}^{-1}(z_I-)\mathbf{D}(z_I+)\mathbf{V}(z_I+) = \mathbf{Q}(z_I-, z_I+)\mathbf{V}(z_I+), \tag{3.15}$$

where the definition of the wave-propagator $\mathbf{Q}$ here is not the same as in equation 3.12.

Expanding this definition in terms of upgoing and downgoing waves, one can write:

$$\begin{bmatrix}\mathbf{V}_U(z_I-)\\ \mathbf{V}_D(z_I-)\end{bmatrix} = \begin{bmatrix}\mathbf{Q}_{UU} & \mathbf{Q}_{UD}\\ \mathbf{Q}_{DU} & \mathbf{Q}_{DD}\end{bmatrix}\begin{bmatrix}\mathbf{V}_U(z_I+)\\ \mathbf{V}_D(z_I+)\end{bmatrix}, \tag{3.16}$$

where the partitions of $\mathbf{Q}$ are 4x4 matrices in the PSVTM system and 2x2 in the SHTE. When a wave travelling downwards hits an interface, the reflection $\mathbf{R}_D$ and transmission $\mathbf{T}_D$ matrices are defined as (Kennett and Kerry, 1979):

$$\mathbf{V}_U(z_I-) = \mathbf{R}_D\mathbf{V}_D(z_I-) \quad \text{and} \quad \mathbf{V}_D(z_I+) = \mathbf{T}_D\mathbf{V}_D(z_I-). \tag{3.17}$$

Similar relations exist for the matrices $\mathbf{R}_U$ and $\mathbf{T}_U$ associated with upward travelling waves. With the equations above it is straightforward to define relations between $\mathbf{Q}$ and the reflection and transmission matrices:

$$\begin{array}{c|c} \mathbf{R}_D = \mathbf{Q}_{UD}\mathbf{Q}_{DD}^{-1} & \mathbf{T}_D = \mathbf{Q}_{DD}^{-1} \\ \hline \mathbf{R}_U = -\mathbf{Q}_{DD}^{-1}\mathbf{Q}_{DU} & \mathbf{T}_U = \mathbf{Q}_{UU} - \mathbf{Q}_{UD}\mathbf{Q}_{DD}^{-1}\mathbf{Q}_{DU} \end{array}. \tag{3.18}$$

It is worthy to show the explicit form of one of the above matrices. Considering a wave propagating downwards, for both PSVTM and SHTE systems one has the following reflection matrices:

$$\mathbf{R}_{\mathrm{D}}^{\mathrm{PSVTM}} = \begin{pmatrix} R_{\mathrm{D}}^{P/P} & R_{\mathrm{D}}^{P/B} & R_{\mathrm{D}}^{P/SV} & R_{\mathrm{D}}^{P/TM} \\ R_{\mathrm{D}}^{B/P} & R_{\mathrm{D}}^{B/B} & R_{\mathrm{D}}^{B/SV} & R_{\mathrm{D}}^{B/TM} \\ R_{\mathrm{D}}^{SV/P} & R_{\mathrm{D}}^{SV/B} & R_{\mathrm{D}}^{SV/SV} & R_{\mathrm{D}}^{SV/TM} \\ R_{\mathrm{D}}^{TM/P} & R_{\mathrm{D}}^{TM/B} & R_{\mathrm{D}}^{TM/SV} & R_{\mathrm{D}}^{TM/TM} \end{pmatrix}, \quad \mathbf{R}_{\mathrm{D}}^{\mathrm{SHTE}} = \begin{pmatrix} R_{\mathrm{D}}^{SH/SH} & R_{\mathrm{D}}^{SH/TE} \\ R_{\mathrm{D}}^{TE/SH} & R_{\mathrm{D}}^{TE/TE} \end{pmatrix}. \tag{3.19}$$

Regarding the indexing of the elements, the leftmost superscript refers to the generated wave while the rightmost refers to the incident wave; that means $R_{\mathrm{D}}^{P/TM}$ controls the amplitude of a P wave generated by an incident TM wave propagating downwards.

The fact one can easily access these reflection and transmission coefficients will prove useful when analysing the electric field component of the interface response, which is usually small compared to the seismic and coseismic wavefields. Additionally, one can analyse the solution for a specific wave-type by zeroing out the coefficients associated with other waves.

3.4 Upper and lower bounds of the media

In Kennett and Kerry (1979), the upper bound of the model is taken as a free-surface. This is an analogy to the situation where an infinite half-space, made up of a material that is physically equivalent to air, superposes the porous media considered. In this case, tangential and normal stresses as well as pressure will vanish, while for electromagnetic waves the boundary conditions between air and a porous medium are considered (Garambois, 1999).

As for the lower bound, Garambois considers that there's an infinite half-space constituted by a porous medium. Therefore the reflections and transmission coefficients at the deepest interface will depend on the constrast between two media. In case no change in properties exists, no reflections will arise.

Point sources will always be at z>0, that implies only upgoing waves can hit the free-surface. Therefore, for waves arriving at z = 0, the following relation describes the reflection coefficients:

$$\mathbf{V}_{\mathrm{D}}(0+) = \mathbf{R}_{\mathrm{U}}(0)\mathbf{V}_{\mathrm{U}}(0+) = \mathbf{R}_{\mathrm{U}}^{\mathrm{FS}}\mathbf{V}_{\mathrm{U}}(0+). \tag{3.20}$$

In the air, only electromagnetic waves can propagate, consequently the electromagnetic components of $\mathbf{B}$ will be continuous across the free-surface. For the PSVTM case one has (Garambois, 1999):

$$\begin{bmatrix} \hat{H}_2 \\ \hat{E}_1 \end{bmatrix}_{z<0} = \begin{bmatrix} \hat{H}_2 \\ \hat{E}_1 \end{bmatrix}_{z>0} = V_{\mathrm{U}}^{\mathrm{TM}} \begin{bmatrix} \epsilon_0 \\ -q_0 \end{bmatrix}, \tag{3.21}$$

where q_0 is the vertical electromagnetic wave slowness in air, given by: $(q_0)^2 = \mu_0\epsilon_0 - (\mathbf{k}/\omega)^2$. The permittivity and magnetic susceptibility of air is approximated by the values in vacuum (see definition in 2.1.3), and all downgoing waves propagating in the air were neglected i.e., $V_{\mathrm{D}}^{\mathrm{TM}} = 0$.

The expression 3.21 above leads to:

$$q_0\hat{H}_2 + \epsilon_0\hat{E}_1 = 0. \tag{3.22}$$

Therefore, at the topmost layer, one can use the partitions of $\mathbf{D}^{\mathrm{PSVTM}}$ (eq. 3.11) to write the free-surface conditions for upgoing and downgoing waves:

$$\begin{bmatrix} \mathbf{n}_{\mathrm{U}} & \mathbf{n}_{\mathrm{D}} \\ q_0\mathbf{hp}_{\mathrm{U}} + \epsilon_0\mathbf{ep}_{\mathrm{U}} & q_0\mathbf{hp}_{\mathrm{D}} + \epsilon_0\mathbf{ep}_{\mathrm{D}} \end{bmatrix} \begin{bmatrix} \mathbf{V}_{\mathrm{U}}(0+) \\ \mathbf{V}_{\mathrm{D}}(0+) \end{bmatrix} = 0. \tag{3.23}$$

Developing this system and using eq. 3.20 the free-surface reflection matrix can be computed by:

$$\mathbf{R}_{\mathrm{U}}^{\mathrm{FS}} = -\begin{bmatrix} \mathbf{n}_{\mathrm{D}} \\ q_0\mathbf{hp}_{\mathrm{D}} + \epsilon_0\mathbf{ep}_{\mathrm{D}} \end{bmatrix}^{-1} \begin{bmatrix} \mathbf{n}_{\mathrm{U}} \\ q_0\mathbf{hp}_{\mathrm{U}} + \epsilon_0\mathbf{ep}_{\mathrm{U}} \end{bmatrix}. \tag{3.24}$$

The expression equivalent to 3.22 for the SHTE case is:

$$\mu_0\hat{H}_1 - q_0\hat{E}_2 = 0, \tag{3.25}$$

which leads to the reflection matrix:

$$\mathbf{R}_{\mathrm{U}}^{\mathrm{FS}} = -\begin{bmatrix} \mathbf{ns}_{\mathrm{D}} \\ \mu_0\mathbf{hs}_{\mathrm{D}} - q_0\mathbf{es}_{\mathrm{D}} \end{bmatrix}^{-1} \begin{bmatrix} \mathbf{ns}_{\mathrm{U}} \\ \mu_0\mathbf{hs}_{\mathrm{U}} - q_0\mathbf{es}_{\mathrm{U}} \end{bmatrix}. \tag{3.26}$$

Finally, if for some reason one wants a free-surface condition at the bottom of the model, in eq. 3.21 $V_{\mathrm{D}}^{\mathrm{TM}}$ needs to be accounted for, while $V_{\mathrm{U}}^{\mathrm{TM}} = 0$. In this

situation, the physical properties of the infite half-space at the bottom must be equal to the deepest layer considered in the model. Therefore the reflection matrix $\mathbf{R}_{\mathrm{D}}{}^{\mathrm{FS}}$, controlling the complex amplitudes of upgoing waves generated when downgoing waves hit the bottom-most free surface, will be given, for both wave systems, by:

$$\begin{aligned} \text{PSVTM:} \quad \mathbf{R}_{\mathrm{D}}^{\mathrm{FS}} &= -\begin{bmatrix} \mathbf{n}_{\mathrm{U}} \\ q_0\mathbf{hp}_{\mathrm{U}} + \epsilon_0\mathbf{ep}_{\mathrm{U}} \end{bmatrix}^{-1} \begin{bmatrix} \mathbf{n}_{\mathrm{D}} \\ q_0\mathbf{hp}_{\mathrm{D}} + \epsilon_0\mathbf{ep}_{\mathrm{D}} \end{bmatrix}, \\ \text{SHTE:} \quad \mathbf{R}_{\mathrm{D}}^{\mathrm{FS}} &= -\begin{bmatrix} \mathbf{ns}_{\mathrm{U}} \\ \mu_0\mathbf{hs}_{\mathrm{U}} - q_0\mathbf{es}_{\mathrm{U}} \end{bmatrix}^{-1} \begin{bmatrix} \mathbf{ns}_{\mathrm{D}} \\ \mu_0\mathbf{hs}_{\mathrm{D}} - q_0\mathbf{es}_{\mathrm{D}} \end{bmatrix}. \end{aligned} \tag{3.27}$$

3.5 A stratified media

The final response of a stratified medium, considering buried point sources and receivers, takes two distinct forms according to Kennett and Kerry (1979). The first considers receivers below the source ($z_{\mathrm{R}} > z_{\mathrm{S}}$) and the second deals with receivers above the source ($z_{\mathrm{R}} < z_{\mathrm{S}}$). For both situations, the equations below give the final stress, displacement and electromagnetic wavefields created by point sources:

$$\begin{aligned} \mathbf{W}(z_{\mathrm{R}} > z_{\mathrm{S}}) =& [\mathbf{c}_{\mathrm{D}}(z_{\mathrm{R}}) + \mathbf{c}_{\mathrm{U}}(z_{\mathrm{R}})\mathbf{R}_{\mathrm{U}}^{\mathrm{RL}}][\mathbf{I} - \mathbf{R}_{\mathrm{U}}^{\mathrm{RS}}\mathbf{R}_{\mathrm{D}}^{\mathrm{SL}}]^{-1} \cdot \\ & \mathbf{T}_{\mathrm{D}}^{\mathrm{RS}}[\mathbf{I} - \mathbf{R}_{\mathrm{U}}^{\mathrm{FS}}\mathbf{R}_{\mathrm{D}}^{\mathrm{RL}}]^{-1}[\mathbf{\Sigma}_{\mathrm{D}}(z_{\mathrm{S}}) - \mathbf{R}_{\mathrm{U}}^{\mathrm{FS}}\mathbf{\Sigma}_{\mathrm{U}}(z_{\mathrm{S}})], \\ \mathbf{W}(z_{\mathrm{R}} < z_{\mathrm{S}}) =& [\mathbf{c}_{\mathrm{U}}(z_{\mathrm{R}}) + \mathbf{c}_{\mathrm{D}}(z_{\mathrm{R}})\mathbf{R}_{\mathrm{U}}^{\mathrm{FR}}][\mathbf{I} - \mathbf{R}_{\mathrm{D}}^{\mathrm{RS}}\mathbf{R}_{\mathrm{U}}^{\mathrm{FR}}]^{-1} \cdot \\ & \mathbf{T}_{\mathrm{U}}^{\mathrm{RS}}[\mathbf{I} - \mathbf{R}_{\mathrm{D}}^{\mathrm{SL}}\mathbf{R}_{\mathrm{U}}^{\mathrm{FS}}]^{-1}[\mathbf{R}_{\mathrm{D}}^{\mathrm{SL}}\mathbf{\Sigma}_{\mathrm{D}}(z_{\mathrm{S}}) - \mathbf{\Sigma}_{\mathrm{U}}(z_{\mathrm{S}})]. \end{aligned} \tag{3.28}$$

Figure 3.1 depicts schematically what each term in eq. 3.28 represents. As suggested in the figure, the superscripts in the transmission and reflection matrices refer to the depth region they are associated with. For example, $\mathbf{R}_{\mathrm{U}}{}^{\mathrm{FS}}$ accounts for all reflection coefficients in-between the source depth (S) and the free-surface (F, z = 0), and $\mathbf{T}_{\mathrm{U}}{}^{\mathrm{RS}}$ represents all transmission coefficients between source and receiver depths.

Both tansmission and reflection matrices are calculated by the methodology of Kennett and Kerry (1979) in a recursive manner, where each interface in a given region is accounted for.

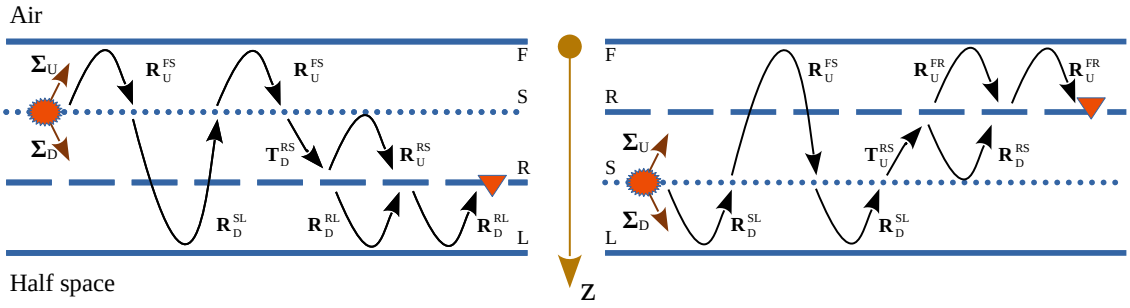

Figure 3.1: Schematic representation of the components controlling the response of a stratified media for two cases: source below receiver (left), and source above receiver (right). The depth levels depicted are: F for free-surface (upper bound), S for source depth, R for receiver depth, and L for lower bound. Adapted from Garambois (1999).

Regarding the source contribution in eq. 3.28, a premise of the numerical method discussed states that sources can not be placed at an interface. Thus they will always exist inside a homogeneous layer, and that implicates:

$$\mathbf{B}(z_S+) - \mathbf{B}(z_S-) = \mathbf{S}(z_S), \tag{3.29}$$

which can be rewritten, using eq. 3.10, as:

$$\mathbf{V}(z_S+) - \mathbf{V}(z_S-) = \mathbf{D}^{-1}(z_S)\mathbf{S}(z_S) = \mathbf{\Sigma}, \tag{3.30}$$

where $\mathbf{\Sigma}$ can be separated into upgoing ($\mathbf{\Sigma}_U$) and downgoing ($\mathbf{\Sigma}_D$) components. It is important to notice that because of the z-axis orientation, the wavefield radiated upwards by the source will have a negative sign associated with it, what explains why $\mathbf{\Sigma}_U$ is always negative in eq. 3.28.

From eq. 3.30 above, it is evident that the complex amplitudes of the waves created by a point source will depend both on the physical properties of the layer it is inside, and on the nature of the source used. $\mathbf{S}$ was previously defined, for both wave systems, in eq. 3.7, and explicit definitions for mechanical and electromagnetical point sources can be found in Haartsen and Pride (1997), Garambois (1999), and Garambois and Dietrich (2002).

Matrices $\mathbf{c}_U$ and $\mathbf{c}_D$ in eq. 3.28 convert the waves arriving at a receiver into the concerned wavefields. Effectively, they will be one of the partitions of $\mathbf{D}$ (see definition 3.11), or even a sub-partition, depending on the wavefield one considers.

Three main contributions can be distinguished in eq. 3.28 in terms of their physical meaning. Considering the case $z_R > z_S$ (left side in figure 3.1) the term $\mathbf{\Sigma}_D(z_S) - \mathbf{R}_U^{FS}\mathbf{\Sigma}_U(z_S)$ is the total downwards source contribution, where $\mathbf{R}_U^{FS}\mathbf{\Sigma}_U(z_S)$ represents waves initially travelling upwards but that were reflected downwards at the free-surface.

The term $[\mathbf{I}-\mathbf{R}_U^{RS}\mathbf{R}_D^{SL}]^{-1}\mathbf{T}_D^{RS}[\mathbf{I}-\mathbf{R}_U^{FS}\mathbf{R}_D^{RL}]^{-1}$ represents the contribution of several reflections and transmissions inside the medium. While $\mathbf{T}_U{}^{RS}$ comprises all transmission coefficients for the interfaces in-between the source and receiver depths, the other two matrices are reverberation operators (Kennett and Kerry, 1979) which express all primary and multiple reflections.

The remaining term is the contribution due to conversions at the receiver, accounting for all downgoing waves as well as those reflected upwards at $z > z_R$.

Finally, as discussed in Garambois (1999), because with this methodology one can directly access the different components of the whole stratified medium response, there's a possibility to suppress and/or enhance specific contributions (e.g. the direct wave, multiple reflections).

3.6 Vertical components of E and H

In the definition of $\mathbf{B}$ (eq. 3.6) the z-component of the electric field is not included. However, due to the geometry adopted for the experiments in this thesis, the component of the electric field measured is the vertical one. Therefore, an expression for the electric field oriented along the z-axis was sought.

Such expression arrives naturally when deriving the PSVTM system (eqs. 3.1). For completeness, the expression for the vertical component of the magnetic field was also derived, but this time from the equations representing the SHTE system (eqs. 3.2). The final expressions are:

$$\hat{E}_z = -\frac{\mathbf{k}}{\omega\tilde{\epsilon}}\hat{H}_2 + \frac{\imath\omega\tilde{\rho}L}{\tilde{\epsilon}}\hat{w}_z - \frac{\imath}{\omega\tilde{\epsilon}}\hat{C}_z, \tag{3.31a}$$

$$\hat{H}_z = \frac{\mathbf{k}}{\mu\omega}\hat{E}_2 - \frac{\imath}{\mu\omega}\hat{M}_z; \tag{3.31b}$$

and Appendix B details their derivation.

It is interesting to notice that in the seismoelectric case, for P waves propagating in a homogeneous medium the coseismic $\hat{E}_z$ wavefield is generated by $\hat{w}_z$. If an

interface is present, however, the interface response in $\hat{E}_z$, which propagates with a much higher velocity than the P wave, will be generated mainly by $\hat{H}_2$.

3.7 Back to time and cartesian coordinates

Until now, all wavefields are functions of ω and $\mathbf{k}$, therefore inverse Hankel and Fourier transformations are necessary to retrieve a time-distance wavefield representation.

Following Kennett and Kerry (1979), the operator defining the inverse of the Hankel-Fourier transform, defined in eq. 3.3, consists of an integral over $\mathbf{k}$ (from 0 to ∞) and a discrete sum over the angular orders n, with $|n| < 2$ for the case of punctual sources. Thus, considering cylindrical coordinates, the equations below transform the ($\mathbf{k}$,n)-dependency into a (r, θ)-dependency:

$$\psi_z(r,\theta,z,\omega) = \int_0^\infty \left\{ \sum_n \left[\mathcal{J}_n(\mathbf{k}r)\hat{\psi}_z(\mathbf{k},n,\omega,z) \right] e^{\imath n\theta} \right\} \mathbf{k}d\mathbf{k}, \tag{3.32a}$$

$$\psi_r(r,\theta,z,\omega) = \int_0^\infty \left\{ \sum_n \left[\frac{n}{\mathbf{k}r}\mathcal{J}_n(\mathbf{k}r)\hat{\psi}_2(\mathbf{k},n,\omega,z) - \imath\mathcal{J}'_n(\mathbf{k}r)\hat{\psi}_1(\mathbf{k},n,\omega,z) \right] e^{\imath n\theta} \right\} \mathbf{k}d\mathbf{k}, \tag{3.32b}$$

$$\psi_\theta(r,\theta,z,\omega) = \int_0^\infty \left\{ \sum_n \left[\frac{n}{\mathbf{k}r}\mathcal{J}_n(\mathbf{k}r)\hat{\psi}_1(\mathbf{k},n,\omega,z) + \imath\mathcal{J}'_n(\mathbf{k}r)\hat{\psi}_2(\mathbf{k},n,\omega,z) \right] e^{\imath n\theta} \right\} \mathbf{k}d\mathbf{k}, \tag{3.32c}$$

where $\mathcal{J}'_n(\xi) = d\mathcal{J}_n(\xi)/d\xi$ is the derivative of the Bessel function. The values of n depends on the nature of the source, such that $n = 0$ refers to explosive and z-oriented sources, and $n = \pm 1$ refers to x and y-oriented sources. These equations apply for all stress, displacement, and electromagnetic wavefields in $\mathbf{B}$, as well as $\hat{E}_z$ and $\hat{H}_z$ introduced in the previous section.

In order to go back to time, an inverse Fourier transform is applied to the wavefield components. Additionally, because cartesian coordinates are easier to work with,

a cylindric-to-cartesian coordinate conversion will also be considered for the radial and azimuthal components. For the latter the following relations apply:

$$\psi_{\mathrm{x}}(\mathrm{x},\mathrm{y},\mathrm{z},t) = \frac{1}{2\pi}\int_{-\infty}^{\infty}[\psi_r(r,\theta,\mathrm{z},\omega)\cos(\theta) - \psi_\theta(r,\theta,\mathrm{z},\omega)\sin(\theta)]e^{-\imath\omega t}d\omega, \tag{3.33a}$$

$$\psi_{\mathrm{y}}(\mathrm{x},\mathrm{y},\mathrm{z},t) = \frac{1}{2\pi}\int_{-\infty}^{\infty}[\psi_r(r,\theta,\mathrm{z},\omega)\sin(\theta) + \psi_\theta(r,\theta,\mathrm{z},\omega)\cos(\theta)]e^{-\imath\omega t}d\omega. \tag{3.33b}$$

Finally, the numerical implementation of the above equations, as carried out by Garambois (1999), involves the discrete wavenumber method of Bouchon (1981) and a Fast Fourier transform with complex frequencies, as explained in Bouchon (1979).

3.8 Electric potential

The numerical solution for the electric potential $\mathbf{\Phi}$ follows Dietrich et al. (2018), which solves the governing equations using the methodology of Garambois (1999).

As a departing point, all electric fields will be considered steady in time, what implies the relation (Feynman et al., 1963, chapter 4):

$$\mathbf{E} = -\nabla\mathbf{\Phi}, \tag{3.34}$$

where $\mathbf{\Phi}$ is a scalar field. In vector calculus this means the vector field describing $\mathbf{E}$ is conservative.

This assumption of static electric fields will necessarily hold for coseismic wavefields. For the EM wave generated at interfaces, we may consider it is due to a transient dipolar concentration of charges (Garambois and Dietrich, 2002), whose momentum's rate of change depends on the seismic wave velocity. Additionally we may suppose that this EM wave is detected at distances considerably smaller than its wavelength. In this case, Feynman et al. (1963) (in chapter 21) shows that eq. 3.34 is sufficient to describe the electric field.

Using eq. 3.34 and the gradient theorem, while considering cylindrical coordinates and an angular frequency-dependency, $\mathbf{\Phi}$ can be obtained from the radial component of the electric field with the equation:

$$\mathbf{\Phi}(r,\theta,\mathrm{z},\omega) - \cancelto{0}{\mathbf{\Phi}(\infty,\theta,\mathrm{z},\omega)} = -\int_{\infty}^{r} E_r(\nu,\theta,\mathrm{z},\omega)d\nu, \tag{3.35}$$

where the value of $\mathbf{\Phi}$ at infinity is reasonably taken to be zero. Inserting eq. 3.32b one can have an expression in terms of the actual wavefields in $\mathbf{B}$:

$$\begin{aligned}\mathbf{\Phi}(r,\theta,\mathrm{z},\omega) = -\int_{\infty}^{r}\int_{0}^{\infty}\Bigg\{\sum_{n}\Bigg[\frac{n}{\mathbf{k}\nu}\mathcal{J}_n(\mathbf{k}\nu)\hat{E}_2(\mathbf{k},n,\omega,\mathrm{z}) \\ -\imath\mathcal{J}_n'(\mathbf{k}\nu)\hat{E}_1(\mathbf{k},n,\omega,\mathrm{z})\Bigg]e^{\imath n\theta}\Bigg\}\mathbf{k}d\mathbf{k}d\nu.\end{aligned} \tag{3.36}$$

The final relation describing $\mathbf{\Phi}$ will depend on the source used i.e., the value of n. In here only axially symmetric sources will be considered, thus $n = 0$. For $n = \pm 1$ Devi (2017) (in chapter 4) shows the expressions for $\mathbf{\Phi}$. Taking $n = 0$ in eq. 3.36 produces:

$$\mathbf{\Phi}(r,\theta,\mathrm{z},\omega) = \int_{\infty}^{r}\int_{0}^{\infty}\Big[\imath\mathcal{J}_0'(\mathbf{k}\nu)\hat{E}_1(\mathbf{k},\omega,\mathrm{z})\Big]\mathbf{k}d\mathbf{k}d\nu. \tag{3.37}$$

With the following relation: $\frac{d\mathcal{J}_0(\mathbf{k}\nu)}{d\nu} = \mathcal{J}_0'(\mathbf{k}\nu)\mathbf{k}$, derived by applying the chain rule, we finally find:

$$\begin{aligned}\mathbf{\Phi}(r,\theta,\mathrm{z},\omega) &= \int_{0}^{\infty}\imath\hat{E}_1(\mathbf{k},\omega,\mathrm{z})d\mathbf{k}[\mathcal{J}_0(\mathbf{k}r) - \cancelto{0}{\mathcal{J}_0(\infty)}] \\ &= \int_{0}^{\infty}\imath\mathcal{J}_0(\mathbf{k}r)\hat{E}_1(\mathbf{k},\omega,\mathrm{z})d\mathbf{k}.\end{aligned} \tag{3.38}$$

As a final step, the time-dependent function can be found after an inverse Fourier transformation. This equation is equivalent to the one shown in Dietrich et al. (2018).

3.8.1 2, 3 and 5-electrodes configurations

Inspired by the work of Thompson (1936), while seeking to enhance the EM interface-generated signal in the context of seismoelectric surveys, Dietrich et al. (2018) studied 2, 3 and 5-electrodes arrangements as a filter acting on the theoretical electric potential in the middle of the electrode array.

Considering equally spaced electrodes placed along a line, the measured signal ϑ_{g}, in time, for a combination of g (2, 3 or 5) electrodes will be:

$$\begin{aligned}\vartheta_2(t) &= \mathbf{\Phi}_1(t) - \mathbf{\Phi}_2(t), \\ \vartheta_3(t) &= \mathbf{\Phi}_1(t) - \mathbf{\Phi}_2(t) + \mathbf{\Phi}_3(t), \\ \vartheta_5(t) &= \mathbf{\Phi}_1(t) - \mathbf{\Phi}_2(t) + \mathbf{\Phi}_3(t) - \mathbf{\Phi}_4(t) + \mathbf{\Phi}_5(t).\end{aligned} \tag{3.39}$$

It is straightforward to see that for electrodes spaced by L, from eq. 3.34, one can arrive at the approximate relation for the electric field in-between two electrodes:

$$\mathbf{E}(t) \approx \frac{\vartheta_2(t)}{L}. \tag{3.40}$$

The differential behaviour of ϑ_2 implies that its value goes to zero for synchronous events, that explains why dipole arrays will not be suited for detecting the interface response.

Complementarily, Dietrich et al. (2018) highligths that ϑ_3 and ϑ_5 lead to the approximate values of the electric potential at the central electrode:

$$\begin{aligned} \vartheta_3(t) &\approx \mathbf{\Phi}_2(t), \\ \vartheta_5(t) &\approx \mathbf{\Phi}_3(t), \end{aligned} \tag{3.41}$$

thus making them more appropriate for studying the interface response.

In order to insert the relations 3.39 in the numerical code of Garambois (1999), the following expressions were derived by Dietrich et al. (2018) for a frequency-wavenumber equivalence:

$$\begin{aligned} \vartheta_2(\mathbf{k}, L) &= 2\imath\sin(\mathbf{k}L/2), \\ \vartheta_3(\mathbf{k}, L) &= 2\cos(\mathbf{k}L/2) - 1, \\ \vartheta_5(\mathbf{k}, L) &= 2\sin(\mathbf{k}L/2) - 2\sin(\mathbf{k}L/4) + 1, \end{aligned} \tag{3.42}$$

where there is an explicit dependency on the electrode spacing. With these equations, a filtered potential can finally be defined from eq. 3.38 as:

$$\mathbf{\Psi}(r, \theta, \mathrm{z}, \omega) = \int_0^\infty \imath \mathcal{J}_0(\mathbf{k}r)\hat{E}_1(\mathbf{k}, \omega, \mathrm{z})\vartheta_\mathrm{g}(\mathbf{k}, L)d\mathbf{k}, \quad \mathrm{g} = 2, 3, \text{or } 5. \tag{3.43}$$

The validity of the eqs. 3.42 regarding 3.39 was confirmed numerically by Dietrich et al. (2018) and experimentally for coseismic fields by Devi et al. (2018).

3.9 Reciprocity tests

In order to check for errors in the code, reciprocity tests were performed. These will highlight any polarity and amplitude inconsistencies, as well as missing or additional events (Garambois and Dietrich, 2002). The idea behind a reciprocity check is best

described by Aki et al. (2002, pg. 27 - 28) as a time-space equivalence between elastodynamic Green tensors. In the present context, a simple way test for reciprocity consists in contrasting seismoelectric with electroseismic fields. If reciprocity holds, mechanical fields oriented along direction i, and generated by EM forces oriented along j, should be equal to the j-oriented EM fields generated by i-oriented mechanical forces; in cartesian coordinates, i and j will correspond to any of the three main axis (x, y, or z).

Two geometries were used in the reciprocity checks, they are depicted in fig. 3.2. The first, designated by DW considers a source at a 0.1 cm depth and 30 receivers with x-offsets varying between 0 and 10 cm, shifted by 5 cm in the y-axis, and at a 10.9 cm depth. The second, from here onwards referred as UP, has a source at a 10.9 cm depth, and 30 receivers at a 0.1 cm depth whose x-offsets range between -10 and 0 cm, and that are shifted by -5 cm in the y-axis.

In the simulations, the media is bounded above and below by free-surface conditions (see section 3.4). It is made-up by a 11 cm thick homogeneous layer (Layer 1). Inside it, there is a 1 cm thick layer (Layer 2), whose top and bottom depths are, respectively, 5 and 6 cm. The input physical parameters describing each layer can be found in table 3.1. The expressions to calculate all other physical parameters, dependent on those in table 3.1, can be found in chapter 2, to calculate ζ for example, equation 2.23 was used.

Table 3.1: Physical properties describing the media used in the reciprocity tests. The asterisk refers to dimensionless values.

Properties	Layer 1	Layer 2
Porosity (ϕ)[%]	15	40
Tortuosity (α_∞) [*]	3	3
Fluid viscosity (η)[Pa·s]	1E-3	1E-3
Intrinsic permeability (k_0) [m^2]	1E-15	1E-11
Geometrical parameter m [*]	6	6
Solid density (ρ_s) [Kg/m^3]	2.7E3	2.7E3
Fluid density (ρ_f) [Kg/m^3]	1E3	1E3
Solid bulk modulus (K_s) [GPa]	36	36
Fluid bulk modulus (K_f) [GPa]	2.2	2.2
Frame bulk modulus (K_{fr}) [GPa]	9E-2	3E-2
Frame shear modulus (G) [GPa]	7E-2	2E-2
Molarity (M_f) [mol/L]	1E-2	1E-5
Solid permittivity (κ_f)[$*$]	4	4
Fluid permittivity (κ_f)[$*$]	80	80
Temperature (T) [K]	298	298

Regarding the discretization parameters, 2048 time samples were used for a 0.8192 ms window. The source is a 100 kHz Ricker wavelet, and a -0.05 ms time-shift was considered in order to map the start of an event to one of the edges of the Ricker waveform.

Oriented mechanical forces (F_x, F_y, F_z) and transient electric dipoles (C_x, C_y, C_z) were employed as sources (recall the definition of the vector of forces $\mathbf{S}$, equation 3.7). For each source and geometry, the cartesian components of the displacement and the electric field are displayed in figures 3.3, 3.4, 3.5, 3.6, 3.7, and 3.8. Figures on the left show the displacement due to oriented dipolar forces while the ones on the right show the reciprocal electric fields created by oriented mechanical forces.

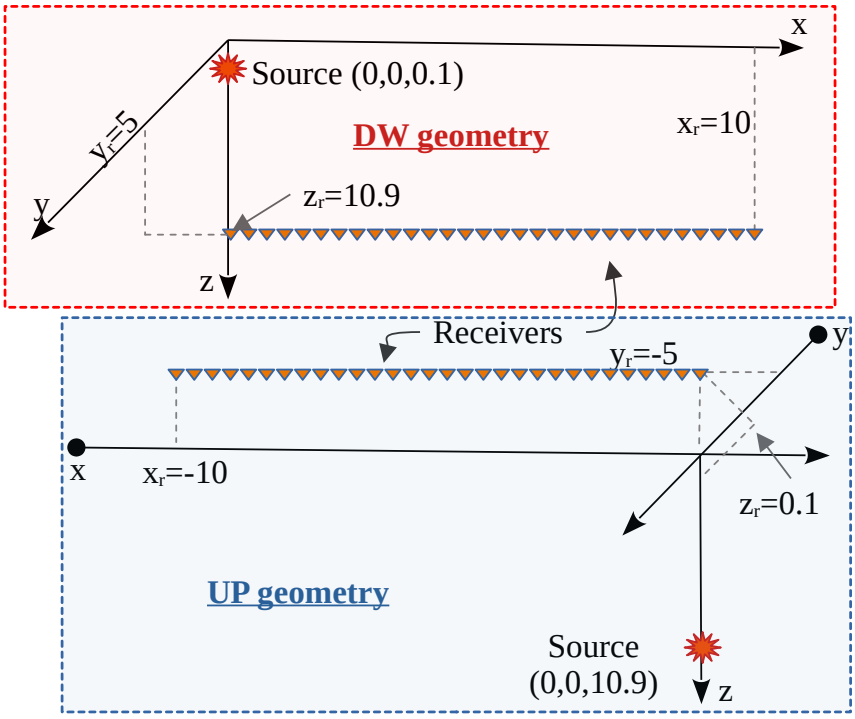

Figure 3.2: Geometries involved in the reciprocity tests. The units of distance are centimeters. Check text for a throughout description.

An inspection of these figures leads to the conclusion reciprocity is satisfied in terms of waverforms, amplitudes, and seismic velocities, for all seismoelectric and electroseismic wavefields. Both coseismic and interface-generated waves can be distinguished in the seismograms/electrograms, even though the latter is more evident in figs. 3.5e, 3.5f, 3.6e, 3.6f, 3.7e, 3.7f, 3.8e, and 3.8f, as the synchronous event between 0 and 0.05 ms. Periodic multiples are also easily identified an occur mainly due to the two free-surfaces bounding the media.

With these tests the numerical calculations carried out by the code of Garambois (1999) are validated, what consequently implies that all the modifications realized in the context of this thesis are valid. Since the electric potential depends on the electric field, its calculation is also taken as correct. Finally, a reciprocity test with the other wavefields calculated by the code leads to the same conclusions.

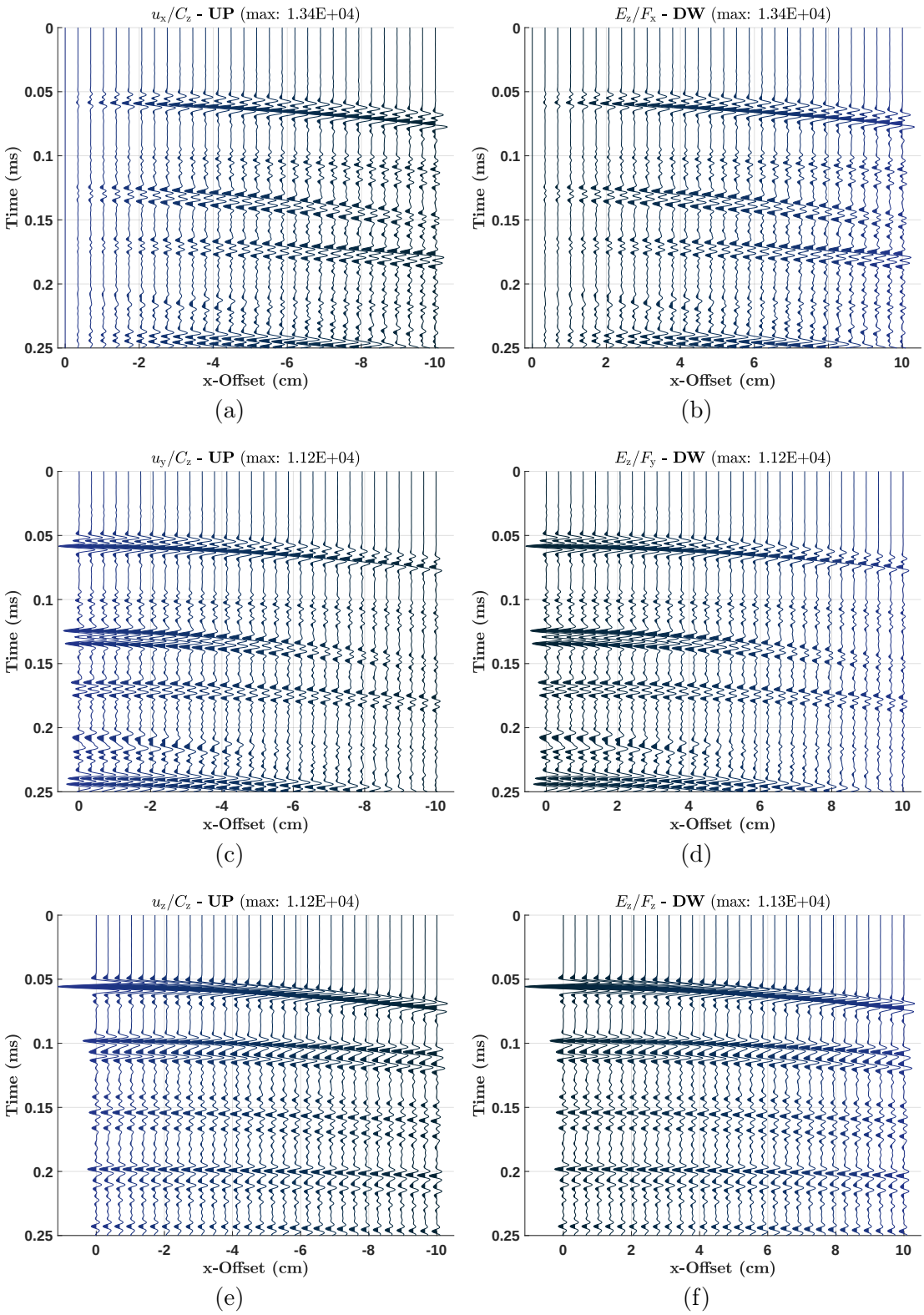

Figure 3.3: Reciprocity check. Cartesian components of the displacement created by a dipole oriented along the z-axis considering the UP geometry, and E_z due to oriented mechanical forces in the DW geometry.

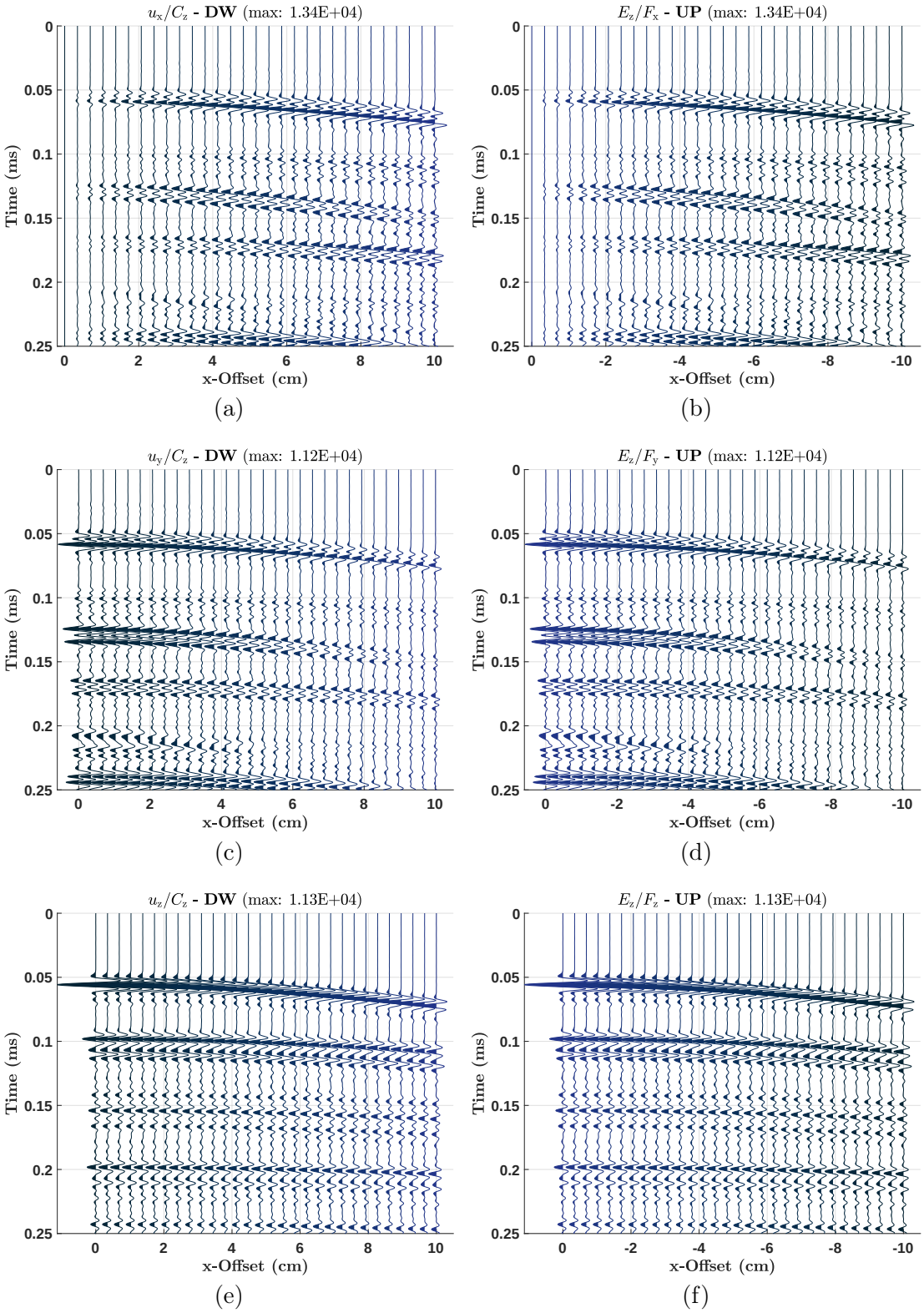

Figure 3.4: Reciprocity check. Cartesian components of the displacement created by a dipole oriented along the z-axis considering the DW geometry, and E_z due to oriented mechanical forces in the UP geometry.

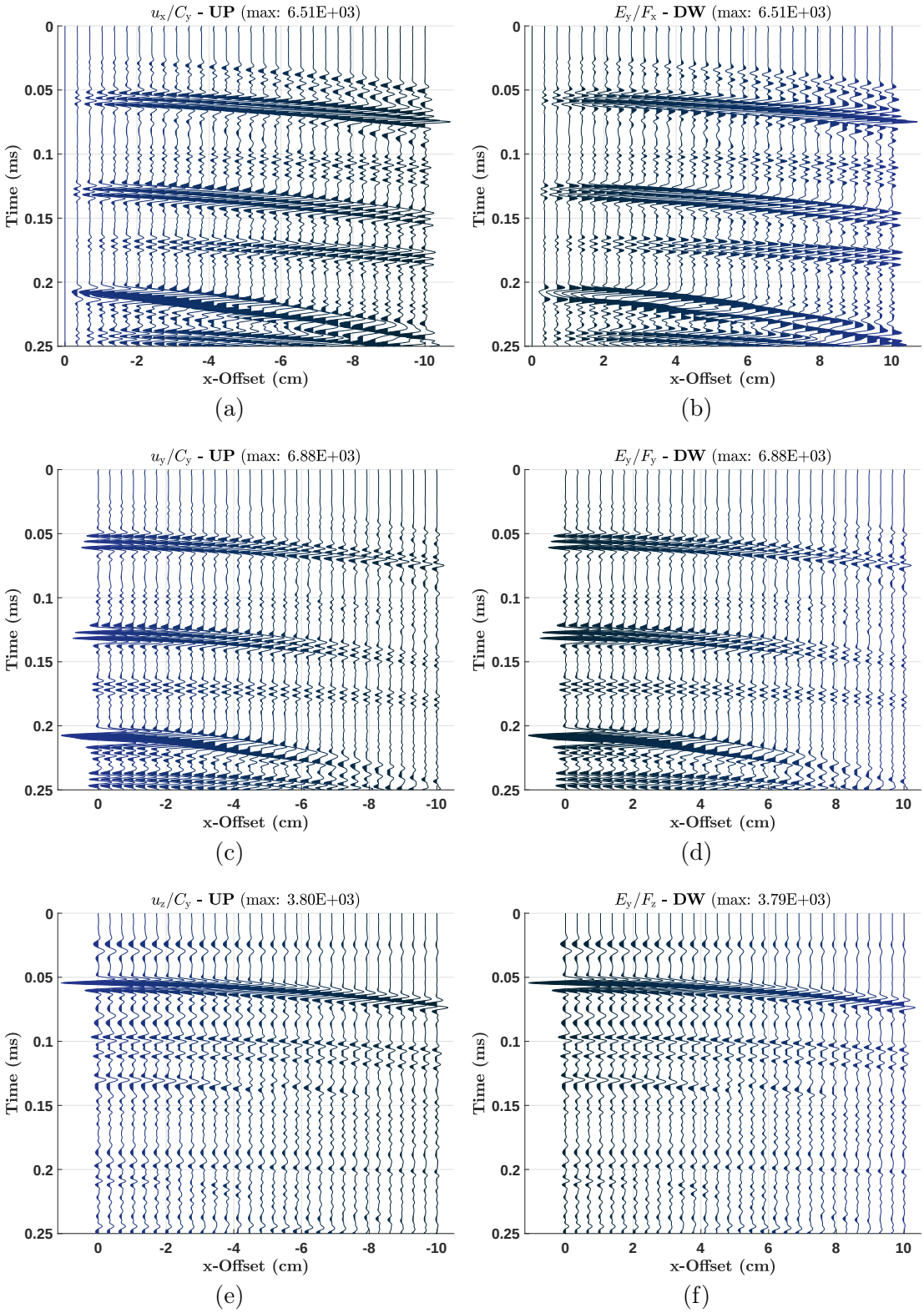

Figure 3.5: Reciprocity check. Cartesian components of the displacement created by a dipole oriented along the y-axis considering the UP geometry, and E_y due to oriented mechanical forces in the DW geometry.

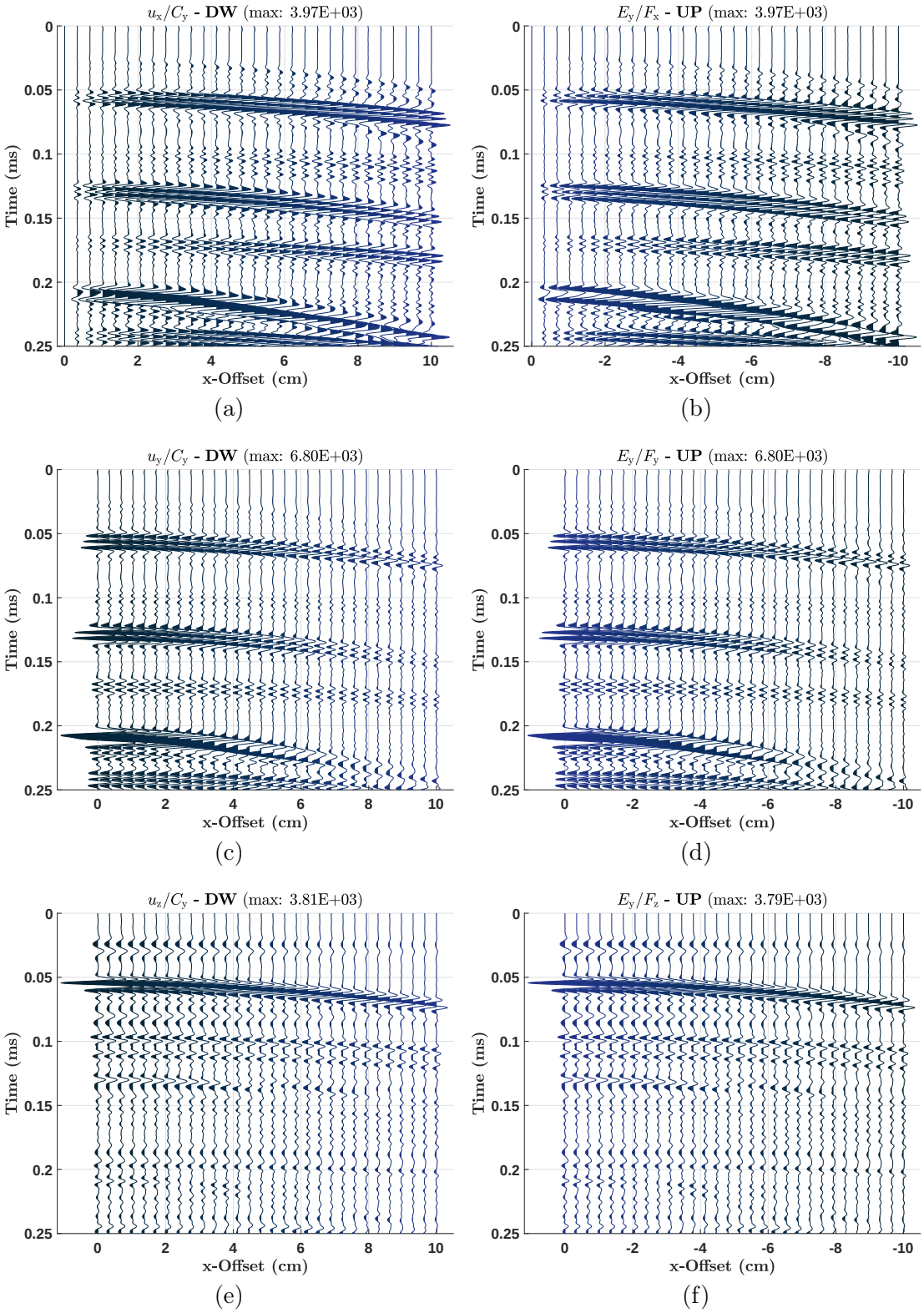

Figure 3.6: Reciprocity check. Cartesian components of the displacement created by a dipole oriented along the y-axis considering the DW geometry, and E_y due to oriented mechanical forces in the UP geometry.

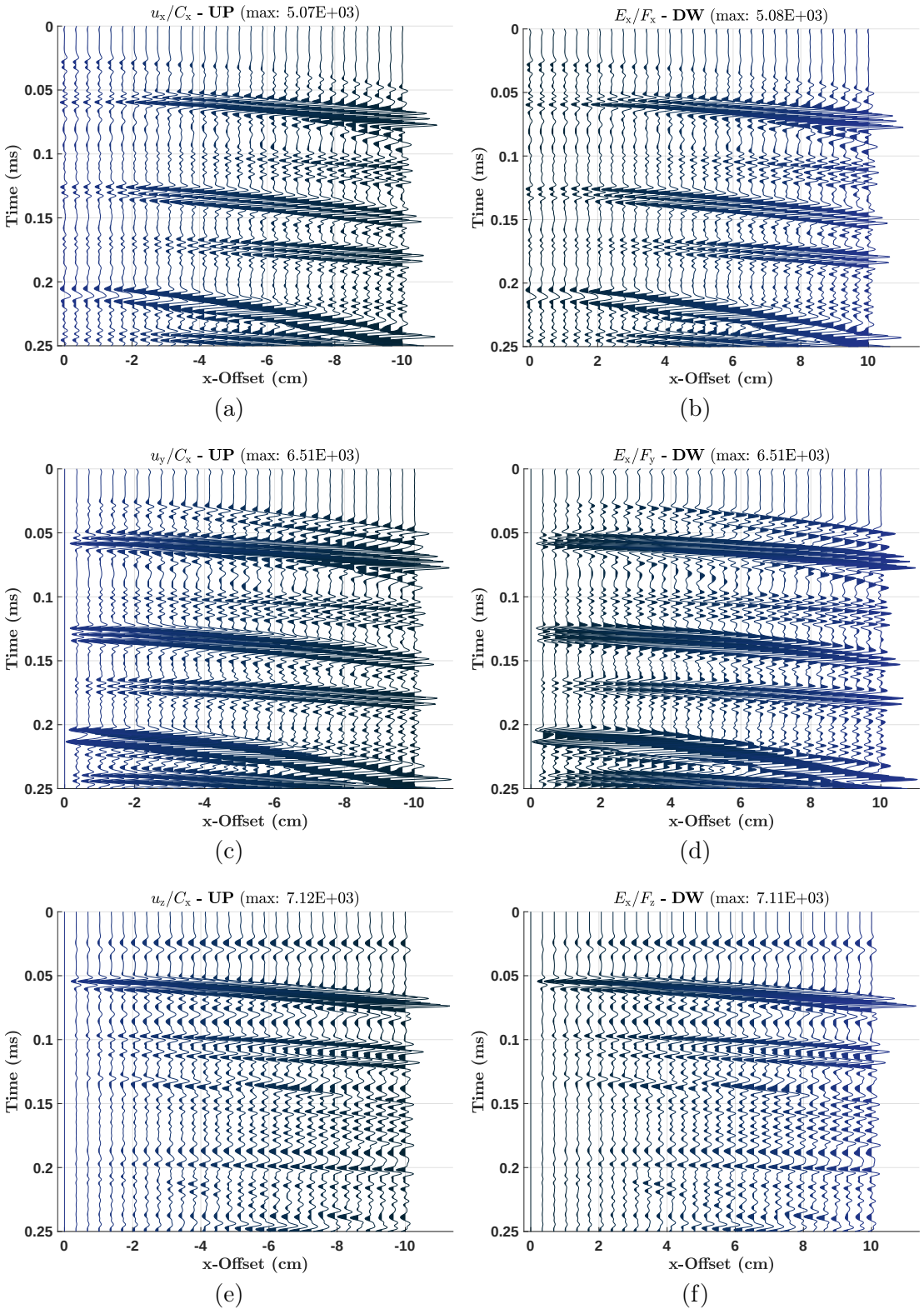

Figure 3.7: Reciprocity check. Cartesian components of the displacement created by a dipole oriented along the x-axis considering the UP geometry, and E_x due to oriented mechanical forces in the DW geometry.

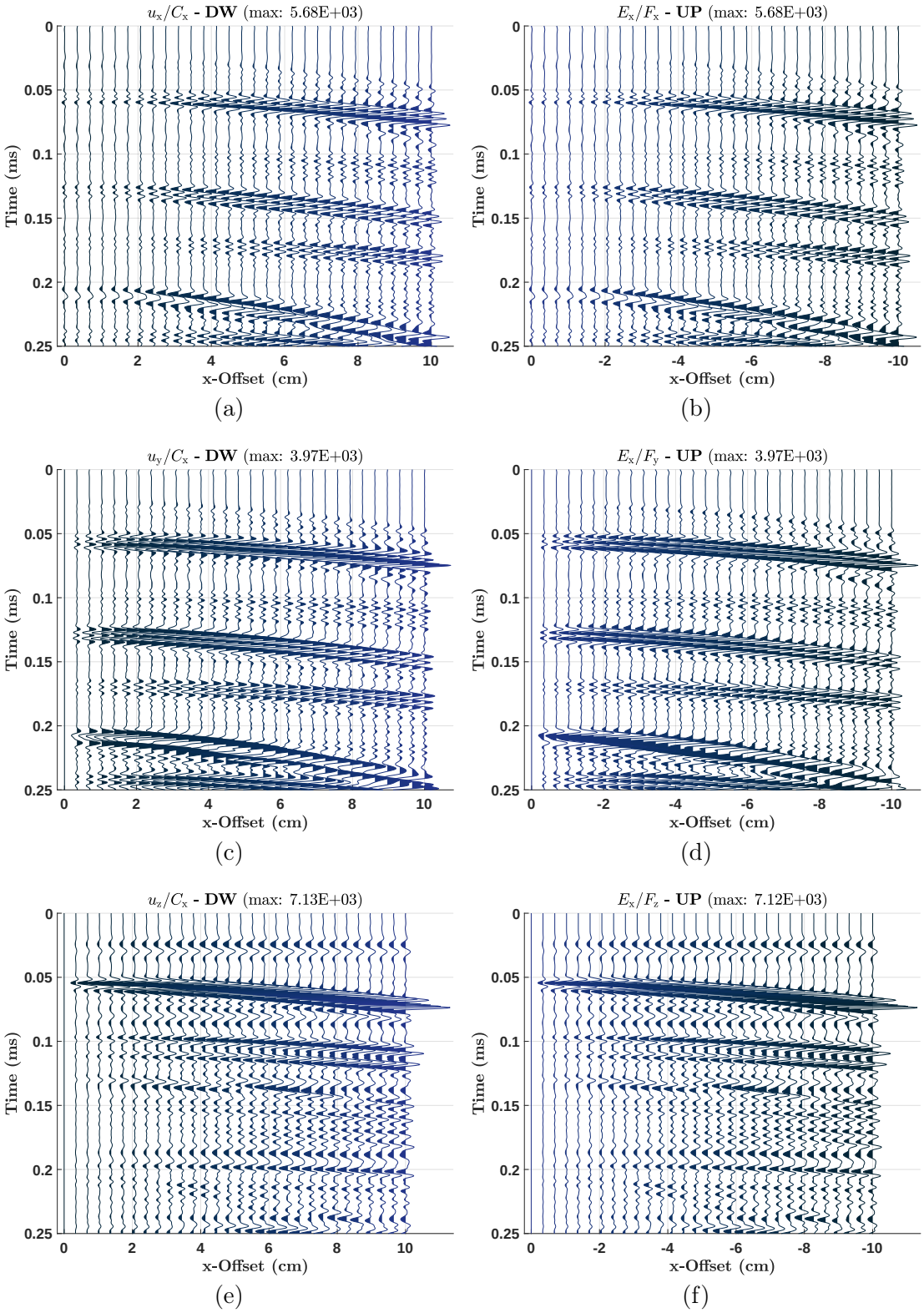

Figure 3.8: Reciprocity check. Cartesian components of the displacement created by a dipole oriented along the x-axis considering the DW geometry, and E_x due to oriented mechanical forces in the UP geometry.

4 Experimental framework

In order to obtain experimental measurements of the electrokinetic phenomena, discussed in the previous chapters, an experiment was designed to allow the detection of both the coseismic and the interface-generated EM signals.

Figure 4.1 details the experimental set-up. A signal is created by a function generator and goes through an amplifier before exciting a piezoelectric transducer, like that a mechanical disturbance is created and propagates in the material contained within a plastic box. Seismic displacement will be detected by a laser vibrometer while pointed at a thin ($\simeq$ 0.1 mm) reflective film, placed on the surface of the material (i.e., in its interface with air). Potential differences associated with seismoelectric phenomena in the medium will be detected by electrodes using a preamplifier to analogically compute the difference of potential measured at two points.

An oscilloscope is in the end of the acquisition chain, recording both seismic and electrical measurements. The orientation of the cartesian axis is explicitly drawn in figure 4.1 to help understand how numerical simulations will relate to experimental data. The origin corresponds to the topmost point of the piezoelectric source, which is usually in the center regarding the x-axis, and in the interface between material and air regarding the y-axis. Finally, in the following sections the individual parts of the experimental set-up will be discussed as well as the choice of parameters used for the numerical simulations and, in the end, I will consider an option to automate the electric acquisition.

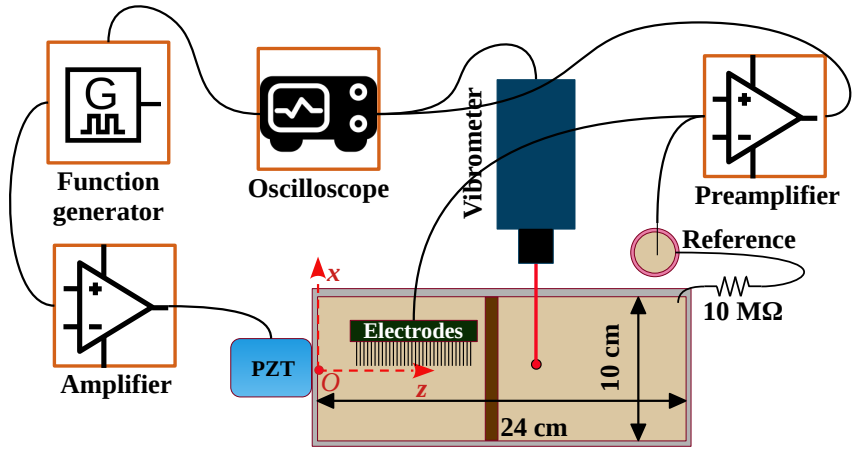

(a)

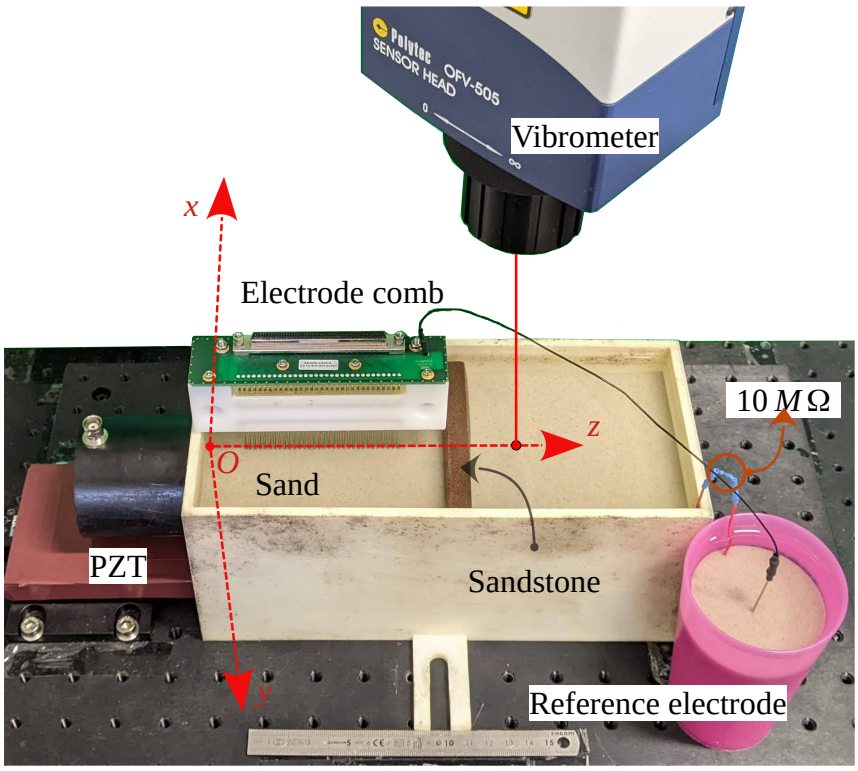

(b)

Figure 4.1: Experimental set-up: (a) diagram highlighting the main electronic components of the acquisition system connected to the sandbox viewed from above, (b) picture of the experimental set-up. The cartesian coordinate system (x, y, z) has its origin O at the top of the sand, centered with respect to the x-axis and corresponding in space to the topmost point of the PZT seismic source.

Table 4.1: Physical parameters of the sand. ⋆ means it is a reference value. DC permeability refers to intrinsic permeability.

Name	Value	Reference
Grain diameter (d_g)[μm]	250	Barrière et al. (2012)
Porosity (ϕ)[%]*	0.4	Barrière et al. (2012)
DC permeability (k_0)[m^2]	1.02E-11	Barrière et al. (2012)
Bulk (solid) modulus (K_s)[Pa]	36E9	⋆
Shear (solid) modulus (G_s)[Pa]	44E9	⋆
Bulk (frame) modulus (K_{fr})[Pa]	2.38E7	Eq. 2.17 and seismic velocities
Shear (frame) modulus (G_{fr})[Pa]	1.43E7	Eq. 2.17 and seismic velocities
Solid density (ρ_s)[kg/m^3]	2.65E3	⋆
Solid permittivity (κ_s)[ ]*	4	⋆
Tortuosity (α_∞)[ ]*	1.65	Holzhauer (2015)
Surface conductivity (σ_s)[mS/m]	[83–128]E-3	$4\Sigma_s/d_g$, Σ_s from Revil and Glover (1998)

4.1 Sand

The main material used during experiments is a quaternary eolian sand from Southwest France, composed mainly of silica ($SiO_2 > 98\%$) and whose mean grain diameter is 250 μm. Additionaly, the solid grain density ranges between 2635 and 2660 kg/m^3. This is the same material used in Barrière et al. (2012), Bordes et al. (2015), and Holzhauer et al. (2017).

Considering $\rho_B = 2650$ kg/m^3 Barrière et al. (2012) found a porosity of 0.4 ± 0.02 for the sand discussed here by comparing the weight of saturated and dry samples. Holzhauer et al. (2017) estimated a value of 0.42 for ϕ based on an empirical equation as well as indirect measurements.

Regarding the intrinsic permeability, using the same method, but different settings, Barrière et al. (2012) and Holzhauer et al. (2017) obtained the values: 1.02E-11 and 2E-11 m^2, respectively. Additionally, the tortuosity was indirectly estimated by Holzhauer et al. (2017) based on measurements of the formation factor and on Equation 2.5.

Frame moduli were calculated using Equation 2.17 with $n_o = 9$ and $p_o = 18$ MPa. The value of p_{eff} in 2.17 was adjusted with respect to the seismic velocities measured in the saturated sand, with the premise that velocities predicted by Biot's theory and experiments should match.

In this study the (electric) surface conductivity will be considered for the quartz, even though its value is negligible with respect to the fluid's. As pointed out in section 2.2.3, it will be estimated using the surface conductance Σ_s of quartz and the grain diameter. Σ_s depends on the ionic concentration of the pore fluid when

$M_f \leq 1E-3$ mol/L but has a constant value of 8E-9 S above this molarity (Revil and Glover, 1998). For the range of conductivities considered in the present work $M_f > 1E-4$ mol/L. Therefore based on Revil and Glover (1998), Σ_s will have values in the range [5.2–8]E-9 S, implying σ_s in [83–128]E-3 mS/m.

Table 4.1 summarizes the physical properties of the sand, provinding their references.

4.2 Sandstones

Two types of sandstone rocks were used when studying the EM phenomena created at interfaces, the first is a Vosges sandstone and the second a Fontainebleau. The samples of these sandstones were cut according to the dimensions of the experiment and introduced in the sand to allow an analogy with a layered medium. Figure 4.2 shows a photo of a sample for each sandstone type and Table 4.2 shows the physical properties considered in this thesis.



(a) Vosges (b) Fontainebleau

Figure 4.2: Photo of samples of sandstones used in this thesis.

The rock samples of Vosges sandstones used contain a fair amount of feldspar, mica, clay, and oxides, thus its properties were considered similar to the samples studied in David et al. (1994) and Lorne et al. (1999b). Consequently, the values of permeability, tortuosity (derived with equation 2.5), surface conductivity, and zeta potential were taken from Lorne et al. (1999b). Regarding the other physical parameters, porosity and density were measured in the laboratory, and frame moduli were

Table 4.2: Physical parameters of the sandstones. ⋆ means it is a reference value. DC permeability refers to intrinsic permeability.

Name	Value	Reference
Vosges		
Porosity (ϕ)[%]*	0.24	Measured
DC permeability (k_0)[m^2]	6.8E-15	Lorne et al. (1999b)
Bulk (solid) modulus (K_s)[Pa]	36E9	⋆
Shear (solid) modulus (G_s)[Pa]	44E9	⋆
Bulk (frame) modulus (K_{fr})[Pa]	3.41E8	Eq. 2.16 and seismic velocities
Shear (frame) modulus (G_{fr})[Pa]	2.1E8	Eq. 2.16 and seismic velocities
Solid density (ρ_s)[kg/m^3]	2.12E3	Measured
Solid permittivity (κ_s)[ ]*	4	⋆
Tortuosity (α_∞)[ ]*	3	Eq. 2.5 with F $= 12.5$ from Lorne et al. (1999b)
Zeta (ζ)[mV]	[-12 – -7]	Lorne et al. (1999b)
Surface conductivity (σ_s)[mS/m]	2E-3	Lorne et al. (1999b)
Fontainebleau		
Porosity (ϕ)[%]*	0.2	Jouniaux and Pozzi (1995)
DC permeability (k_0)[m^2]	1.22E-12	Jouniaux and Pozzi (1995)
Bulk (solid) modulus (K_s)[Pa]	36E9	⋆
Shear (solid) modulus (G_s)[Pa]	44E9	⋆
Bulk (frame) modulus (K_{fr})[Pa]	3.6E9	Eq. 2.16 and seismic velocities
Shear (frame) modulus (G_{fr})[Pa]	2.34E9	Eq. 2.16 and seismic velocities
Solid density (ρ_s)[kg/m^3]	2.65E3	⋆
Solid permittivity (κ_s)[ ]*	4	⋆
Tortuosity (α_∞)[ ]*	12.2	Eq. 2.5 with F $= 61$ from Jouniaux and Pozzi (1995)
Zeta (ζ)[mV]	-21.9	Jouniaux and Pozzi (1995)
Surface conductivity (σ_s)[mS/m]	30E-3	Lorne et al. (1999b)

estimated using the P-wave velocity, obtained from the experiments, and equation 2.16 with a consolidation parameter equal to 330.

Considering the Fontainebleau sandstone, it is a well studied rock mainly composed by quartz. For the sample used here porosity, permeability, tortuosity, and zeta potential are those found in Jouniaux and Pozzi (1995), while surface conductivity was again taken from Lorne et al. (1999b). Frame moduli were obtained with the same approach used for the Vosges sandstone but with a consolidation parameter equal to 330.

At last, in-between experiments, all rock samples were kept immersed in water to ensure full saturation, and fluid conductivity was routinely controlled to ensure it remained in the range [1.2 – 1.8] mS/m.

4.3 Pore-fluid water

Distilled water is the main component of the fluid-phase used in the experiments. It has a conductivity of about 0.3 mS/m, as output from the filtering system at

LFCR. Additionally, a 0.9% NaCl solution was used to increase the conductivity in the corresponding experiments.

4.4 Plastic container

A parallelepipedal container was 3D printed, using a PA-12 plastic, to hold the sand and sandstones used in the experiments (white box in figure 4.1b). The walls of this box have all 5.2 mm, except for the one where the piezoelectric source is positioned which has 2.5 mm, in order to reduce the attenuation due to the signal propagating in the plastic.

The effective volume inside the container has a 24 cm length (z-axis), 10 cm width (x-axis), and 11 cm height (y-axis). An auxiliary container is used to insert a reference electrode; it is the pink cylindrical box in figure 4.1b. These containers do not touch, such that there is no (measurable) direct mechanical wave arriving at the reference electrode placed inside the pink cylinder.

4.5 Source

Due to the size of the experiment, dictated by the dimensions of the plastic container used, the wavelength of the seismic waves needs to be small enough to ensure the data will have a good resolution. Considering the physical parameters of the sand used in the experiments (table 4.1), Pride's theory (section 2.3.1) predicts P-wave velocities in the range [1682 – 1789] m/s, for frequencies varying between 1 Hz and 1 MHz, and a transition frequency of about 3.88 KHz. Therefore, to attain wavelengths smaller than 1 cm, frequencies above 178 kHz need to be considered (i.e., ultrasonic frequencies).

An ultrasonic P-wave source frequently used in laboratory studies is a piezoelectric transducer (Lebedev et al., 2011; Devi et al., 2018; Shen et al., 2022), and it is this type of source that will be used in the experiments conducted during this thesis. Following Devi et al. (2018), the piezoelectric transducer (PZT) shown in figure 4.3 was used; it generates mainly longitudinal waves and performs best when excited with a signal whose central frequency is 250 kHz.

Using a function generator (model RIGOL DG4102), a half sinus signal is sent to an amplifier (model Falcon Systems WMA 300) and then to the PZT. Three main parameters of the function generator will control the final displacement waveform

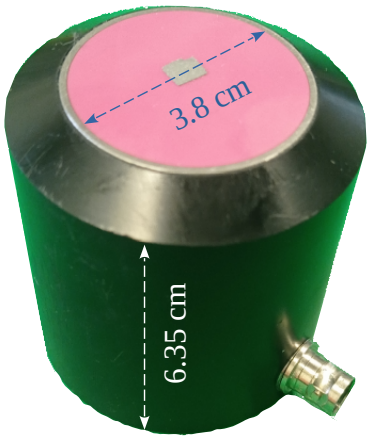

Figure 4.3: Piezoelectric transducer *Panametrics Olympus* V1012.

measured (using the equipment detailed in the next section): the frequency, the peak-to-peak voltage, and the period; to determine the best value of each parameter they were individually studied and figures 4.4 and 4.5 summarize the results.

The study of source parameters involved measuring the displacement on top of the saturated-sand, at (x=0, y=0, z=8 cm) following the geometry in figure 4.1, when no layer is present. Figure 4.4 shows the results when the frequency of the signal created by the waveform generator is changed. Both the duration and the amplitude of the waveform in figure 4.4a vary considerably, with amplitudes reaching a maximum when the frequency is 120 kHz (figure 4.4b). Moreover, the form of the signal measured may change due to secondary events like reflections on the sides and bottom of the sandbox.

Figures 4.4c and 4.4d show, respectively, how the measured magnitude spectra and the peak frequency (f_{peak}) vary. Looking at the f_{peak} estimated from the FFT magnitude spectra of figure 4.4c it is clear that after 120 kHz, no matter the frequency used to excite the PZT, a $\simeq$ 122 kHz component will dominate the seismic signal. On the other side, if we use maxima and minima to get an approximate value for the half-period of each waveform (red circles in figure 4.4d), the estimated f_{peak} increases with input frequency until 500 kHz, with a linear behaviour until 200 kHz.

From the analysis of the influence of input frequency, no clear choice seem to be the best. Nevertheless, it was previously stated that frequencies should be higher than 178 kHz, and from the PZT specifications it should perform best when the input frequency is 250 kHz, therefore that is the input frequency chosen here.

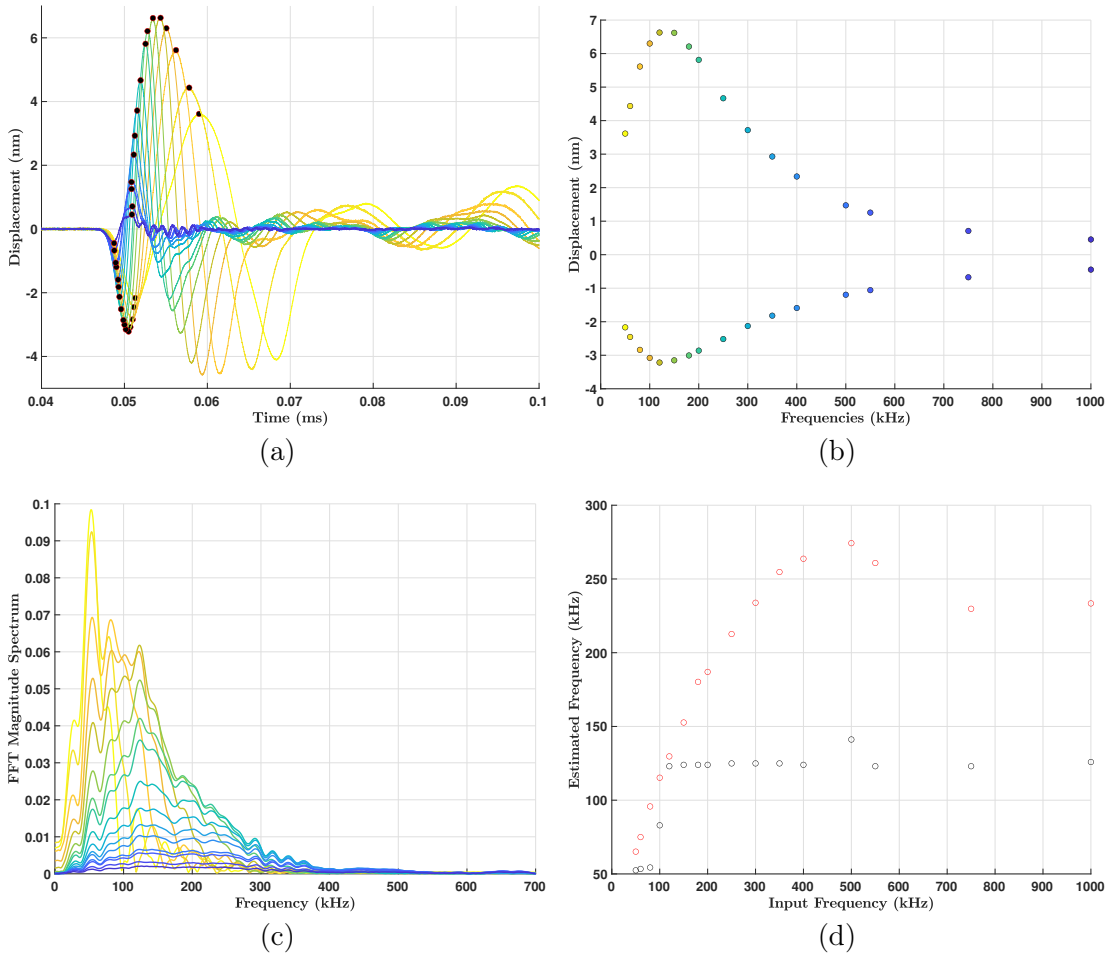

Figure 4.4: Displacement measured when the peak frequency of the signal exciting the PZT source varies from 50 kHz until 1 MHz. The colors associated with frequencies in (b) indicate the colors of the corresponding curves in (a) and (c). The input peak-to-peak voltage used was 14 V and the source period was set to 100 ms. (a) focuses on the first arrivals for each frequency, and highlights their corresponding maxima and minima. (b) details the values of maxima and minima. (c) shows the FFT magnitude spectra of the waveforms in (a). (d) displays the estimated peak frequency using the FFT (black), and based of the apparent half-period given by the maxima and minima positions (red).

Another parameter controlled by the waveform generator is the peak-to-peak voltage of the signal sent to the amplifier and then to the PZT. While the function generator has an upper limit of 20 V, the amplifier used will create a signal 50x higher than the one input to it, but limited to $\pm$ 150 V, that means the maximum peak-to-peak voltage recommended by the amplifier specifications is 6 V. However, after this limit the amplifier will still amplify the signals input to it.

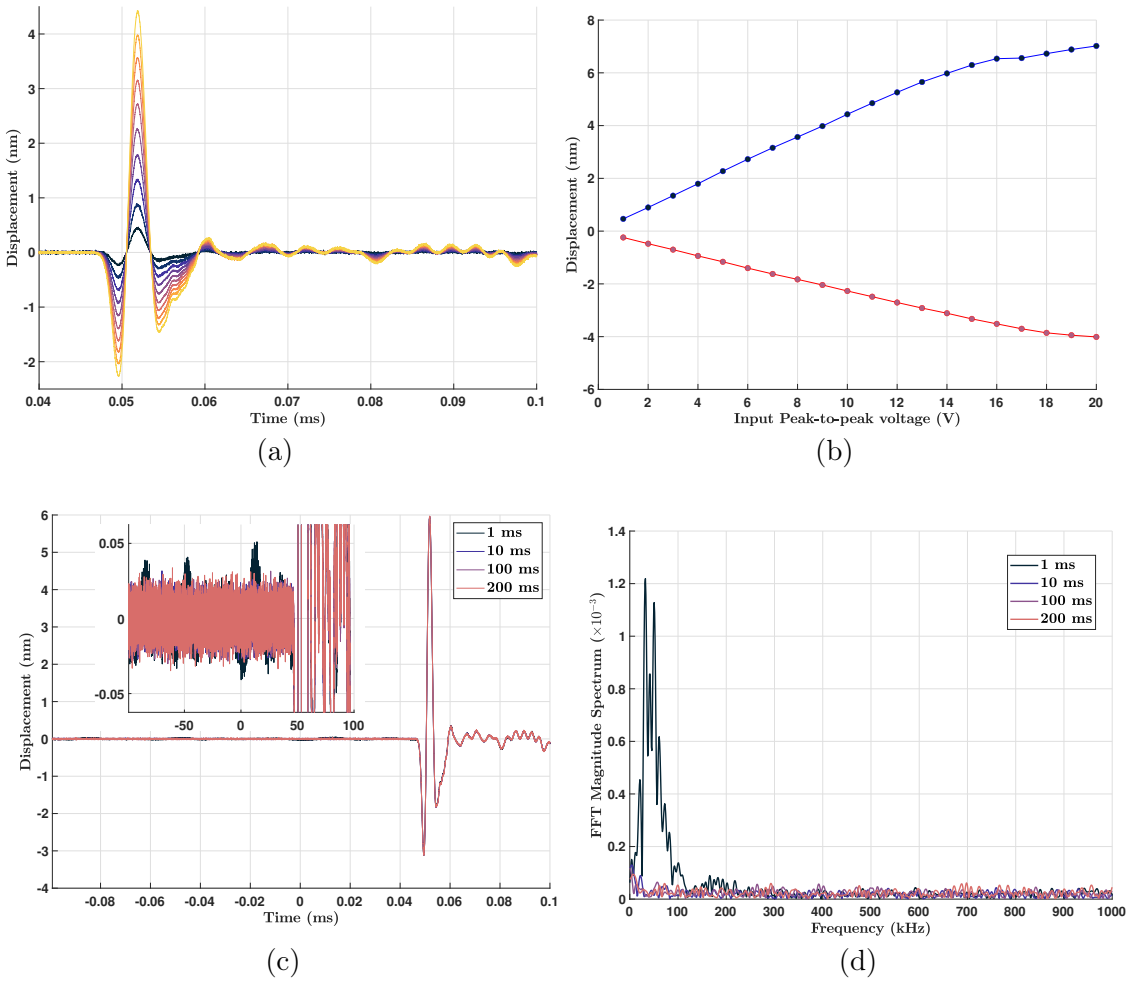

Figure 4.5: Study of the influence of input voltage and period of the signal input to the PZT. A 250 kHz signal was used as reference. (a) details how the magnitude of the measured displacement will increase while increasing the input voltage from 1 to 20 V. (b) shows how maxima and minima will vary with input voltage. (c) displays the measurements, using 14 V, and varying the source period; in the upper left there is a zoom in the region preceding the arrival of the seismic wave. (d) presents the FFT magnitude spectra of each signal in (c), but considering only times before 0.

Figures 4.5a and 4.5b show the measurements performed exactly as when studying the frequency, but for changes in the peak-to-peak voltage. From these figures, it is clear the amplifier still amplifies after 6 V, and as a matter of fact it appears that there is a linear increase until about 16 V. Because in the experiment higher amplitudes of the signals generated by the PZT imply higher signal-to-noise ratios of the measured signals, a value of 16 V was chosen, since after that amplitudes do

not increase significantly (check figure 4.5b) and the risk of damaging the amplifier may also increase.

The last parameter is the source period (i.e., pulse repetition frequency), the time after which a new signal is output to the preampliier and then to the PZT. If the period is not big enough, when a new wave is created by the PZT, there may still exist higher order reflections taking place inside the sandbox that can interfere with the newly generated P-wave. Conversely, if the period has a very large value, the acquisition will take a long time to finish; the choice of period must account for these two factors.

Figures 4.5c and 4.5d show the signal measured (using the same configuration as in the previous cases) for four different periods. It is evident from figure 4.5c that when a period of 1 ms is used, there still exists waves propagating inside the sandbox; figure 4.5d corroborates with this idea, showing that there is a band-limited signal preceding the direct P-wave (which should be the first to arrive). Additionally, results using 10, 100, or 200 ms are practically equivalent, what motivated the value of 10 ms to be chosen, since it leads to considerably faster acquisition times, compares with 100 or 200 ms.

4.6 Laser vibrometer (displacement receiver)

The seismic receiver included in the experimental setup is a laser Doppler vibrometer (LDV) designed by Polytec Inc., which allows contactless measurements based on the principles of laser interferometry. It consists of a OFV-505 single-point sensor (Polytec, 2017) and a OFV-5000 vibrometer controller that includes a DD-300 decoder to allow for displacement measurements up to values of $\pm$ 75 nm, in the frequency range [0.03 – 24] MHz (Polytec, 2016). Figure 4.6 shows a picture of the LDV sensor and controller.

Because of the small diameter of the region affecting the LDV, compared with the dimensions of the experiment, seismic measurements are practically punctual. This property of the LDV makes it more attractive, in terms of spatial resolution, than other seismic receivers commonly employed for seismic studies in the laboratory scale, like mini hydrophones (Zhu et al., 1999) or accelerometers (Bordes et al., 2015). Complementarily, by using a LDV, issues linked to bad coupling between receiver and media can be avoided.



Figure 4.6: Laser doppler vibrometer. On the top there's a picture of the OFV-505 sensor and below it the OFV-5000 controller.

Using a LDV to study the propagation of ultrasonic waves in the laboratory is not a novelty as there are plenty of works devoted to this subject, like Scales and Malcolm (2003), Lebedev et al. (2011), Bodet et al. (2014), Devi et al. (2018), and Shen et al. (2022). It has been sucessively pointed as a promissing alternative to other receivers, thus justifying the choice of adopting it in this thesis.

Besides the advantages of using a LDV, it is fairly sensitive to the reflectance of the surface it is pointed to. This means a LDV may not perform well in rough surfaces, such that the intensity of the energy being reflected back to the sensor will not be strong enough to allow high signal-to-noise ratios, and consequently a quantification of the seismic displacement will not be possible. As a matter of fact, as observed in the laboratory, this will be the case for measurements realized on the sand surface. A standard alternative is to use a thin reflective tape to ensure an optimal surface reflectance (Lebedev et al., 2011; Hasanian and Lissenden, 2017; Devi et al., 2018; Shen et al., 2022) and allow a precise measurement of the out-of-plane (perpendicular to the tape) displacement component.

Considering the reflective tape is not made of the same material as the medium studied, its influence on the measurements needs to be evaluated. Hasanian and Lissenden (2017) studied different alternatives to enhance the reflectance of an aluminium surface, including a reflective tape similar to the one used here, concluding below 1 MHz the out-of-plane displacement component measured by LDV is not impacted by the tape. Complementarily, Shen (2020) discusses that it is unwise to use a reflective tape when the goal is to perform a multi-component acquisition or

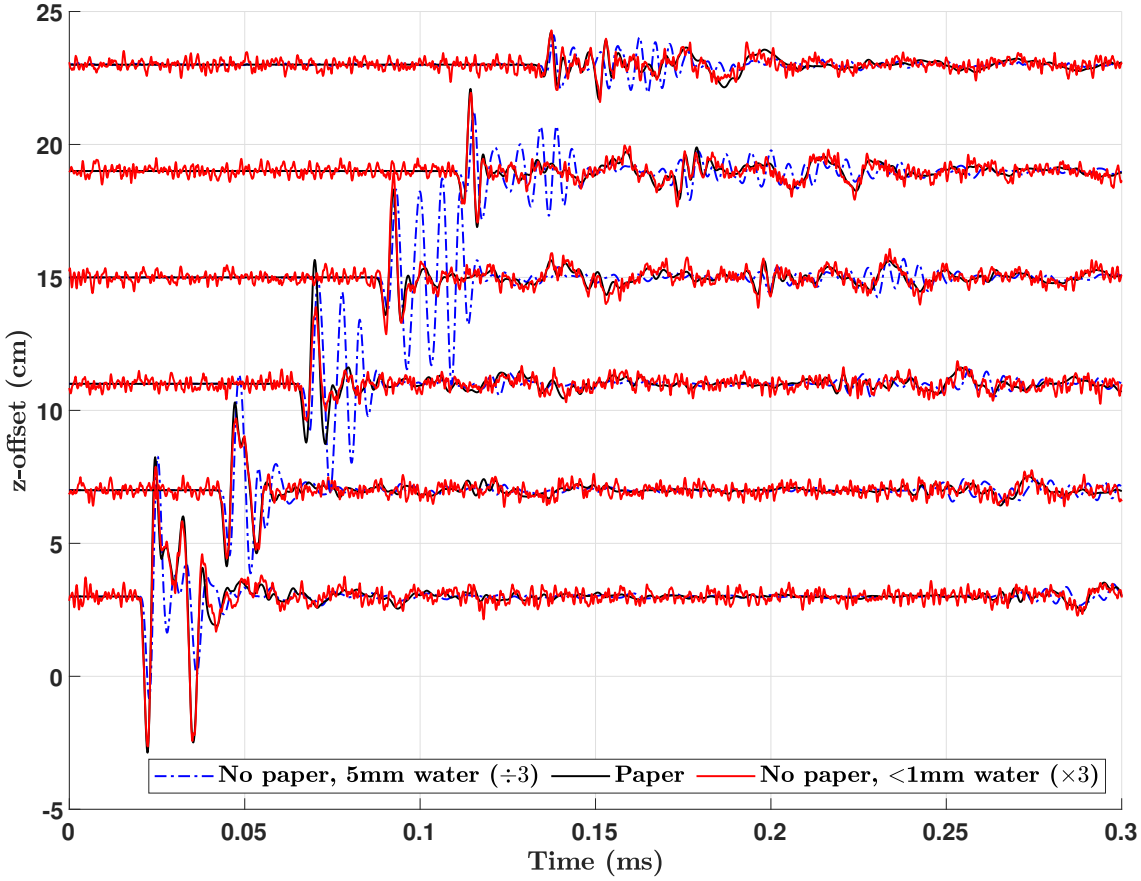

Figure 4.7: Acquisition using a LDV for 6 points inside the saturated sand-filled plastic box. Three cases are presented in order to study the need of a reflective paper on top of the sand (see details on the text).

to study wave polarization. In order to understand how LDV measurements will be influenced in the present experiment (figure 4.1), three situations will be compared: (1) measurements on the sand surface without any reflective tape and a 5 mm water layer; (2) also no reflective paper but with only a very thin water layer, such that the top of the sand grains are practically at the same level as the air-water interface; and (3) is the same water level as (2) but with a 4 mm^2 reflective paper (provided by Polytec Inc.).

In figure 4.7 the three situations mentioned above are compared, in blue case (1), in red case (2), and in black case (3). Data acquisition involved the PZT source from the last section, and each measurement is a stack of 2000 traces. All 6 measurement locations lie in a line in the center of the plastic box (x=0), on the top of the sand (y=0); the first z-offset is 3 cm away from the source and the others are equally spaced with a 4 cm step (see figure 4.1 for reference). It is important to note that

all signals are given in Volts and therefore must be multiplied by the factor 50E-9 to find the correct displacement values in meters.

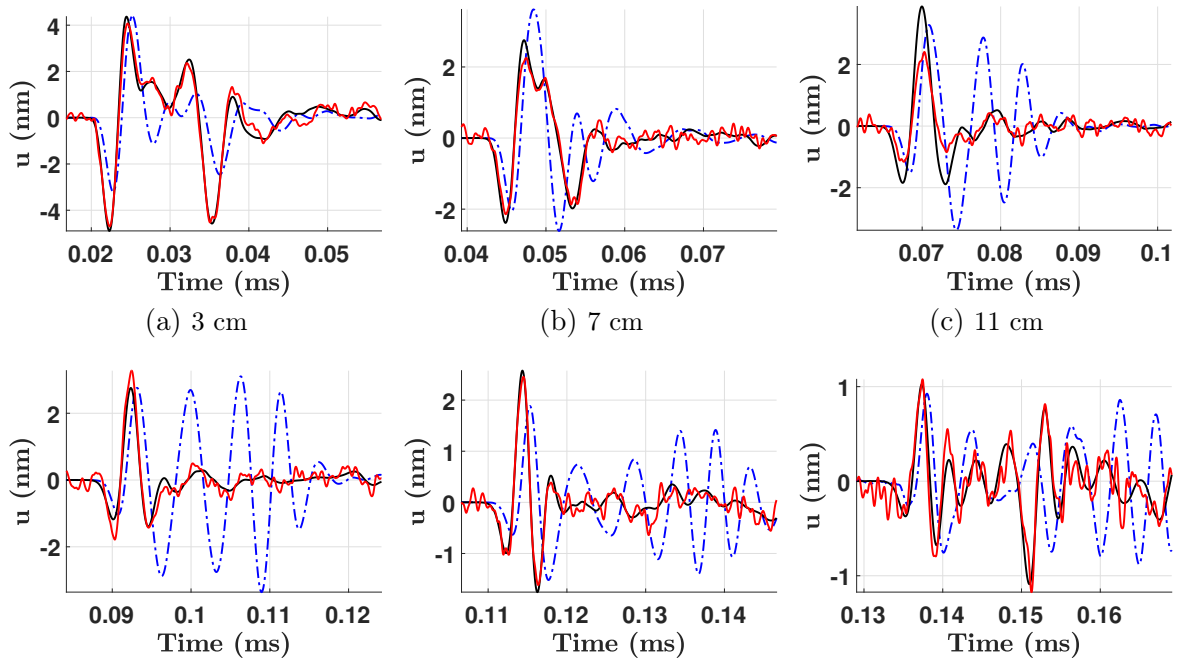

(a) 3 cm (b) 7 cm (c) 11 cm

(d) 15 cm (e) 19 cm (f) 23 cm

Figure 4.8: Zoom-in on the first arrival of the traces in figure 4.7; the same legend applies.

The first thing to notice in figure 4.7 is that the main events, like the direct P-wave (signal with highest energy), are synchronous for cases (2) and (3), and have a slight delay for case (1), probably because of the 5 mm water layer. Figure 4.8 shows a zoomed version of the first arrivals and help confirm the previous assertion. Another noticeable feature in both figures is the fact that the traces corresponding to case (2) are more noisy than in the two other cases; they are also the ones with smaller amplitudes, note that they were multiplied by 3 in order to have amplitudes that are comparable to (1) and (3).

Data corresponding to case (1) have amplitudes three times higher than case (3) and contain events that do not correlate to the ones found in none of the other two cases, what suggests it must be due to the presence of a thicker water layer that creates multiple reflections. Conversely, the data corresponding to cases (2) and (3) match almost perfectly, except by a factor 3, which is possibly due to the fact that the use of a reflective paper leads to more energy being reflected back to the LDV sensor.

Because when using a reflective tape, as in case (3), the signal measured is less noisy and the seismic events seem to match what is expected in the absence of the tape, the choice of carrying out all seismic acquisitions with a reflective paper and a very thin water later was made. However it is worth commenting that a drawback of this choice is that acquisitions will take longer since everytime one changes the measurement point, the small piece of tape will need to be moved.

A last point to discuss is the distance of the sensor to the surface studied. While the datasheet of the equipment (Polytec, 2017) suggests optimal measurements (visibility maxima) can only be attained at stand-off distances (measured from the focusing ring of the OFV-505 sensor) of 23.4 cm + $l \cdot 20.4$ cm ($l = 0, 1, 2, \ldots$), Shen (2020) searchs for visibility maxima at stand-off distances smaller than 23.4 cm, and finally decides to work with a value of about 5 cm. However, in the datasheet 10 cm is suggested as a minimum for the stand-off distance, and during the initial tests with the LDV when the front lens of the sensor was at distances smaller than 10 cm from the sand, the LDV system struggled to focus. Between 10 and 15 cm no significant change was perceived, and due to a setup limitation on how far the laser can be from the experiment, a value of about 10 cm was chosen for the distance of the front lens from the sand. Finally, the results of Shen (2020) for various stand-off distances, using a PZT source, do not seem to suggest there is a big impact of this variable on the measured amplitudes.

4.7 Electric data receiver

In the present experimental setup, the electric data receiver consists of a comb of electrodes, depicted in figure 4.9a, connected to an oscilloscope, either through a probe or a preamplifier, using coaxial cables. The comb was manufactured by Aquitaine Electronique and contains 0.1 cm thick and 8 cm long electrodes (effective length that can be inserted in the sand), with a centre-to-centre spacing equals to 0.25 cm. The oscilloscope probes are passive RIGOl RP2200 probes (see figure 4.9b) whose ground leads are connected, using alligator connectors, to a reference point (electrode) inside the experiment. Regarding the acquisition using a preamplifier, for most experiments a model SR560 (see figure 4.9c) was used in differential mode; however an in-house 8-channel preamplifier, based on the INA111 amplifier, was also used.

The 8-channel preamplifier was designed seeking to reduce the duration of acquisitions while allowing simultaneous measurements with more than one electrode. The last property is important when data from two, or more, electrodes are to be combined, like when calculating the electric field as a difference of neighbor electrode measurements (i.e., $\mathbf{E} = -\nabla\mathbf{V}$), or when exploring multi-electrode arrays. Regarding the making of this preamplifier, it is worth mentioning each channel (electrode) is connected to an INA111 amplifier in differential mode with a reference electrode, that is common to all channels. Moreover, a gain of 10 is applied to every output.

Because the signal measured in the oscilloscope must be equal to the actual signal created by seismoelectric phenomena at the electrode, the equipment used for measurements must preserve any signal it measures. With that in mind, in what follows, data acquired with the preamplifiers and with the oscilloscope probes will be compared, the placement of the reference will be explored, and three characteristics of the electrodes will be discussed: its depth, its thickness, and the centre-to-centre-spacing between electrodes.

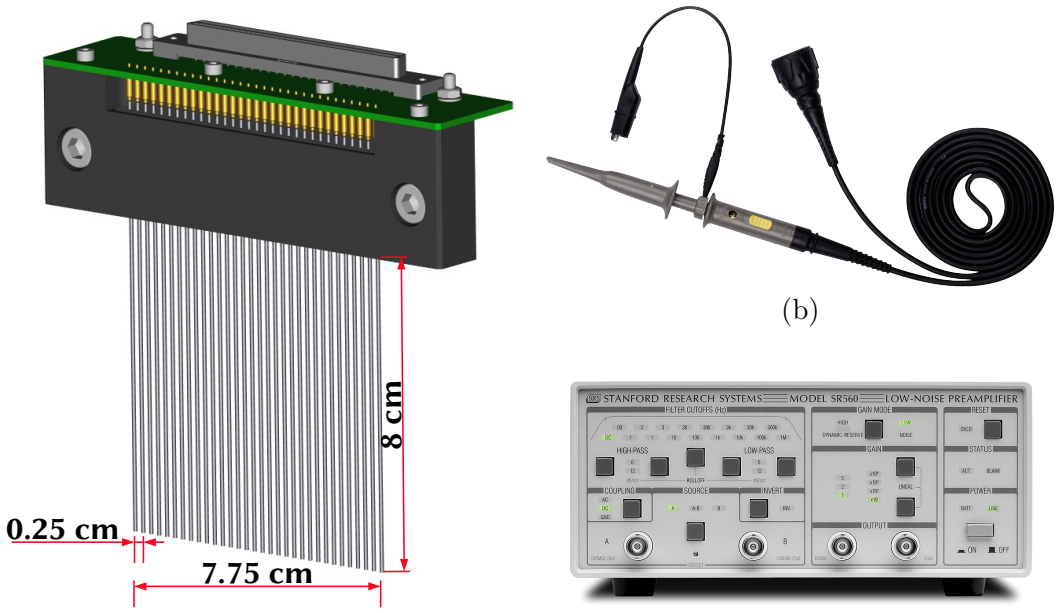

(a) (b) (c)

Figure 4.9: Elements that compose the electric data receiver. (a) shows the electrode comb and its dimensions. (b) is a picture of the RIGOL RP2200 oscilloscope probes. (c) shows a picture of the SR560 low-noise voltage preamplifier used.

4.7.1 Difference between acquisitions with oscilloscope probes and preamplifiers

In order to understand how the equipment used during acquisitions will influence measurements, two experiments were conducted: the first was designed to compare data acquired using oscilloscope probes with that using the SR560 preamplifier, while the second meant to compare data using both preamplifiers.

Probes *vs* SR560 preamplifier

A homogeneous medium (saturated sand) was used in the first experiment, with three electrodes positioned along the z-axis (x = 0), specifically at 4.7 cm, 8.7 cm, and 12.7 cm. Measurements were first done with the oscilloscope probes and then with the SR560 preamplifier, preserving, all the while, the electrodes' position. Besides, all acquisitions used a reference electrode placed in a secondary container. Figure 4.10a displays the data.

In figure 4.10a, the amplitudes of measurements obtained with the SR560 were divided by 4.4 to make sure the coseismic signals are in the same range of the data acquired using the probes; this value ensures the best similarity of coseismic maxima and minima, as demonstrated by figure 4.10b. Another feature that can be noted in figure 4.10a is the fact measurements made with the probes contain more noise. To put that in evidence, figure 4.10c shows the SNR calculated using the maxima and minima of the noise (referring to time samples before 0 s, thus data acquired in the absence of seismoelectric wavefields) and of the coseismic event. It is evident, from the SNR *vs* Offset plot that using the SR560 preamplifier leads to data with less noise, which is an expected result, considering the SR560 operating in differential mode will attenuate all EM signals arriving synchronously at the measurement and reference electrodes. Additionally, note that the intrinsic 0.03 Hz – 1 MHz pass-band of the preamplifier also contributes to noise attenuation.

With the objective of further understanding the $\simeq 4.4$ amplitude factor, the electronic circuits corresponding to the acquisitions using the probes and the SR560 will be studied. The premise to be analyzed, while comparing both circuits, is that the difference in amplitudes is linked to the input impedance (resistance, capacitance, and inductance).

The electronic circuit equivalent to the data acquisition using oscilloscope probes is presented in figure 4.11. ΔV_{SE} represents the difference between the local electric po-

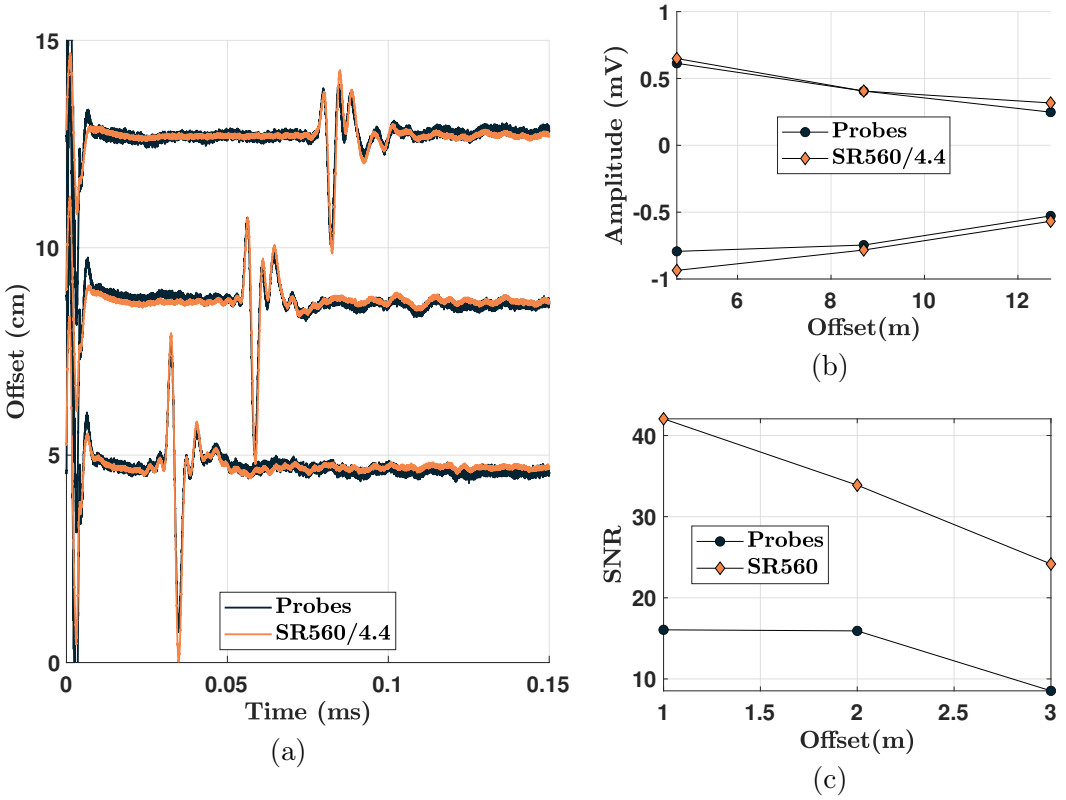

Figure 4.10: Electric data acquired using the oscilloscope probes (dark blue) and the SR560 preamplifier (orange). (a) show the measurements, (b) the maxima and minima of the coseismic, and (c) the SNR calculated with respect to the coseismic signal. Note that the factor 4.4 allows the best amplitude correspondence in (b).

tentials at the measuring (V_A) and at the reference (V_0) electrodes ($\Delta V_{SE} = V_A - V_0$). Therefore, considering there's no wave arriving at the reference electrode while waves arrive at the measuring one, ΔV_{SE} is the local electric potential due to seismoelectric phenomena ocurring at the measuring electrode ($\Delta V_{SE} \simeq V_A$). R_A is a resistance that accounts for the electrical contact resistance between medium and electrode, plus the internal electrode's resistance. R_B, C_B, and L_B are, respectively, the probe's resistance, capacitance, and inductance. R_{in} and C_{in} are the input impedance and capacitance of the oscilloscope. At last, because the ground of the system is connected to the reference electrode, the signal measured by the oscilloscope is defined by $V_{exp} = V_{in} - V_0$.

In the circuit of figure 4.11, all capacitive effects at the contact between medium and electrode were assumed negligible. By ignoring the contact capacitance, the circuit described becomes almost identical to the ones proposed in Kepic and Butler

(2002) and Dupuis (2008, p.59) for seismoelectric field acquisitions, and in Zonge and Hughes (1985) for controlled source audi-frequency magnetotellurics field measurements.

Concerning the transfer function of the circuit in figure 4.11, it relates the signal measured by the oscilloscope and the actual potential difference created by seismoelectric conversion in the medium, ΔV_{SE}. This relation will now be derived using the Laplace transform to facilitate the task. At first, from Kirchoff's voltage law and using Ohm's law, one can write:

$$\Delta V_{SE} = (V_{in} - V_A) + (V_{in} - V_0) = I(s)(R_A + R_B) + I(s)\left[\frac{R_{in}}{1 + sR_{in}(C_B + C_{in})}\right], \quad (4.1)$$

where s refers to the Laplace domain variable, I is the electric current, and the probe's inductance was not considered.

Using $V_{exp} = V_{in} - V_0$, the electric current can be written as a function of the signal measured:

$$I(s) = \left[\frac{1 + sR_{in}(C_B + C_{in})}{R_{in}}\right] V_{exp}. \quad (4.2)$$

Finally, this expression can be inserted into 4.1 to find the relation between ΔV_{SE} and V_{exp}:

$$V_{exp} = \frac{R_{in}}{R_{in} + [1 + sR_{in}(C_B + C_{in})](R_A + R_B)} \Delta V_{SE}. \quad (4.3)$$

Analysing equation 4.3 above, it becomes evident that, ideally, having $(R_A + R_B) << R_{in}$ would guarantee that the signal measured by the oscilloscope is the same as the one created in the medium. However, since the contact resistance, included in R_A, is an unknown, and depends mainly on the structure of the electrode's surface and on the pore-fluid electrical conductivity, V_{SE} can not be accurately estimated from V_{exp} using equation 4.3.

Looking now at the acquisition system when the SR560 preamplifier is present, figure 4.12 depicts the equivalent electronic circuit. V_A and V_B are the local electric potential around the measuring electrode and the reference one, respectively; that way the potential difference due to seismoelectric phenomena is $\Delta V_{SE} = V_A - V_B$. R_A, R_B, C_B, and L_B represent the exact same property as they did in figure 4.11. Regarding R_{in} and C_{in}, now they correspond to the input resistance and capacitance of the SR560 preamplifier, while R_C is its output resistance. V_{in} and V_{in}^{ref} are the signals detected by the electrodes such that the output of the preamplifier will be $V_{in} - V_{in}^{ref}$. Concerning the oscilloscope, its input resistance and capacitance

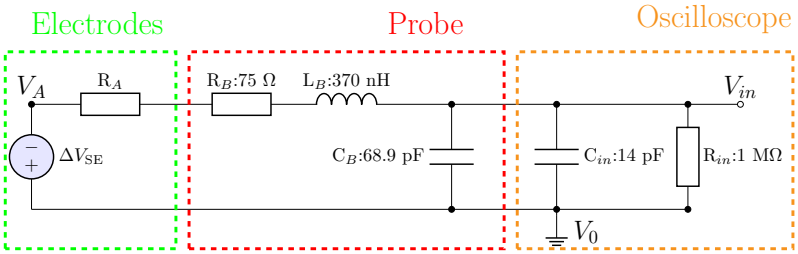

Figure 4.11: Electronic circuit used to describe the seismoelectric acquisition with oscilloscope probes. Values of resistances, capacitances, and inductances are the real values of the equipments.

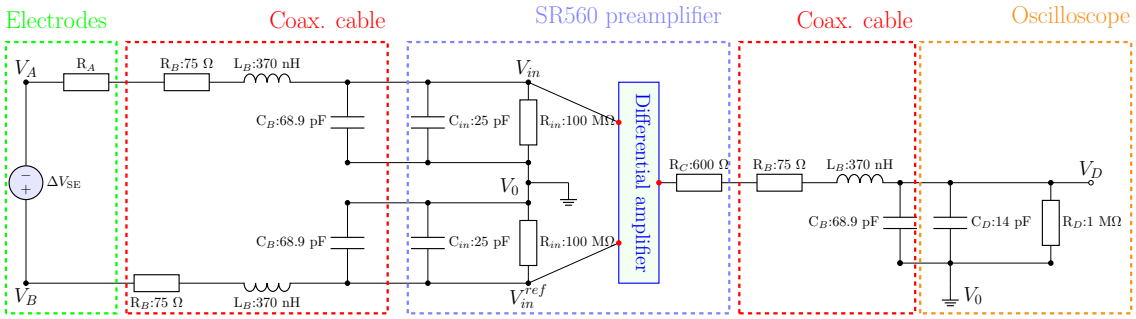

Figure 4.12: Electronic circuit regarding the seismoelectric acquisition when a SR560 preamplifier is included. Values of resistances, capacitances, and inductances were extracted from the datasheet of the equipments.

are, respectively, R_D and C_D. Finally, it follows that the signal recorded by the oscilloscope is $V_{exp} = V_D - V_0$ and, for all intents and purposes, it will be considered equal to the output of the preamplifier: $V_{exp} = V_{in} - V_{in}^{ref}$.

To find the transfer function of the circuit of figure 4.12 the same procedure as before can be followed, therefore:

$$\Delta V_{SE} = (V_A - V_{in}) + (V_{in} - V_{in}^{ref}) + (V_{in}^{ref} - V_B). \tag{4.4}$$

Now, applying Ohm's law to equation 4.4 one can express ΔV_{SE} as a function of the electric current:

$$\Delta V_{SE} = I(s)(R_A + R_B) + I(s)\left[\frac{2R_{in}}{1 + sR_{in}(C_{in} + C_B)}\right] + I(s)R_B. \tag{4.5}$$

Note that the inductance of the coaxial cable was not included in equation 4.5.

Using Ohm's law and $V_{exp} = V_{in} - V_{in}^{ref}$ one finds:

$$I(s) = \frac{1 + sR_{in}(C_{in} + C_B)}{2R_{in}} V_{exp}. \tag{4.6}$$

Inserting 4.6 into 4.5 one gets:

$$\Delta V_{SE} = \left[(R_A + 2R_B) \frac{1 + sR_{in}(C_{in} + C_B)}{2R_{in}} + 1 \right] V_{exp},$$

which can, finally, be rearranged into:

$$V_{exp} = \frac{2R_{in}}{2R_{in} + (R_A + 2R_B)[1 + sR_{in}(C_{in} + C_B)]} \Delta V_{SE}. \tag{4.7}$$

With the aid of the two relations above, equations 4.3 and 4.7, describing the output of the circuits in figures 4.11 and 4.12, the value of R_A that can explain the factor 4.4 can be calculated. Using the values shown in these figures and combining both equations, one arrives at $R_A \simeq 3.48$ MΩ. The value found is bigger than the input resistance in the circuit of figure 4.11, on the other side it is two orders of magnitude smaller than the input resistance of the circuit in figure 4.12. Assuming that all the hypothesis considered in the derivations above are correct, the use of the SR560 preamplifier guarantees the amplitudes of the signal recorded in the oscilloscope correspond, with a small error, to those of the actual seismoelectric signal inside the medium studied; conversely, that won't be true when using the probes.

SR560 preamplifier *vs* INA111 (in-house equipment)

The second experiment discussed in this section was carried out in a layered medium, such that the layer, a $\simeq 0.73$ cm Vosges sandstone sample was placed at z = 12.05 cm. In total there were 80 measurement positions, 40 before and 40 after the layer, however when using the INA111 (in-house) preamplifier several measurements were repeated to study the behaviour of the channels in the preamplifier. The electrode comb (0.25 cm of electrode spacing) of figure 4.9a was positioned around $x = 0$, the first electrode was placed at z = 1 cm and the 41st at z = 13 cm. Figure 4.13 shows the measurements obtained using the in-house amplifier, note that both the coseismic, associated with direct and reflected P-waves, and the EM interface response were detected.

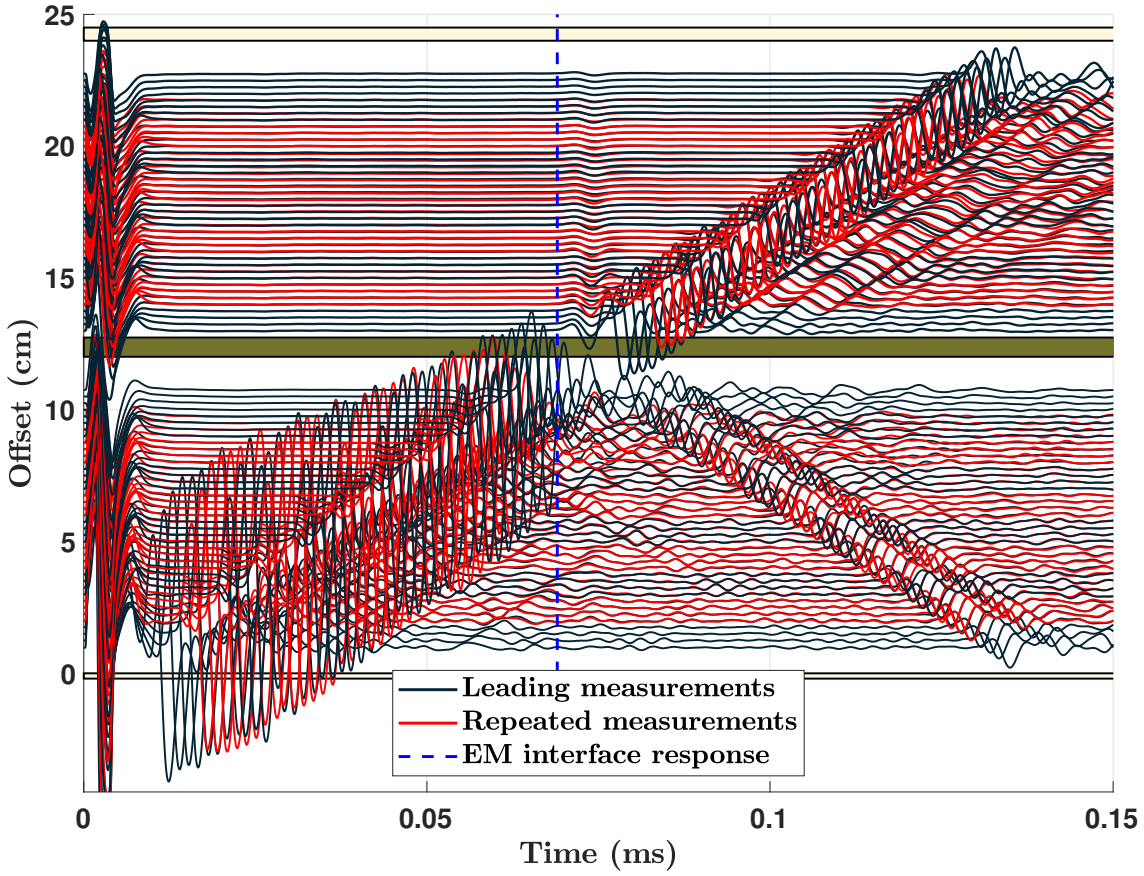

Figure 4.13: Electric acquisition using the INA111 (in-house) preamplifier. Many measurements were repeated (traces in red) in order to check the channels of the preamplifier. The interface response was highlighted for convenience.

Because most details are indiscernible in figure 4.13, the coseismic and the interface response were isolated and plotted individually in figure 4.14. Besides that, the measurements using the SR560 preamplifier were superimposed to the previous (blue traces) for comparison. To create figure 4.14a, the coseismic waveforms were aligned with respect to their first-breaks (FB), therefore in this figure events that are usually synchronous will have a hyperbolic trend of arrival times. This fact is most evident in the bottom-left part of figure 4.14a, where the interface response associated with SR560 measurements can be perceived.

An important characteristic of the measurements in figure 4.14a can be noticed by magnifying the region inside the green rectangle. Observe that a synchronous non-causal (referring to the fact is seems to arrive before the coseismic arrives) noise becomes evident. This noise appears in all channels, interacting with the coseismic

and the interface response (for z-offsets close to the layer), even though the waveform of the coseismic measured by both preamplifiers seem quite similar.

Looking now at figure 4.14b, there's an overall agreement between the interface response waveform measured with both preamplifiers. However, when using the in-house amplifier, a clear dissimilarity exists when comparing measurements made at the same z-offset; this indicates there may exist a difference between the channels of this preamplifier, in the sense they do not output the same result.

It remains to discuss the difference in amplitudes between the two acquisition systems. With that purpose, figure 4.15a displays the first maxima and minima of the coseismic (as a function of z-offset) and figure 4.15b shows the absolute maxima of the interface response. Note that, because the INA111 amplifier applies a gain of 10, it is expected that all its outputs will need to be divided by 10. Nevertheless, in 4.15a the best fit between data acquired with both preamplifiers occurs when the data measured with the INA111 is divided by 65, meaning there's and additional gain of 6.5 which, as in the previous subsection, might be related to the difference of input impedance of both preamplifiers. Another important feature in figure 4.15a is the fact measurements made using channels 1 and 2 are considerably far from global trend. Additionally it is quite clear both maxima and minima show a periodic behaviour every 8 channels.

Regarding the comparison of absolute maxima from the interface response in figure 4.15b, the periodic behavior is also evident. Additionally, even though the maxima associated with both preamplifiers cover the same range of values, the global trend is not very similar, considering offset bigger than 13 cm, which are the ones that matter, since the interface response at smaller offsets is considerably changed by coseismic waves becoming practically indistinguishable (see figure 4.13). On the other side, the fact only the gain of the INA111 amplifier needs to be corrected, indicates that contact resistance does not influence the measurements of the interface response, only the coseismic.

Although the use of the in-house preamplifier still seems like a complicated task due to the problems discussed above, for completeness and to try to explain the factor 6.5, the electronic circuit of the acquisition system, when using the INA111 amplifier, will be studied. After that it will be compared with the one in figure 4.12 in order to find the R_A that explains the factor mentioned.

The circuit including the INA111 preamplifier is shown in figure 4.16. The variables in the present circuit have essentially the same meaning as those in figure 4.12,

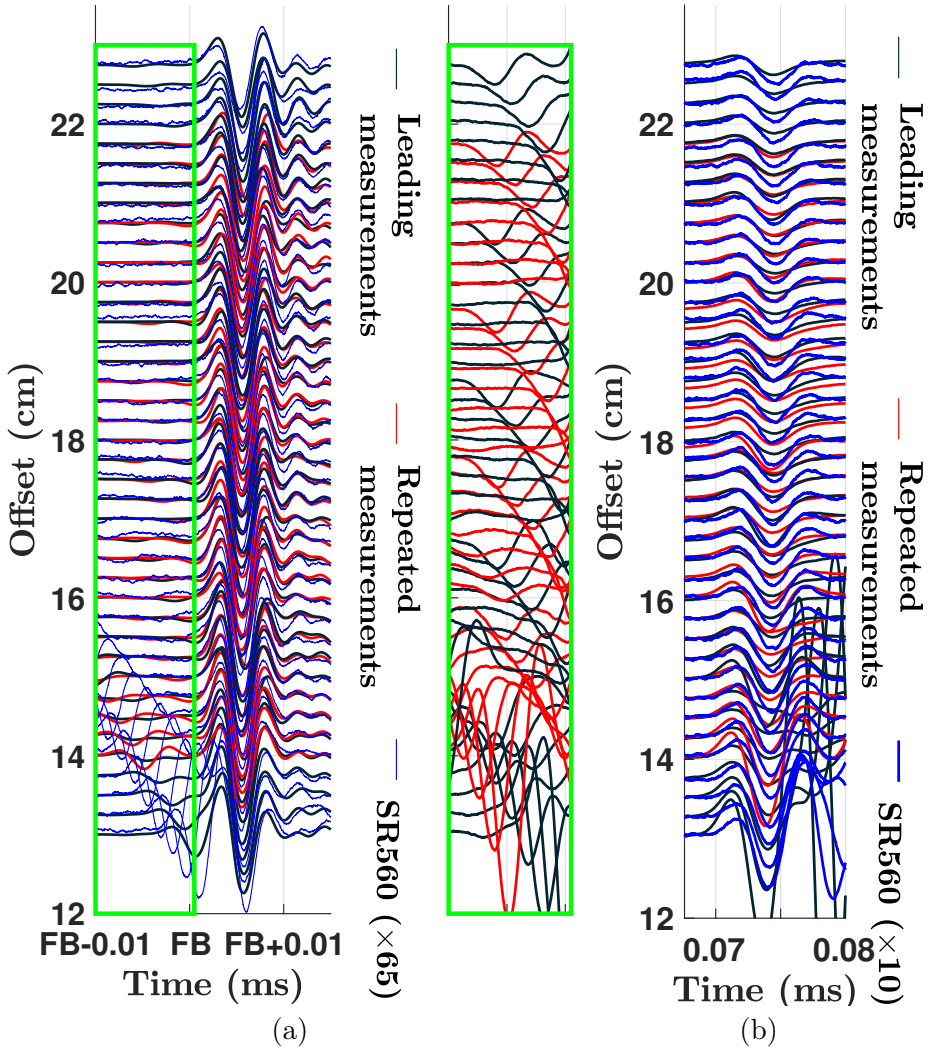

(a) (b)

Figure 4.14: Highlighting the coseismic (a) and the interface response (b) of figure 4.13. In (a) the coseismic events are plotted with respect to their First-Breaks, referred by FB in the x-axis. The region delimited by the green square appears magnified in the right side of (a). In (b) there's only the EM interface response. Note that in (a) the measurements using the SR560 were multiplied by 65 while in (b) they were multiplied by 10 (which corresponds to the gain applied by the INA111 preamplifier).

once they are very similar. Besides the difference in values, the input resistance and capacitance of the reference electrode are not equal to those of the measuring electrode, as was the case in 4.12. This dissimilarity comes from the fact that in the in-house preamplifier the references of the 8 channels are connected in parallel.

In order to find the transfer function relating the actual seismoelectric phenomena with the signal measured by using the INA111 preamplifier, the same procedure used

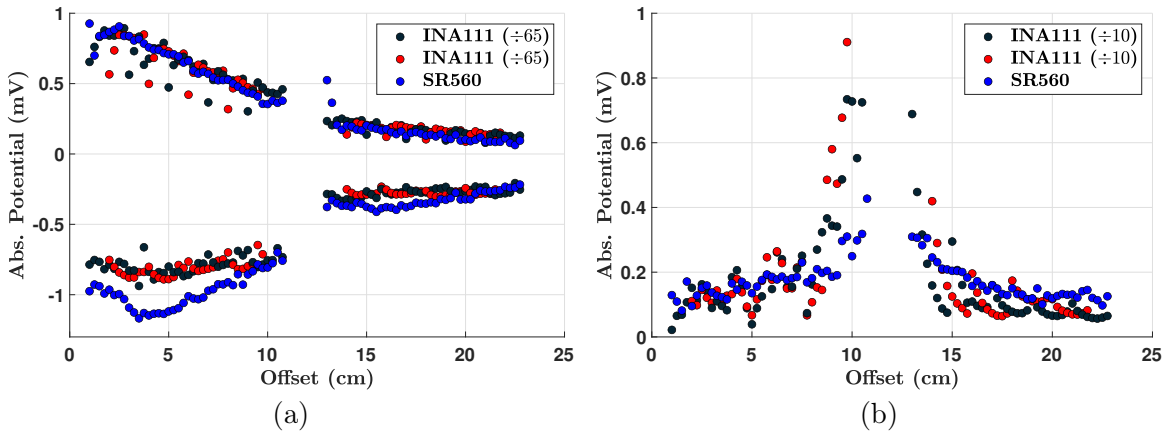

Figure 4.15: (a) Maxima and minima of the coseismic signal displayed in figure 4.14a. (b) Absolute maxima of the interface response measurements shown in figure 4.14b.

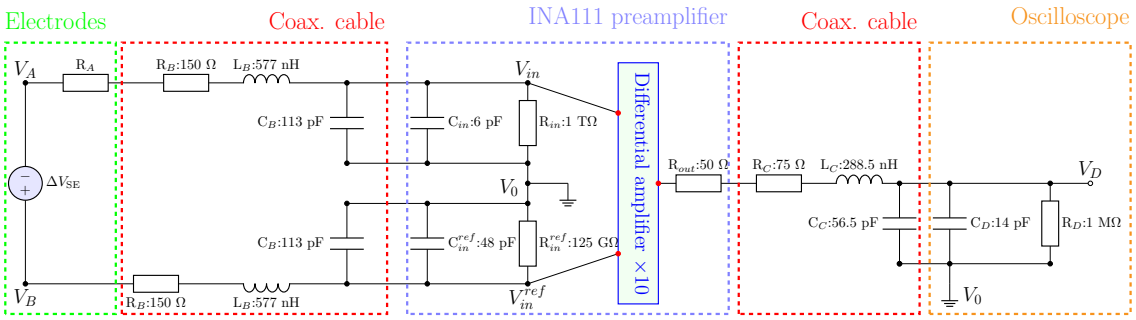

Figure 4.16: Electronic circuit associated with the seismoelectric acquisition when using the in-house, INA111-based, preamplifier. Values of resistances, capacitances, and inductances are the real values of the equipments.

in the previous subsection can be used. With Kirchoff's voltage law, equation 4.4 will appear again, then by applying Ohm's law one finds:

$$\Delta V_{SE} = I(s)(R_A+R_B)+I(s)\left[\underbrace{\frac{R_{in}}{1+sR_{in}(C_{in}+C_B)}}_{\texttt{D1}}+\underbrace{\frac{R_{in}^{ref}}{1+sR_{in}^{ref}(C_{in}^{ref}+C_B)}}_{\texttt{D2}}\right]+I(s)R_B, \tag{4.8}$$

where, for convenience, `D1` and `D2` will designate the denominators in what follows. Note also that: should R_{in} be equal to R_{in}^{ref}, equation 4.8 would be exactly the same as equation 4.5.

As before, the electric current can be expressed with a V_{exp}-dependency:

$$I(s) = \frac{\mathtt{D}_1\mathtt{D}_2}{R_{in}\mathtt{D}_2 + R_{in}^{ref}\mathtt{D}_1} V_{exp}; \tag{4.9}$$

subsequently, it can be inserted into equation 4.8 to allow the final expression relating ΔV_{SE} and V_{exp}:

$$V_{exp} = \frac{R_{in}\mathtt{D}_2 + R_{in}^{ref}\mathtt{D}_1}{(R_{in}\mathtt{D}_2 + R_{in}^{ref}\mathtt{D}_1) + \mathtt{D}_1\mathtt{D}_2(R_A + 2R_B)} \Delta V_{SE}. \tag{4.10}$$

With the hypothesis the factor 6.5, discussed above, can be related to R_A, equations 4.10 and 4.7 may be combined using the values shown in figures 4.16 and 4.12. By doing so, the value $R_A \simeq 550$ MΩ will be found, thus implying the input resistance of the SR560 preamplifier is not large enough to ensure the amplitudes of the measured signal correspond to those of the true signal in the medium. However, because the medium and the electrodes are essentially the same used in the experiment presented in the previous subsection (when comparing probes and the SR560 preamplifier), both values found for R_A should also be the same.

Even though the new value calculated for R_A implies the INA111 preamplifier is more suited to the experimental setup, in terms of amplitude preservation, an unquestionable fact is that the SR560 amplifier is a validated equipment whereas the in-house amplifier is not. Moreover, the artifacts associated with the use of the INA111, studied throughout this subsection, suggests there is still some improvements to be made before comparing the results of this equipment with those obtained with the SR560. To conclude, in this thesis, the measurements of seismoelectric signals using the SR560 preamplifier will be considered reliable enough, whereas measurements using the INA111 will be discussed only in the last chapter under the subject of suggestions to future improvements.

4.7.2 Placement of the reference electrode

Because in the experiments, conducted throughout this thesis, the goal is to measure absolute electric potentials, or a signal that satisfactorily approximates the real electric potential due to seismoelectric phenomena, choosing where to place the reference electrode is an important task, since a wrong choice may alter the data measured.

The electric potential measured in the experiment V_{exp} is a difference between the potential detected by the measurement electrode and that detected by the reference electrode. Therefore, ideally, the electric potential measured by the latter should be zero, in order to ensure V_{exp} equals to the potential in the measurement electrode.

In the context of the present experimental setup, six configurations were tested. At first, the reference was placed at two positions inside the sandbox, positioned right above the setup (i.e., in the air), connected to the laboratory ground, and inserted in a second plastic container filled with the same medium contained in the main sandbox. Afterwards, the reference was also placed inside the sandbox but closer to the PZT source. Figures 4.17 and 4.18 show the experimental data corresponding to each reference electrode configuration.

The first set of tests, represented in figure 4.17, were carried out using 8 electrodes of the electrode comb shown in figure 4.9a and no sandstone layer was present. For each electrode, measurements were made with all reference configurations before moving to the next electrode, in order to avoid any change of amplitude with time. A comparison of the datasets shows that, data measured with a reference in the air (4.17c) and in a second container (4.17e) are quite similar, on the other side, when the reference is connected to the ground (4.17d) the noise increases considerably. Moreover, in the two cases where the reference was inside the sandbox (4.17a and 4.17b), synchronous events (indicated by the red boxes) associated with the passage of P-waves through the reference electrode exist. These events are acquisition artifacts and they can change considerably the amplitudes of the coseismic as well as the interface response.

Figure 4.17f shows a comparison of the first maxima and minima of the coseismic signal, measured with the five reference configuration discussed until now. From this figure, it becomes evident that the coseismic amplitudes recorded, when the reference is inside the sandbox, are higher than those obtained with other configurations; the first case (figure 4.17a) being the most discrepant from the others. To understand this behaviour, notice that when the coseismic wave (or the interface response if it exists) is detected in the measuring electrode, if the reference is inside the sand a coseismic wave will eventually travel through it, such that its amplitudes will be accounted in the final V_{exp} recorded by the oscilloscope. That means the farther the reference is from the PZT source, the less the chances of V_{exp} being affected by coseismic signals arriving at the reference electrode: notice how, in figure 4.17f, the amplitudes of the data in 4.17b (using a reference at z = 23.5 cm) are closer to

the amplitudes obtained with other configurations than the data in 4.17a (using a reference at z = 12.3 cm).

Conversely, when the reference is not in the sand the amplitudes are more concordant. Additionally, the absence in figures 4.17c, 4.17b, and 4.17d of coseismic events due to P-waves arriving at the reference, shows that the premise of zero electric potential at the reference electrode can be satisfied for these configurations, and therefore a better approximation of the actual absolute electric potential at the measurement electrode can be achieved.

In order to complement the previous experiments, a sixth electrode configuration was studied, with the reference at $z = 0$ cm, which is considerably close to the PZT source. Moreover, a 0.73cm sandstone layer, placed at $z = 12$ cm, is present in this experiment, in order to demonstrate how the reference configuration can also impact the interface response. Figure 4.18a shows a superimposition of the measurements made with the reference in a secondary container (orange) and inside the sandbox (dark blue); for each case, a total of 64 measurements positions, 32 in each side of the layer, were used. The blue rectangle in the figure highlights the interface response, such that on the right less traces are shown to put in evidence the differences that appear with the superimposition. Another important feature, that calls attention in figure 4.18a, is the synchronous event indicated by the red rectangle; it appears only in the measurements acquired with a reference inside the sand (dark blue traces) and corresponds to the passage of the P-wave, after being reflected in the sandstone layer, through the reference electrode.

Looking now at figures 4.18b and 4.18c, they show the comparison of first maxima and minima of the coseismic and the absolute maxima of the interface response, respectively, as functions of z-offset. From 4.18b, one can notice that the comparison of absolute maxima and minima, of the coseismic signal, indicates that when the reference is inside the sand the values measured are higher, but the difference between datasets reduces with increasing offset; this same behaviour can be noticed when comparing the data in figure 4.17a and 4.17e (see amplitudes in figure 4.17f).

Regarding the impact on the interface response, figure 4.18c shows how the amplitudes change with the reference configuration. Focusing on the values measured at z-offsets bigger than the layer position (i.e., > 12 cm), when the reference is inside the sand the amplitudes are boosted up, whereas for smaller offsets (< 12 cm) they are reduced, in comparison with the amplitudes measured with a reference in a second container. It should be noticed that, even though the enhancement of the

interface response at some offsets seems promising once it makes this signal easier to detect, what happens is an artificial amplification that will compromise comparisons with theoretical predictions.

From the experiments and discussion of this section, the best reference configuration for the present experimental setup is either the reference in the air or in a secondary container. Additionally, it is easier to insert a reference electrode in a secondary container than to hang it somewhere near the experiment. Besides that, using a secondary container, filled with the same material as the main sandbox, is theoretically equivalent to having a very large sandbox with the reference placed quite far from the source; a concept that can be explored in field acquisitions. For these reasons, the configuration with an auxiliary plastic container will be adopted throughout this thesis.

4.7.3 Electrode characteristics

This section discusses two properties of the electrodes used, considering how they may change the seismoelectric signals measured. The first property studied was the electrode thickness, the second its depth inside the medium.

Even though the electrode comb in figure 4.9a, whose electrodes are 1 mm thick, were adopted in this thesis, thinner electrodes (0.4 mm thick), made of the same material, were also used in a previous phase of the experimental conception, in order to evaluate how the amplitudes of V_{exp} vary with electrode thickness. Figure 4.19 shows a comparison between data acquired with two electrode thicknesses, with measurements made at about z = 13.7 cm, in a medium composed of water-saturated sand and a 0.73 cm sandstone layer positioned at about 11.1 cm. Moreover, all measurements were carried out with the oscilloscope probes only, without a preamplifier.

Both the coseismic wave (indicated by the red rectangle) and the EM interface response (indicated by the blue rectangle) can be observed in the measurements of figure 4.19. Looking at the interface response, it does not seem to depend on the thickness since the signals measured with both electrodes give the same result. On the other side, the coseismic signal appears to depend on the electrode thickness, considering the difference between the two datasets in figure 4.19.

To explain the difference in coseismic amplitudes, recall the comparison between acquisitions with the oscilloscope probes and with the SR560 preamplifier in section 4.7.1, where it was discussed that the input resistance of the oscilloscope is not high

enough, in comparison with the contact resistance, to preserve the amplitudes of the signals measured. Therefore, because the two electrodes compared are made of the same material, the difference of amplitudes may come from a reduction of contact resistance, which is proportional to the thickness; that can explain why thinner electrodes detect coseismic signals with higher amplitudes. As a matter of fact, in Bataller et al. (2009) and Ingeman-Nielsen et al. (2016), the properties controlling the contact resistance of an electrode in the earth are discussed, one of them being the geometrical shape of the electrode. Nevertheless, the higher input impedance of the SR560 preamplifier, that will be used throughout the experiments, helps to overcome problems due to the contact resistance and therefore compensates differences due to electrode thickness. Finally, even in the experiments shown in figure 4.19 (i.e., when only using oscilloscope probes), the discrepancy in coseismic amplitudes is too small to be considered.

Focusing now at the electrode depth, meaning the total electrode length inside the medium, figure 4.20 shows the coseismic signal measured with 6 different electrode depths. In the experiments no layer was present, the position of the measurement electrode was $x = 0$ cm and $z = 6.1$ cm, and the SR560 preamplifier was used. From the comparison of signals in figure 4.20, it can be noticed that amplitudes increase with electrode depth until 3.6 cm of the total electrode's length is inside the sand. After 3.6 cm the amplitudes seem to stabilize. For a depth of 0.4 cm, even though the signal is week, there is a discernible event, but its amplitudes are too close to the noise level. Notice also that the apparent arrival time of the signal appears to change with the electrode depth.

The PZT source has a 3.8 cm diameter (see figure 4.3) and in the experiment realized, its topmost point was practically at the surface of the sand, y $\simeq$ 0 cm. By picturing the PZT surface as random point sources distributed along a circle, one can show that the amplitudes of a signal detected by an electrode in front of the source (as is the case) will only stabilize after the electrode depth becomes bigger than the PZT diameter. That happens because the signal measured by an electrode is the result of complex wave interference at the electrode's position, this way if an electrode's depth is half the PZT diameter, there will be less energy arriving at the electrode than when its depth is equal to the PZT diameter. With the same argument, the change in arrival times can be explained: the wave interference, creating the coseismic signal recorded with the electrode, can result in a destructive

interference that results in the maxima and minima of signals shifted to later times, thus creating apparent arrival times which are bigger than the real ones.

Regarding the interface response, it is not as sensitive to the electrode depth as it is to the distance from the interface creating it. Because it can also be detected in the air, the amplitudes recorded by varying the electrode depth will not necessarily correspond to the change in depth but rather to the distance of the electrode from the interface.

Finally, an electrode depth of about 5.2 cm was chosen for convenience, once this depth is the biggest that one can achieve in the present setup, besides the fact it leads to one of the highest amplitudes of the coseismic signals in figure 4.20. It should be noticed, however, that the choice of a different depth will not impact the comparison with numerical data (i.e., with theoretical predictions) as long as the electrode length and the PZT diameter are accounted for in the modeling.

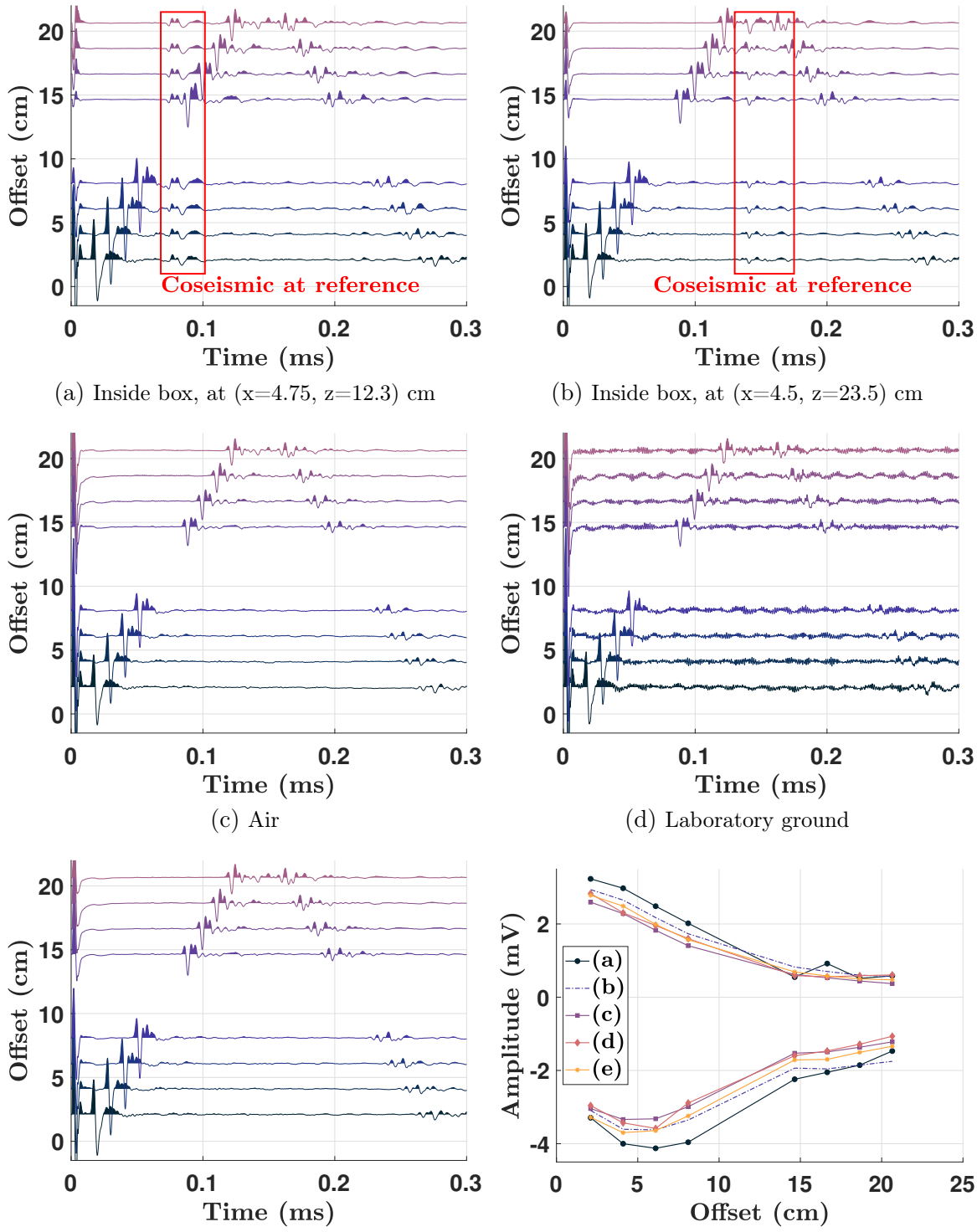

(a) Inside box, at (x=4.75, z=12.3) cm

(b) Inside box, at (x=4.5, z=23.5) cm

(c) Air

(d) Laboratory ground

(e) In second container

(f) Coseismic maxima and minima

Figure 4.17: Comparison of measurements using 5 different configurations for the reference electrode. (a) and (b) were obtained with the reference inside the sandbox at the positions specified in the sub-captions. (c) refers to data acquired with the reference in the air, (d) to the measurements obtained when the reference was connected directly to the laboratory ground, and (e) is the data measured with the reference in a second plastic container filled with the same material inside the main container. (f) shows the first maxima and minima of the direct coseismic wave.

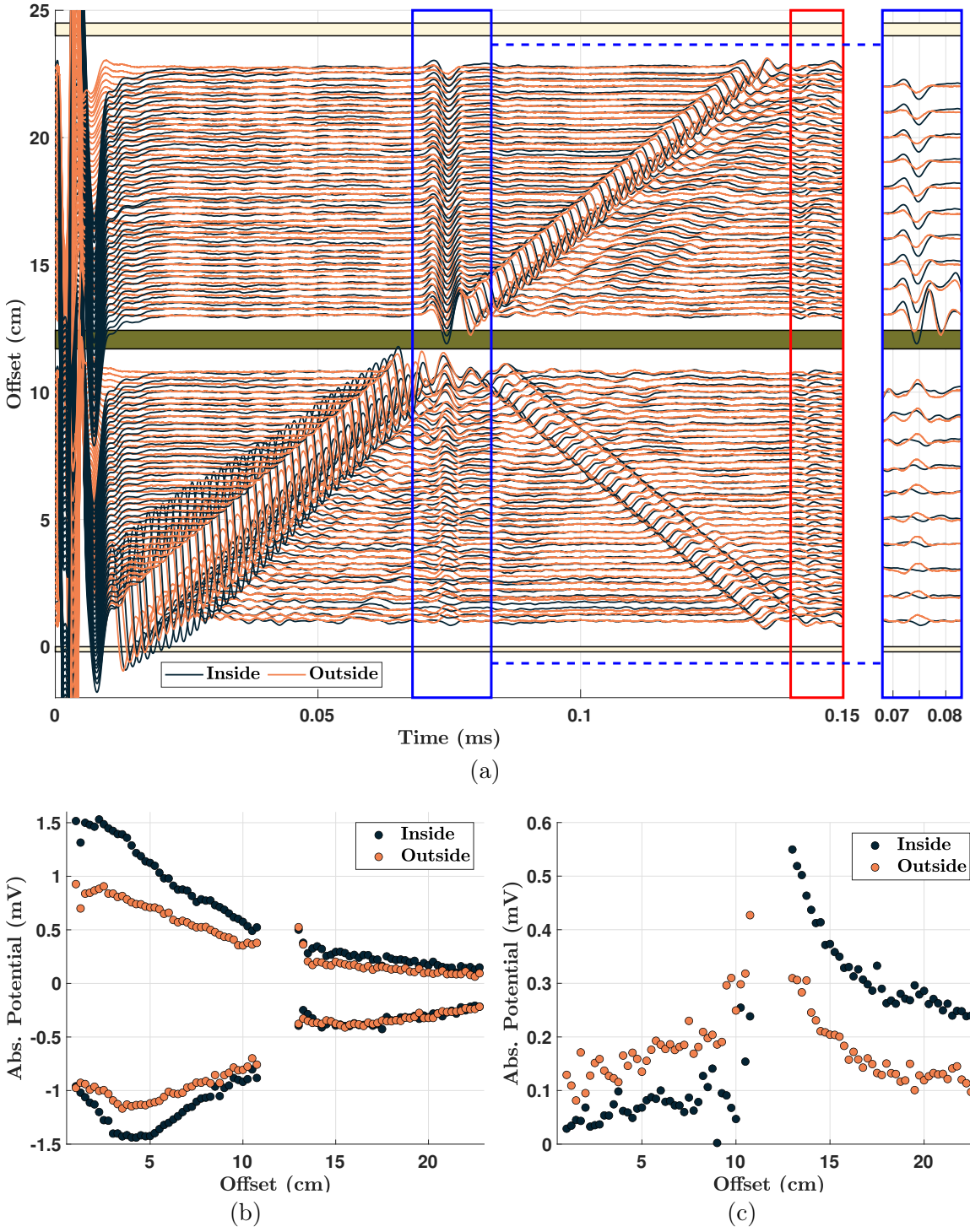

Figure 4.18: Comparison of measurements using a reference at x = 5 cm and $z = 0$ cm, and using a reference placed in an auxiliary container filled with the same material as the main sandbox. In (a), (b) and (c) the colors refer to the same dataset: dark blue to reference inside the sandbox, and orange to reference in the secondary container. (a) shows the superimposition of measurements, highlighting the interface response with a blue rectangle (less traces are shown on the rigth to facilitate the comparison), and the coseismic at the reference electrode with a red rectangle. (b) displays the first maxima and minima of the coseismic associated with the direct P-wave. (c) shows the absolute maxima of the interface response.

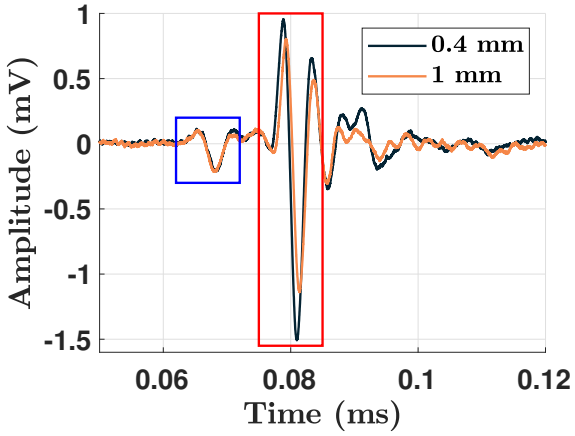

Figure 4.19: Comparison between measurement using electrodes with two diameters: in orange 1 mm and in dark blue 0.4 mm. The medium used consists of a 0.73 cm thick sandstone layer inserted in water-saturated sand, at about z = 11.1 cm. The measurement electrode is positioned around 13.7 cm. The blue rectangle indicates the EM interface response and the red rectangle the coseismic.

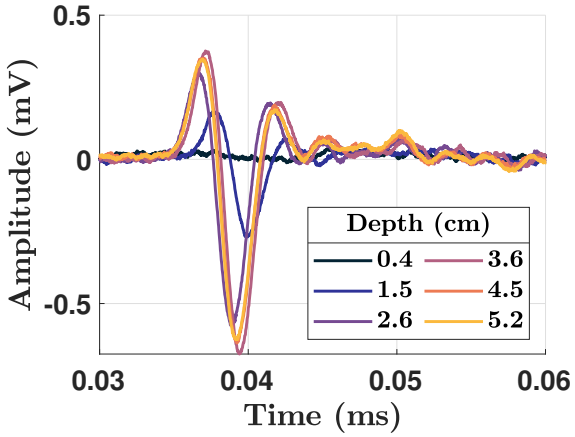

Figure 4.20: Seismoelectric measurements in a homogeneous medium with varying electrode depth. The measurement electrode was placed at about z = 6.1 cm. Six depth values were investigated and the coseismic signals detected are superimposed to allow comparison.

4.8 Acquisition procedure

After detailing the apparatus used to acquire seismic and electric data, as well as the media studied, this section summarizes the steps involved in the acquisition. First, the preparation of the media will be discussed, then the stabilization time will be defined. Next, the oscilloscope parameters wil be treated, and finally the operational aspects of the acquisition will be explained.

4.8.1 Preparation

Before every acquisition the medium is prepared with the intent of ensuring full saturation and adjusting the fluid conductivity to the range of interest. Additionally, in-between acquisitions the sand-filled plastic box is stored inside a desiccator to avoid as much as possible the contamination of the experiment by particles in the air.

The first step in preparing the experiment consists in cleaning the sand with distilled water. Essentially, water is poured into the sand then mixed and drained until the desired value of fluid conductivity (of the drained water) is reached. This process depends on the initial fluid conductivity, but it does not usually lasts longer than 1 hour. At the end, a 1 cm thick water layer is left on top of the sand, to ensure there is more water than what is needed to fill the pores when the medium is fully saturated.

After adjusting σ_f, the sandstone layer may be introduced and the whole experiment is put into the desiccator before a vacuuming process starts. In this step, air will be pumped out of the desiccator and, therefore, the medium, to ensure it will be as close as possible to fully saturated. The process is only stopped when no air bubbles can be seen coming out of the sand. To achieve the best saturation, the experiment was usually vacuumed for 2 hours, left to stabilize in the desiccator during the night, and the next morning it was vacuumed again for a period of 4 hours.

It takes up to 10 minutes to depressurize the desiccator, after that the whole experiment is set in place with the PZT source turned on. Measurements will then be made continuously; however, only after a specific stabilization time that data will actually be recorded.

Lastly, it should be noted that electrical measurements are performed with a layer of water above the sand. However, just before starting the seismic acquisition, this

water layer is carefully removed with a syringe to allow the reflective paper to touch the sand.

4.8.2 Stabilization time

As mentioned in the previous sub-section, once the acquisition begins, measurements will only be saved after a stabilization period has passed. During this period the amplitudes of the signals measured will vary. Thus, to define how long one should wait before effectively start recording, seismic and electrical data were continuously acquired along the z-axis (see figure 4.1), at a point 5.7 cm away from the PZT source; figure 4.21 shows the measurements at 9 instants of time, the first at 00:00:00 hours and the last 03:09:23 hours later.

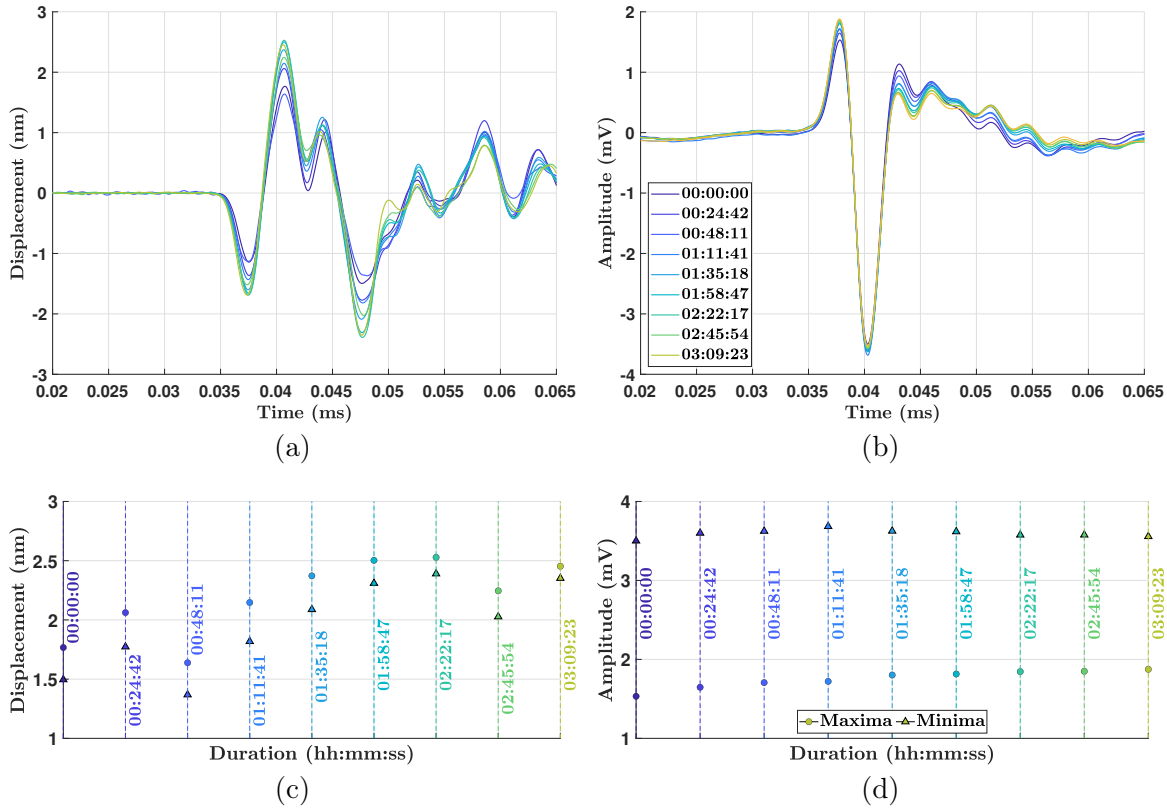

Figure 4.21: Vertical seismic displacement (a) and electric potential (b), measured in the same point, at 9 instants of time. Maxima and minima are shown in (c) and (d), respectively.

From figure 4.21 it is evident there is no change of waveform with time, mainly amplitudes vary. Additionally, the seismic measurements are more influenced by temporal variations than the electrical ones, possibly due to the fact that measuring

points are on the saturated sand-air interface, where evaporation takes place and creates local changes in saturation.

It follows from the experiment presented in figure 4.21, that waiting for at least 1 hour and 30 minutes helps to avoid the larger variation of amplitudes in the measured signals. Additionally, as it will be seen in the chapters of results, mainly the region of z-offsets larger than 8 cm will be accounted for in the comparison with theoretical predictions. Considering it takes more than 30 minutes to acquire the data at z-offsets shorter than 8 cm, the measurements used in this thesis were only acquired about 2 hours after the actual beginning of the experiment. To conclude, for all data presented in the next chapters, the effective experimental data acquisition only started after about 1 hour and 30 minutes that the experiment was in place and running.

4.8.3 Oscilloscope parameters

The oscilloscope controls all data acquisition and storage, therefore its configuration parameters will have a big impact on the quality of the data measured. Due to their significance, it is worth citing four of these parameters: the sampling rate, the number of samples, the time window, and the averaging/stack number (AN).

Temporal resolution is strictly linked to the sampling rate, thus to have a high enough resolution data was sampled at 500 MHz; that means data was acquired with a 2E-9 s time step. The time window dictates the initial and last time samples, bounding the time range of the data recorded; for all experiments the time range was [-0.025 – 0.825] ms. This time window is considerably smaller than the period selected for the source (10 ms, see section 4.5); that is because throughout this work the main seismoelectric events (direct waves and 1st reflections on the plastic box) happen during the period covered. Regarding the number of samples, it is given by the last two parameters (time step and time range), thus it follows that, in this thesis, every time record (seismic or electrical) has 425000 points.

Averaging/stacking measurements, acquired in the same place, is an effective way to increase the signal-to-noise ratio (SNR), however, because averaging may be a time consuming procedure, the choice of the AN (the amount of time records being averaged) must reflect a compromise between the increase in SNR and in acquisition time. In order to choose the AN, both seismic and electrical data were acquired, with AN ranging from 500 to 10000, at a z-offset of about 7.2 cm; results are shown in figure 4.22.

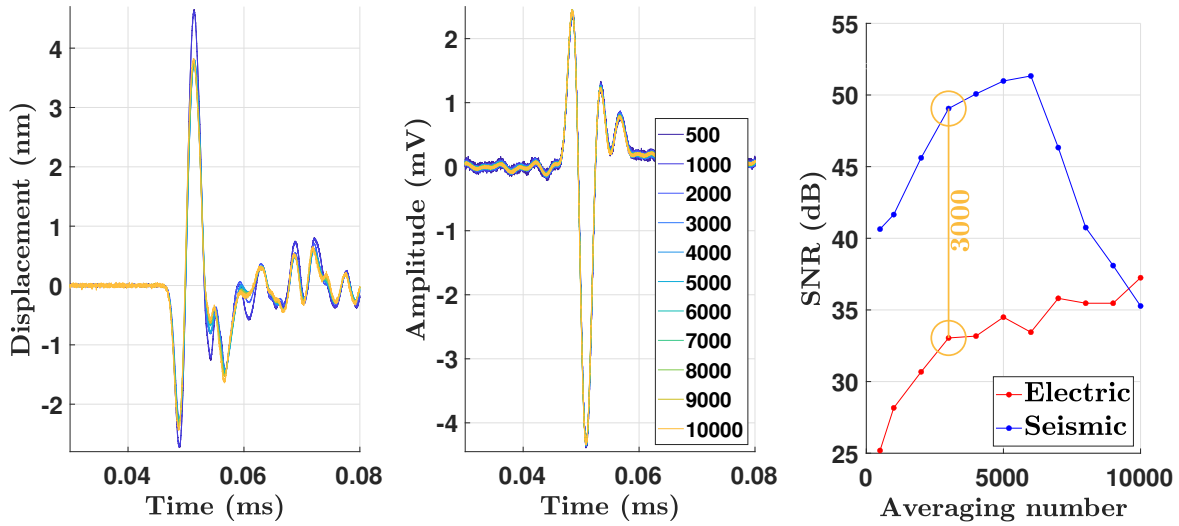

(a) Seismic (b) Absolute electric potential (c) Signal-to-noise ratio

Figure 4.22: Analysis of the effect of averaging measurements in terms of amplitude and waveform. The number of records averaged vary from 500 until 10000. (a) shows the displacement measurements, (b) the electric data, and (c) the SNRs calculated.

From figure 4.22a and 4.22b, one can notice that the increase of AN changes mainly amplitudes while waveforms are preserved. Besides that, the seismic displacement measurements vary more than the absolute electric potential. Looking at the plot SNR *vs* AN in figure 4.22c, SNR increases sharply until AN equal to 3000, for both data-types; after this AN value the SNR increases smoothly. An exception occurs in the seismic data, as can be seen by the sharp decrease of SNR when AN is bigger than 6000.

Considering the duration of the acquisition, the theoretical time to make one measurement is directly proportional to the source period. With a 10 ms period (see section 4.5), and AN equal to 3000, a measurement should take about 30 s to finish; however, in practice, it takes more than one minute. Finally, a AN value of 3000 was chosen once it represents a good compromise between acquisition time and SNR.

4.8.4 Operational details of acquisition

Both seismic and electrical data acquisition were controlled using python routines, as the one presented in appendix C. These routines control the oscilloscope and the function generator, being responsible for most of the acquisition.

Three operations can not be controlled by the python scripts. Between electric measurements the acquisition pauses and the measurement electrode is manually changed; additionally, the electrode comb will also be manually moved. The focus of the vibrometer head needs to be adjusted every time the measuring point changes; to do that a secondary Labview script was used. At last, after each displacement measurement finishes the acquisition pauses and a Labview routine moves the vibrometer head, using Soprolec motors, to the next measuring point.

4.9 Varying the conductivity

A part of this thesis (chapter 6) concerns the variation of fluid conductivity in one of the media in the experiment. As will be seen, this parameter was only changed in the sand, because of its simplicity, as opposed to the sandstone used in the experiments.

Additionally, to avoid ionic migration by osmosis a (polyethylene) zip lock bag was used to separate sand and sandstone. The wall thickness of the bags are $<<$ 1 mm. Besides that, they are designed to hold liquids inside, what implies they work for the task of inhibiting water to flow between the two media; this last characteristic was tested before experiments.

The use of a plastic inside the experiment raises a question about the actual influence it will have on the waves propagating inside the media, specially on the EM interface response. To address this question, two experiments were carried out, the first without the plastic bag and the second with it. Between both experiments, all physical properties, as well as the position of the sandstone layer and of the electrodes, remained essentially unchanged. Figure 4.23 compares the results of both experiments.

Focusing on figure 4.23a, there is a good similarity between both cases (with and without bag) for all waves. Nevertheless, some differences can be observed, due to a different placement of the layer and electrodes, and small variations in the sand's fluid conductivity.

As a matter of fact, in the case the plastic was used, the arrival times of the EM interface response and of the coseismic P-wave, reflected on the layer, are shorter than their counterparts in the case there is no plastic bag; furthermore, the coseismic transmitted through the layer arrives later. These observations indicate the layer,

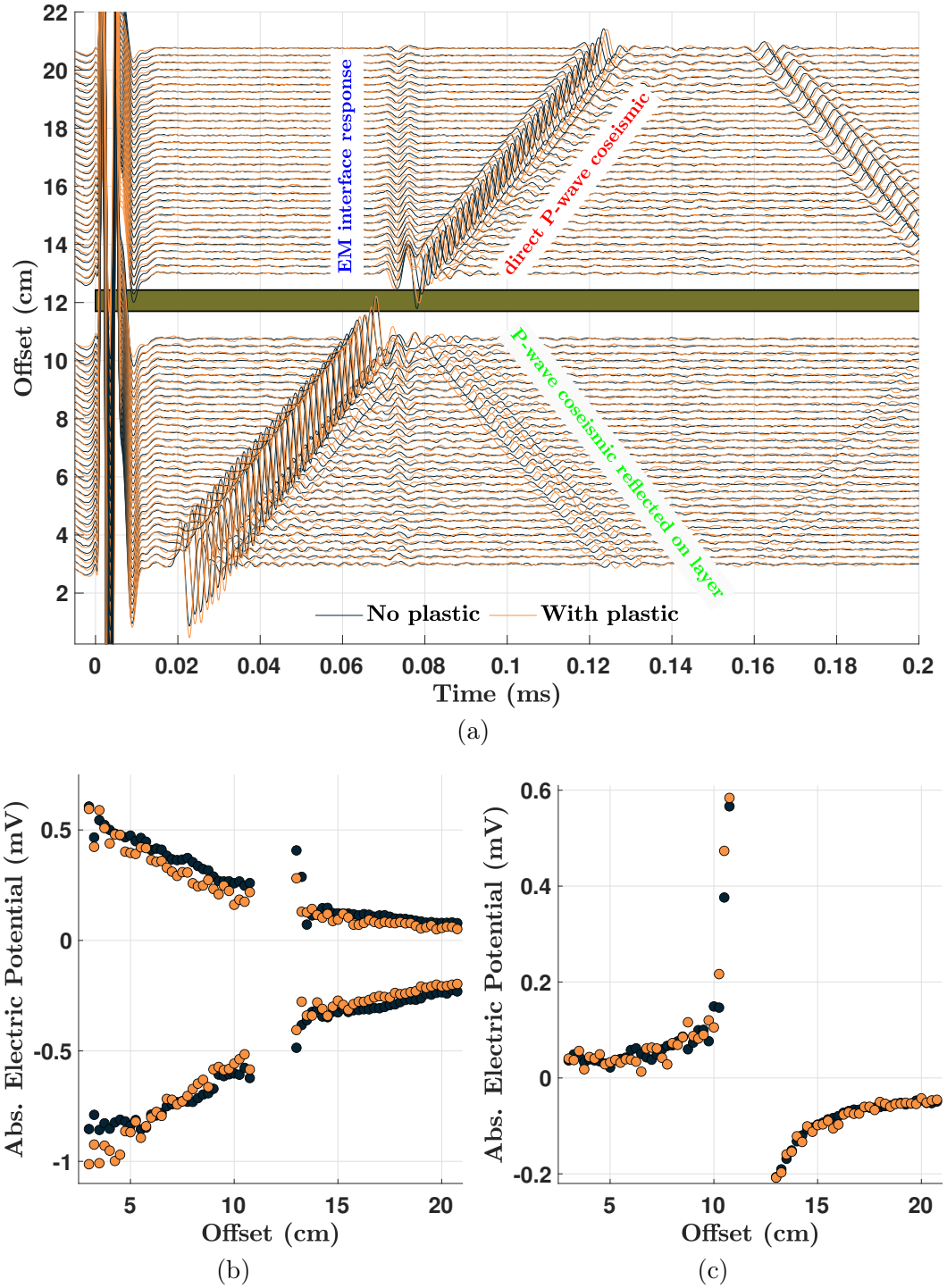

Figure 4.23: Comparison of experiments with and without a plastic bag to isolate sand and sandstone. (a) shows the comparison of traces with the main events indicated, as well as the position of the sandstone layer. (b) compares first maxima and minima of the coseismic direct P-wave. (c) compares the absolute maxima of the EM interface response. Colors in (a) are the same for (b) and (c).

enveloped by the plastic bag, was placed closer to the source, relative to the other situation.

In figures 4.23a and 4.23b, a small difference in coseismic amplitudes can be noticed. It is due to, also small, variations in fluid conductivity in-between experiments. Considering the two acquisitions were conducted in two subsequent days, and that before the second experiment (with the plastic bag) only the layer was changed (to insert it in the bag), in spite of the preparation procedure described in section 4.8, changes in fluid conductivity are to be expected.

At last, figure 4.23c compares the EM interface response, showing a perfect superposition of the two curves. This shows the presence of a plastic bag does not impact the EM interface response in the experiment. Eventually, it can be affirmed that the use of a very thin ($<<$ 1 mm) plastic interface, to separate sand and sandstone, does not impact the waves inside the experiment and therefore it does not affect the measurements. With that in mind, the fluid conductivity of the sand can be changed at will for the experiments demanding it.

4.10 Towards automation

Seeking to reduce the duration of electrical acquisitions while allowing more measurements to be made in a single day, an electronic card was designed as a solution, in partnership with Aquitaine Electronique. It is essentially a relay card that controls two electrode combs, like the one in figure 4.9, at once; thus 64 measurements can be simultaneously acquired.

Figure 4.24 depicts the acquisition chain of absolute electric potentials when the relay card is used. A computer running with Windows is the main element of the chain, operating the oscilloscope and the electronic card through a RaspberryPi. While the oscilloscope reads and saves all data sent by the relay card, the RaspberryPi commands the card using a SPI (Serial Peripheral Interface) communication protocol, implemented using python.

In order to validate the use of the relay card, several tests were realized. Figure 4.25 shows the results of a test where the absolute electric potential was measured, in the same electrode, with the oscilloscope probe (see figure 4.9), and using the relay card as in figure 4.24. For this experiment no preamplifier was used, a sandstone layer was placed at (x=0,z=11.6) cm and the electrode at (x=0,z=13.9) cm. Observing the signals in figure 4.25, three main events can be distinguished: first

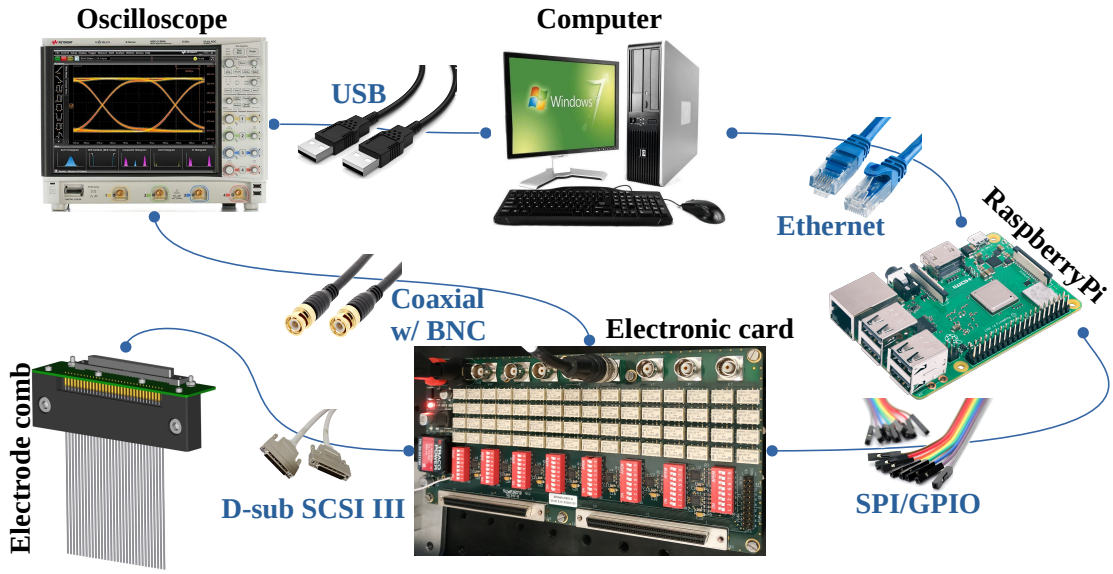

Figure 4.24: Electrical acquisition chain using a relay card to operate 64 electrodes at once. This card is connected to electrode combs using D-sub connectors, and it is controlled with a RaspberryPi through a SPI protocol. All signals measured by the card+electrodes is sent to the oscilloscope. Finally, a Windows-based computer manages simultaneously the RaspberryPi (using ethernet connectors) and the oscilloscope (using usb connectiors).

the EM noise, of piezoelectric nature, that is created when the source is triggered, second the EM interface response, and lastly the coseismic associated with the direct P-wave.

One can also notice in figure 4.25 that the noise level of measurements made with the card is considerably high, corrupting the data to a point where the interface response becomes indistinguishable. Conversely, the coseismic could be detected when using the relay card, with its waveform fairly corresponding to that measured using only the oscilloscope probe.

Seeking to further understand the noise introduced by the relay card, figure 4.26 shows the FFT magnitude spectra of the EM interface response, the coseismic, and the noise. To calculate each spectrum the regions highlighted in figure 4.25 and a 0.025 ms time window, corresponding to times before 0 ms (not shown in figure 4.25), were respectively used. Looking at the noise spectrum, the frequency band [0.75 – 1] MHz is the most prominent in terms of magnitude, therefore it is the one affecting the most the measurements. Regarding the coseismic spectrum, it shows an overall consistency between the two data. At last, the spectrum of the interface

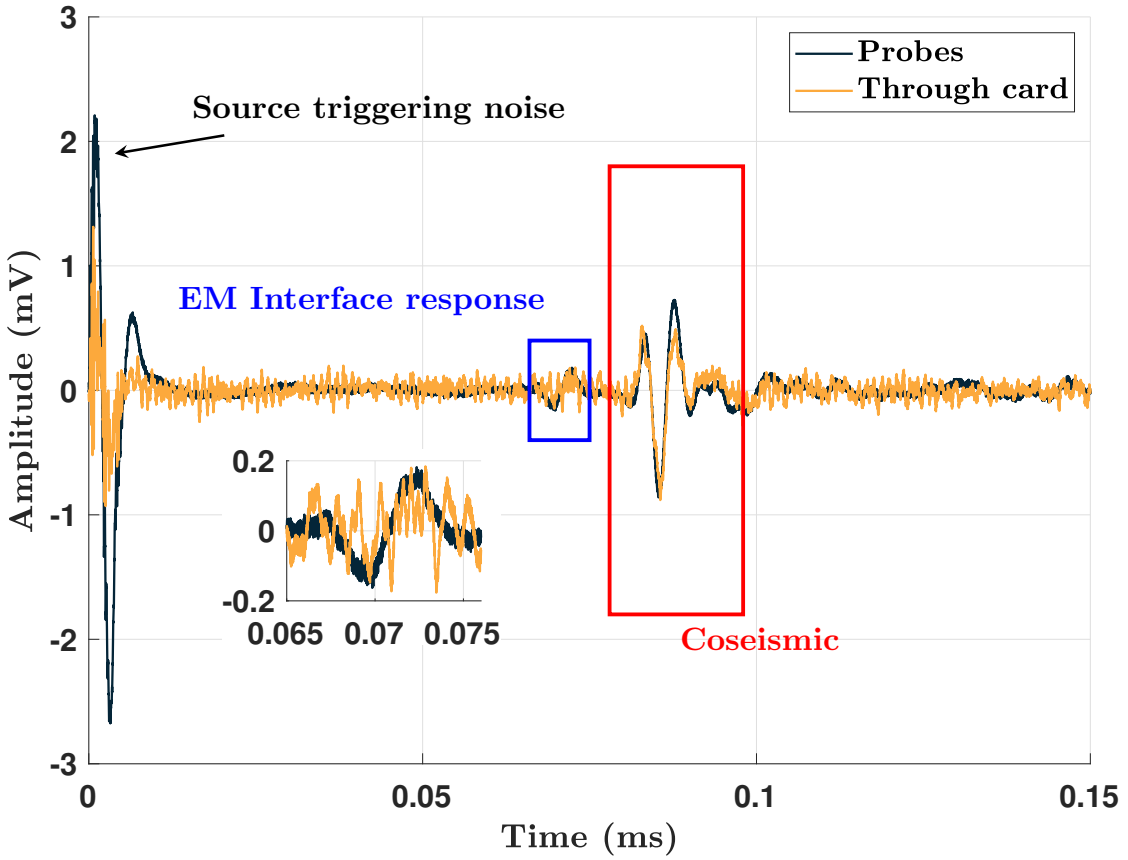

Figure 4.25: Comparison of absolute electric potentials measured using the oscilloscope probe (dark blue), and the relay card (orange). The three most pronounced events were highlighted, with a close-up of the interface response.

response shows that, when measurements are made with the relay card, the FFT magnitudes of frequencies associated with noise surpass those related with the signal of interest; nevertheless one can still distinguish the frequency band of the interface response.

As shown above, the use of the relay card introduces an important amount of noise in the measurements, thus making it inappropriate for the present experiment. On the other side, it is clear that working with signals containing higher amplitudes, more than one order of magnitude higher, may allow the use of this card. Therefore including a preamplification step between electrodes and relays is a reasonable solution. With that in mind, a second experiment was carried out, but this time in a homogeneous (water-saturated sand) medium, with electrodes directly connected to the SR560 preamplifier. In this new test the electrode comb (figure 4.9a) was positioned at x=0, with its first electrode at z=4.55 cm, then the preamplifier gain

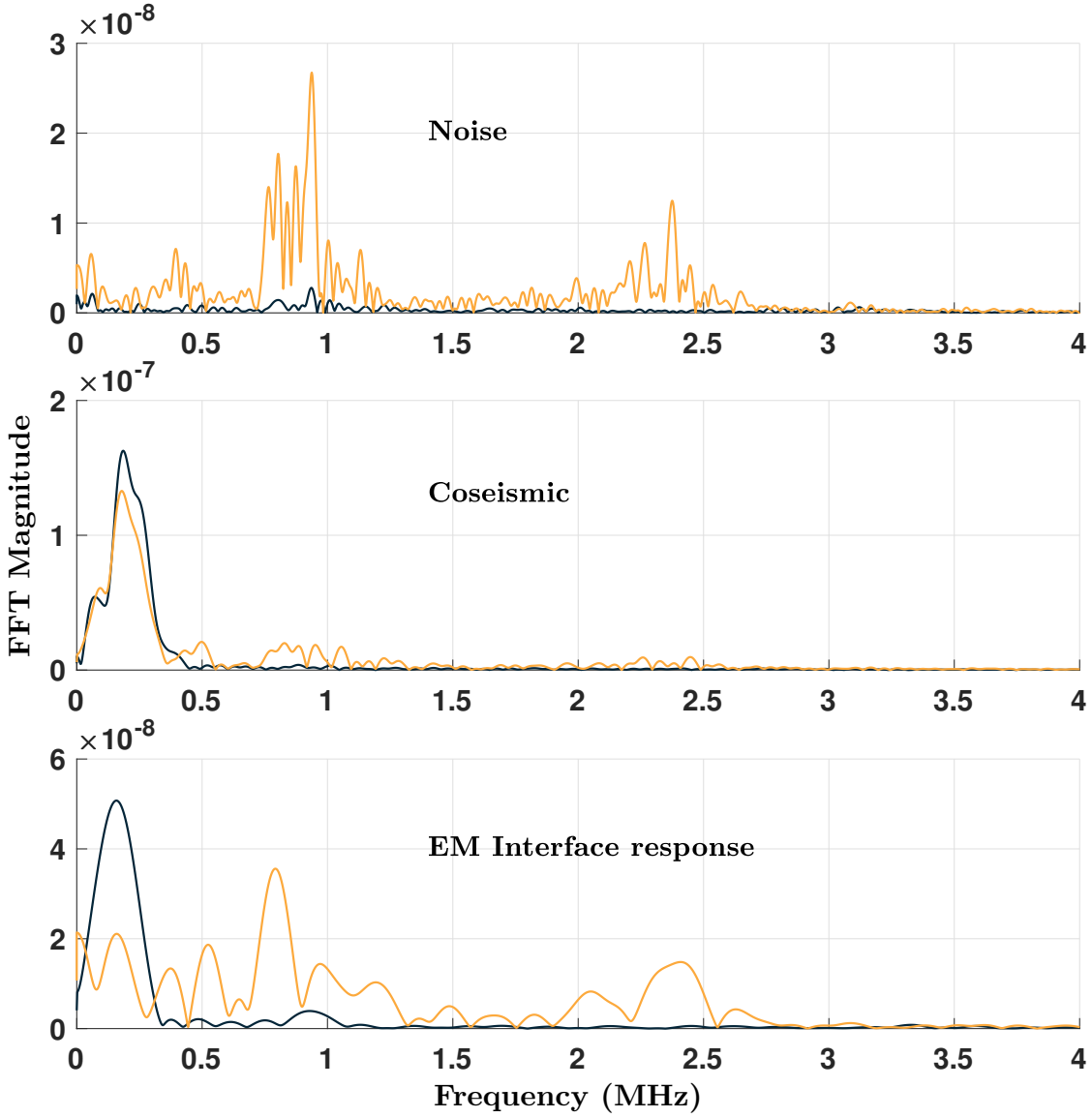

Figure 4.26: FFT magnitude spectra of noise, coseismic, and EM interface response. Except for the noise, the region used to calculate the FFT is highlighted in figure 4.25. A 0.025 ms window corresponding to time samples smaller than 0 ms, also part of the measurements, was used to calculate the FFT of the noise.

was varied from 1 until 20. Figure 4.27 shows the measurements, focusing on the coseismic associated with the direct P-wave, when the card was used and when it was not.

The absolute electric potentials in figure 4.27 were measured with the first two electrodes in the comb, and the dipole acquisition refers to measurements of electric potential difference using the same two electrodes. The results were obtained with

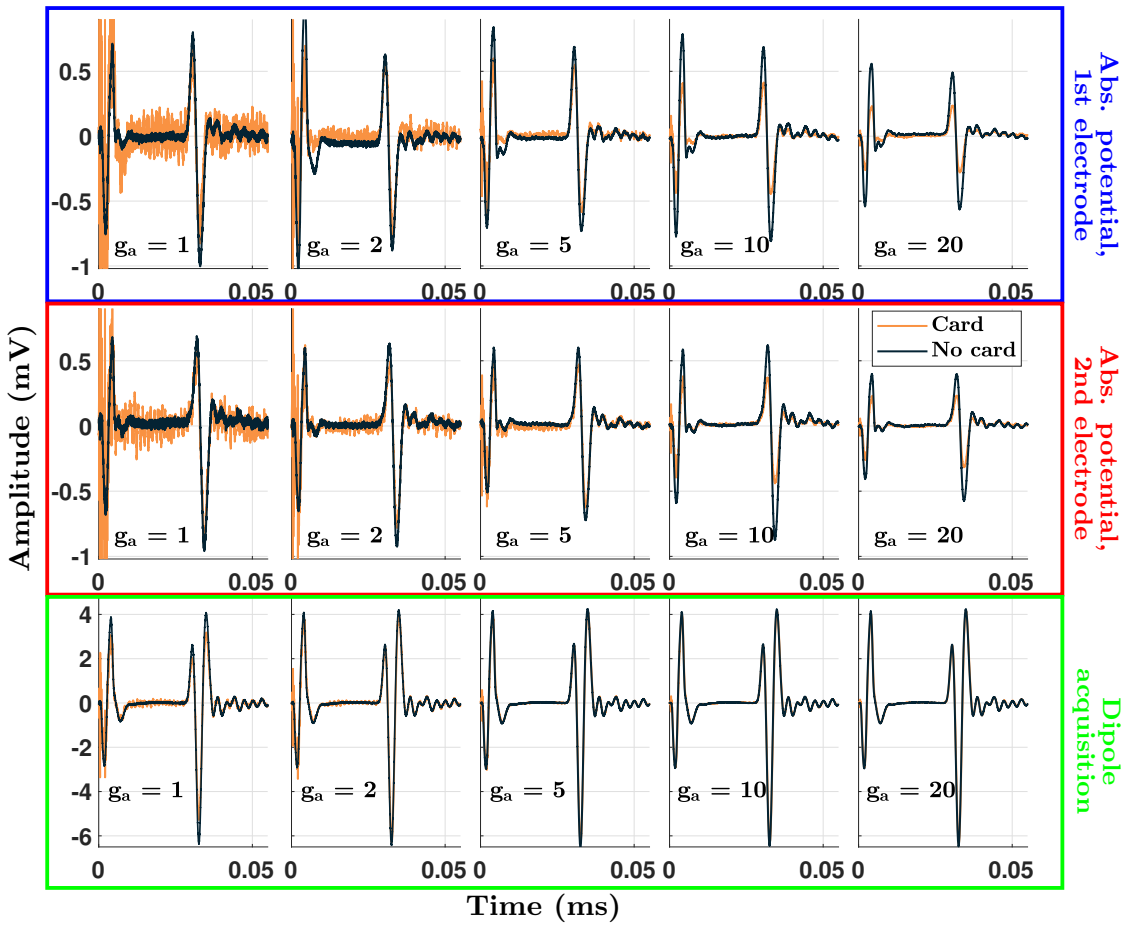

Figure 4.27: Absolute electric potential measurements (first and second line) obtained with electrodes positioned at z=4.55 and 4.8 cm. The electric potential difference between these two electrodes (acquired directly, not derived from the electric potential measurements) is shown in the last line. Data was acquired with a SR560 preamplifier, whose gain was varied from 1 to 20 such that each column of the figure corresponds to a different gain. At last, orange lines refer to data acquired using the relay card and dark blue lines when the card is absent.

five different gains and, to facilitate the comparison, amplitudes were divided by the gain applied by the preamplifier. By comparing measurements with and without the relay card, an increase in the gain reduces the noise in the coseismic event as well as in the signal created by triggering the PZT. Because the later (the PZT noise) is essentially an EM wave, the results shown for this signal can be extrapolated for the EM interface response, that means a preamplification step before the relay card does improve the electric data acquisition in the present experiment.

Looking at the bottom line in figure 4.27, it shows that measuring electric potential differences introduces less noise to measurements, when using the relay card, besides showing a linear relation between gain and amplitude increase. That means electric fields can still be measured using this card, even though measuring the EM interface response remains a problem, once this acquisition geometry (dipole) lead to very small amplitudes of the interface response, as previously discussed.

In the absolute potential measurements of figure 4.27, contrarily to differential measurements, one can notice that the amplitudes do not vary linearly with the preamplifier gain. Besides that, the best match between measurements made with and without the card happens when the gain is 5. To help understand in a quantitative way these results, figure 4.28 shows how the SNR (calculated using the peak-to-peak voltage of signal and noise), the measured gain (calculated with respect to the data obtained using an unitary gain), and the maxima and minima ratios (between data obtained with and without the relay card), of the coseismic, vary when the gain increases.

Figure 4.28a reaffirms the fact that using the relay card introduces noise, and thus reduces the SNR. Looking at the measured gain, in figure 4.28b, it does not increase linearly with the applied gain, for gains bigger than 5. This behaviour was only seen when measuring absolute potentials, not when potential differences were directly measured with the preamplifier, therefore it is probably a characteristic of the acquisition setup (a measuring electrode and a reference far away). Now, considering the amplitude ratio in figure 4.28c, it becomes evident the coseismic amplitudes, measured with and without the relay card, diverge with increasing gain.

From the discussion above, even though adding a preamplification step between the electrodes and the relay card shows promissing results, the non-linear behaviour of the amplitudes with increasing gain still needs some understanding. Besides, to properly adapt the relay card, one preamplifier per relay would be needed, thus implying the necessity of designing a new electronic card. Finally, due to lack of time and considering the drawbacks of using the relay card, it was put aside and wasn't used to acquire any dataset presented in the next chapters.

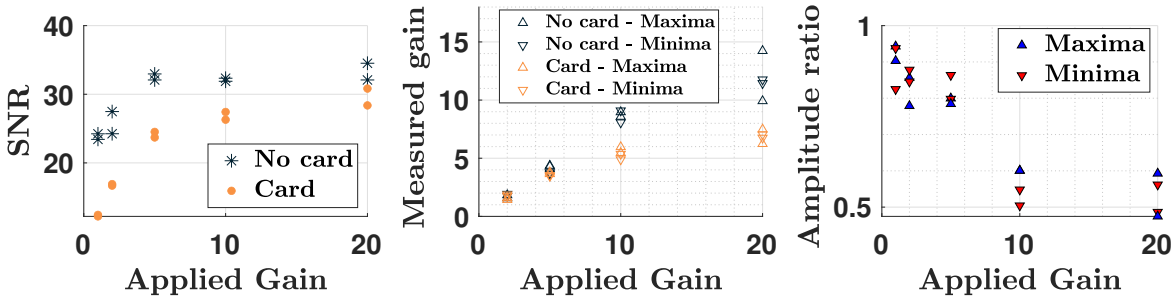

Figure 4.28: Analysis of the coseismic, obtained from the absolute electric potential measurements in figure 4.27, *vs* preamplifier gain. (a) shows the SNR, (b) the gain measured with respect to the data obtained with an unitary gain, and (c) shows the ratio between the amplitudes (maxima and minima) of measurements with and without the relay card. The three figures superpose the results of the coseismic measured with the two electrodes.

5 Quantitative comparison between laboratory and numerical data in ligth of electrokinetic theory

The contents of this chapter compose a paper in preparation for submission to the Geophysical Journal International.

Quantification of seismoelectromagnetic conversions at the laboratory scale

V. M. Gomes[1,2], D. Brito[1], S. Garambois[3], M. Dietrich[3], C. Bordes[1], H. Barucq[2]

[1] *Universite de Pau et des Pays de l'Adour, E2S UPPA, CNRS, TotalEnergies, LFCR, Pau, France*

E-mail:daniel.brito@univ-pau.fr

[2] *Universite de Pau et des Pays de l'Adour, E2S UPPA, CNRS, Inria, équipe Makutu, LMAP, Pau, France*

[3] *Univ. Grenoble Alpes, Univ. Savoie Mont Blanc, CNRS, IRD, Univ. Gustave Eiffel, ISTerre,*

38000 Grenoble, France

5.1 Summary

Seismoelectromagnetic phenomena, electrokinetic in nature, take place whenever a seismic wave propagates in fluid-bearing media, its energy depending mainly on the electric properties of the fluid and the hydraulic properties of the porous medium. They result from a conversion of mechanical into electromagnetic energy due to the transient ionic interactions happening at the pore scale. Two of these phenomena are usually studied: the electric field accompanying seismic waves, and the electromagnetic field that travels independently, generated wherever a discontinuity of physical properties exist in the porous medium. While the first is sensitive to physical parameters of the medium surrounding the receiver, the second catches information about

interfaces in the subsurface making it very attractive to near surface exploration. In this context we propose a new experimental set-up where both phenomena can be studied simultaneously: at first we use a porous medium composed of homogeneous saturated sand and study the characteristics of the coseismic electric field, afterwards a thin Vosges sandstone layer is inserted acting as an interface within the sand and thus generating an electromagnetic converted wave. We record the seismic displacement field using a laser vibrometer at the top of the sand while the electric field is derived through absolute potentials measurements using stainless steel electrodes buried in the sand. With the help of direct numerical simulations we perform a comparison between experimental measurements and theoretical predictions, based on a well established set of governing equations. For both types of experiments, the quantitative comparison shows that experimental and numerical data agree successfully, validating the concerned theory. The absolute electric potential data also show that the signal generated at interfaces can clearly be recorded at about ten seismic P-wavelengths away from the interface. In contrast, when using classical dipolar electric arrays like in field acquisitions, the same signal could barely be discerned at the receivers adjacent to the layer. Our results also support that the electromagnetic signal generated at interfaces can be explained by a group of short electric dipoles generated along the first Fresnel zone, with electric moments depending on the direction of the wavefront of the incident P-wave with respect to the interface. At last, our results demonstrate that it is possible to compare electrokinetic theory to real data in a precise and quantitative way, what in turn opens the path for future field surveys.

5.2 Introduction

Research on seismoelectric (SE) and its reciprocal electroseismic (ES) phenomena, electrokinetic in nature, remounts to the 1930's (Blau and Louis, 1936; Thompson, 1936); however oriented laboratory studies only started around 1960, although a likewise phenomenon had already been observed in 1918 (Parkhomenko, 1971). Theoretical attempts to establish governing physical relations were firstly made in Frenkel (1944), departing from Ivanov's field observations (Ivanov, 1939; Ivanov, 1940), and later in Neev and Yeatts (1989). Nonetheless it was Pride (1994), complemented by Pride and Haartsen (1996) and Haartsen and Pride (1997), that really attained it through the coupling of Biot's theory and Maxwell's electromagnetic

formulation by flux-force relations. More recently, Revil and Mahardika (2013) and Jardani and Revil (2015) conceptualized an electrokinetic model capable of describing seismo-electromagnetic phenomena for a broader class of porous media, in comparison with the model proposed by Pride (1994).

Following Pride's electrokinetic theory, research has been mainly directed towards two effects of seismic-to-electromagnetic conversion. For a propagating compressional seismic wave, the first effect is an (coseismic) electric field whose support is strictly binded to that of the mechanical wave (Pride and Haartsen, 1996); the second has its origins linked to the discontinuities of electrical and/or mechanical properties across interfaces, existing as an elctromagnetic-disturbance (EM-disturbance) moving at much higher speeds than that of the generating seismic wave (Haartsen and Pride, 1997). Both have already been studied experimentally (e.g., Zhu et al., 1994; Bordes et al., 2008; Zhu et al., 2008; Schakel et al., 2011a) but given the focus of this work, we are particularly concerned with the latter.

The first study to propose a numerical solution to seismoelectrics based on Pride's formulation was Haartsen and Pride (1994), with further details in Haartsen (1995) and Haartsen and Pride (1997). It makes use of the global matrix method (Chin et al., 1984) to solve the governing equations for point sources in stratified porous media. Garambois (1999) and later Garambois and Dietrich (2002) introduced a methodology slightly different to the previous, using an extension of the generalized reflection and transmission matrix method (Kennett and Kerry, 1979) to solve for the wavefields. It is the latter that will be employed here for the simulation of seismoelectric fields, with an adaptation to compute electric potentials (as proposed by Dietrich et al. (2018)). Complementarily, for the same type of media, Ren et al. (2010) and Grobbe et al. (2016) also developed numerical techniques to simulate the propagation of seismoelectric wavefields. While the works cited proposed semi-analytical solutions, more recently numerical approximation methods to solve partial differential equations were used by Zyserman et al. (2010) (finite-element method), Morency et al. (2021) (spectral-element method), and Meyer (2021) (discontinuous Garlekin method) to tackle the problem of simulating the seismoelectric phenomena in complex 3D media.

Experimental studies of the coseismic wave, in the kilohertz range, focus mainly on the influence of physical properties on the coseismic amplitude; Zhu et al. (2000) investigate the effect of conductivity, Bordes et al. (2015) the influence of increasing saturation, and Holzhauer et al. (2017) analyse the results of varying both conduc-

tivity and saturation. Reported laboratory experiments devoted to the observation of interfacial seismoelectric responses have begun with the works of Haartsen et al. (1995) and Zhu and Toksöz (1996), where EM-waves were created by a compressional seismic wave generated by a transducer at the interface between fluid-saturated lucite sandstone and man-made sandy porous medium. Most of the experimental work up until now used either a water-filled fracture borehole model with a cross-hole acquisition geometry (Zhu and Toksöz, 2003a; Zhu and Toksöz, 2003b; Zhu and Toksöz, 2005), a sand-based model whose layers differ mainly in terms of saturating fluids (Chen and Mu, 2005; Block and Harris, 2006; Liu et al., 2008), and a rock sample (real or synthetic) immersed in a water tank (Zhu et al., 2008; Charara et al., 2009; Schakel et al., 2011b; Schakel et al., 2011a; Schakel et al., 2012; Smeulders et al., 2014; Zhu et al., 2016; Peng et al., 2016a; Peng et al., 2017; Peng et al., 2018a; Peng et al., 2019) where the seismo-electromagnetic phenomena is generated by a fluid-rock interface.

In the present wotk we perform a quantitative study of the seismoelectric phenomena based on the above mentioned electrokinetic theory (Pride, 1994; Pride and Haartsen, 1996). To achieve that we adopt a new laboratory set-up, seeking to ease comparison with numerical modelling while proposing a simple and effective way to simultaneously record the coseismic and the interface response. At first a homogeneous medium will be used to investigate the limitations of the electrokinetic theory when the latter is used to predict the experimental data. Subsequently we employ a thin layer to study the EM signal created at interfaces and analyse the validity of a conceptual model based on a group of short dipoles distributed along the interface, which can be used to assess geometrical properties like layer depth and thickness without relying in (complex time-consuming) full-waveform modelling/inversion.

Section 5.3 is a brief introduction to the SE theory. Sections 5.4 and 5.5 are devoted respectively to the presentation of the experimental set-up and the numerical simulation tool. We compare the experimental data to the simulations in the case of the homogeneous medium in section 5.6 and to the case with an interface in section 5.7. Finally, conclusions are drawn in section 5.8

5.3 Theoretical basis

The formulation proposed in Pride (1994) and Pride and Haartsen (1996) regarding seismoelectromagnetic effects taking place in porous media will be used in the

present study. It accounts for porous media whose pores are filled by an electrically conducting solution such that the coupling between seismic and electromagnetic fields has an electrokinectic origin. Microscopically (i.e., for grain size dimensions), the time-varying interaction between charges adsorbed to the surface of the grains and the moving ions in the pore fluid engender the seismoelectric phenomena.

Assuming there is a thin electric double-layer (Stern, 1924; Bockris and Reddy, 1970) surrounding every grain, Pride (1994) applies an averaging theorem (Slattery, 1967; Whitaker, 1969) to the microscopic Maxwell and Biot equations thereby establishing a macroscopic mathematical model describing the aforementioned physics. Pride and Haartsen (1996) complement the latter by presenting the solution for point-sources and plane-waves for homogeneous isotropic whole spaces, inferring the existence of four wavetypes: two longitudinal seismic waves (slow and fast-P), one transverse seismic wave (shear or S) and one transverse EM-wave; additionally they derive the boundary conditions that hold at the interface of distinct porous media.

For the seismoelectric case, the amount of mechanical energy being converted into electromagnetic fields is given by the dynamic (frequency-dependent, f the frequency, $\omega = 2\pi f$ the pulsation) transfer functions (TF) (Bordes et al., 2015):

$$\mathbf{E}(\omega) = \frac{i\omega\tilde{\rho}(\omega)L(\omega)\beta_{\mathrm{L}}(\omega)}{\tilde{\epsilon}(\omega)}\mathbf{u}(\omega) = \frac{\tilde{\rho}(\omega)L(\omega)\beta_{\mathrm{L}}(\omega)}{\tilde{\epsilon}(\omega)}\dot{\mathbf{u}}(\omega) = \frac{\tilde{\rho}(\omega)L(\omega)\beta_{\mathrm{L}}(\omega)}{i\omega\tilde{\epsilon}(\omega)}\ddot{\mathbf{u}}(\omega), \tag{5.1}$$

where $\mathbf{E}$, $\mathbf{u}$, $\dot{\mathbf{u}}$ and $\ddot{\mathbf{u}}$ are, respectively, the coseismic electrical field, the (average) solid particle displacement, velocity and acceleration. $\tilde{\rho}(\omega)$ is the effective complex density of the pore fluid defined by eq. 2.57. $L(\omega)$, as detailed in eq. 2.48, is a first-order coefficient in seismoelectric phenomena, controlling all couplings between mechanical and electromagnetic fields governed by the transport equations given in eqs 2.45a and 2.45b (Pride, 1994). $\beta_L(\omega)$ is the ratio between the relative-displacement vector $\mathbf{w}$ and the solid frame displacement $\mathbf{u}_{solid}$, defined by $\mathbf{w} \equiv \beta_L(\omega)\mathbf{u} \equiv \phi(\mathbf{u}_{fluid} - \mathbf{u}_{solid})$, where $\mathbf{u}_{fluid}$ is the fluid displacement and ϕ the porosity of the medium. $\tilde{\epsilon}(\omega)$ is the effective electric permittivity detailed in eq. 2.59.

All other physical parameters involved indirectly in eq. 5.1 (Tiab and Donaldson, 2015; Revil et al., 2015) are discussed and detailed in chapter 2. The parameters relevant to the quantitative analysis of SE phenomena in experiments and numerical modeling of the present study are all listed in table 5.1.

5.4 Experimental setup

The experiment takes place in a parallelepipedal box filled with sand as shown in fig. 4.1. A piezoelectric transducer (PZT) acts as the seismic source, placed against the 24.7(length) $\times$ 11.5(height) $\times$ 11(width) cm plastic box filled with water-saturated sand. The walls of this box measure 5.2 mm each, except for the one where the PZT is, which has a 2.5 mm thickness. A comb of electrodes is vertically inserted in the sand to measure absolute electric potentials (noted V hereafter) using a reference electrode positioned in an auxiliary plastic container also filled with sand. A laser vibrometer (Lebedev et al., 2011; Shen et al., 2022) measures vertical seismic displacement u_y with the laser beam pointing towards the top of the sand (e.g., Devi et al. (2018)). When experiments seek to measure the EM interface response, a saturated sandstone layer is inserted in the sand, approximately in the middle of the box, as sketched and pictured in fig. 4.1.

5.4.1 The porous media

Both porous media, sand and sandstone, are kept saturated with distilled water whose fluid conductivity ranges between 1.2 and 1.8 mS/m. To ensure full saturation, a desiccator is used to pump the air out of the pores during 2.5 hours. In sequence, the experiment is set in place and left to stabilize while amplitudes of either seismic or electric signals are monitored. The experiment will only begin when no amplitudes change takes place (after a period of about 2 hours). At the end of each experiment both the plastic box and the auxiliary container (reference electrode) are put in the desiccator and monitored until new measurements are carried out.

Sand

The main material used in experiments is a homogeneous and well-sorted sand from Southwest France, composed mainly of quartz (>98%) and whose mean grain diameter is 250μm (e.g., Barrière et al. (2012), Bordes et al. (2015) and Holzhauer et al. (2017)).

Concerning the mechanical properties of the sand, the drained bulk K_{fr} and shear G_{fr} moduli (see table 5.1) are adjusted accordingly, in order to be consistent with the seismic velocities measured from first-break (FB) picking during experiments

Table 5.1: Input physical parameters for the sand and sandstones used in the SE experiments and numerical simulations. Relevant constants are also added in the list. * refers to dimensionless properties. ⋆ refers to standard values. When two references are present in the column References, the first one refers to the sand and the second one to the sandstone.

Name, symbol, units	Sand	Sandstone	References
Porosity (ϕ)[%]*	0.4	0.24	Barrière et al. (2012), measured
Saturation (S_w)[%]*	100		-
DC permeability (k_0)[m^2]	1.02E-11	6.8E-15	Barrière et al. (2012) Lorne et al. (1999b)
Bulk (solid) modulus (K_s)[Pa]	36E9	36E9	⋆
Shear (solid) modulus (G_s)[Pa]	44E9	44E9	⋆
Bulk (fluid) modulus (K_f)[Pa]	2.5E9	2.5E9	⋆
Bulk (frame) modulus (K_{fr})[Pa]	2.38E7	3.41E8	Pride (2005) and seismic velocities
Shear (frame) modulus (G_{fr})[Pa]	1.43E7	2.10E8	Pride (2005)
P-wave velocity (v_P) [m/s]	1.78E3	2.2E3	measured (with FBs)
Fluid viscosity (η)[Pa·s]	1E-3		⋆
Solid density (ρ_s)[kg/m^3]	2.65E3	2.12E3 ± 0.31	⋆, measured
Fluid density (ρ_f)[kg/m^3]	1E3		⋆
Fluid Conductivity (σ_f)[mS/m]	1.2 – 1.8 ± 0.01		Measured
Molarity (C_0)[mol/l]	1.28E-4 – 1.95E-4		$C_0 = \sigma_f/(e^2(b_{Na} + b_{Cl})N_A)$, Pride (1994)
Surface Conductivity (σ_n)[mS/m]	8.3E-2	2	Revil and Glover (1998) and Lorne et al. (1999b)
Temperature (T)[Kelvin]	288.35		Measured
Fluid permittivity (κ_f)[ ]*	80		⋆
Solid permittivity (κ_s)[ ]*	4		⋆
Tortuosity (α_∞)[ ]*	1.65	3	Holzhauer (2015) Lorne et al. (1999b)
Pore geometry number (m)[ ]*	6		Pride (1994), Haartsen and Pride (1997)
Zeta potential (ζ)[mV]	6.79 – 12.91		Guichet et al. (2003)
		-12	Lorne et al. (1999b)
Electrokinetic coefficient (C_{ek})[V/Pa]	2.18E-6 – 5.78E-6	-1.13E-7 – -2.18E-7	Guichet et al. (2003): eq. 2.29 and eq. 2.31
Constants			
Avogrado's number (N_A)[mol^{-1}]	6.02E26		-
Elementary charge (e)[C]	1.60E-19		-
Ionic mobility ($b_{l=Na=Cl}$)[$m/(sN)$]	3E11		-
Vacuum permittivity (ϵ_0)[F/m]	8.85E-12		-
Vacuum permeability (μ_0)[H/m]	4πE-7		-
Boltzman constant (k_b)[J/K]	1.38E-23		-

(see sections 5.6 and 5.7), using the modified Walton's model (1987) presented in Pride (2005) as a reference.

Regarding the electrical properties, Guichet et al. (2003) studied a sand whose properties are similar to the one used here, therefore the zeta-potential ζ was calculated following their empirical law as indicated in table 5.1. Additionally, to account for a non-negligible surface conductivity (see values in table 5.1), Guichet's equation (Guichet et al., 2003; Guichet et al., 2006) for the electrokinetic coupling coefficient C_{ek} is adopted.

Sandstone layer

The thin layer inserted in the sand is a Vosges sandstone (Eastern France) with dimensions: 0.74(length) $\times$ 5.7(height) $\times$ 9.3(width) cm. Its density and porosity are measured and its fluid conductivity is routinely adjusted to keep it constant and equal to the one of the fluid in sand.

Complementarily, the frame moduli is calculated using the experimentally estimated seismic velocities, with the aid of the model for consolidated media discussed in Pride (2005).

The sample used here has a fair amount of feldspar, mica, clay, and oxides and is similar to the Adamswiller sandstone sample studied in David et al. (1994) and Lorne et al. (1999b). Permeability, tortuosity (derived from the definition of formation factor, $F = \alpha_\infty/\phi$), surface conductivity, and zeta potential are finally taken from Lorne et al. (1999b) (see table 5.1).

5.4.2 Seismic source

A PZT model Olympus V1012 whose effective diameter is 3.8 cm and nominal frequency is 250 kHz, is used as a source of mechanical waves in the experimental setup. It is positioned in the exterior of the plastic box containing the sand such that its topmost point marks the origin of the cartesian system (x,y,z) used in this work, and coincides with the sand surface (see fig. 4.1 (a) and (b)).

We show in fig. 5.1 a signal generated by a 250 kHz half-sine burst with an amplitude of 8 V using a RIGOL DG4102 waveform generator sent to an amplifier (Falcon Systems WMA 300) and then to the PZT (see fig. 4.1). We have verified that the PZT seismic signal is spatially homogeneous throughout its surface and fig. 5.1 shows, as an example, the time and frequency responses measured at a point in

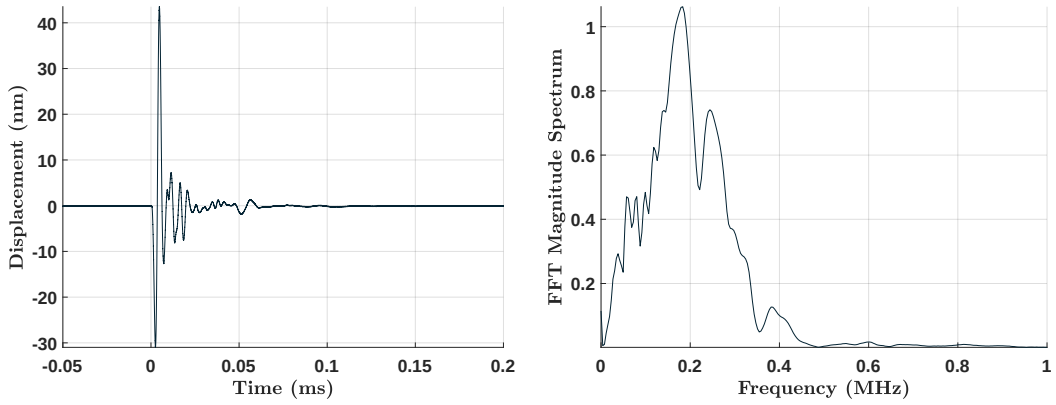

(a) (b)

Figure 5.1: Source signature of the PZT measured in the center of its surface using a laser vibrometer. (a) shows the seismic displacement u_y perpendicular to the surface of the PZT *vs* time and (b) shows its Fast-Fourier-Transform (FFT) magnitude spectrum.

the center of the active surface with a laser vibrometer. It is clear from the time series and the magnitude spectrum in fig. 5.1 that the main wavelet has a 180 kHz peak frequency, followed by a series of lower amplitude oscillations that last until about 65μs.

5.4.3 Seismic measurements description

A laser vibrometry system was used to measure particle displacements of the sand, it consists of a OFV-505 head sensor that detects particle movement and a OFV-5000 controller which analyses and transmits the recorded displacement using a DD-300 decoder. The system bandwidth is [3E-4 – 24] MHz, and the upper bound for the absolute displacement is 75 nm.

In the experiment, measurements are carried out on the surface of the sand in such a way that the displacement component u_y is orthogonal to the axis of the seismic source (y-direction in fig. 4.1 (b)) is measured. To increase the signal-to-noise ratio, a 4 mm^2 piece of retro-reflective film was placed at each measuring point at the top of the sand. The water-level was kept constant and equal or slightly lower than the sand-level in the box to make sure the displacement detected is as close as possible to the sand grain displacement, assuming that the reflective paper has no influence on the measurements at our working frequencies (Shen, 2020; Hasanian and Lissenden, 2017).

The laser vibrometry measurements are performed during experiments along a central line along the box's length (z-axis in fig. 4.1) covering the range z=[1 – 10.75] cm and z=[13 – 22.75] cm, with a 0.125 cm spacing between points, resulting in 159 offsets. Finally, each seismic trace is stacked 3000 times and recorded during 10 ms.

5.4.4 Seismoelectric measurements description

In seismoelectric studies, the measurements of the electric field are usually obtained from potential differences ΔV using dipolar arrays of electrodes (Garambois and Dietrich, 2001; Bordes, 2005; Dupuis, 2008; Holzhauer et al., 2017). However, Dietrich et al. (2018) and Devi et al. (2018) questioned this choice of arrays when the goal is to record EM waves generated at interfaces, once they strongly attenuate signals whose arrival times are practically synchronous at all electrodes. Alternatively, they propose configurations using an odd number of electrodes because those can provide reliable estimates of the absolute electric potential V, which they consider as the ideal choice to measure the interface response. Measuring absolute potentials implies that a reference electrode is used, what in field surveys is often unpracticable due to noise issues (Devi et al., 2018). Conversely, seismoelectric laboratory studies that intend to detect the EM interfacial signal generally adopt a reference electrode which is either taken as the common-ground, referring to the laboratory Earth (Zhu et al., 1999; Smeulders et al., 2014; Zhu et al., 2016; Peng et al., 2017), as a point inside the experimental setup which is sufficiently far from the measuring electrodes (Chen and Mu, 2005; Zhu and Toksöz, 2005; Devi et al., 2018), or as an adapted/modified common-ground to which all the acquisition equipment is connected to (Block and Harris, 2006).

The measurement of absolute seismoelectric potentials V_{exp} are performed with an electrode comb made of 32 stainless steel electrodes with an inter-electrode distance of 0.25 cm. Each electrode has a diameter of 1.1 ± 0.2 mm and a length of 10.8 cm, however only 5.7 ± 0.2 cm are buried in the sand. A total of 80 measurements are carried out (40 in each side of the box) in a way that the electric measuring points cover the exact same range in z than that of the seismic with the laser measurements.

To measure with precision the absolute potential V at each electrode, a reference electrode is inserted in a second container filled with the same sand as the one in the main plastic box (pink container in the bottom-left part of fig. 4.1 (b)). A

copper wire connected to a 10 MΩ resistance is used to link both plastic containers, ensuring the potential in the reference stays close to zero at all times. Each electrode in the comb is connected to a preamplifier (model SR560) in differential mode with the reference electrode, no gain is imposed and a [3E-4 - 1] MHz band-pass filter is applied. The preamplifier is in floating mode (not grounded), thus its output is the difference between the potential in the sand and the reference electrode. Finally, the 100 MΩ input impedance of the preamplifier is considered high enough to ensure our measurements are consistent, in terms of amplitude, with the absolute potential voltages mainly due to the electrokinetic phenomena taking place inside the sandbox.

5.5 Numerical modelling tool

The numerical solution of Pride's equations was explored by research groups, using different numerical techniques. The first work to show numerical calculations, for a homogeneous horizontally layered (1D) media, was Haartsen et al. (1995) followed by Haartsen and Pride (1997). In order to model more complex 2D and 3D media, finite-difference (Haines and Pride, 2006; Guan and Hu, 2008), finite-element (Zyserman et al., 2010), and more recently spectral-element (Morency et al., 2021) methods are employed. In here, numerical simulations based on the laboratory experiments rely on the numerical code developped by Garambois and Dietrich (2002), which is capable of computing separately the mechanical and electromagnetic fields due to a point source excitation in homogeneous poro-elastic layered media. It also allows a straightforward modification of reflection and transmission coefficients, a convenient property if small amplitude events, often hidden, need to be enhanced. Except for the methodology to calculate the reflection and transmission coefficients, this code is similar to Haartsen and Pride (1997) and Ren et al. (2010); as a whole it is also analogous to the code of Grobbe et al. (2016).

5.5.1 A brief description

Departing from Pride (1994), Garambois and Dietrich (2002) adopts a cylindrical coordinate system $(\rho, \theta, \mathrm{z})$ and the formalism of Hudson (1969) to rewrite the governing equations with seismoelectric fields decomposed in vertical and horizontal components, for homogeneous layered media with azimuthal symmetry. Afterwards, a Fourier-Hankel transformation is applied to the ρ and θ-coordinates, thus in

the frequency-wavenumber domain the wavefields will be decomposed in cylindrical waves. Isolating the partial derivatives in z, a system of 12 first-order differential equations is found:

$$\frac{\partial}{\partial z}\mathbf{Y} = \mathbf{A}\mathbf{Y} + \mathbf{F}, \tag{5.2}$$

where $\mathbf{Y}$ is the displacement-stress-EM vector, $\mathbf{F}$ is the source vector and $\mathbf{A}$ is the system matrix containing the physical properties of the media.

This system of equations contains two well-known independent sets: PSVTM (8 equations) and SHTE (4 equations). The first considers the coupled propagation of fast P-waves, Biot slow waves, vertically polarized S-waves and EM-waves whose magnetic field has a transverse polarization. The second deals with S-waves horizontally polarized and EM-waves with a transverse polarization of the electric field. Thus $\mathbf{Y}$ can be subdivided in $\mathbf{Y}^{PSVTM}$ and $\mathbf{Y}^{SHTE}$.

To solve eq. 5.2 and find the propagated seismoelectric wavefields, $\mathbf{Y}$ is expressed as:

$$\mathbf{Y} = \mathbf{D}\mathbf{P}, \tag{5.3}$$

where $\mathbf{D}$ contains the eigenvectors of $\mathbf{A}$ and $\mathbf{P}$ contains the upward and downward potentials (i.e., complex amplitudes) of all wavetypes. For each interface in the media the methodology described in Kennett and Kerry (1979) is applied with the proper adaptations to the specific case of seismoelectrics.

Since all elements of $\mathbf{Y}$ are in the frequency-wavenumber domain, to go back to the space-time domain an inverse Hankel transform followed by an inverse Fourier transform is applied. The integral over the horizontal wavenumber (k), inherent to the inverse Hankel transform, uses the discrete summation procedure described in Bouchon (1981). To avoid aliasing due to the discrete Fourier transform, complex frequencies are used throughout the implementation as suggested by Bouchon (1979). Finally, the transformation to time domain uses the fast Fourier transform with a correction to extra attenuation of the wavefields as a consequence of assigning an imaginary part to frequencies.

5.5.2 Extension of the existing numerical code

To be consistent with the geometry of the experiment the electric field in the z-direction E_z (see fig. 4.1), in-between electrodes, needs to be calculated in addition to the fields in $\mathbf{Y}^{PSVTM}$. Because it was not included in the original code of Garam-

bois and Dietrich (2002), the calculation of E_z is detailed in Appendix B and was implemented in the numerical simulation.

Additionally, since in the experiments absolute electric potentials V_{exp} are measured, the electric potential calculation was implemented in the code as well, based on the procedure developed in Dietrich et al. (2018) for the numerical code of Garambois and Dietrich (2002). Following Dietrich et al. (2018), as long as sources are axially symmetric (e.g., explosion), the electric field E will not have a transverse component, and the solution for V can be derived from the cylindric radial component of the electric field using a double integral, in cylindric coordinates

$$V = \frac{1}{2\pi} \int_{-\infty}^{\infty} e^{-i\omega t} d\omega \int_{0}^{\infty} \hat{E}_{\rho}(\omega, \mathtt{k}, z) J_0(\mathtt{k}\rho) d\mathtt{k}, \tag{5.4}$$

where J_0 is the zero-th order Bessel function and $\hat{E}_{\rho}$ is the radial component of the electric field in the Fourier-Hankel domain.

5.5.3 Particularities of the numerical modelling of the experiments

Numerical modelling of PZT source

The signal displayed in fig. 5.1 (restricted to the time-window [0 – 0.5] ms and band-pass filtered to [10 kHz – 1 MHz]) is used as the input seismic source in the numerical simulations of the experiments. Since the surface area of the PZT source is relatively large compared to the dimensions of the experimental setup, the seismic source is discretized and modelled as a group of $N_{sources}$ synchronous explosive point sources, distributed along the line defined by the coordinates x=0, z=0 and y $\in [0, 3.8]$ cm, thus corresponding to a y-oriented linear distribution of point sources equally spaced along the PZT diameter.

It follows that for a point on top of the sand, the numerically computed vertical displacement u_{y-num}, accounting for contributions from all sources, will be obtained from a summation of the displacements generated by each individual source u_{y-n}, weighted by the interspace between sources:

$$u_{y-num}(x = 0, y = 0, z, t) = \sum_{n=1}^{N_{sources}} u_{y-n}(x = 0, y = 0, z, t)\, \delta y, \tag{5.5}$$

with $\delta y = l_{PZT}/N_{sources}$ the spatial discretization step, and $l_{PZT} = 3.8$ cm the diameter of the PZT. After a numerical parametric study on the influence of the value

of $N_{sources}$ on the total displacement u_{y-num}, $N_{sources} = 80$ was deemed appropriate, thus the value for δy used in eq. 5.5 was 0.475E-3.

Numerical modelling of the experimental data recorded by elongated electrodes buried in a medium

While the experimental seismic measurements are numerically modeled as punctual receivers, seismoelectric measurements account for the experimental absolute electric potential V_{exp} measured by a long electrode. Therefore, considering there is a length $l_{elec} = 5.7$ cm of each electrode buried in the sand (see sec. 5.4.4), the numerically estimated values for the absolute potential V_{num} at a specified z-position was estimated by integrating the potentials along the buried electrode in the y-direction such that:

$$V_{num}(x = 0, z, t) = \int_0^{l_{elec}} V_{num}(x = 0, y, z, t)\, dy. \tag{5.6}$$

To formulate a discrete version of eq. 5.6, each electrode was discretized using $N_{elec} = 120$ points such that δy, the discretization spatial step, is equal to the one used in the PZT discretization (see eq. 5.5). Finally, the discrete form of eq. 5.6, accounting for the $N_{sources} = 80$ seismic sources is:

$$V_{num}(x = 0, z, t) = \sum_{p=1}^{N_{elec}} \sum_{n=1}^{N_{sources}} V_{n,p}(x = 0, z, t)(\delta y)^2, \tag{5.7}$$

where $V_{n,p}$ is the electrical potential signal computed at a point p of an electrode, and generated by the source n from the PZT discretization.

5.6 Seismoelectrics in a homogeneous medium

5.6.1 Experimental data

Seismic measurements

The y-oriented displacement traces u_{y-exp} measured during the experiment performed in homogeneous saturated sand are displayed in fig. 5.2. The main wave, the direct compressional P-wave, is clearly observed with its linear trend of arrival times (dashed line); it is followed by reflected P-waves (on the sides, bottom, sand-air interface, and back) highlighted by red dash-dotted lines. All the reflected waves

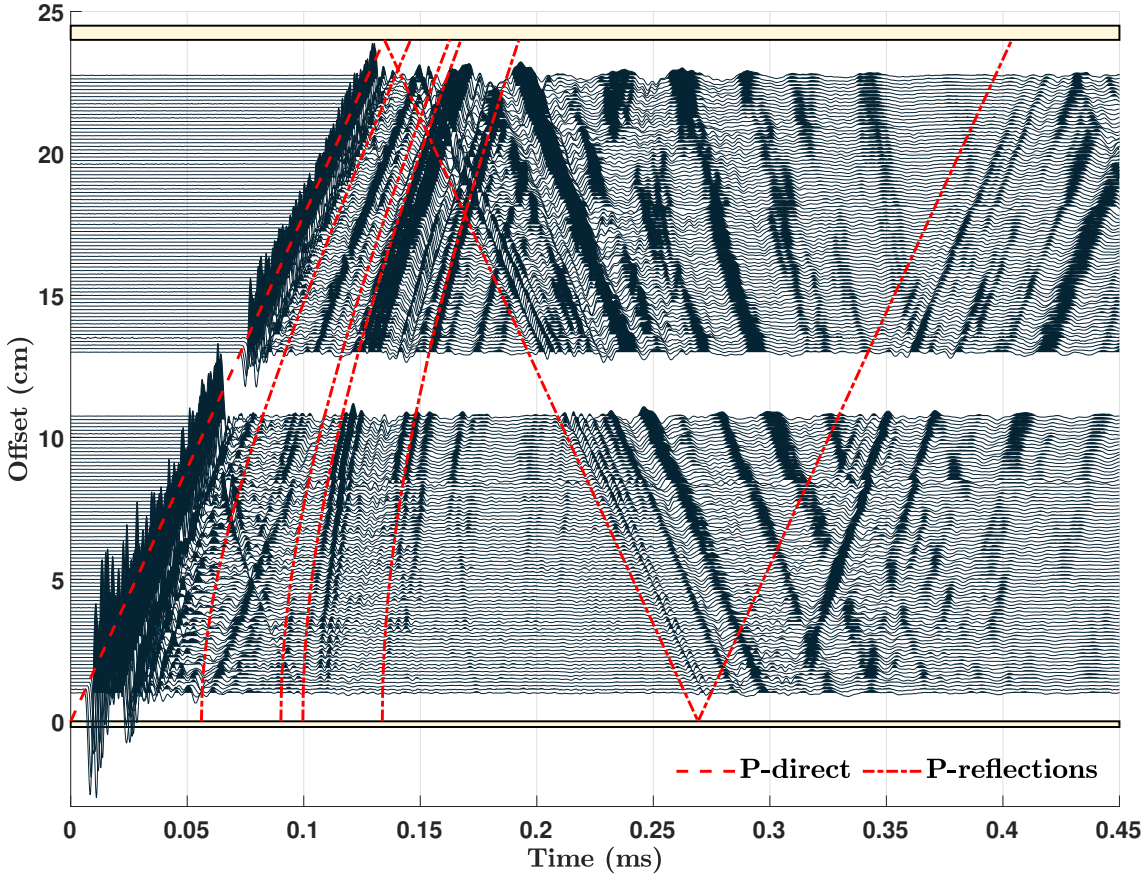

Figure 5.2: Measured displacement u_{y-exp} as a function of time and offsets for the 158 seismic traces. Front and back wall of the plastic box are depicted for convenience. The dashed red line highlights the direct P-wave while the dashed lines indicate the reflections on the lateral and bottom walls of the box and on the upper interface between sand and air.

are hardly distinguishable one from the other, except for the one reflected on the back wall (that opposite to the PZT source).

A static correction was applied to all seismic traces in fig. 5.2 assuming that the P-wave velocity v_p of the medium is near 1782 m/s (determined from the first-breaks (FBs) regression of the absolute potential measurements). Finally, u_{y-exp} in fig. 5.2 was low-pass filtered using a 1 MHz cut frequency and the gap between offsets 10.75 and 13 cm was intentionally planned to insert a sandstone layer (section 5.7, experiments with a layer).

In order to compare the amplitude decay of the experimental data with what Biot's theory predicts, the first minima and maxima of u_{y-exp} were selected and displayed *vs* offsets in fig. 5.3 (a). In order to interpret the decay of these extrema and extract information about the geometrical spreading and the intrinsic attenuation

of the direct P-waves in the experiments, a curve fit was applied to the data in fig. 5.3 (a) using functions with the form $u_0 e^{-\alpha r} \cdot r^{-1}$, where r is the radial source-receiver distance at the top of the sand (distance r between O and the measuring point of the laser), u_0 is the parameter to estimate and α_P is the intrinsic attenuation of the seismic P-wave, as predicted by Biot for the range of frequencies studied and the parameters displayed in table 5.1. The term r^{-1} accounts for the geometrical spreading assuming a pure 3D seismic wave propagation in the far-field (Aki et al., 2002, chap. 4). The value $\alpha_P = -7.5\text{E}-3$ m^{-1} was used to calculate the curves in fig. 5.3 (a), once it is the value theoretically predicted (with eq. 2.72) for a frequency of 225 kHz; complementarily, the fit for α_P(150 kHz) and α_P(300 kHz) were also computed (to be consistent with the frequency range [150 – 300] kHz of the experimental seismic data) but the difference between the three curves is so small that only one is shown in fig. 5.3 (a). We conclude from fig. 5.3 (a) that the experimentally observed seismic attenuation agrees remarkably with Biot's predictions for 3D wave propagation.

Seeking to convey an idea about the frequency content of the displacement field u_{y-exp}, fig. 5.3 (b) shows the evolution of the first arrival peak frequency (f_{peak}) with increasing offset; in dark blue it was estimated from the magnitude spectra obtained with a fast Fourier transform (FFT) of a 0.011 ms window, whose first point is the FB so it contains the first arrival, and in orange it was computed supposing the first arrival has a sinusoidal shape such that the dominant frequency is the inverse of the maximum-to-minimum lag multiplied by two (i.e., the lag corresponds to the half-period). No matter how it is calculated, f_{peak} increases with offset, which is an uncommon behaviour that will, henceforth, be attributed to P-wave interference.

Examining the acquisition geometry of the present dataset, one can analytically confirm the increase in f_{peak} with offset; to do so we calculated the expected travel times of the first arrival, considering waves coming from three point sources equally spaced along the y-axis to simulate the top, middle and bottom of the PZT. The results are shown in fig. 5.4, superimposing a close-up of the experimental data. It is straightforward to conclude, from fig. 5.4, that the large dimension of the PZT generates hyperbolic seismic contributions (green and pink lines) that progressively merge (as a function of offset) with the direct wave propagating at the top of the sand (dark blue line). This gradual merging *vs* offsets due to wave interferences explains why f_{peak} increases, as indicated by fig. 5.3 (b).

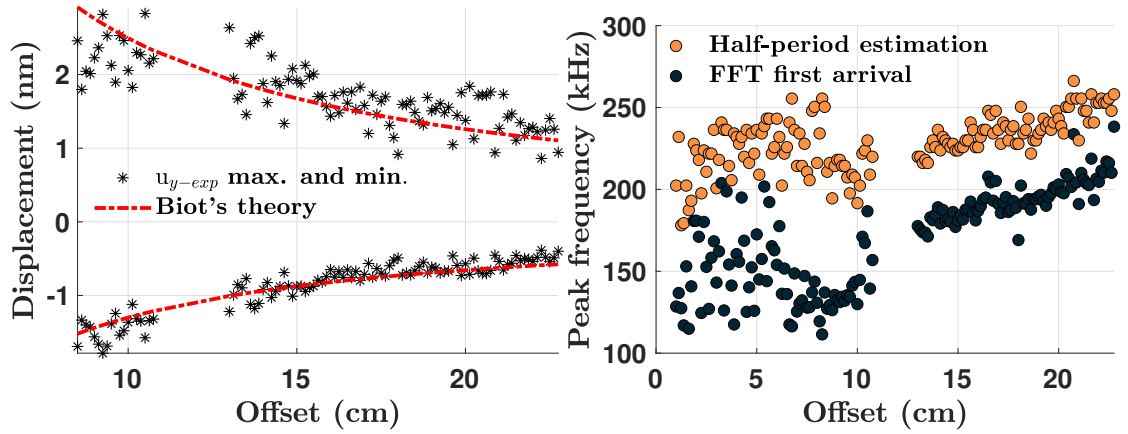

Figure 5.3: (a) Maxima and minima (stars) of the displacement u_{y-exp}, measured in the direct P-wave (first arrival), *vs* offset. In red dashed lines, theoretical fits based on the decay predicted by Biot's theory, with $0.25e^{-7.5\mathrm{E}-3\cdot r}\cdot r^1$ used for the maxima, and $-0.13e^{-7.5\mathrm{E}-3\cdot r}\cdot r^1$ for the minima. (b) Peak frequency f_{peak} of the first arrival *vs* offsets: in orange it was calculated from the maxima and minima, and in dark blue from the fast Fourier transform.

While this large source effect explains the behavior of f_{peak} vs. offsets, it raises questions about its influence on the amplitudes once (constructive/destructive) wave interference usually changes amplitudes. Nevertheless, because our analysis of the attenuation in fig. 5.3 (a) only accounted for offsets larger than 8.5 cm, where the merge between waves is almost complete, our comparison with Biot's theory is not affected by these wave interferences.

Electric measurements

The electrogram of absolute potentials V_{exp} measured using buried electrodes in the sand, as described in section 5.4.4, is displayed in fig. 5.5. As expected for a homogeneous medium, there is a main coseismic phenomenon of electromagnetic nature that has the same velocity v_P as the seismic P-wave. The FB of the direct coseismic and the reflections in the back and front of the box are underlined in fig. 5.5. The outstanding event near $t = 0$ is an EM noise intrinsic to PZT sources, and the synchronous events around 0.05 and 0.12 ms are electric acquisition artefacts, certainly due to discontinuities in the porous medium created by the presence of the electrode comb. Filtering and static corrections applied to create this electrogram are the same used in the seismogram shown in fig. 5.2.

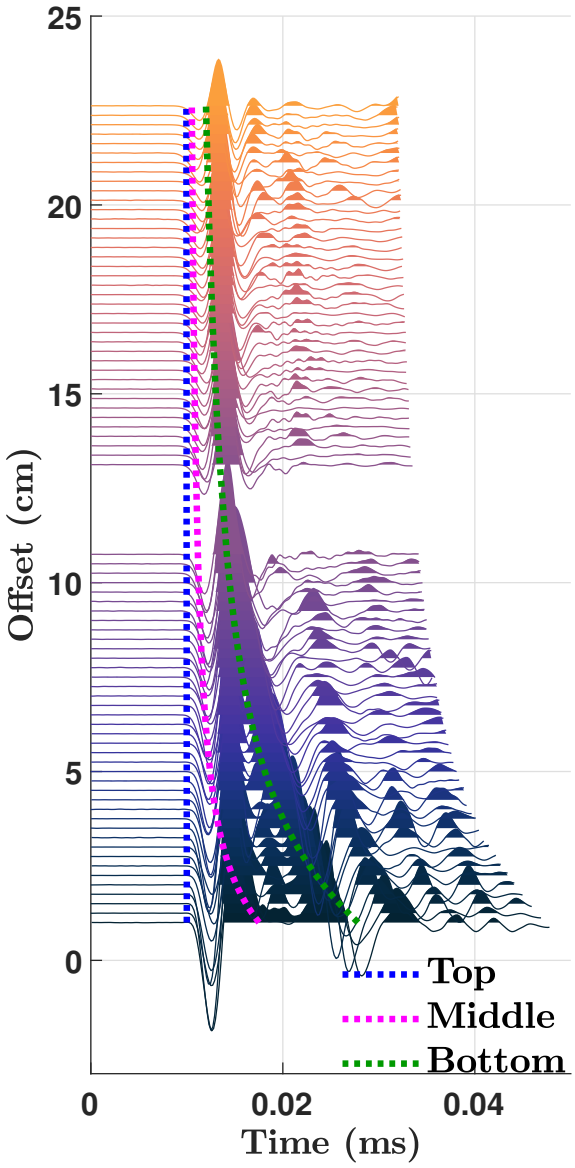

Figure 5.4: Seismic traces u_{y-exp} coming from a close-up of fig. 5.2 for times between 0 and 150 μs. The first-time arrivals, analytically computed, considering waves arriving from three point sources distributed along the y-axis and corresponding to top, bottom and middle of the PZT are respectively represented in blue, magenta and green dashed lines.

A comparison between the electrogram V_{exp} and the seismogram u_{y-exp} (fig. 5.2) raises a question about missing events, once in fig. 5.5 only the direct wave and the reflections on the front and back walls are evident. The seismic fields created by the PZT concentrate most of their energy right in front of the source such that, due to the acquisition geometry of the electrical experiment, z-oriented coseismic fields will contribute the most to the measured absolute potentials. Conversely, P-waves reflected at the box's laterals and bottom, as well as at the sand-air interface, will have most of their energy either on the y or the x-components when they arrive at the electrodes, with less significant z-components. However, by symmetry, these reflected wavefields will interact destructively, since the electrodes are in the centre of the box. Consequently, the respective reflected coseismic wavefields will also be attenuated, what may partially explain the absence of some events in the electrogram of fig. 5.5.

We look now at the decay of coseismic amplitudes based on the first minima and maxima of the first event, like for the seismic data. These extrema are plotted *vs* offset in fig. 5.6 (a) and their trend studied with a curve fit (dashed lines), like the approach used for the seismic maxima and minima (see fig 5.3 (a)), with the same attenuation factor α_P as before, and with r the z-offset of each measurement electrode. The fits in fig. 5.6 (a) indicate that the geometrical spreading plays no role since the data trend is correctly reproduced in the absence of a factor (r^{-1}). This means the coseismic signal has an apparent 1D propagation, as a consequence of using a long electrode positioned at the centre of the box, which integrates the data along the vertical direction (y-axis).

Peak frequency for the absolute potential data f_{peak} is plotted against offset in fig. 5.6 (b); like for the seismic case it is computed with two approaches. The f_{peak} estimated with the minima-maxima methodology, orange dots in fig. 5.6 (b), display an almost constant trend, with values varying mainly in the range [200, 230] kHz. For f_{peak} estimated with a FFT (dark blue dots), the values increase until 5 cm and afterwards reach a plateau, with values around 180 kHz; this increase in frequency is probably due to wave interference at offsets smaller than 5 cm, as well as the influence of the PZT noise. At last, the fact that for offsets greater than 5 cm the value of f_{peak} is practically constant, implies that dispersive phenomena and wave interference due to the large PZT source do not have a big impact on seismoelectric wavefields at the scale of the experimental sandbox, possibly due to a combination of using a long electrode and measuring close enough to the source.

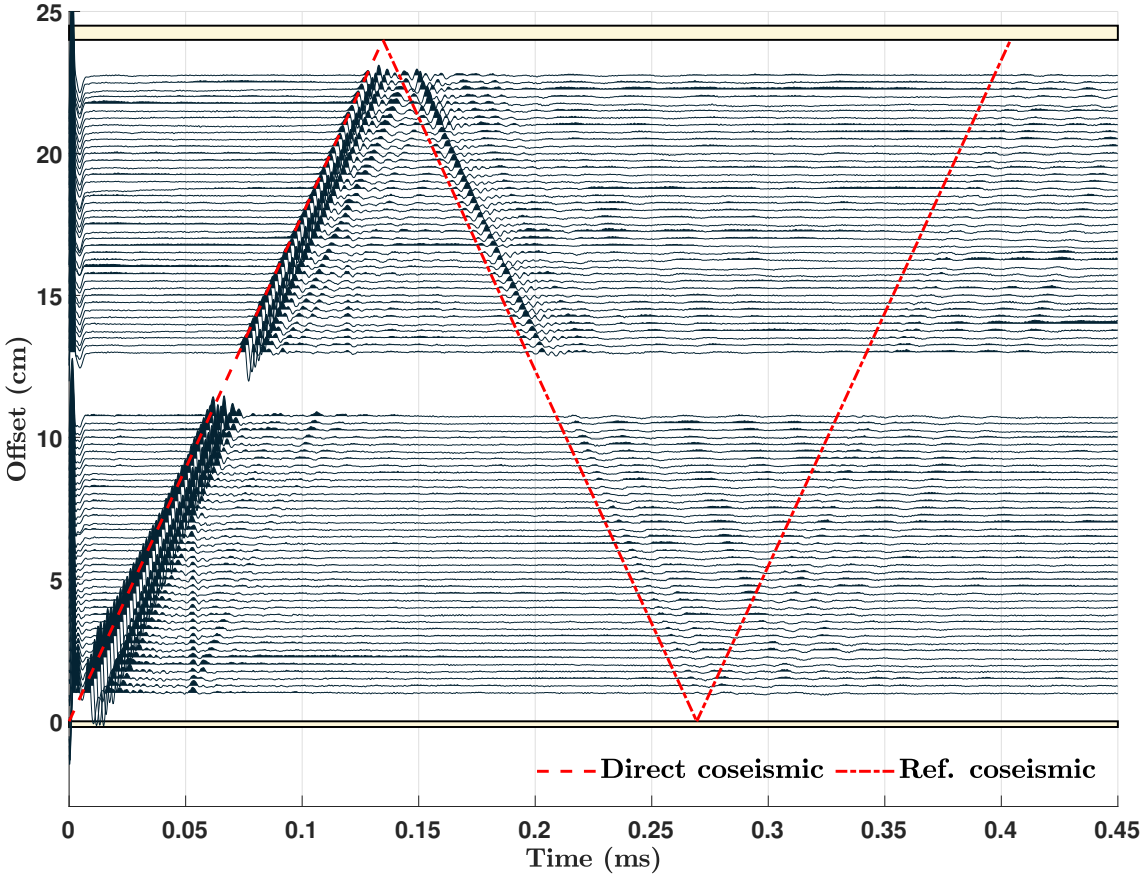

Figure 5.5: Absolute potentials V_{exp} as a function of time and offsets for the 80 electrode locations. The measurements are performed in a line oriented along the z-axis. Front and back walls of the plastic box are depicted for convenience. For clarity, the direct coseismic and the reflections at the back and front of the plastic box are pointed.

5.6.2 Comparison between experiments and theory

Transfer function TF analysis

The first step to compare experiments with theory is to estimate transfer functions TF (Eqs. 5.1) (Pride and Haartsen, 1996) from the laboratory data. For that, the experimental z-oriented electric field E_{z-exp} was estimated from the absolute potentials V_{exp} using the static approximation: $\mathbf{E} = -\nabla V$ (i.e., electric fields are steady in time). Holzhauer et al. (2017) experimentally demonstrates that for an accurate estimative of the electric field using this approximation, the electrode spacing should be smaller or equal to $\lambda/5$, where λ is the P-wave wavelength. In the present case, if we consider the centre-to-centre distance between electrodes (i.e., 0.25 cm), the present set-up will not satisfy this optimal spacing, since $\lambda \simeq 0.8 - 1$ cm. However, if

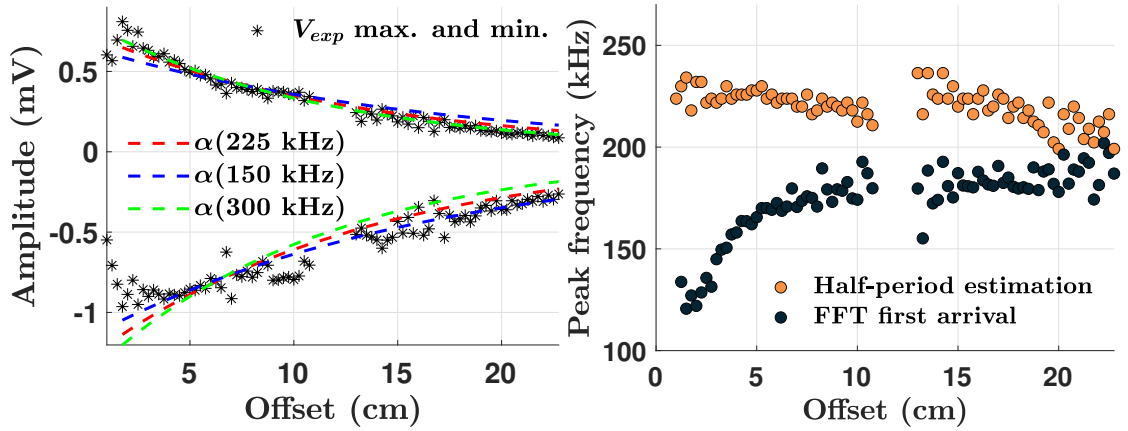

(a) (b)

Figure 5.6: (a) Maxima and minima (stars) of the electric absolute potential V_{exp}, measured in the direct P-wave (first arrival), *vs* offset. Red, blue and green dashed lines, correspond to the fits based on the decay predicted by Biot's theory for three different frequencies, repectively: 225, 150 and 300 kHz. For 225 kHz $0.25e^{-7.5\text{E}-3 \cdot r} \cdot r^1$ was the equation fitted to the maxima, and $-0.13e^{-7.5\text{E}-3 \cdot r} \cdot r^1$ to the minima. (b) Peak frequency f_{peak} of the first coseismic arrival *vs* offsets: in orange it was calculated from the maxima and minima, and in dark blue from the fast Fourier transform.

the effective spacing (i.e., 0.15 cm), that accounts for the 0.1 cm electrode diameter, is considered, this criteria on the spacing will be satisfied for most frequencies in the frequency band of the experimental data ($f \leq 250$ kHz).

Regarding how to calculate TF, the most straightforward way uses the first maxima and minima (of the first arrival) of the experimental electric field and particle displacement (seismic), thus it considers that the magnitude spectra of both seismoelectric fields overlap, or in other words that f_{peak} is the same for the electric and the mechanical wavefields selected for the comparison. In Bordes et al. (2015) this strategy is referred as "static appoach", therefore hereinafter this terminology will also be used. Another possibility to get TF is through a "dynamic approach" which consists in the analysis of the ratio of the magnitude spectra (first arrivals only) of both wavefields.

The choice of which version of the TF (see eq. 5.1) to use ($\mathbf{E/u}$, $\mathbf{E/\dot{u}}$, or $\mathbf{E/\ddot{u}}$) is of primary importance, although in theory equivalent. While the TF is generally calculated using the acceleration (Garambois and Dietrich, 2001; Bordes et al., 2015; Holzhauer et al., 2017) due to the (approximate) frequency-independency of $\mathbf{E/\ddot{u}}$ at frequencies lower than the transition frequency f_t (defined in eq. 2.46), the effective

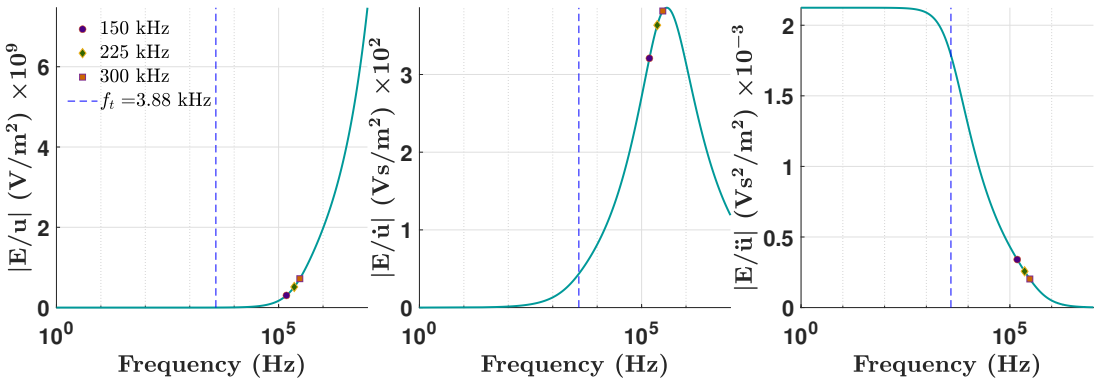

(a) (b) (c)

Figure 5.7: Values of the TF *vs* frequency obtained from the analytical solution of Pride's equations (see eq. 5.1) using parameters in table 5.1. (a) considers the displacement $\mathbf{u}$, (b) the velocity $\dot{\mathbf{u}}$, and (c) the acceleration $\ddot{\mathbf{u}}$. The TF values for three frequencies inside the frequency-band of the experimental data are shown with colored symbols. For convenience, the blue dashed vertical line indicates the value of the transition frequency f_t (see eq. 2.46).

frequency band of the data in this study is about two orders of magnitude higher than the value of $f_t \simeq 3.88$ kHz (using parameters in table 5.1). Therefore, the choice of which variation of the TF is more suited to the present dataset depends upon the analytical solution of Pride's transfer functions (Fig. 5.7) and on the comparison between the first arrivals' waveforms of E_{z-exp} and u_{y-exp} (fig. 5.8).

Looking at fig. 5.7, it can be seen that none of the versions of the TF plateau in the range of frequencies of interest, yet a maximum exists in $\mathbf{E}/\dot{\mathbf{u}}$ such that values vary significantly less than they do, for the same frequency range, in the other two version of the TF. Therefore, theoretically, one can expect to see more similarity when comparing $\mathbf{E}$ waveforms with $\dot{\mathbf{u}}$ than with $\mathbf{u}$ or $\ddot{\mathbf{u}}$.

Qualitatively, from fig. 5.8, where the experimental z-oriented electric field E_{z-exp} is compared with the y-oriented displacement u_{y-exp}, velocity $\dot{u}_{y-exp}$, and acceleration $\ddot{u}_{y-exp}$ at nine offsets, one can directly conclude that the velocity waveform is the most similar to the electric field one, even though different components of vectorial fields are compared; this observation complementarily supports the previous discussion concerning fig. 5.7. As a consequence, in what follows comparisons between experiments and theory will consider preferentially the velocity wavefield.

Finally, the values of $E_{z-exp}/\dot{u}_{y-exp}$ using both the static and the dynamic approaches are displayed in fig. 5.9. In both cases, the values of TF have the same range, roughly [50 – 300] Vs/m^2, moreover they are hardly distinguishable for differ-

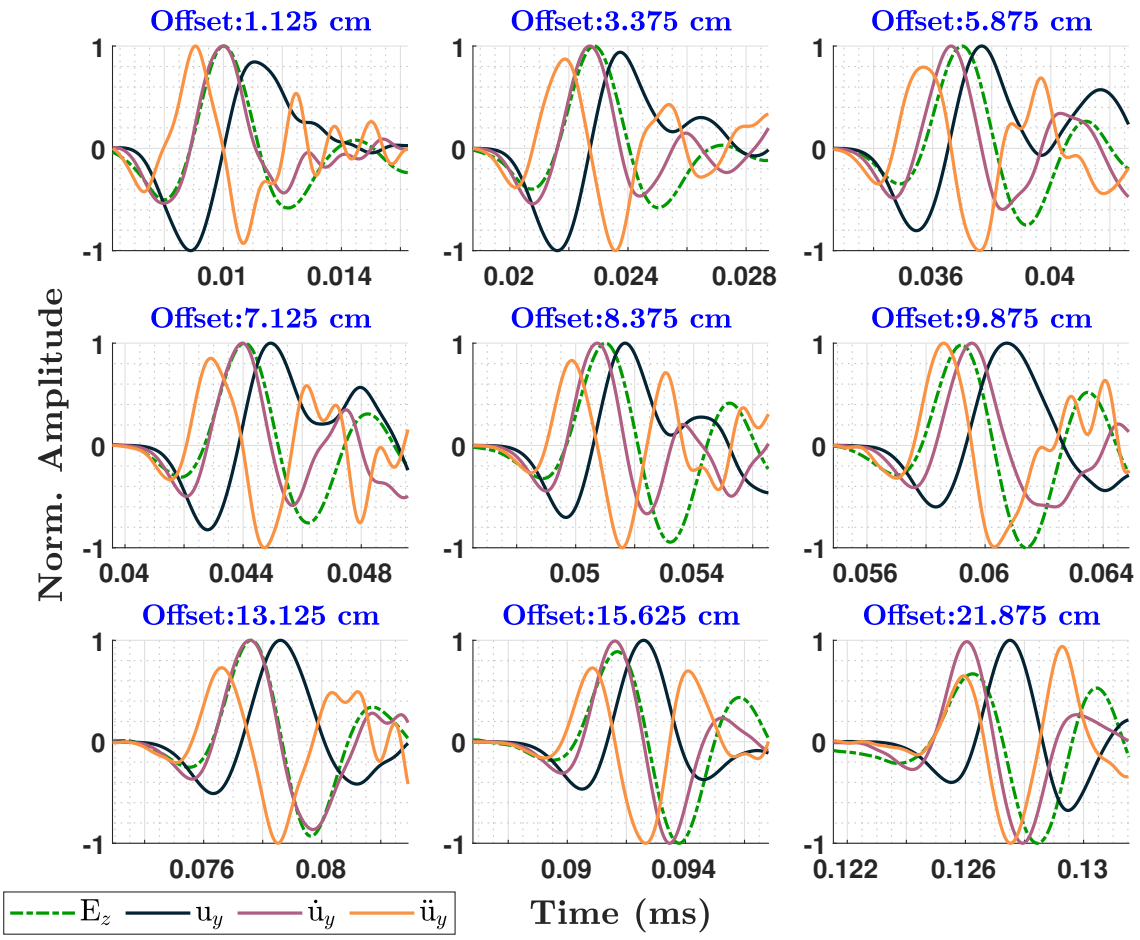

Figure 5.8: Comparison of experimental waveforms of u_{y-exp} (dark line), $\dot{u}_{y-exp}$ (pink line), $\ddot{u}_{y-exp}$ (orange line) and E_{z-exp} (dashed green line) at 9 distinct offsets. Amplitudes are normalized to allow the superimposition of waveforms.

ent frequencies in the dynamical case (fig. 5.9 (b)). In general, values are reasonably close to theoretical predictions (fig. 5.7 (c)), which spans the interval [320 – 380] Vs/m^2, thus experiments and theory, using the parameters in table 5.1, are in good agreement. In cartesian coordinates, eq. 5.1 evidently relates collinear components of the seismoelectric fields (Garambois and Dietrich, 2001), and it is fair to assume that, in the experiments, the z-component of both seismic and electric wavefields contains more energy than the other cartesian components during wave propagation. Consequently, the relative mismatch between the theoretically predicted and the experimental TF values may be attributed to the fact we are actually comparing z and y-components (E_{z-exp} and a u_{y-exp}, respectively), instead of only z-components. Finally, to provide a more meticulous comparison between seismic and electric fields, we will resort to the results of numerical simulations.

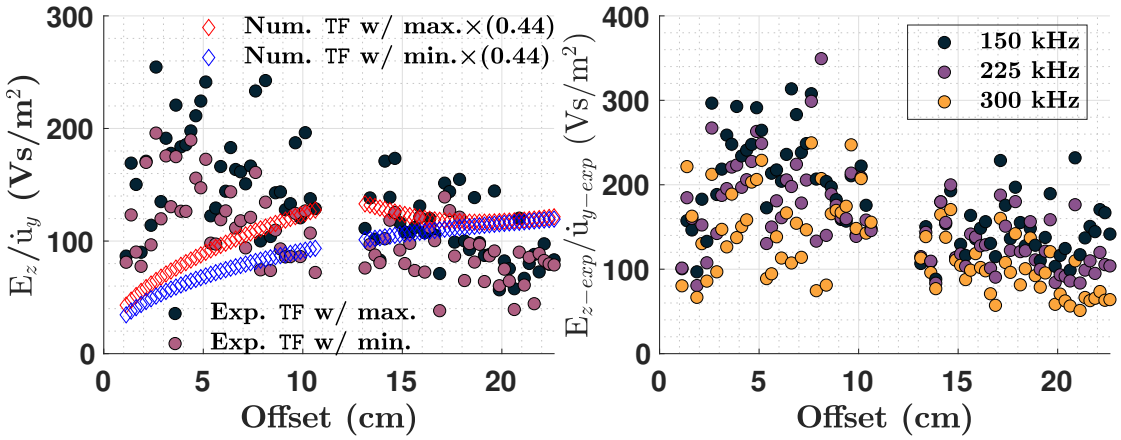

(a) (b)

Figure 5.9: Ratio between the electric field E_z and the velocity $\dot{u}_y$ (i.e., eq. 5.1) *vs* offset. (a) shows a comparison of the TF obtained from synthetic (accounting for the factor 0.44) and experimental data using a static, frequency independent approach based on the maxima and minima of the temporal data. (b) uses a spectral approach (FFT of the isolated first seismic and coseismic arrival) to estimate the TF values from the experimental data for three specific frequencies, respectively 150, 200 and 300 kHz.

Numerical modelling

To complement the discussion in the previous section, the results from the numerical simulation of the experiments, performed with the code discussed in section 5.5, will now be presented. Both amplitudes and waveforms of the velocity and the electric potential wavefields from experiments will be compared with what Pride's theory numerically predicts for the input parameters in table 5.1, considering the fluid conductivity $\sigma_f = 13.1$ mS/m.

Fig. 5.10 presents the comparison between the first minima and maxima amplitudes of the experiments and simulations for the velocity field $\dot{u}_y$ and for the electric potential V; note that the numerical calculations used eqs. 5.5 and 5.7 to account for the large seismic source and for the long buried electrode. Focusing on $\dot{u}_y$, as in 5.6.1, only offsets higher or equal to 8.5 cm were considered in the comparison and it turns out that there is an excellent correpondance between numerical and experimental data. Regarding the absolute electric potential V, the trend of maxima and minima is again quite similar for offsets bigger than 8 cm, where near-field effects and/or interference between waves close to the source can be avoided. It is important to specify, however, that the amplitudes of the simulated wavefields were adjusted seeking a correspondence for the seismic data, what led to slightly

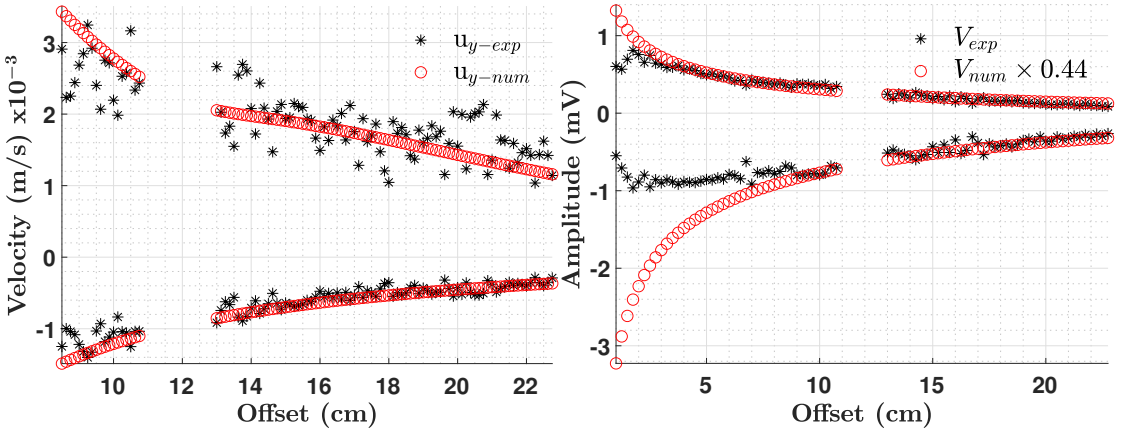

Figure 5.10: Comparison of maxima and minima between numerics (red circles) and experiments (black asterisks) for $\dot{u}_y$ (a) and V (b). Note that the amplitudes of the numerical electric potential was multiplied by a factor 0.44.

over-predicted V_{num} and E_{z-num} fields. Because of that the amplitudes of V_{num} in fig. 5.10 (b) were multiplied by a factor of 0.44 to arrive at a good superposition of both curves.

Based on the previous discussion about amplitudes, the TF ($E_z/\dot{u}_y$) obtained using maxima and minima, for both experimental and numerical data, is presented in fig. 5.9 (a). Again, using the factor 0.44 as an amplitude correction of the numerically obtained E_z, results from modelling fall within the expected range of experimental values, thus confirming that, in terms of amplitudes, Pride's theory provides a reasonable solution.

We proceed now with a quantitative comparison of experimental and simulated seismograms ($\dot{u}_y$) and electrograms (V) in figs. 5.11 and 5.12, respectively. In order to emphasize the overall excellent agreement between experiments and simulations, we show a close-up of four specific traces.

Observing more closely the seismic (velocity) section in fig. 5.11, it can be seen that the simulated traces nicely represent the first arrival of the experimental records in terms of waveform and frequency content. However, because none of the sandbox's walls (where reflections occur) are considered in the modelling, events subsequent to the first arrival in the seismogram of fig. 5.11 are not comparable to the simulation.

Coming now to the V electrogram in fig. 5.12, at least for the first half period, it shows an outstanding match of numerical and experimental first arrivals when the correction factor 0.44 is taken into account. On the second half period,

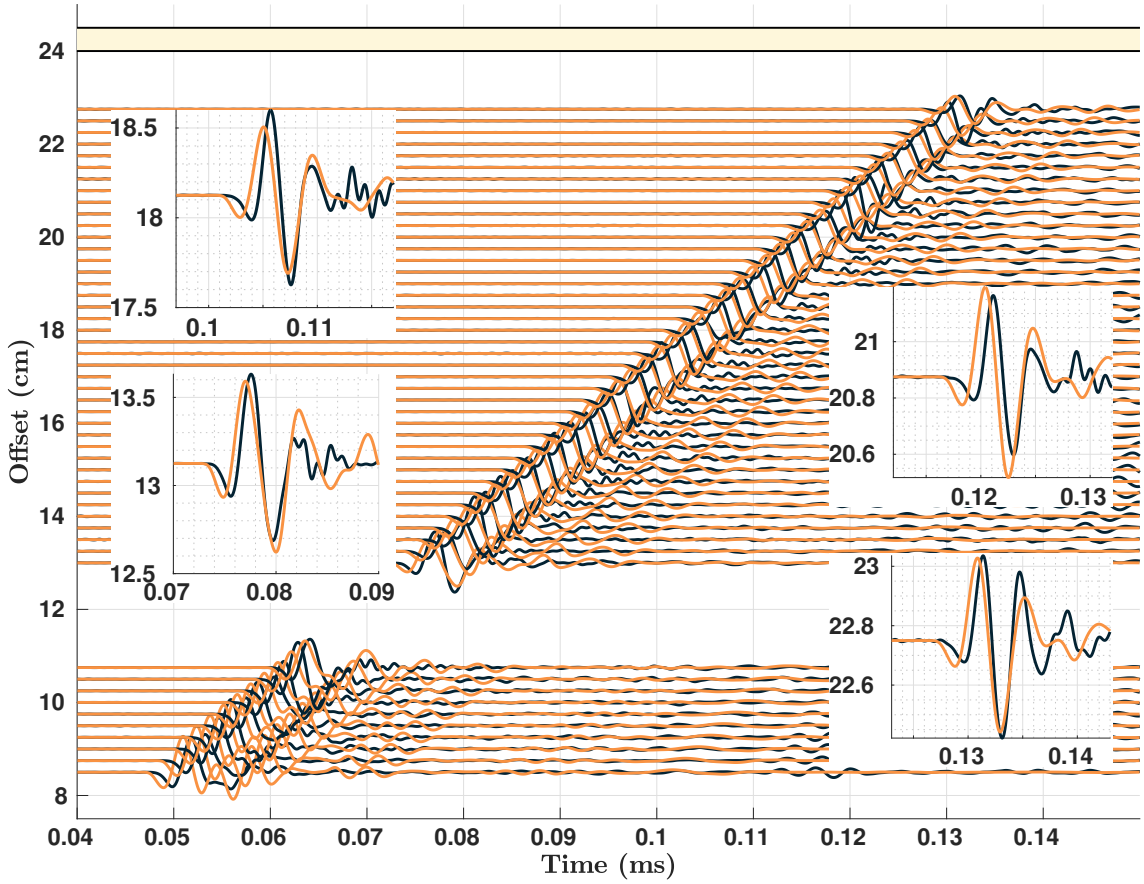

Figure 5.11: Comparison between the experimental velocity records $\dot{u}_{y-exp}$ (dark blue) and the numerical ones $\dot{u}_{y-num}$ (orange) *vs* time and offsets. The first arrival of some seismic traces are highlighted in sub-figures to demonstrate the excellent match between both datasets.

however, some mismatch appear between waveforms at some offsets but the overall comparison remains remarkably good. Although the agreement between measured and simulated V is satisfactory, it is however important to stress that the diameter of the buried electrodes, about 1 mm and close to the receiver spacing, was not accounted in the simulation; considering the possible role of the electrode diameter on the measurement of the electric potential would certainly improve the results.

Finally, the discussion above supports that Pride's equations and, consequently, the numerical tool employed, comprising the changes proposed to compute E_z and V, are able to describe the laboratory experiment not only qualitatively, as demonstrated in a similar manner by Devi et al. (2018), but also quantitatively in the case of a homogeneous medium i.e., for mechanical and coseismic wavefields. Seek-

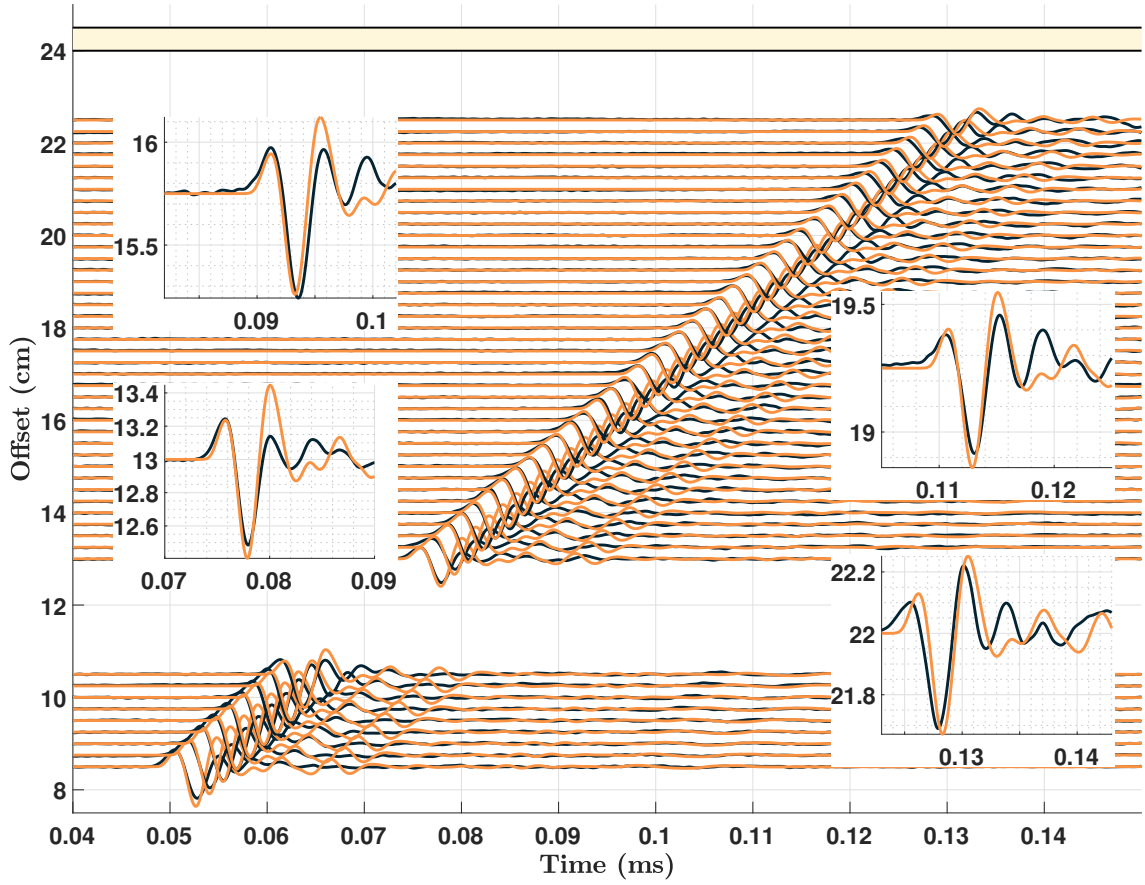

Figure 5.12: Comparison between the experimental absolute potential records V_{exp} (dark blue) and the simulated ones V_{num} (orange) *vs* time and offsets. The first arrival of some electric traces are highlighted in sub-figures to demonstrate the excellent match between both data-sets, and V_{num} was multiplied by 0.44.

ing completeness, the next section proceeds with the discussion about the EM-wave generated at the interface of a thin layer.

5.7 Seismoelectrics in a layered medium

To study the seismoelectric signal generated at an interface between two porous media, a layered medium was designed by inserting a 0.74 cm thick sandstone layer in the middle of the sandbox, around z = 11.88 cm. Table 5.1 lists the physical properties of the sandstone used, and the P-wave velocity was experimentally estimated as $v_P = 2200$ m/s, slightly higher than the velocity obtained for the saturated sand. Like in the homogeneous case, both seismic and electric acquisitions employ the geometry displayed in fig. 4.1. Static corrections are again performed in the seismic and electric sections, and both datasets were low-passed using a cut-off frequency of 1 MHz, as in the previous case.

5.7.1 Experimental data

Seismic measurements

Experimental measurements of the displacement u_{y-exp} compose the seismogram in fig. 5.13. As expected, the main events are similar to the homogeneous case (fig. 5.2), except for the P-wave reflections in the sandstone layer (highlighted with the magenta line).

Fig. 5.14 (a) shows the difference between the FBs (picked in the raw data) of both studied cases. At short offsets, before the layer (left side in fig. 5.14), differences range around 0 and at offsets on the other side of the layer, the difference has a mean value of about 1μs, as a consequence of the higher P-wave velocity in the sandstone. The dispersion of the values in fig. 5.14 is related to the precision of the measurements, as well as possible uncertainties in the picking.

In order to compare even further the homogeneous and the layered situations, amplitudes of the minima and maxima of the first P-wave arrivals are superimposed in fig. 5.14 (b). While they are in the same range and show the same trend, there is no apparent effect due to the layer, as a matter of fact at shorter offsets (before the layer) amplitudes are slightly higher when the layer is present. The reason for this difference lies in the fact the medium's physical parameters (like saturation and/or bulk and shear moduli) are not strictly identical during both acquisitions thus changing amplitudes between experiments by a small factor.

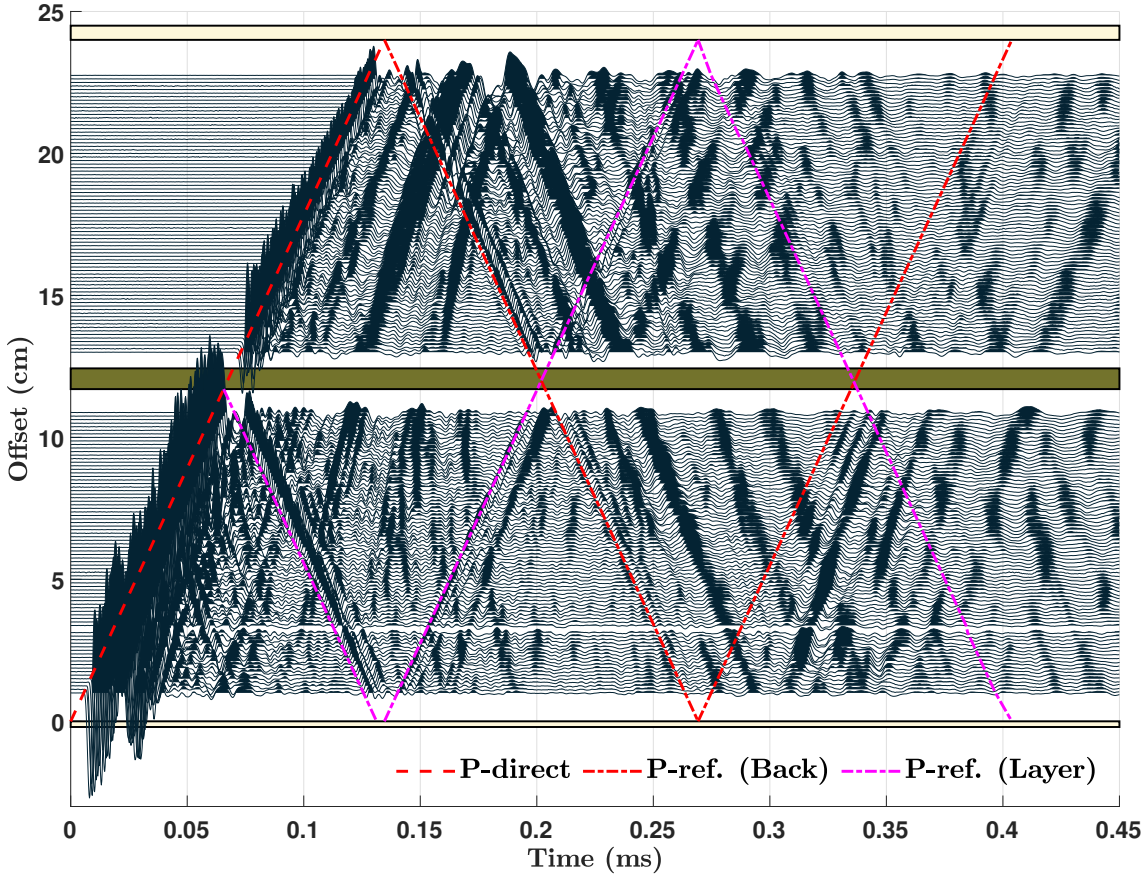

Figure 5.13: Measured displacement u_{y-exp} as a function of time and offset for an experiment performed with a sandstone layer inserted in the sand, at mid-length of the sandbox. The direct P-wave, reflections on the front and back wall of the plastic box, and on the sandstone layer are highlighted. Box's walls and the layer are shown for convenience.

Electric measurements

The electric potential section, after filtering and static corrections, is displayed in fig. 5.15 with its most significant events highlighted. It is remarkably similar to the seismoelectrogram in fig. 5.5, apart from the presence of two new signals that exist because of the layer: the coseismic created by the P-wave reflection on the layer (magenta) and the EM-wave (green line) emerging from the interface. From here onwards the term interface response or EM interfacial wave will be used to refer to the event pointed by the green line in fig. 5.15.

In fig. 5.16 (a) maxima and minima of the first coseismic arrival are compared with those of the homogeneous experiment, shown in fig. 5.5. There is a good coherency in values for traces before the sandstone layer while, as expected, the

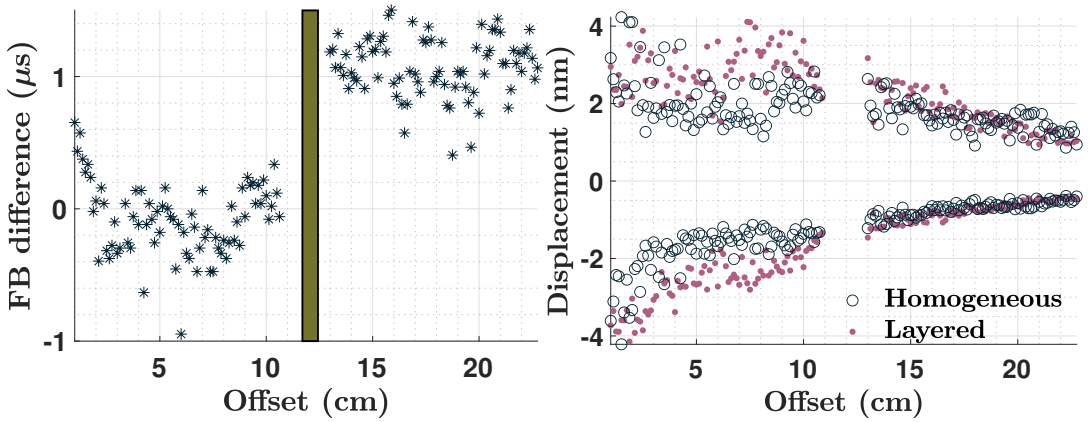

Figure 5.14: Comparison of the homogeneous and layered experiments in terms of the measured seismic displacement u_{y-exp}. (a) shows the difference between FB picks (from raw data) *vs* offsets, and (b) the maxima and minima of both datasets *vs* offsets.

amplitudes after the sandstone layer are relatively smaller, due to a loss of energy while the seismic wave travels through the sandstone.

Focusing now on the event associated with the EM interfacial wave V_{exp-EM}, indicated by the green dashed line in fig. 5.15, fig. 5.16 (b) displays its absolute maxima *vs* offsets. In this case it is more convenient to analyse the absolute extrema of this EM signal instead of maxima and minima, since at offsets shorter than the layer position the waveform of this EM event is rather altered by interferences with the coseismic wavefield. For this same reason, the amplitudes of the six closest traces to the layer (cyan-colored points in fig. 5.16 (b)), three at each side, are strongly affected by the coseismic signal. The most noticeable feature of the V_{exp-EM} amplitudes in fig. 5.16 (b) is the change in sign with respect to the layer, indicating that the EM wave has an opposed polarity on both side of the layer, a known feature already reported in the literature (Dupuis et al., 2009; Schakel et al., 2011b; Peng et al., 2017; Liu et al., 2018).

Another important characteristic of the data in fig. 5.16 (b) is the decay rate of the V_{exp-EM} amplitudes *vs* offset; it is clearly different on each side of the layer. Like in the homogeneous experiment, we perform a curve fit of the data considering the intrinsic attenuation of the EM wave $\alpha_{EM}(225\,\text{kHz})$ = -2.9E-4 m^{-1} predicted by Pride's theory (eq. 2.72) using the sand parameters in table 5.1. The curves fitted to the data in fig. 5.16 (b) suggest that the EM-wave has a slower decay, with a $r^{-0.5}$ dependence, before the layer than after, where it decays with r^{-1}. This

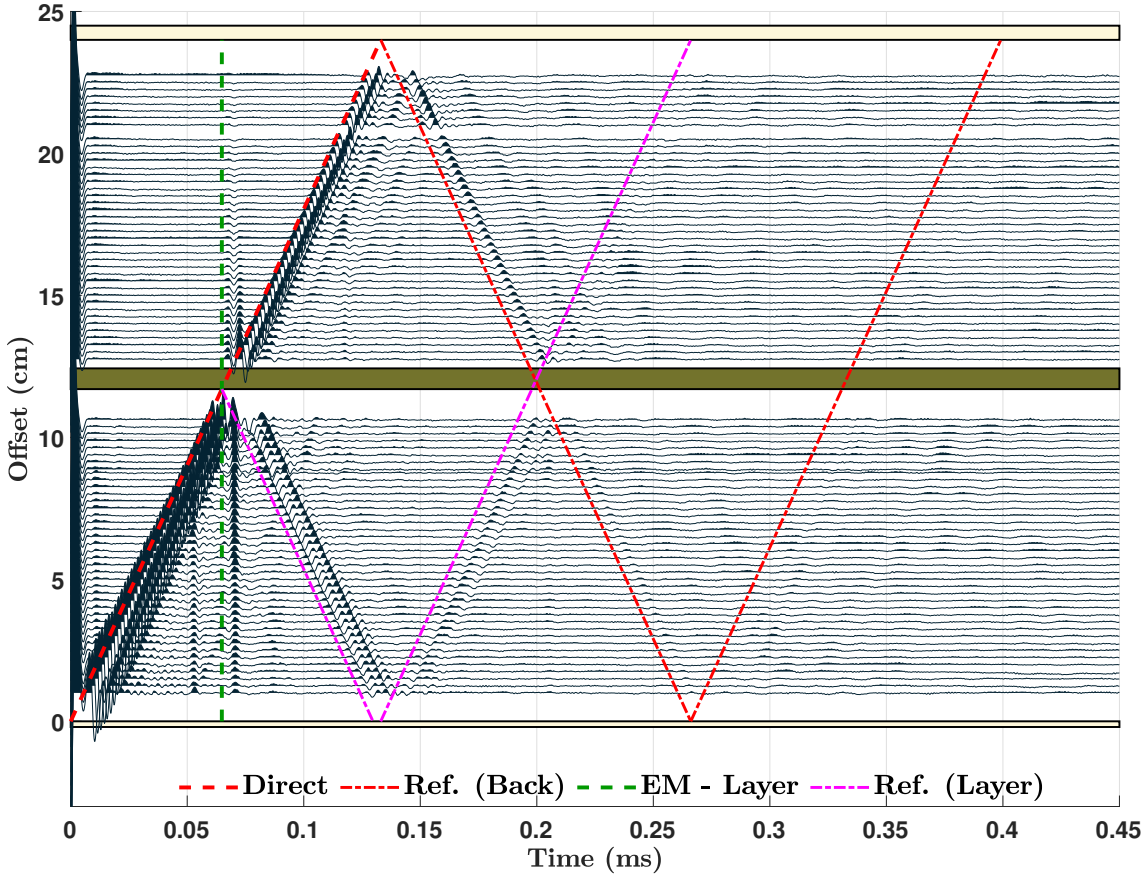

Figure 5.15: Absolute electric potential V_{exp} as a function of time and offset during an experiment performed with a sandstone layer inserted in the sand. The direct coseismic wave, reflections on the front and back wall of the plastic box, and on the sandstone layer are highlighted. An EM event linked to the layer (green dashed line) is also pointed. Box's walls and the layer are shown for convenience.

difference in decay is easy to notice in fig. 5.15 and it may, again, be explained by constructive and destructive wave interference: in the first half of the electric section, corresponding to electrodes before the layer, at the same time that V_{exp-EM} is recorded coseismic waves are actively interacting with the electrodes whereas after the layer the EM wave reaches synchronously the electrodes before any coseismic field.

At last, fig. 5.17 (a) shows a close-up of the measured EM interfacial signal V_{exp-EM}, highlighting its regularity and decay over offsets 13–17.75 cm. Fig. 5.17 (b) shows the peak-frequency of the waveforms in fig. 5.17 (a); one can see that the f_{peak} values (obtained either by the half-period approximation or by the FFT

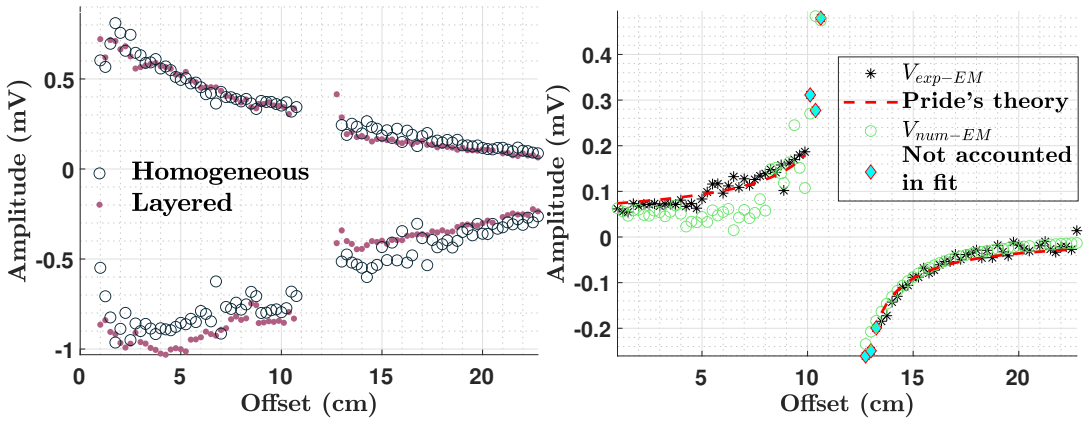

Figure 5.16: Amplitude analysis of the seismoelectric absolute potential V_{exp} data acquired during the experiment with a sandstone (fig. 5.15). (a) Comparison between the homogeneous (empty circles) and the layered (filled circles) cases in terms of the direct coseismic wave maxima and minima. (b) Absolute maxima of the EM interfacial wave V_{exp-EM} (stars) *vs* offsets; the closest points to the layer, highlighted in cyan, were not taken into account in the curve fit based on Pride's theory (dashed red lines). In the left side, the equation fitted was $0.25e^{-2.9\mathrm{E}-4\cdot r} \cdot r^{-0.5}$ while in the right side $-0.33e^{-2.9\mathrm{E}-4\cdot r} \cdot r^{-1}$ was used. Also in (b), the absolute maxima of the numerical data V_{num-EM} is shown (green circles).

magnitude spectrum) are quite similar to those of the coseismic first arrivals (see fig. 5.6 (b)).

5.7.2 Numerical modelling

Like in the homogeneous case, we performed a full direct numerical simulation of the experiment with a sandstone layer, the physical parameters used are in table 5.1 and the fluid conductivity we considered is the same used in the homogeneous case, $\sigma_f = 13.1$ mS/m. Because the difference between both experiments is mainly due to the electromagnetic interface response, in what follows we will focus only on the analysis of absolute electric potentials and electric fields.

The absolute potential electrograms obtained from the experiment V_{exp} and from the simulation V_{num} are superimposed in fig. 5.18, where V_{num} was multiplied by the same 0.44 amplitude correction factor used in the homogeneous case. As it is the case for the coseismic wavefields, the waveform of the numerically modelled EM interfacial response corresponds remarkably well to the measurements. In general, it can be observed that the polarity, the decay rate, and the amplitudes of V_{exp-EM}

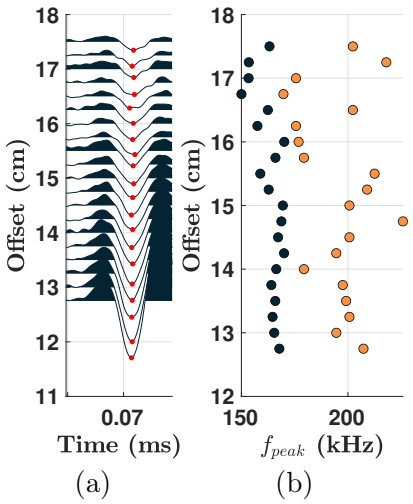

Figure 5.17: Focus on the EM interfacial wave. (a) Close-up of the electric potential V_{exp} records between offsets 13 and 17.75 cm. The red points are the maxima of the EM signal used in fig 5.16(b). (b) Peak frequency of the EM waveforms shown in (a), orange refers to frequency values estimated using the maxima and minima of the temporal data, and dark blue using the FFT spectra approach.

were fully retrieved by the direct numerical simulation in the upper half in fig. 5.18, where the EM wave is not strongly affected by coseismic waves.

An alternative choice to study the interface response, experimentally and numerically, is to analyse the vectorial electric field **E**. As mentioned in section 5.6.2, the experimental E_z can be obtained from the difference of the absolute potential measured by two neighbour electrodes. Accordingly, fig. 5.19 displays the complete electrograms of the experimental and computed E_z; from the trace superposition it becomes evident that, again, there is a striking agreement between experiments and simulations, for both the coseismic field and the EM interface response.

The most important information contained in the E_z electrogram, fig. 5.19, is that the amplitudes of the interface response, relative to the coseismic signal, are significantly smaller than what is observed with the absolute electric potential. This is an expected result, since the electric field is calculated as a difference of electric potentials of two adjacent traces, a procedure that strongly impacts any signal arriving simultaneously at all electrodes. Quantitively, while the EM response could be analysed until a distance of about 10 cm from the sandstone layer in the absolute potential measurements (fig. 5.18), it was barely observed at 1–2 cm away from the interface when looking at the electric field records in fig. 5.19. Eventually, it is straightforward to conclude that it is best to favor absolute electric potential

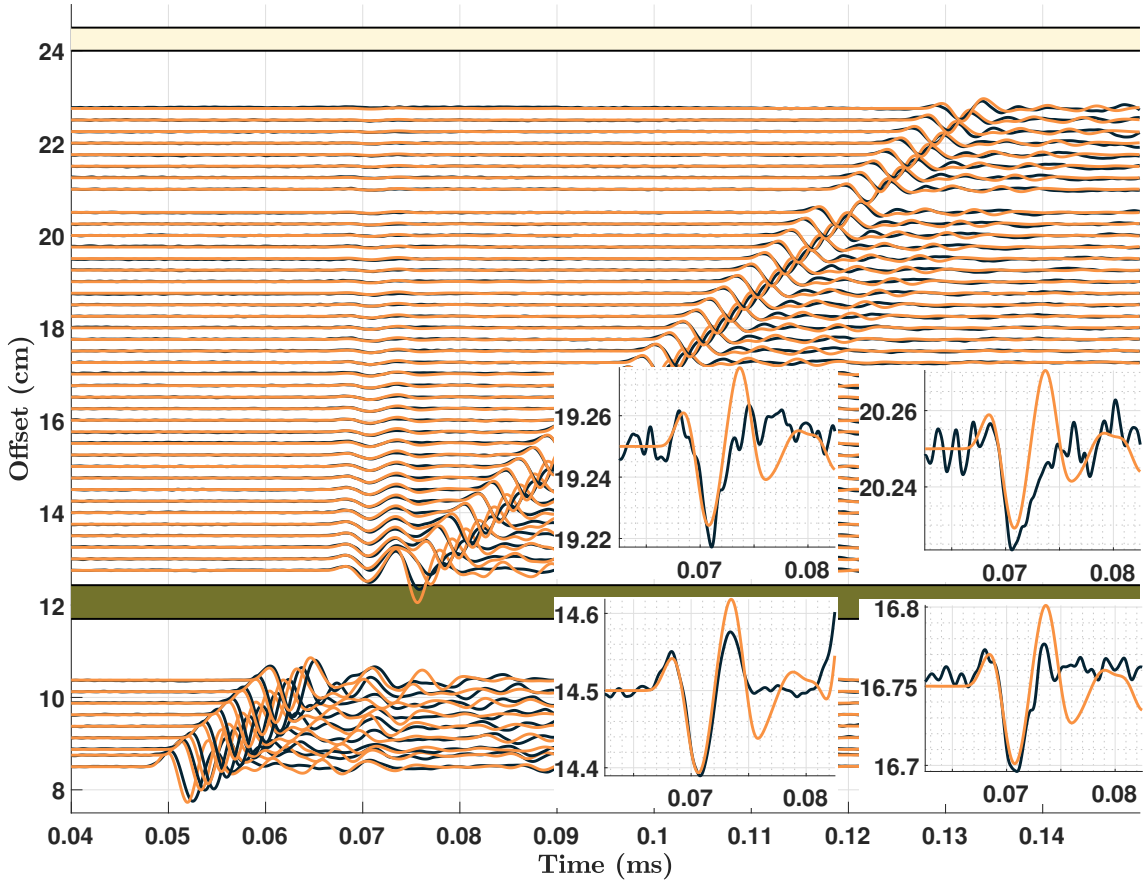

Figure 5.18: Absolute electric potential V section *vs* time and offset: comparison between experimental traces (dark blue) V_{exp} and modelled ones (orange) V_{num} using an amplitude correction factor of 0.44, like in fig. 5.12. 4 sub-figures show a close-up of the interface response at specific offsets.

measurements instead of electric field ones, when the goal is to study the interface response, as also mentioned in Dietrich et al. (2018).

In fig. 5.16, the maxima of the modelled interfacial response, obtained from the numerical electric potential V_{num-EM}, was plotted as a function of offset after properly multiplying it by 0.44. The comparison between V_{exp-EM} and V_{num-EM} amplitudes shows that, in the first half of the sandbox (offsets $<$ 13 cm), the co-seismic and the EM response interaction leads to a disagreement between the two data, certainly because the numerical code used is not able to model all the wave interference taking place at these offsets. However, on the other side of the layer, the agreement is excellent, as expected from the previous analysis of fig. 5.18.

During the numerical simulations we could conclude that by varying sand and sandstone molarities, always within the range shown in table 5.1, results do not

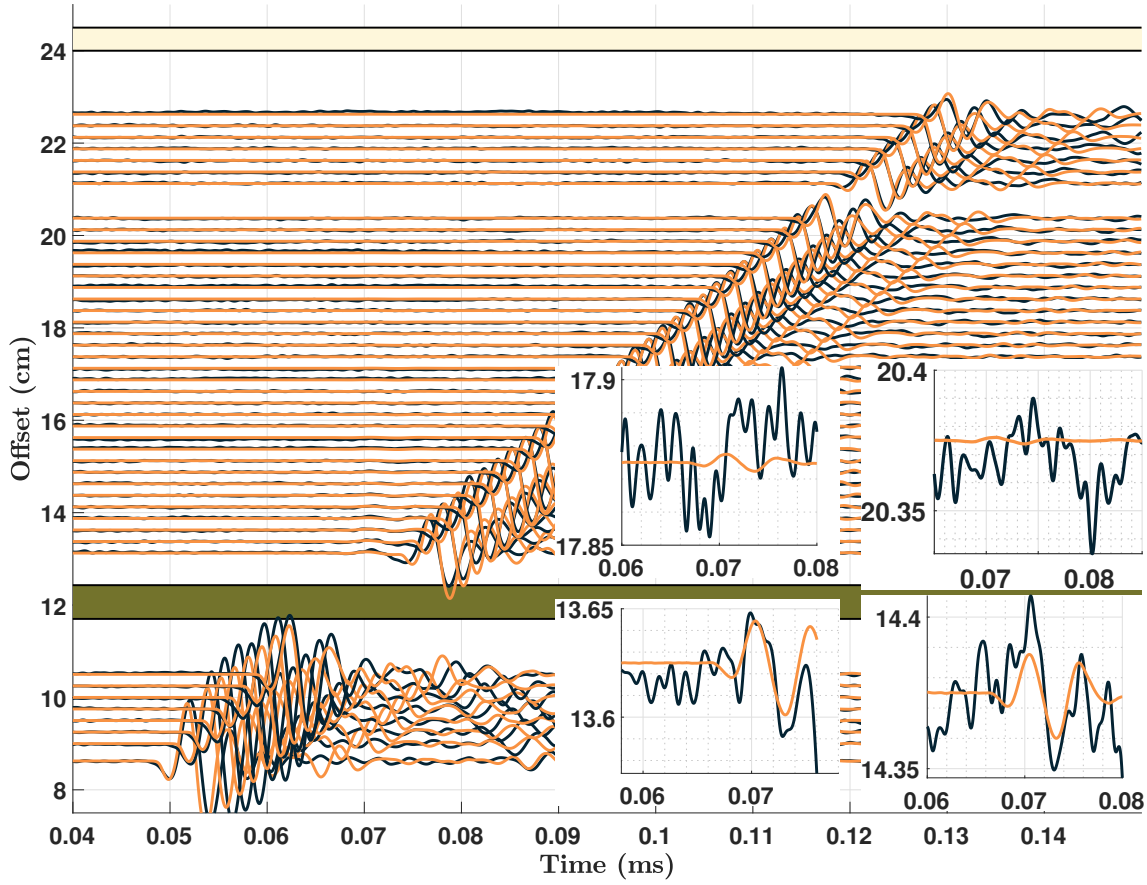

Figure 5.19: z-oriented electric field E_z data *vs* time and offset: comparison between experimental traces (dark blue) E_{z-exp} and modelled ones (orange) E_{z-num} multiplied by the factor 0.44. The 4 sub-figures show a close-up of the interface response at specific offsets.

significantly change from the ones presented here, even though this parameter is one of the most influential when it comes to the interface response (see Garambois and Dietrich, 2002). Ultimately, this good match indicates that the physical parameters used are relatively well constrained.

5.7.3 Interpreting the interface response

Seeking to understand both the physical phenomena that governs the generation of EM-waves at the sand-sandstone interface, and the physical factors controlling its intensity decay as a function of distance from the interface, we ran a new numerical modelling, using the same layered medium as in the previous simulation, but, for simplicity, with a single punctual seismic source placed at the origin of the coordinate system. Punctual receivers spread throughout the x-z plane, with z ranging

from 1 to 23 cm and x from -8 to 8 cm, measure the displacement $\mathbf{u}_{num}$ and the electric potential V_{num}. In this particular simulation, all P-to-EM conversions were amplified 1000 times (i.e., the respective reflection and transmission coefficients were artificially increased) in order to clearly distinguish the interface response from the coseismic signals.

We note that, because our goal is to analyse the EM interface response, whose wavelength (calculated using eq. 2.71 and the frequency-band of the V_{exp-EM} data) is about three orders of magnitude larger than the dimensions of the model used in the numerical simulations, both the PZT source and the electrode may be considered as a punctual. This argument supports the validity of the following comparisons between the present modelling an the experiments.

In fig. 5.20 we display four snapshots in time of the simulation. There are four columns for each selected time and they show, respectively, from left to right: the displacement $\mathrm{u}_{\mathrm{z}-num}$, the vertical electric field $\mathrm{E}_{\mathrm{z}-num}$, the absolute potential V_{num} and the potential measurements corresponding to a z-oriented line (in yellow) of receivers positioned in front of the seismic source. We will focus on what happens inside the sandstone layer, whose boundaries, representing the two sand-sandstone interfaces, are depicted in fig. 5.20 as the two horizontal green lines at z-offsets 11.88 cm and 12.62 cm, like in the experiments.

Regarding $\mathrm{u}_{\mathrm{z}-num}$ in the first column of fig. 5.20, we observe that the perfectly spherical P-wavefront (single source) evolves in time with no reflections on the sides, as a consequence of the numerical code used (Garambois and Dietrich, 2002); moreover it undergoes only minor changes through the interface, since P-wave velocities in the saturated sand and in the sandstone are relatively close. The seismic source's signature has a rather long duration, as a consequence of using the PZT signature shown in fig. 5.1 (a), with a secondary lower frequency pulse arriving about $50\mu s$ after the main pulse. These secondary impulses can be observed in all snapshots of fig. 5.20, near the origin of the coordinate system.

The four time values associated with the snapshots in fig. 5.20 were chosen such that the first one corresponds to the approximate arrival of the first trough of the P-wave at the sandstone, at offset 11.88 cm, and the second one is when the first crest touches the sandstone. Likewise, the third and fourth times are, respectively, concerned with the arrivals of the first trough and crest of the P-wave, but on the second sand-sandstone boundary, at offset 12.62 cm.

A remarkable feature in fig. 5.20, at time 67.97μs, is the fact that once the P-wave reaches the sandstone an immediate electric charge separation across the interface occurs (Pride and Haartsen, 1996), and that leads to an outstanding discontinuity in the absolute potential records. This charge imbalance can be readily noticed in the fourth column, where a dipolar-like structure exists. Moreover, the existence of a positive and a negative lobe in V_{num}, as well as two negative lobes in $\mathrm{E}_{\mathrm{z}-num}$, indicates the charge separation takes place preferentially along the z-axis. At the next instant, 70.01μs, the second lobe of the P-wave, with opposite sign and higher in magnitude than the first (see PZT signature, fig. 5.1 (a)), touches the sandstone and generates a new dipole-like charge separation, sign-reversed with respect to the previous. These two successively generated dipoles are responsible for, respectively, the first and second lobes of the EM-wave, as suggested in the V_{num} time records of fig. 5.21, measured with virtual point-receivers (electrodes) whose positions are implied by the magenta triangles in fig. 5.20. The other two time snapshots, of fig. 5.20, depict the instants when the two main lobes of the direct P-wave hit the second sand-sandstone interface, creating a charge separation across it, and consequently EM-waves. These waves interact with the analogous EM-signals generated simultaneously at the first interface, due to the secondary maxima and minima of the source signature used in the simulation (fig. 5.1 (a)). After a certain time, these EM-wave interference will dictate the shape of the signals in fig. 5.21 until the moment the propagation of mechanical waves ceases at the sand-sandstone interfaces. Eventually, because the layer is thinner than the wavelength, in both experimental and numerical cases, it is difficult to distinguish the individual EM-waves associated with each interface in the records of fig. 5.21. Though the first two lobes can be assigned to the first boundary, all that comes after was generated at both interfaces.

Seeking to understand the role of an extended seismic source, in comparison with a punctual one, on the global pattern of the EM interface reponse, we repeated the previous simulation (fig. 5.20) but with 5 punctual seismic sources, equally spaced along the y-axis, over the length l_{PZT} of the PZT diameter, to allow for an analogy with the experiments. Fig. 5.22 shows a snapshot in time of this simulation in the same instant of the first line in fig. 5.20, where we observed that an extended source generates a larger P-wavefront, compared to the punctual seismic source, as well as a spatially wider dipolar pattern in V_{num} due to an enlarged first Fresnel Zone radius (r_{FZ}) (Thompson, 1936).

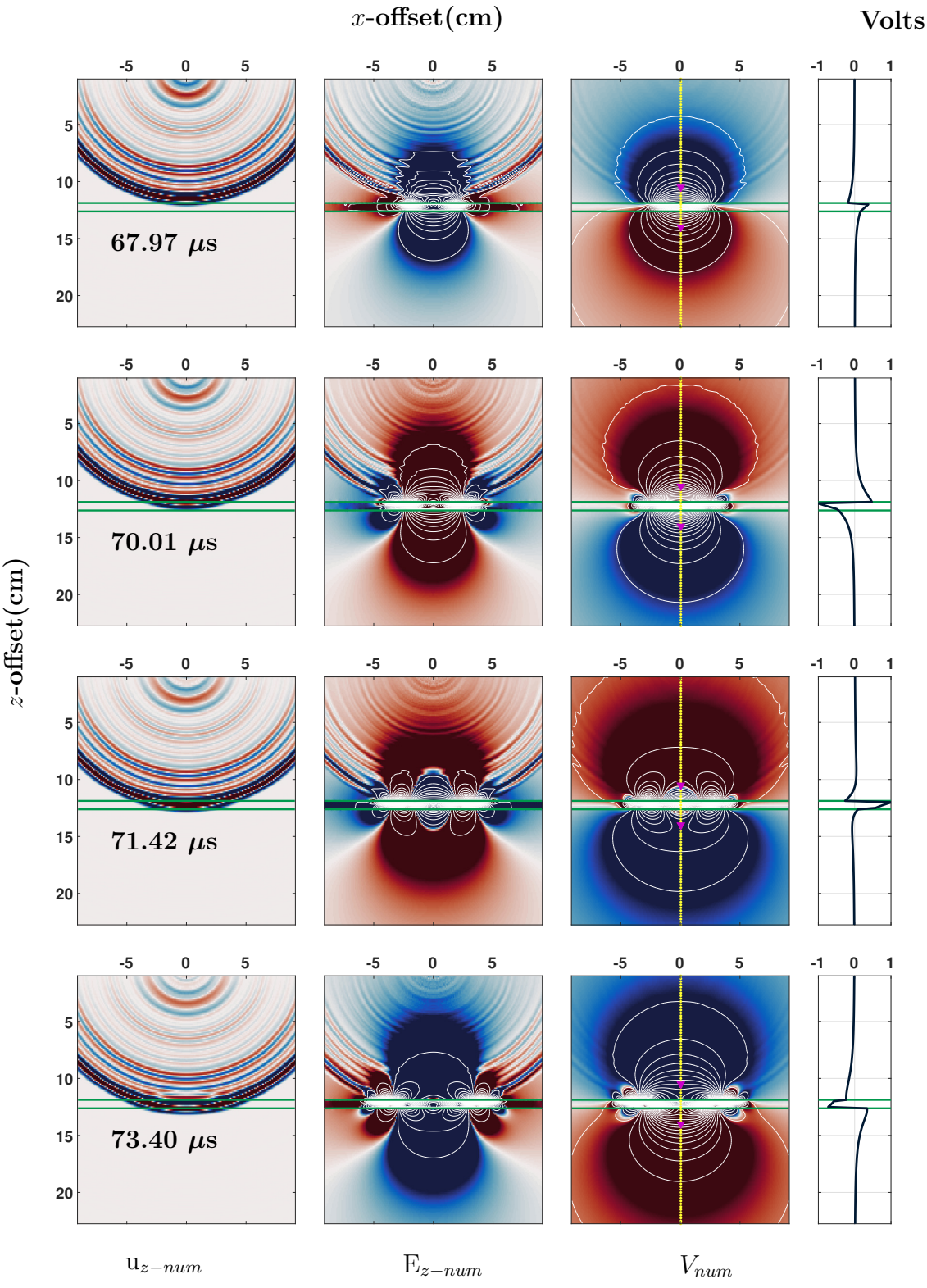

Figure 5.20: From left to right: snapshots of u_{z-num}, E_{z-num} and V_{num} *vs* z and y offsets at four instants. These correspond to the seismoelectric simulation of a point source (at the origin) inside the model used in section 5.7.2, and where the horizontal green lines indicate the sandstone boundaries. White lines in the second and third columns are iso-contours. The rightmost column shows the values of V_{num} at the points indicated by the dotted yellow line. The two magenta triangles, in V_{num}, refer to the position of virtual receivers whose records are shown in Fig. 5.21.

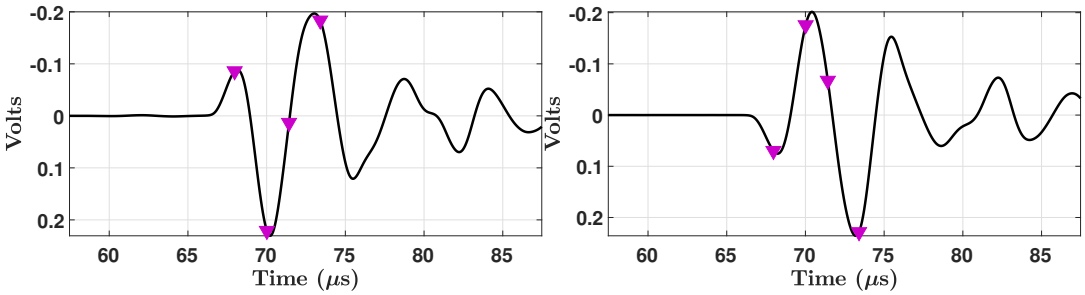

(a) (y,z)=(0.0435,10.5) cm (b) (y,z)=(0.0435,14) cm

Figure 5.21: Absolute electric potentials V_{num} *vs* time, recorded at offsets 10.5 and 14 cm, at the locations indicated with the magenta triangles in fig. 5.20. (a) is recorded before the sandstone layer and (b) after. The triangles refer to the time of each snapshot in fig. 5.20.

The distinct electric dipole-like structure, in both the potential V_{num} and the electric field E_{z-num} snapshots of fig. 5.20, is often interpreted using the model of a short electric dipole positioned on the interface, right beneath the source, where the seismic-to-EM wave conversion takes place (Thompson and Gist, 1993; Garambois and Dietrich, 2002). Butler et al. (1996) and later Dupuis et al. (2009) proposed a more complex model, consisting of two electrically charged spherical caps of opposite sign, joined at the interface, the radius of the base of the spherical cap being linked to the first Fresnel zone and the height of the cap to the P-wavelength λ. Similarly, Garambois (1999) proposed a distribution of many electric dipoles along a circular region on the interface, with radius equal to r_{FZ}; in that model, the amplitude of each electric dipole's moment, distributed all over the first Fresnel zone, is proportional to the magnitude of the normal seismic displacement (u_z in our case) disturbing the interface at the location of the dipole.

In order to attain an analytical interpretation of the EM interface response experimentally recorded V_{exp-EM}, as a function of offset, we adopted the model of Garambois (1999). All the details of this analytical modelling approach are given in Appendix D. Fig. 5.23 (a) illustrates the main idea: the uneven ionic concentration across the interface acts as short dipoles, whose moments depend on the shape of the P-wave wavefront, such that the variation in time of the total dipole moment, as the seismic wave traverses an interface, will be perceived, in the surface, as an EM signal.

We confront in fig. 5.23 (b) experimental and numerically modeled absolute potentials, as a function of offset from the first sand-sandstone interface, with the

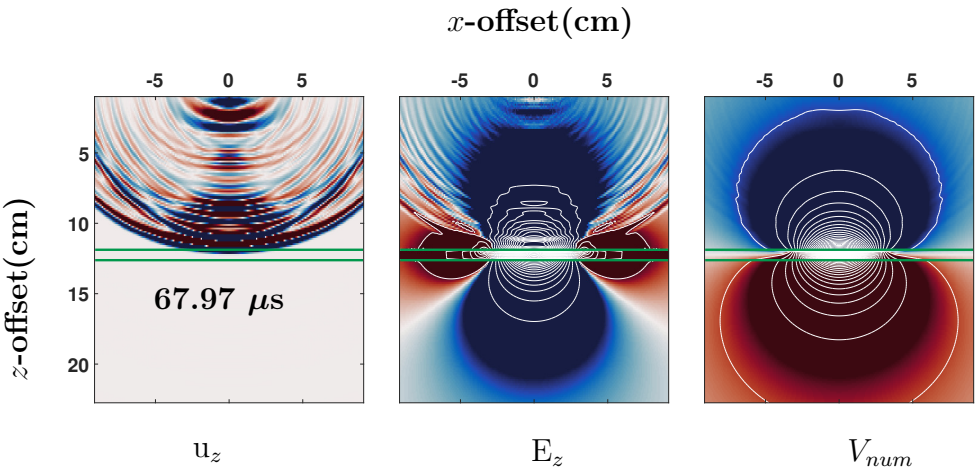

Figure 5.22: u_{z-num}, E_{z-num}, and V_{num} snapshots (from left to rigth, respectively) associated with the numerical simulation using an extended seismic source centred at the origin, with point sources equally spaced along a length equal to the diameter of the PZT used in the experiments. Calculations employed the same model treated in section 5.7.2, such that the horizontal green lines illustrate the boundaries of the sandstone layer. The instant presented 67.97 μs matches the arrival of the P-wave at the first sand-sandstone interface, and the white lines, in E_{z-num} and V_{num}, are iso-contours of these wavefields.

response of four distinct dipole distributions at the interface (cases A to C), obtained using the methodology detailed in Appendix D. Case A considers a single dipole positioned at the first interface (the one closer to the source), right in front of the seismic source's centre. Case B involves dipoles in a circular region, at the first interface, with a 2.9 cm radius, approximately equivalent to the r_{FZ} of a point source. Finally, case C is similar to B, but using an r_{FZ} that accounts for the PZT diameter ($\simeq$ 4.8 cm).

In fig. 5.23 (b), all models of absolute potentials agree well with the experimental data and the numerical simulation at offsets greater than 4 cm from the first sand-sandstone interface. Focusing on the absolute potential decay close to the interface, a comparison of cases A, B, and C indicate that a single dipole produces a decay of amplitudes that is too strong, and conversely, that dipoles distributed over a relatively large area at the interface are best suited to reproduce both experimental and numerical data; with case C leading to the best fit of curves at all offsets.

Additional tests with these dipole-based models evaluated their sensibility to the layer depth. The fact all four models deviate significantly from the experimental data, if this parameter is incorrectly chosen, implies that the analysis based on these

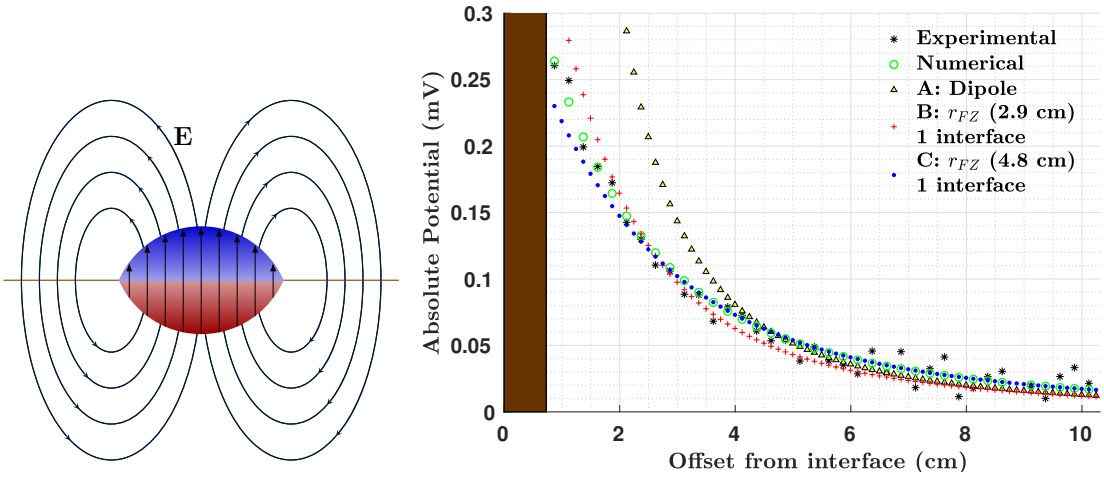

(a) (b)

Figure 5.23: (a) Schematic representation of the lens-shaped region in which the interface response originates, with arrows indicating the variation of dipole moment. The magnitude of the moments is proportional to the amplitude of the seismic displacement perpendicular to the interface. (b) Comparison of models using dipoles (see text) and the maximum amplitude of the interface response from experimental and numerical data, V_{exp-EM} and V_{num-EM} respectively. The brown rectangle in the left represents the interface.

models can be used to estimated the layer depth. An example of this application can be found in Garambois and Dietrich (2001).

5.8 Conclusions

An experimental set-up was proposed as a laboratory analogy to field experiments, regarding its capability to measure both the coseismic and the interface response simultaneously, contrarily to most of the set-ups reported in the literature (devoted to study seismoelectric phenomena). Employing a saturated homogeneous medium, using the experimental source signature and based on the electrokinetic theory of Pride (1994), the numerical modelling was confronted with the measurements. The comparison showed that, in terms of amplitudes both experiments and numerics are in the same order of magnitude (differing by a factor of about 0.44), while waveform-wise they agree satisfactorily. The same conclusions can be drawn when a thin layer is present with an almost perfect match between waveforms.

Using a group of transient electric dipoles distributed along the first Fresnel zone, and whose amplitudes depend on the geometrical spreading of the incident P-wave,

led to a reliable representation of the interface response's amplitude decay with offset. This model can be used as an alternative to estimate (or at least confirm) depths and thicknesses of layers, acting as an auxiliary tool when interpreting seismoelectric data.

Both the experimental and the numerical data confirmed that measuring absolute potentials over electric fields (i.e., using dipolar arrays) favors the recording of EM waves generated at interfaces, similarly to what was observed in the numerical simulations of Dietrich et al. (2018) and Devi et al. (2018). Implementation of the proposed electrode configuration in field surveys would need very long shielded cables, to position the reference electrode very far from the measuring ones, as a consequence it is unlikely the EM noise acting upon the electrodes would cancel out. Another way is by properly shielding the reference electrode to avoid the interfacial EM wave from reaching it. The multi-electrode configuration of Dietrich et al. (2018) is also a valid alternative and remains to be tested in our experimental set-up.

Finally, in the absolute potential records the amplitude of the interface response showed an approximate decrease of 90% at a point 10 wavelengths away from the interface. In a near surface applications, considering a geology similar to the model used here, and both source and receivers at the surface, using a $f_{peak} = 180$ Hz source ($\lambda \simeq 10$ m) the EM-wave generated at a depth of 100 m would appear as very weak signal. However, since contrasts in fluid conductivity have a big impact on the amplitudes of the interface response (Garambois and Dietrich, 2002), and in the present study both media had practically the same fluid conductivity, we expect that in a real scenario at least the first tens of meters can be readily investigated using the seismoelectric method. Future field surveys based on the absolute potential records will need to confirm this.

5.9 Complementary studies

This section shows two additional studies, complementary to the results discussed in this chapter. At first a new numerical modelling, alternative to the one presented in section 5.7.2, will be presented. Following that, experimental data acquired along different xpositions will be used to study the amplitude distribution of the interface response throughout the sandbox; in complment to the discussion carried out in section 5.7.3.

5.9.1 Modelling with different parameters for the sand

Even though the numerical simulations reported in this chapter successfully reproduce the experimental data, in what follows a new simulation, achieved by changing a couple of physical parameters, will be compared, in terms of similarity, to the numerical and the experimental data, previously presented in section 5.7.2.

Table 5.2 summarizes the parameters that differ from those in table 5.1. The most significant ones are ζ and σ_n. The zeta potential of the sand was calculated using the equation provided by Holzhauer et al. (2017) ($\zeta = 0.044 + 0.026\log_{10}\mathtt{M_f}$), adapted from the one in Pride and Morgan (1991) to a water-saturated sand that is essentially the same as the one studied here. Regarding the ζ of the sandstone, it is again a value from Lorne et al. (1999b) but smaller in absolute value than before. Only the surface conductivity of the sand was changed in the new modelling, to be equal to 0 mS/m, as suggested in the original formulation of Pride (1994).

Table 5.2: New physical parameters associated with the sand and sandstone used in the SE numerical simulations. When two references are present in the column References, the first one refers to the sand and the second one to the sandstone. A 0-valued surface conductivity for sand grains is a standard adopted by Pride (1994) in the case of quartz-water boundaries.

Name, symbol, units	Sand	Sandstone	References
Fluid Conductivity (σ_f)[mS/m]	1.2	2	Measured
Molarity (C_0)[mol/l]	1.28E-4	2.18E-4	$C_0 = \sigma_f/(e^2(b_{Na} + b_{Cl})N_A)$, Pride (1994)
Surface Conductivity (σ_n)[mS/m]	0	2	Lorne et al. (1999b)
Zeta potential (ζ)[mV]	-57.19		Holzhauer et al. (2017)
		-7	Lorne et al. (1999b)
Electrokinetic coefficient (C_{ek})[V/Pa]	-2.25E-5		Eq. 2.29
		-1.18E-7 – -2.18E-7	Guichet et al. (2003): eq. 2.29 and eq. 2.31

Figs. 5.24 and 5.25 compare the experimental data V_{exp} (black) and the previous simulation V_{num-1} (red), treated in section 5.7.2, with the new simulation V_{num-2} (blue). The superimposition of experimental and numerical data in fig. 5.24 shows that the new modelling agrees quite well with V_{exp}, and consequently with V_{num-1}, considering the amplitude trends and the waveform shape of both coseismic and interface response.

To superimpose the data in fig. 5.24, a factor 0.44 was multiplied to V_{num-1}, as in section 5.7.2, while a factor 0.07 was used with V_{num-2}. By comparing these two factors, one can conclude that modelling with the parameters in table 5.2 leads to absolute electric potentials that are about 6.3 times higher, in magnitude, than

those estimated with the parameters in table 5.1. Consequently, it means V_{num-2} is further apart from V_{exp} than V_{num-1}, in terms of amplitudes.

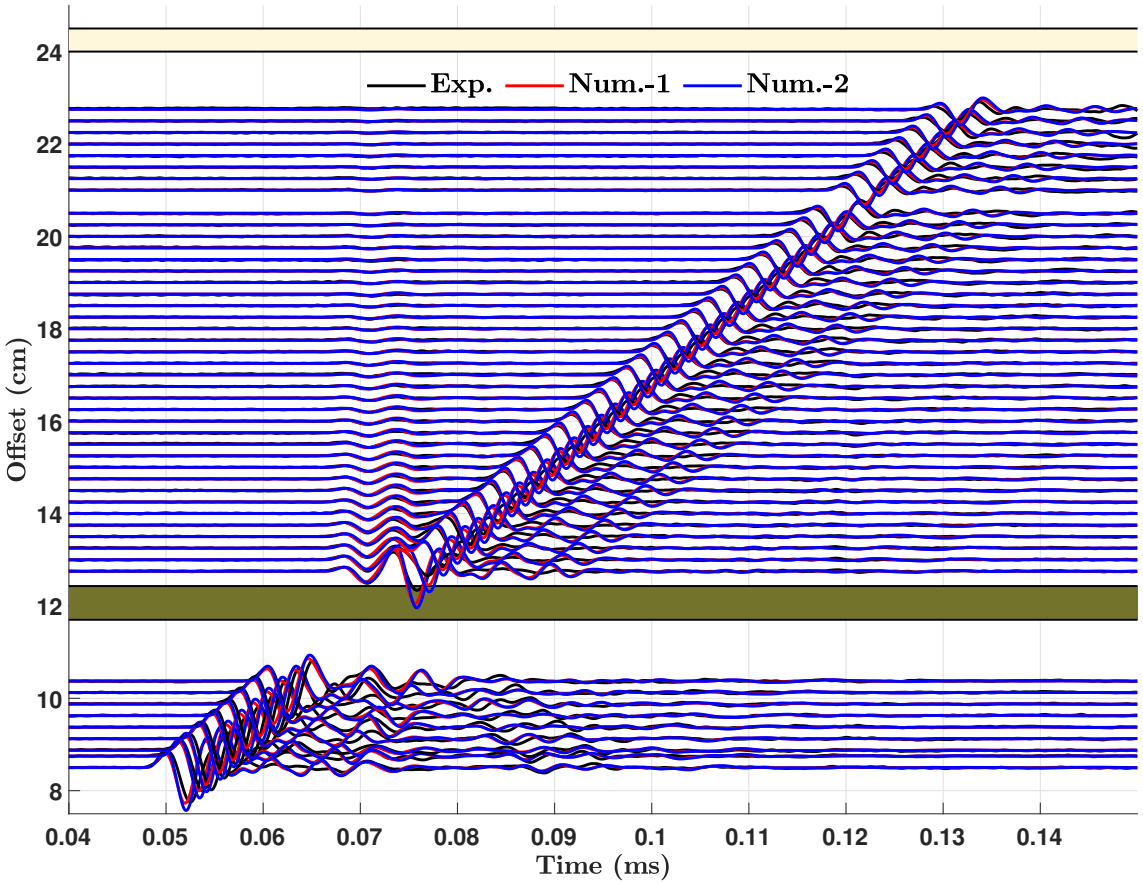

Figure 5.24: Comparison of absolute electric potential data obtained from experiments (black), numerical modelling V_{num-1} using parameters in table 5.1 (red), and numerical simulation V_{num-2} whose difference from the previous resides in the physical parameters indicated in table 5.2. To superimpose the datasets, V_{num-1} was multiplied by 0.44 and V_{num-2} by 0.07.

In fig. 5.25 the first maxima and minima of the coseismic and the absolute maxima of the EM interface response, corresponding to V_{exp} (black), V_{num-1} (red), and V_{num-2} (blue), are displayed *vs* offset. The good agreement of amplitudes, shown in fig. 5.25, between V_{num-2} and V_{exp} is equivalent to that found when comparing V_{num-1} and V_{exp} in section 5.7. As a matter of fact, the coseismic maxima and minima, corresponding to V_{num-1} matches almost perfectly the values from V_{num-2} in fig. 5.25a, as is the case for the absolute maxima of the interface response in fig. 5.25b. At last, from the results presented above, the main difference between V_{num-1} and V_{num-2}, is the factor by which the V modeled is overestimated when compared with V_{exp}.

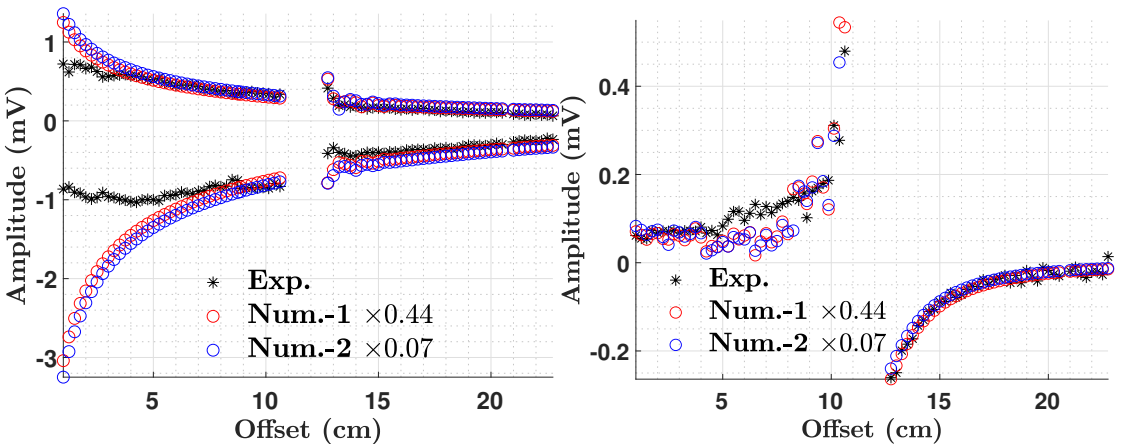

Figure 5.25: Comparison between first maxima and minima of the coseismic signal in (a) and between absolute maxima of the EM interface response in (b). Regarding the data compared, black circles correspond to V_{exp}, red to $0.44 \cdot V_{num-1}$, and blue to $0.07 \cdot V_{num-2}$.

A factor equal to 0.03 was used by Schakel et al. (2011a) to correct the overestimation of the simulated interface response when modeling (using Pride's theory) a medium formed by a porous sample, made of sintered-glass particles, immersed in water, and with the following properties: $\zeta = -51.7$ mV, $\sigma_f = 1.27$ mS/m, and $\sigma_n = 0$. This factor is close to the 0.07 factor found for V_{num-2}, modeled using the values in table 5.2, indicating that for the range of σ_f and ζ values used, the discrepancy found, when comparing numerical and experimental data, agrees with what has already been reported in the literature. Schakel et al. (2011a) suggest the factor 0.03 are related to surface conductivity effects and uncertainty in the value adopted for ζ. As a matter of fact, the comparison in fig. 5.25b supports this explanation, showing that modifying ζ and accounting for σ_n leads to simulations that are closer to the experimental data.

One can draw the following conclusions from the results and discussions above: first, they show the importance of knowing with certitude the physical properties of the materials composing the medium, furthermore they confirm how problematic inverting SE data can be, if the physical models associated with each physical property are not in agreement with the reality of the medium studied. Additionally, it is safe to affirm the value of ζ has a big influence on the seismoelectric phenomena, and constraining it is a mandatory step before achieving proper numerical modeling

results. The same goes for the surface conductivity, though its impact on modeling depends on the actual σ_n value of the medium and on σ_f.

5.9.2 Experiments parallel to layer

The discussion in section 5.7.3 lacks experimental data showing how the amplitudes of the EM interface response are distributed on the x-z plane. With that in mind an experiment was conducted using a medium similar to the one in section 5.7, except for the fact the sandstone layer was around z = 11.7 cm. During the experiment the electrode comb was oriented along the x-axis and shifted along the z-axis (see fig. 4.1b). For every z-offset there will be 32 measuring points, equally spaced by the usual 0.25 cm electrode spacing, between x-offsets -3.75 cm and 4 cm. There are 11 z-offsets before the layer, the first at z = 1 cm, and 11 after, starting at z = 13 cm. At last, the step between z-offsets in each side of the layer is 1 cm, with an exception at the last position which is equal to z = 22.9 cm.

Fig. 5.26 shows the measured absolute maxima, of the EM interface response, on the x-z plane. In order to aid the visualization, the data, on both sides of the layer, was linearly interpolated to generate points spaced by 0.25 cm along the z-axis. The contour lines indicate a pattern of amplitudes that is similar to the one discussed in section 5.7.3, note the similarity with the V_{num} snapshots in figs. 5.20 and 5.22. Focusing on the amplitudes at z-offsets smaller than 8 cm, one can also observe how

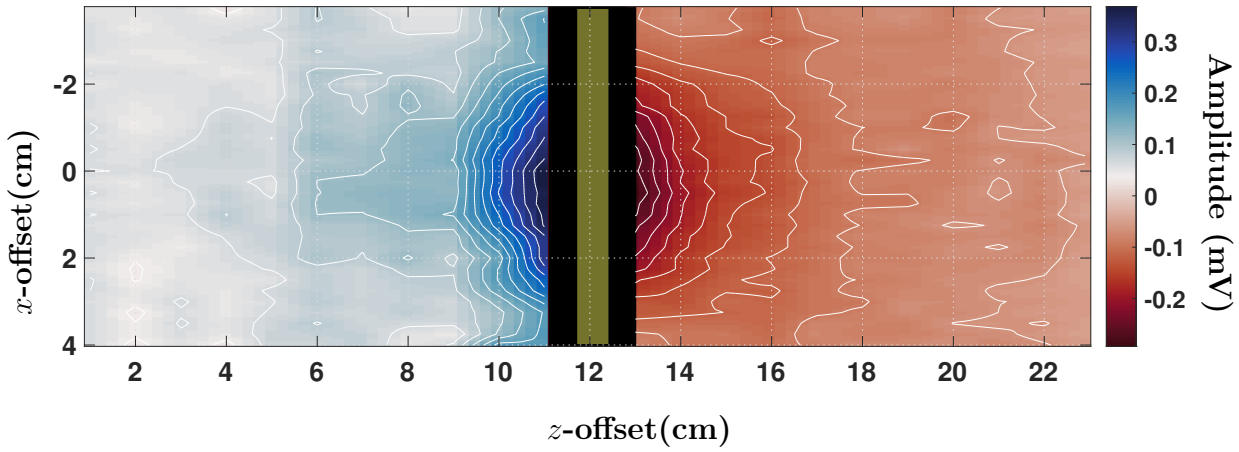

Figure 5.26: Amplitude map and contour plot showing the absolute maxima of the EM interface response along the x-z plane. Values were obtained from an experiment detailed in the text. The original values were linearly interpolated to create points spaced by 0.25 cm along z, and thus to improve visualization.

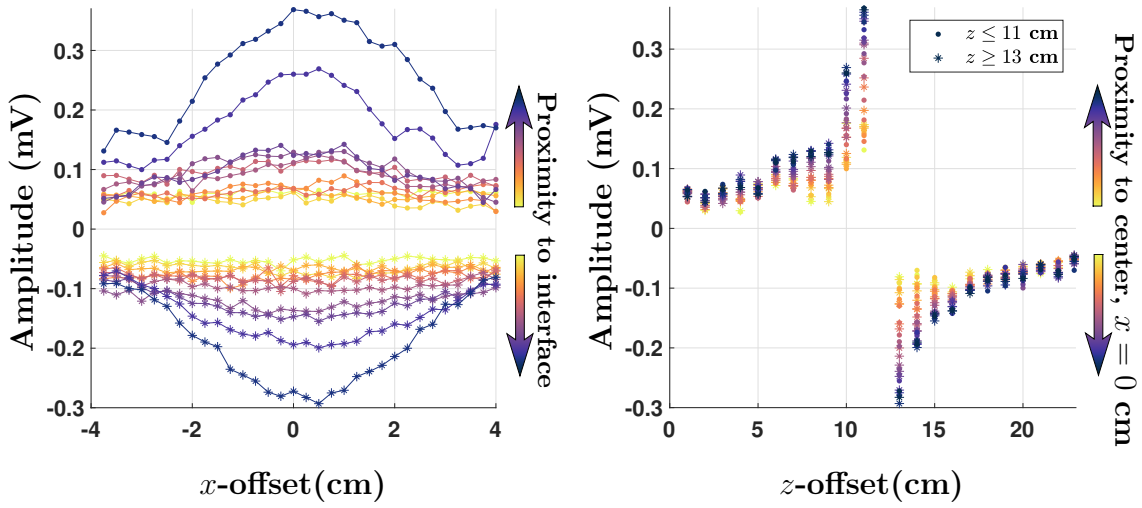

(a) (b)

Figure 5.27: Absolute maxima of interface response along x-axis (a) and z-axis (b). In (a) the distance of each x-oriented acquisition line from the interface (z = 11.7 cm), generating the EM phenomena, is represented by the color pattern: the darker the color, the closest the line is to the interface, and vice-versa. In (b) the color pattern indicates the distance, of the z-oriented acquisition lines, from the center of the box (x = 0 cm): the darker the closer. In both figures, points refer to data acquired at z-offsets smaller or equal to 11 cm, and asterisks to points acquired at z-offsets bigger or equal to 13 cm.

coseismic waves interfere with the interface response by the absence of ellipse-shaped contour lines.

In order to better understand how the interface response amplitudes vary inside the experiment, fig. 5.27a shows how the absolute maxima vary along x, and fig. 5.27b shows the variation along z. These two figures demonstrate how the higher amplitudes happen at measuring points closer to the interface (z = 11.7 cm), and to x = 0 cm. Most importantly, fig. 5.27a puts in evidence the resemblance between the amplitude *vs* x-offset distribution, obtained from experiments, and the lens-shaped model, treated in section 5.7.3 and in Appendix D. Finally, the experimental data shown in this sections supports the analytical modeling detailed in Appendix D.

6 Experimental and numerical study on the effect of layer thickness and constrasts of fluid conductivity upon the EM interface response

6.1 Effect of thickness

The effect of thin layers on seismo-electromagnetic signals, created at geological interfaces, has been an active subject of research since the development of a set of governing equations by Pride (1994). It was, possibly, Haartsen and Pride (1997) that first discussed the boost of electroseismic waves created by replacing a thick (relative to the seismic wavelength) sand layer with a thin one. Pride and Garambois (2005) arrived at the same conclusion about the potential of thin layers to increase seismoelectric interface-generated waves, even though the bulk increase in this case may not only be due to the thin layer, but also due to the high permeability contrast associated with the thin layer. Haines and Pride (2006) used a 2D finite-difference modeling, based on Pride's theory, to study the influence of layer thickness and lateral extent on the EM interface response. They conclude, from the simulations, that the seismoelectric method is effective to detect thin (regarding the P-wavelength) and narrow (with respect to the first Fresnel zone radius) layers. More recently Grobbe and Slob (2016) investigated the effects of a layer composed of thin-beds on the interface response, with a focus on S-to-EM wave conversion on the interface. For that, the thickness of the layer and of the beds within it were varied. In what regards the effect of the total layer thickness, the authors found that the highest amplitude happened when thicknesses were close to the P and S-wavelengths. Finally, it is likely that, to this date, the only experimental work concerned with the effect of a single layer thickness, on the interface response, is Peng et al. (2017). Their experiment employed a wedge-shaped rock sample and the results showed that the amplitude of the interface response increased with thinning of the wedge. In this context, the present work brings new experimental and numerical data as a means to further investigate the relation between the layer thickness and the EM interface response.

6.1.1 Layer thickness, thin beds and seismic waves

When the thickness of a layer inside a medium is smaller than the seismic wavelength, constructive and destructive interference will control the wavefields reflected on said layer. As a consequence, both the seismic amplitude and its waveform will change with layer thinning, such that the vertical seismic resolution will dictate the smallest thickness that can be perceived in a seismogram; below the seismic resolution, layers will be detected as single interfaces, or not detected at all.

In order to define the thickness threshold below which the seismic waveform stops changing, Widess (1973) uses elementary concepts, in a methodical way, to show that: for a layer sandwiched between two identical half-spaces, as long as thickness are smaller than an eighth of the P-wavelength (inside the layer), the character of reflected seismic signals remains unchanged. Thus the author defines the concept of thin beds (used here as a synonym of thin layers) as those whose thickness is smaller than λ_P. Figure 6.1 summarizes the results of Widess (1973).

Another important observation made by Widess (1973), and represented in figure 6.1, is the fact that for very thin beds ($< \lambda_P/8$) the resulting waveform will resemble the derivative of the incident waveform, such that the thinner the layer, the more alike it will become.

Tatalovic et al. (1988) uses a wedge model to create synthetic and experimental data, in order to study the accuracy with which the thickness of thin beds can be estimated. It complements, showing a real world application, the work Widess (1973). The results of Tatalovic et al. (1988) that are of interest to this thesis are those showing how the waveform of reflected P-waves will vary with layer thickness. Figure 6.2 (a) shows the amplitude *vs* thickness (as fractions of the seismic wavelength in the layer) behaviour, obtained from synthetic data calculated using a (standard) Ricker wavelet. It is representative of the curve that would be obtained if the amplitudes of the signals in figure 6.1 (d) were plotted against thickness. It also shows the peak-to-through time separation to connect amplitude and waveform changes, while explicitly defining a thick bed as one whose thickness does not lead to interference between waves reflected on both interfaces of the layer. Note also that a maxima occurs when the thickness is equal to $\lambda/4$.

Figure 6.2 (b) shows the amplitude trend obtained by Tatalovic et al. (1988) from laboratory data. As expected the real data is not as perfect as the synthetic one in figure 6.2 (a), even though it shows a fair resemblance. One can notice two extra maxima at thicknesses bigger than $\lambda/4$. These are due, as suggested in Tatalovic

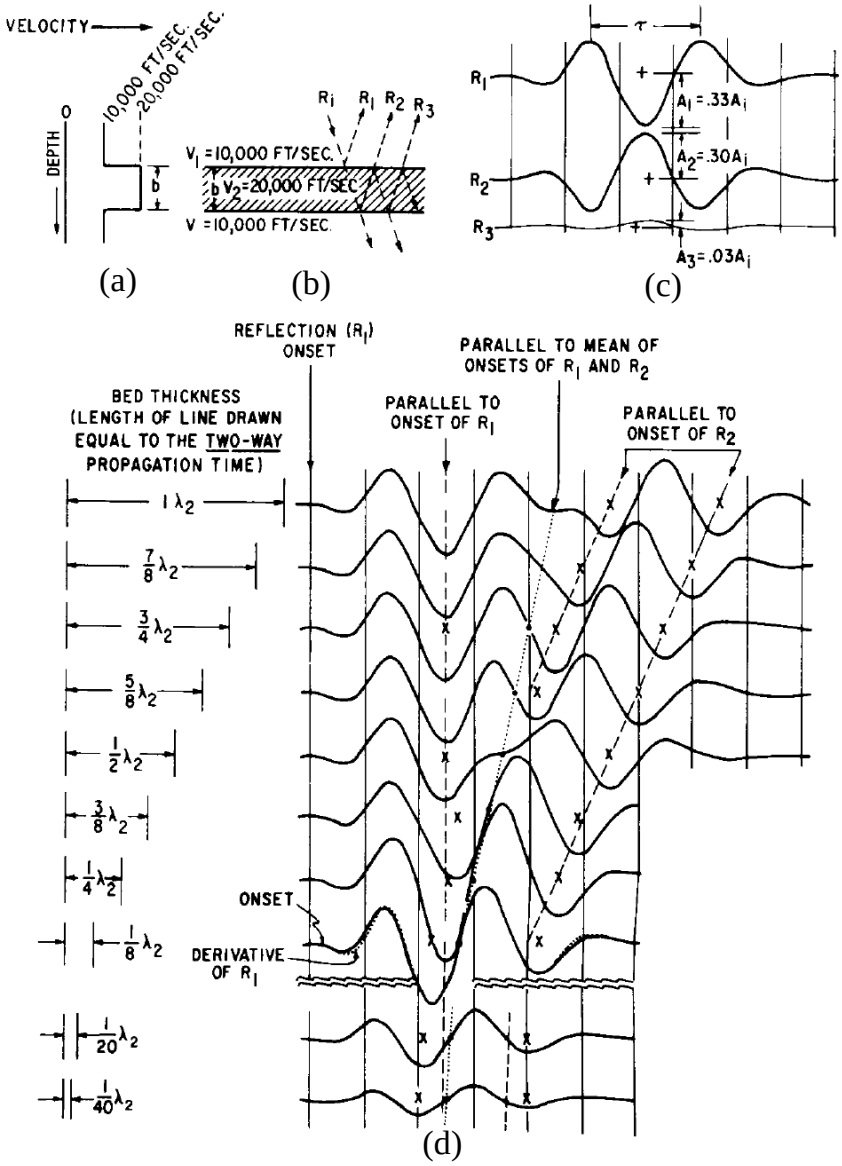

Figure 6.1: Effect of layer thickness on seismic reflections. (a) shows the velocity log, in ft/s (multiply by 0.3084 to get values in m/s). (b) shows a diagram with rays indicating the reflection on the first interface (R_1), on the second interface (R_2), and a first-order multiple inside the layer (R_3). (c) depicts the signature of the P-waves reflected on the layer, calculated analytically using the velocities and thickness given in (b). τ is the predominant period of the incident P-wave. (d) presents the resulting waveform as a function of layer thickness, with x pointing to through, and • to the zero-amplitude time (center of combined waveforms). The vertical lines are spaced by 0.5τ and λ_2 is the P-wavelength inside the layer, which can be calculated using the layer velocity V_2 and τ. All amplitudes are relative to the incident wavelet shown in (c), and its derivative is the dotted line waveform superimposed (after proper scaling) to the resultant waveform at a $\lambda_2/8$ thickness. Extracted from: Widess (1973).

et al. (1988), to the presence of side-lobes and side-tail oscillations in the signature of the source used in the experiment, which are also responsible for interference effects. Besides, Tatalovic et al. (1988) also cites that multiple reflections may also be responsible for the two extra lobes in figure 6.2 (b).

The discussion above will serve as the basis for the incoming analysis of seismo-electric data. Both the definition of thin beds and the amplitude tuning (with layer thinning) will be explored in the context of EM interface responses. In the end, by analogy with the seismic case, thin beds and the increase of amplitudes with bed thinning will be defined for interface responses created by P-wave incidence.

6.1.2 Experimental and numerical methodology

Experimental and numerical simulations follow closely the procedure described in the previous chapter (see figure 4.1 and sections 5.4 and 5.5). The only changes are due to the different layers used, specifically the layer positioning inside the sand varies. Consequently, because of the thickness of the layers, some experiments have more measuring points than others, even though the measuring lines are still oriented along the z-axis and practically centered around the x-axis ($x \simeq 0$). All the layers used in the experiment are made of the same material, a Vosges sandstone (described

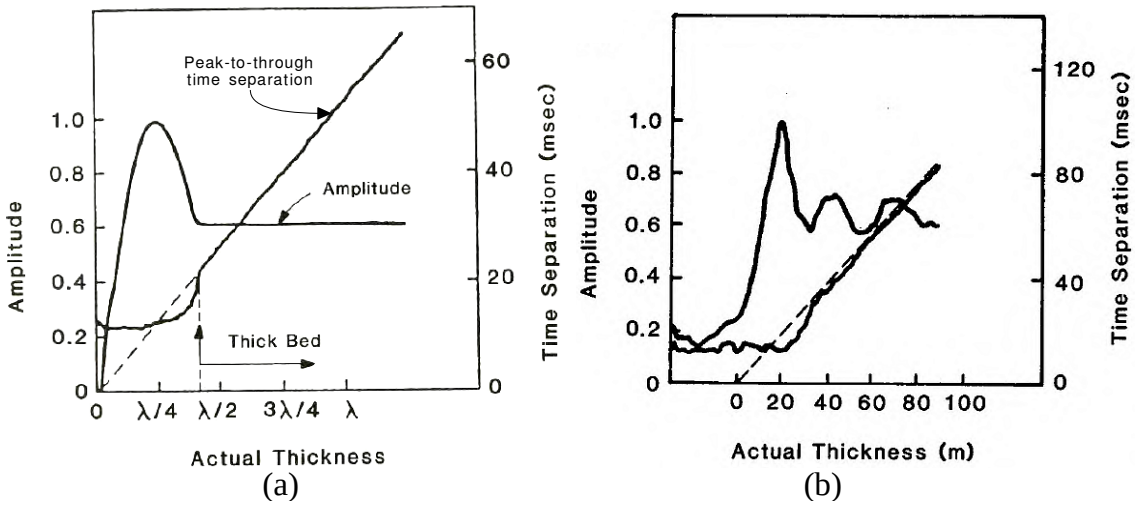

Figure 6.2: Trend of amplitudes and peak-to-through time separations *vs* layer thickness, for a layer in-between two half spaces. (a) shows the results obtained from synthetic data created using a Ricker wavelet. (b) presents the results obtained from the raw experimental data. The dashed line represents the ideal trend of a thick layer. In both figures, amplitudes were normalized. Figures are as extracted from: Tatalovic et al. (1988).

in section 4.2), and their dimensions and positioning inside the experiment are shown in table 6.1.

In the numerical simulation, as in chapter 5, a three (horizontally infinite) layer model was used to represent the experiment. Following the orientation of the z-axis in figure 4.1, the first and the third (which is modeled as an infinite half-space) layers are made of saturated sand while the second is a sandstone. The physical properties used in the simulations are, for the most part, those in table 5.1. However, some parameters were adjusted to better represent the experimental data, with their new values displayed in table 6.1. The changes in the frame moduli (K_{fr} and G_{fr}), and consequently in the P-wave velocity, were made to ensure the simulations are coherent with the velocities obtained from the experimental data.

Regarding the changes in fluid conductivity, values outside the bounds defined in table 5.1 occur only for the thicknesses of 2.5 and 5 cm, in table 6.1. These higher values were chosen based on the amplitudes of coseismic signals, since they are lower than theory predicts, as a means to proper model the experiment. These lower-than-expected amplitudes may be due to heterogeneity inside the layers (unseen from outside due to their thickness), which further attenuate the P-waves and, therefore, results in lower coseismic amplitudes on the third layer.

Finally, the numerical simulation described above (using the parameters in table 6.1) will be referred as Num. 1 when analyzing the results. That is because a second numerical simulation (Num. 2) was realized, but this time the physical properties of the three layers did not change with thickness, and were equal to the values of the 0.74 cm layer in table 6.1. While Num. 1 was planned seeking to better fit the experimental data, Num. 2 was planned to provide an idealized example of the general behaviour of the interface response when the thickness of the sandstone layer is reduced.

6.1.3 Results and discussion

Following the experiments, the raw data was de-trended, band-passed (10 kHz – 1 MHz), and static corrections were applied to correct eventual electrode misplacement and the initial delay associated with the triggering time (time between the actual source excitation and the oscilloscope recording). In order to be succinct all the forthcoming discussion will concern only the EM interface response.

The processed experimental records, as well as the corresponding numerical simulations, are displayed in figure 6.3. Two z-offsets, 16.5 and 18.5 cm, were chosen to

Table 6.1: Input physical parameters for the three layer model, used in the numerical simulations, and that are different from the ones presented in table 5.1. The dimensions and the limits along the z-axis of each layer are also presented. Note that, even though some values were not changed (with respect to table 5.1) they were still presented, for the sake of completness.

		Sandstone thickness (cm)							
Name, symbol, units		**0.2**	**0.5**	**0.74**	**0.9**	**1.63**	**1.91**	**2.5**	**5**
Sanstone x and y dimensions [cm]		5.2×8.6	8.5×9.5	5.65×9.2	5.8×9.2	5.8×9.15	8.6×9.4	6.7×9	8.7×9.5
Sandstone z-limits [cm]		[11.98, 12.18]	[11.65,12.15]	[11.88,12.62]	[11.61,12.51]	[11.6,13.23]	[11.96,13.87]	[11.8,14.3]	[11.75,16.75]
Bulk (frame) modulus (K_{fr})[Pa]	**Sand**	2.38E7	2.89E8	2.38E7	2.38E7	1.06E8	2.44E8	2.38E7	2.38E7
	Sandstone	3.41E8	3.41E8	3.41E8	3.41E8	3.41E8	2.1E9	3.41E8	1.83E9
	Sand	2.38E7	2.89E8	2.38E7	2.38E7	1.06E8	1.47E8	2.38E7	2.38E7
Shear (frame) modulus (G_{fr})[Pa]	**Sand**	1.43E7	1.74E8	1.43E7	1.43E7	6.33E7	1.47E8	1.43E7	1.43E7
	Sandstone	2.1E8	2.1E8	2.1E8	2.1E8	2.1E8	1.33E9	2.1E8	1.16E9
	Sand	1.43E7	1.74E8	1.43E7	1.43E7	6.33E7	8.81E7	1.43E7	1.43E7
P-wave velocity (v_P) [m/s]	**Sand**	1.78E3	1.82E3	1.78E3	1.78E3	1.79E3	1.81E3	1.78E3	1.78E3
	Sandstone	2.2E3	2.2E3	2.2E3	2.2E3	2.2E3	2.5E3	2.2E3	2.46E3
	Sand	1.78E3	1.82E3	1.78E3	1.78E3	1.79E3	1.8E3	1.78E3	1.78E3
Fluid conductivity (σ_f)[mS/m]	**Sand**	1.8	1.8	1.8	1.31	1.8	1.31	1.8	1.8
	Sandstone	1.31	1.31	1.31	1.31	1.31	1.8	1.8	1.8
	Sand	1.8	1.8	1.8	1.31	1.8	1.8	2.2	2.5

Table 6.2: Summary of the multiplying factors used to superimpose the traces of Num. 1 and Num. 2 to the experimental data in figure 6.3.

	Sandstone thickness (cm)														
Simulation	**0.2**		**0.5**		**0.74**		**0.9**		**1.63**		**1.91**		**2.5**		**5**
Num. 1	0.81	0.95	1.21	1.75	0.74	0.78	0.82	1.17	0.9	1	0.7	0.88	0.64	0.78	1.46
Num. 2	1.25	1.3	1.52	1.94	0.92	0.88	1.94	2.45	1.17	1.17	1.67	1.75	0.88	0.93	1.6
Offset (cm)	**16**	**18**	**16**	**18**	**16**	**18**	**16**	**18**	**16**	**18**	**16**	**18**	**16**	**18**	**18**

illustrate how the interface response changed when layers with different thicknesses were used. The vertical axis indicate to which layer thickness the data belongs to. Note that, due to the position of the 5 cm layer (see table 6.1) there was no measuring point at z = 16.5 cm. Additionally, the (horizontal) time axis was adjusted so the time 0 corresponds to the onset of the interface response signal. This onset is an approximate value obtained using the layer position and the velocity estimated from the measurements.

Regarding the numerical data in figure 6.3, the multiplying factors, used to fit it to the experimental data, are summarized in table 6.2 for the two numerical simulations performed, for every layer thickness, and for both z-offsets discussed. For the thickness of 0.74 cm, Num. 1 and Num. 2 were calculated using identical parameters, therefore the dissimilarity of factors in table 6.2 is due to truncation errors, inherent to the method of Bouchon (1981), used to discretize the integral over the wavenumber (see section 3.7). As a consequence, in concerning the simulations of the other thicknesses, the discrepancies between Num. 1 and Num. 2 are also, in part, due to numerical errors in the simulation, and for the rest of it, due to the use of different input parameters.

Focusing on the comparison between numerical and experimental data in figure 6.3, it is clear the simulations reproduce satisfactorily the measurements, for all layer thicknesses. Because the amplitudes of the interface response are rather low (< 0.1 mV at the z-offsets displayed in figure 6.3), some features predicted by the theory appear as attenuated events, for example: the second maxima of the interface response for the 0.74 cm thickness, recorded at z = 18.5 cm, and the second maxima of the 1.63 cm dataset in both offsets. The interface response created at the second interface of the 5 cm layer was strongly attenuated, if compared with the numerical predictions, what implies the parameters input into the modeling do not correspond to those of the rock sample used. Nevertheless the P-wave velocity (of the sandstone) in Num. 1 was adjusted to match the arrival times of this interface

response, as observed in figure 6.3b, contrarily to Num. 2 that underestimates the P-wave velocity in the 5 cm layer.

Now, comparing the results in figure 6.3 with those of Widess (1973) in figure 6.1 (d), there is an undeniable similarity. This resemblance comes from the fact the waveform of EM interface responses are created, and controlled, by the time-dependent charge imbalance across an interface, which appears as a seismic wave travels through it (Haartsen and Pride, 1997). One aspect of disagreement, between the results in both figures, is the correspondence between the resulting waveform and the P-wavelength fraction generating it. Because the interface response propagates with electromagnetic velocities ($v_{EM} >> v_P$), its detection by the electrodes is essentially synchronous to its genesis at the interface. Therefore, if interpreted in the context of EM interface response, the resulting waveforms in figure 6.1 will

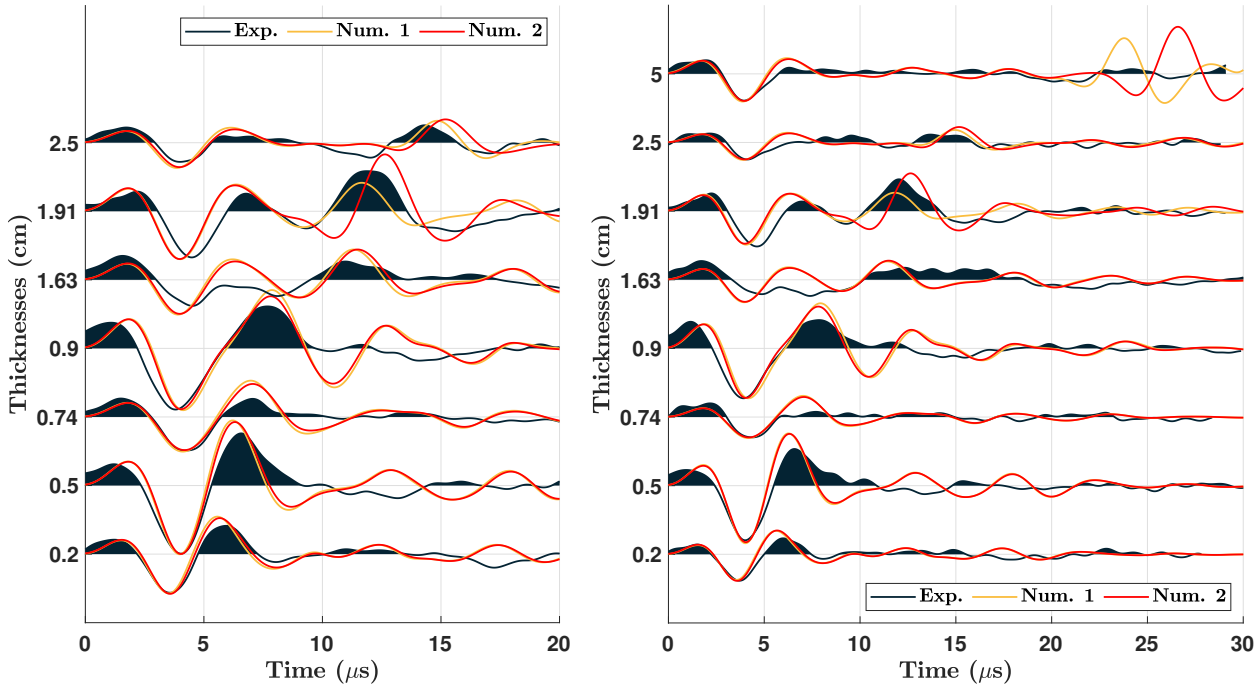

Figure 6.3: Comparison between seismoelectric data obtained from experiments (dark blue) and from numerical simulations (orange and red), with focus on the EM interface response created by P-waves. The vertical axis represents the thickness of the layer each trace corresponds to. The horizontal time axis starts at the approximate onset of the interface response, which was determined using the measured P-wave velocity and the position of each layer. (a) corresponds to the 16.5 cm z-offset and (b) to 18.5 cm. The details and differences between the numerical data (Num.1 and Num. 2) are discussed in the text.

correspond to double the thickness indicated. This can actually be verified (considering in the experiment the P-wavelength is about 1 cm) by comparing the traces associated with a 0.5 cm thickness in figure 6.3 and that linked with a quarter of the seismic wavelength in figure 6.1; or, alternatively, the traces corresponding to 1.91 cm in figure 6.3 an that related with one wavelength in figure 6.1.

In order to explore further the consequences of layer thinning on the interface response, an analytic modeling was conducted, as an alternative to hundreds of time-consuming numerical simulations using the code discussed in chapter 3. This modeling relies on the wavelet associated with the first interface response created at the 5 cm layer in the Num. 2 simulation (i. e., the event taking place between 0 and 10 μs in figure 6.3b). After properly isolating the wavelet, it was padded with zeros and added to its time shifted and amplitude reversed reciprocal, what allowed the creation of synthetic traces representing the interface response waveform associated with layer thicknesses ranging from 0.014 until 5 cm (with a 0.014 cm step). For the same layer thicknesses presented in figure 6.3, figure 6.4 shows the comparison between the analytic approach and Num. 2. For the sake of completeness, the wavelet used in the analytic computations as well as its derivative (properly amplitude normalized) are also shown.

The comparison in figure 6.4 shows that the analytic simulation agrees satisfactorily with Num. 2, despite small amplitude inconsistencies that arise from the fact attenuation was not considered in the calculations. Therefore, because Num. 2 in figure 6.3b fits well the experimental data, so should the analytic data. Moreover, the evolution of the main waveform towards its derivative, with layer thinning (Widess, 1973), is put in evidence by figure 6.4, confirming this behavior is also true for EM interface responses.

Figure 6.5 focuses on the amplitude behavior of first maxima and minima (6.5a), and on variation of peak-to-through time separation with thickness (6.5b). The curves calculated using the analytic approach detail the ideal trend, thus for a 1 cm P-wavelength (based on experiments) four main observations can be made regarding the amplitudes. First, the maxima will increase with thickness until a value of about $3\lambda/8$; after that it reaches a plateau indicating that the interface response, created at the second interface, stops affecting the first maxima. Second, the absolute value of the minima will increase with thickness until $\simeq \lambda/2$, where it reaches a peak value which is nearly 1.5 times higher than the amplitude associated with a single interface. Third, for thicknesses bigger than $\lambda/2$, the absolute minima will decrease until $\simeq \lambda$,

and after this point it will remain constant. Fourth and last, for thicknesses smaller than $\simeq \lambda/4$, maxima and minima decrease almost linearly with thickness.

Now, concerning the ideal trend of peak-to-through time separation in figure 6.5b, the variation with thickness is essentially linear for values bigger than λ. Moreover, when thicknesses are smaller than $\simeq \lambda/4$, the peak-to-through separation practically ceases to change, stabilizing around the value 2 μs, and implying the two interface responses, created in the layer, will behave as the response of a single interface. At last, it is the tendency observed in the amplitudes (figure 6.5a) and peak-to-through separation (figure 6.5b), for layer thicknesses smaller than $\lambda/4$, that has led Widess (1973) to define $\lambda/8$, in the context of seismic waves, as the upper limit for thin layer thickness. In other words, by analogy with the criteria of Widess (1973) and based on the results presented in this section, to define a thin layer, in the context of EM interface responses, a thin layer is one whose thickness is smaller than a quarter of the P-wavelength inside the layer.

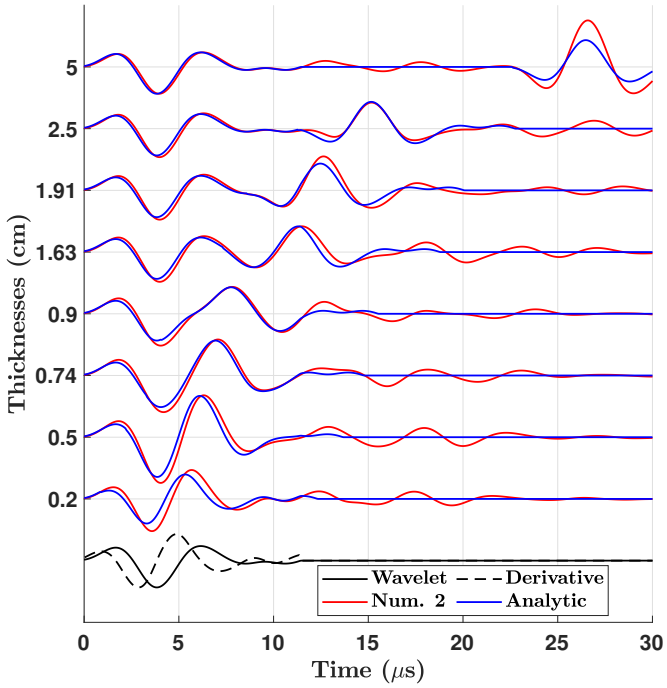

Figure 6.4: Comparison between analytic simulations (blue), based on a wavelet (black) extracted from Num. 2, with Num.2. The dashed black signal is the derivative of the wavelet, after normalizing its amplitudes so it has the same energy as the main wavelet. No multiplying factor was applied to Num.2, thus its amplitudes are as predicted by theory. Notice that this figure is equivalent to figure 6.3b and, therefore, all traces correspond to the experimental data measured at z = 18.5 cm.

By comparing experimental and analytically calculated data in figure 6.5, one can notice a good agreement in the first maxima amplitudes and in the peak-to-through time separation. Concerning the amplitudes of the first minima, the experimental data varies considerably, nevertheless they still appear to follow the ideal trend (black dots in figure 6.5a). Because the analytic data used the wavelet associated with the 18 cm z-offset, the amplitudes of the experimental data obtained at z = 16 cm are slightly higher, as one would expect. However the general amplitude behavior of the experimental data at both offsets is practically identical. In figure 6.5b, for thicknesses smaller than 1 cm, the agreement between the analytic calculations and the experiments is considerable. For bigger thicknesses, on the other side, there exists a disagreement that can be explained by an underestimation of the P-wave velocity in the layer during the analytic computations.

The results in figure 6.5 can be compared with those of Tatalovic et al. (1988), presented in figure 6.2. The ideal trends (compare amplitudes associated with minima in 6.5) agree almost perfectly with those in figure 6.2 (a). The behavior of experimental minima is arguably similar as well, even though the lack of data from more thicknesses limits the comparison. Notice that in figure 6.2 (b) there are two extra maxima occurring at thicknesses about two and four times the one where the main maximum exists. This is also true in the minima of the experimental data shown in figure 6.5a, suggesting a similarity with the raw data of Tatalovic et al. (1988).

To explain the extra maxima, and consequently the amplitude variation, in their raw data, Tatalovic et al. (1988) suggested the interference due to secondary oscillations in the experimental source signature, as well as multiple reflections inside the layer. That may also be the case here, considering the source signature in the experiments (see figure 5.1) has many secondary oscillations. Additionally, the physical properties of sand and sandstone, may not exactly be the same throughout the experiments (for each layer thickness a new set of measurements was realized), what can also lead to changes in the amplitude of the interface response. As demonstrated numerically by Haines and Pride (2006), the dimensions of the layer on the xy-plane also affect the amplitudes of the EM interface response: when the diameter of the Fresnel zone is halved, the authors show that amplitudes drop by about 30%. In the experiments realized in the present work, the Fresnel zone radius, accounting for the PZT diameter, is about 4.8 cm (see previous discussion in section 5.7.3 and appendix D). Therefore, considering the dimensions of the layers used in the exper-

iment (detailed in table 6.1), the amplitudes of the measured EM interface response will always be smaller than what theory predicts for layers whose x and y dimensions are bigger than, or equal to, the Fresnel zone diameter. On the other side, in the experiments, all layers have x and y lengths larger than half the Fresnel zone diameter, what implicates that the amplitudes of the measured interface responses drop by less than 30%. At last, a proper quantitative study of how the x and y dimensions change the amplitudes could not be carried due to the premise of the numerical code used that all layers be infinite along these dimensions.

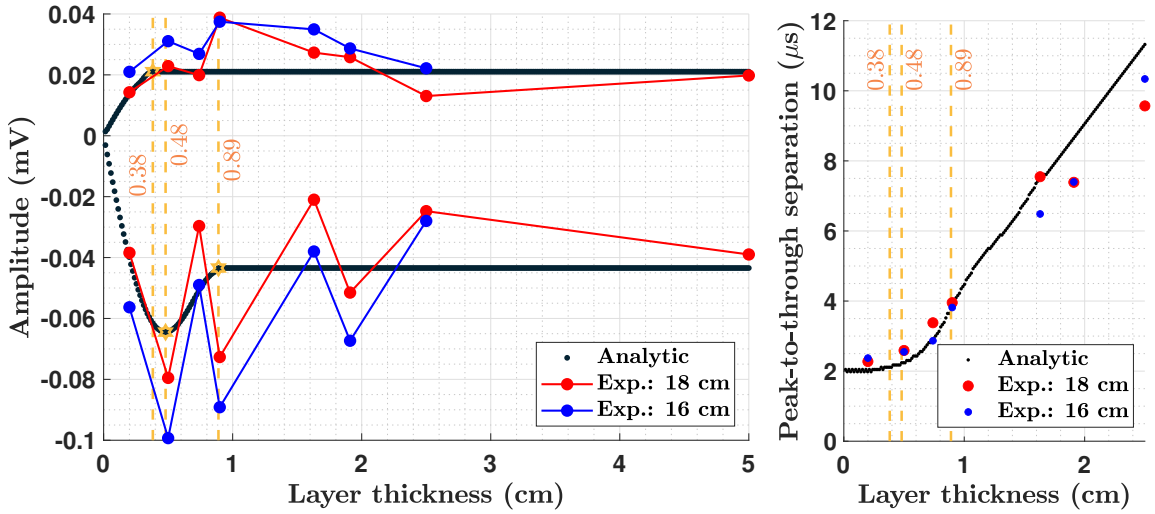

(a) (b)

Figure 6.5: Comparsion, of first maxima and minima (a) and (manually-picked) peak-to-through separation (b), between experimental and analytically derived data. The vertical orange lines highlight thicknesses where the amplitude curves (a) change their behavior. The same two z-offsets of figure 6.3 are displayed: 16.5 cm (blue) and 18.5 cm (red). The 5 cm thickness was omitted for covenience.

The results presented in this section confirm that the relation between the interface response and the layer thickness follows strictly what can be observed for seismic waves. Based on Widess (1973), it became clear that, in analogy to its seismic counterpart, a thin layer for an EM interface response must have a thickness smaller than 1/4 of the P-wavelength inside the layer. Moreover it was found that, as long as only the layer thickness matter, an amplitude enhancing will occur when the layer has a thickness of $\lambda/2$. These results are in agreement with the numerical observations of Haines and Pride (2006), but disagree with the, also numerical, conclusions of Grobbe and Slob (2016) that reported a maximum amplitude increase for thicknesses close to the dominant P-wavelength. There is also a disagreement

with the experimental results of Peng et al. (2017), that found, considering a 1 cm P-wavelength, that amplitudes always increased with layer thinning, even for thicknesses smaller than $\lambda/2$.

6.2 Effect of fluid conductivity

In the porous media forming the Earth's crust, the properties of the fluids filling up the pores of the different geological layers will vary significantly with pressure, temperature, and rock type, among others. Fluid conductivity is one of the properties used by geophysical methods to infer, for example, the nature of the fluid or the presence of contaminants in the soil. In the context of seismoelectrics, this parameter has a strong influence on the amplitudes of both coseismic and EM interface-generated waves, which decrease with increasing conductivity, as already confirmed by experimental and numerical studies (Zhu and Toksöz, 2003b; Chen and Mu, 2005; Block and Harris, 2006; Schakel et al., 2011a; Zhu and Nafi Toksöz, 2013; Holzhauer et al., 2017). Nevertheless it is not this amplitude behaviour that appeals to seismoelectric exploration, but the fact that the interface response can be used to detect contrasts of fluid conductivity, whereas seismic waves (and consequently the coseismic) are, in effect, insensitive (see Haartsen and Pride, 1997). With that in mind, the point of this section is to use experimental data and numerical simulations to access the effect of varying conductivities on seismoelectric wavefields. By doing so, the present work acts as a complement to previous studies on the subject by providing a quantitative analysis of the dependency of coseismic and interface response on this fluid property.

6.2.1 Methodological aspects of experiments and numerical simulations

The experimental setup adopted, depicted in figure 4.1, follows closely the experiments already discussed in this thesis, whose main porous medium is water-saturated sand, described in section 4.1. Two Vosges sandstone (see details of the rock in section 4.1) layers, with 0.74 and 1.63 cm thicknesses, were used. Both displacement and electric potential measurements were made along the z-axis. Displacement was measured at 158 points, 79 in each side of the sandstone layer, spaced by 0.125 cm. Electric potential measurements consists of 80 points evenly spaced, by 0.25 cm, on each side of the layer (i.e., 40 in each side). Regarding how conductivities were changed, the procedure was detailed and validated in section 4.9. It consists, essen-

Table 6.3: Conductivities, layer position along the z-axis, and zeta of the sand in the experiments where the conductivity of the fluid, filling the pores of the sand, vary. While the first two parameters were measured from the experiment, the third was empirically estimated by comparing numerical simulations and experiments.

Layer thickness (cm)	**Sand conductivities (mS/m)**			
0.74	1.31	3.65	7.6	15.3
1.63	1.31	4.1	7.7	15.2
	***z*-limits (cm)**			
0.74	[11.88, 12.62]	[11.6, 12.34]	[11.62, 12.36]	[11.82, 12.56]
1.63	[11.6, 13.23]	[11.69, 13.32]	[11.86, 13.49]	[11.73, 13.36]
	ζ (mV)			
0.74	11.51	1.15	1	1.76

tially, in isolating sand and sandstone using a very thin ($<<$ 1 mm) impermeable plastic bag. By doing so, the fluid conductivity in the sand can be adjusted using a NaCl solution, before the bag-protected layer is inserted in the sand. The actual conductivities, measured for each case studied, are summarized in table 6.3, along with the limits/positioning of the layers along the z-axis during each experiment.

Regarding the numerical modeling, as in the previous simulations, a three layer model was used: the first and third layers adopt the physical properties of the saturated sand, and the second layer the properties of the sandstone, all listed in table 5.1. Besides the different fluid conductivities, the zeta potential was also adjusted to numerically simulate the experiments, with both parameters detailed in table 6.3, along with the z-position of the sandstone layer's boundaries.

The dependency of ζ on the fluid conductivity, in a porous medium, has been studied by several authors (Ishido and Mizutani, 1981; Pride and Morgan, 1991; Lorne et al., 1999a; Revil et al., 1999a; Vinogradov et al., 2010; Vinogradov et al., 2018; Walker and Glover, 2018; Li et al., 2018). Nevertheless, while most researchers note an increase of ζ with conductivity, here an inverse behaviour was considered, much like that reported in Guichet et al. (2003). Moreover, positive ζ values are less likely to happen, as opposed to negative ones, but they do exist in certain situations, like reported by Ishido and Mizutani (1981) and Dukhin et al. (2005) for experiments where aluminium nitrate ($Al(NO_3)_3$) and alumina (Al_2O_3), respectively, exist in the pore fluid. Positive ζ was also observed by Guichet et al. (2006), when the fluid has a PH of 11.7, and the authors associate this positive value to calcite precipitation. At last, because neither ζ nor the fluid composition were measured, to define the ζ values to use in the numerical simulations, a sensitivity study focusing on its influence on the ratio between interface response and coseismic amplitudes

was performed. In the end, the ζ that best describes the experimental data was employed in the simulations and for each σ_f value considered in this section, the corresponding ζ value are displayed in table 6.3.

6.2.2 Experimental results and discussions

After the experimental acquisition, both electric and displacement datasets were band-limited ([50 kHz – 1 MHz]) to attenuate low and high-frequency noise. A detrending procedure was also applied to remove possible linear trends in the measurements. Figures 6.6 and 6.7 show part of the electric potential measurements obtained with both layers. Notice that for the 0.74 cm layer a fifth dataset is also shown, which correspond to measurements made when the fluid conductivity, of sand and sandstone, was the same (about 2 mS/m). This is the same data presented in section 4.9 to represent acquisitions without a plastic bag to isolate the sandstone layer. This data was acquired around the same period as the other three higher conductivities, contrarily to the datasets obtained with $\sigma_f = 1.31$ mS/m, which were obtained 11 months before all other data treated here. At last, to superimpose the traces in figures 6.6 ad 6.7, a time shift was applied to ensure the interface response of all datasets are synchronous, for that the experiment with $\sigma_f = 1.31$ mS/m was used as a reference.

In the two measurements displayed in figure 6.6a, the synchronous event before 0.08 ms is the interface response and those after 0.09 ms correspond to the coseismic due to P-waves. From the coseismic signals it is evident amplitudes reduce when increasing the fluid conductivity in the sand. The discrepancy in terms of time while superimposing the coseismic signals is mainly due to electrode positioning, and given a P-wave velocity of 1783 m/s (typical in the experiments) the mean error in position is about 0.5 mm, which is half the electrode diameter (see section 4.7), thus above the experiment's spatial precision. Figure 6.6b shows a close-up of the interface response at 9 different offsets, in order to facilitate the understanding of how it evolves with offset and changes in fluid conductivity. It can be noticed that the interface response seems to decay with increasing fluid conductivity, except when $\sigma_f = 1.31$ mS/m which results in EM interface responses whose amplitudes are lower than what one would expect, based on the coseismic behaviour. Similar observations can be made by analyzing figure 6.7, corresponding to the experiments with a 1.63 cm layer. In this configuration both the coseismic and the interface response display the same amplitude behaviour (as a function of σ_f in the sand) as

they do when the 0.74 cm-thick layer was used. Note also in figure 6.7b the effect of changing the layer thickness in the waveform of the interface response, a subject discussed in the previous section, 6.1.

Instead of comparing the waveforms of each experiment, a broader perspective can be attained by the analysis of amplitudes. With that goal, figures 6.8 and 6.9 show the first maxima and minima of the velocity ($\dot{u}_y$), calculated from the displacement measurements on top of the sand, and coseismic measurements (V_{exp}), as well as the absolute maxima of the interface response (V_{EM-exp}), for both layer thicknesses considered in this section. In the following discussion, mainly z-offsets bigger than those of the sandstone layers (see table 6.3) will be of interest, seeking to avoid wave interference effects linked to the large PZT source diameter, which influence both amplitudes and waveforms of $\dot{u}_y$, as discussed in the previous chapter.

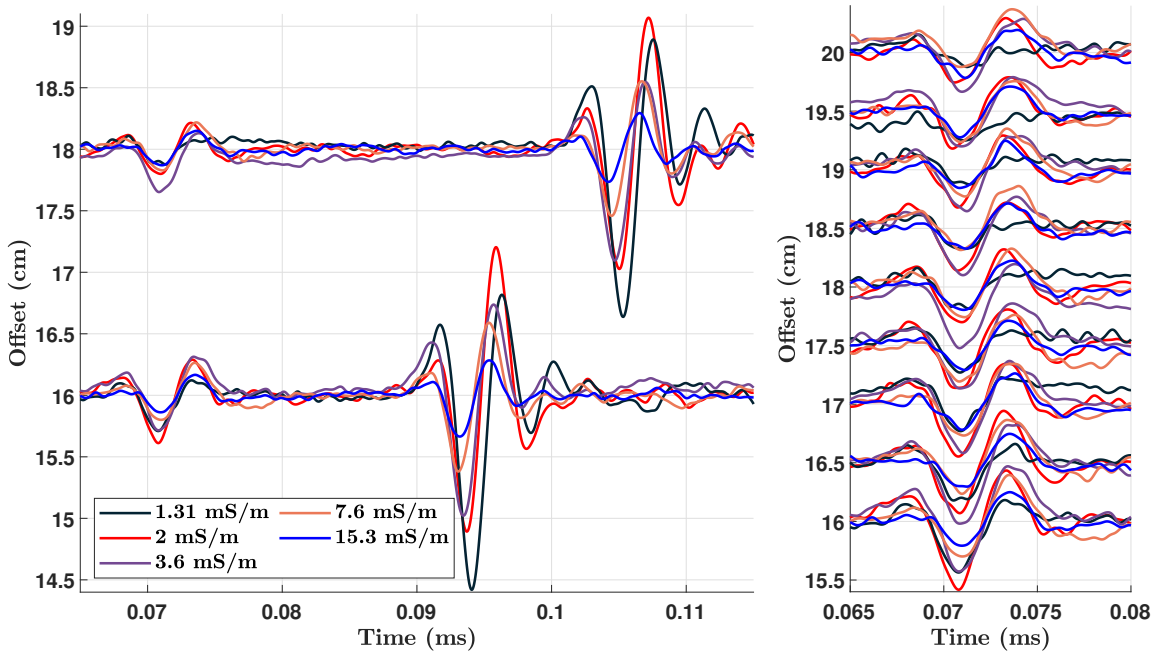

Figure 6.6: Comparison of experimental measurements obtained by varying the fluid conductivity in the sand (see details in the text), while using Vosges sandstone layer whose thickness is equal to 0.74 cm. (a) shows the EM interface response (earlier event) and the coseismic, associated with P-waves, measured at two offsets of the acquisition line. (b) focuses on the interface response at 9 offsets, seeking to detail the waveform and amplitude changes of this signal in the experiment.

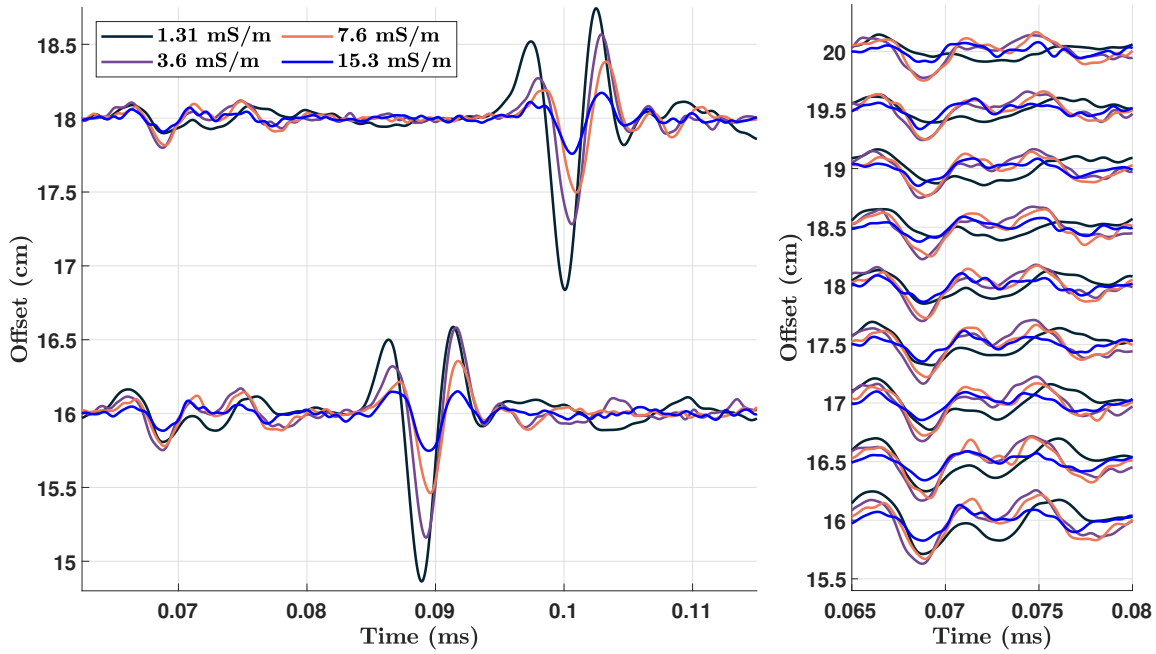

Figure 6.7: Superimposing measurements obtained from the experiments when fluid conductivity (of the sand) was varied and a 1.63 cm-thick sandstone layer used. In (a) the experimental records are displayed for two offsets and the interface response (earlier event), as well as the coseismic, can be seen. (b) shows a zoomed-in extract of the data, which concentrates on the interface response at 9 different offset.

Concerning the amplitudes of $\dot{u}_y$, one can notice in figures 6.8 and 6.9 that instead of being the same for all experiments (since it should only mildly depend on σ_f), it does vary. However, this variation does not seem to be connected with σ_f, once no direct or inverse proportionality is evident, e.g., in 6.8a the amplitude when $\sigma_f = 15.3$ mS/m are closer to those when $\sigma_f = 1.31$ mS/s, not $\sigma_f = 3.6$ mS/m as one would expect if a proportionality relation existed. Focusing now in the coseismic amplitudes, figures 6.8b and 6.9b, notice that their decrease with increasing σ_f is obvious. Nevertheless, this amplitude *vs* σ_f trend is not linear, as anticipated by the fact ζ also varies with σ_f, in a non-linear manner (see Pride and Morgan, 1991), and that both physical properties (σ_f and ζ) are first-order parameters in the seismoelectric transfer function (equation 2.66b) describing the coseismic amplitudes. One can also observe, in the coseismic amplitudes, that at small z-offsets ($<\simeq 5$ cm) a change of behaviour is present, which is more pronounced for $\sigma_f = 15.2$ mS/m in figure 6.9b, where even the minima shows positive values. This effect, at small off-

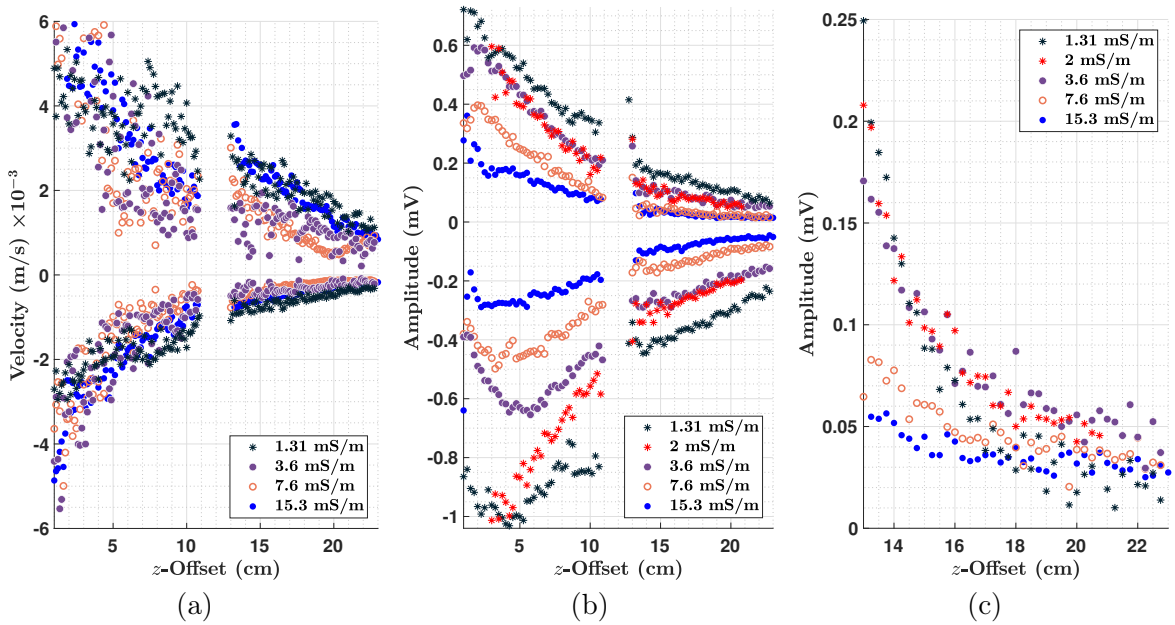

Figure 6.8: Amplitude *vs* z-offset obtained from the experimental acquired by varying the fluid conductiity of the sand, when a 0.74 cm-thick sandstone layer was present. (a) shows the first maxima and minima of the seismic velocity, (b) the first maxima and minima of the coseismic, and (c) the absolute maxima of the EM interface response (only at offsets bigger or equal to 13 cm). Note the y-axis in (a) was bounded for values between -6E-3 and 6E-3 m/s in order to highlight the differences between all datasets.

sets, is a consequence of the EM signature of the PZT source, which is a synchronous and strong (in terms of amplitude) event recorded in the beginning of every electric measurement (see the various electric potential records in chapter 4).

The maximum absolute amplitudes of the EM interface response appear in figures 6.8c and 6.9c, for both layer thicknesses considered in this section. In theses figures, there are two zones that must be analyzed separately, defined in terms of z-offsets: the first occurs at 13cm $\leq$ z $\leq$ 15cm, and the second at z $>$ 15 cm. The first region is marked by wave interference between coseismic and EM interface response, controlling the values of amplitudes which, consequently, decay with increasing σ_f. In the second region, the amplitudes obtained when both media had $\sigma_f = 1.31$ mS/m are, in general, equal or lower to amplitudes obtained with other fluid conductivities. Moreover, when $\sigma_f > 1.31$ mS/m, amplitudes show, again, an inverse proportionality with the fluid conductivity, which is more pronounced in figure 6.8b.

In order to put the results presented so far into perspective, it is worth comparing them with the literature. While most of the experimental work in seismoelectrics

report a decay of coseismic amplitudes with increasing fluid conductivity (e.g., Chen and Mu, 2005; Holzhauer et al., 2017), there's less consensus regarding the EM interface response. Most laboratory studies (and their corresponding numerical simulations) focus on fluid-porous medium interfaces, and even though it is not exactly the case here, there are similarities that should be pointed out. For example, in Schakel et al. (2011a), the numerical and experimental data used to explore the influence of σ_f on the interface response, shows the latter has higher amplitudes when $\sigma_f = 12$ mS/m than when it is equal to 1.27 or 101 mS/m. That essentially suggests amplitudes increase with σ_f until a certain value, after which it decays proportionally with increasing σ_f. This same behaviour was reproduced numerically by Block and Harris (2006) and experimentally by Zhu and Toksöz (2003b). The three studies mentioned corroborate the results of this section, even though they did not consider different fluid conductivities across the interfaces studied.

Following the analysis of how coseismic and interface response vary with fluid conductivity, it is also primordial to comprehend how they change with σ_f relative

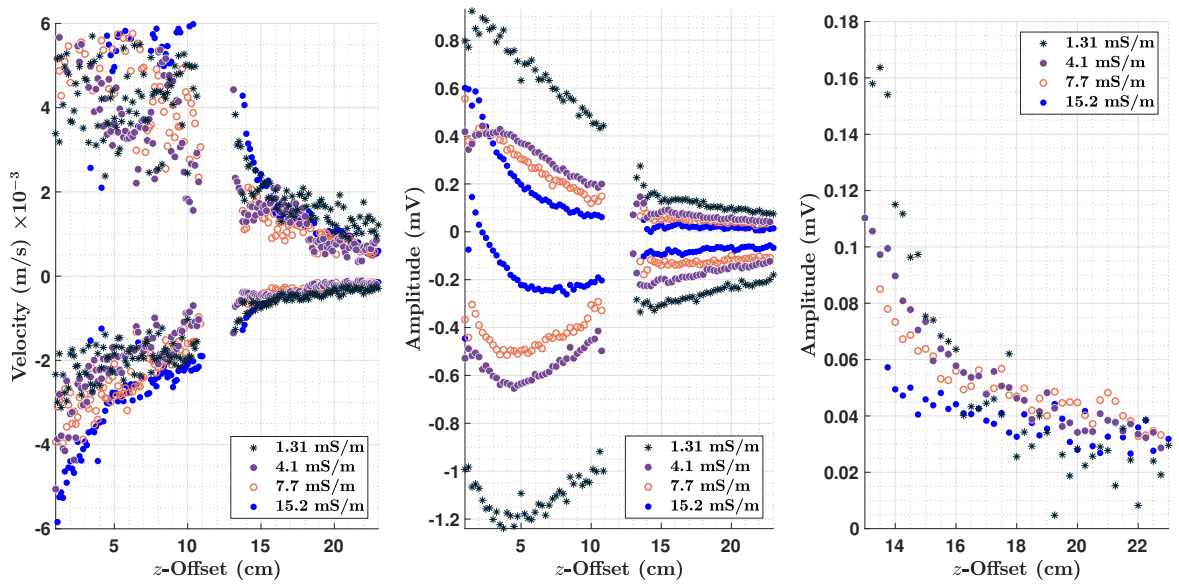

Figure 6.9: Comparison of experimentally measured amplitudes, obtained by varying the fluid conductiity of the sand when a 1.63 cm-thick sandstone layer was present. (a) displays the first maxima and minima of the seismic velocity, (b) the first maxima and minima of the coseismic, and (c) the absolute maxima of the EM interface response (only at offsets bigger or equal to 13 cm). Seeking to highlight the differences between all datasets, the y-axis in (a) was bounded for values between -6E-3 and 6E-3 m/s.

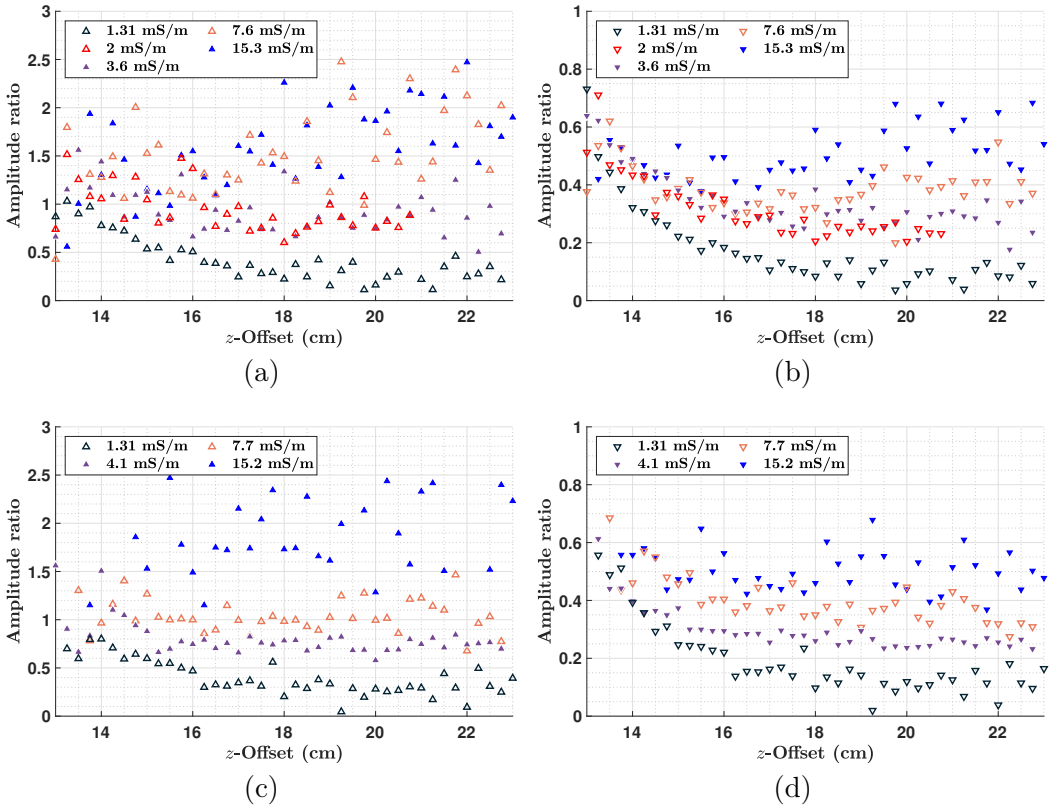

Figure 6.10: Amplitude ratio between the EM interface response and the coseismic due to P-waves. (a) and (b) represent the case when a 0.74 cm-thick Vosges sandstone layer was inserted in the sand, and (c) and (d) the case with a 1.63 cm-thick layer. Regarding the amplitude ratio, (a) and (c) consider the first maxima of the coseismic, while (b) and (d) the first minima; note that all figures used the absolute maxima of the interface response.

to each other. The comparison can be seen in figure 6.10, with 6.10a and 6.10b showing, for the case when a 0.74 cm-thick layer is present, the ratio between the interface response's amplitudes and the first coseismic maxima and minima, respectively. In addition, for experiments in which a 1.63 cm-thick layer was used, figures 6.10c and 6.10d show the interface response-to-coseismic amplitude ratio considering, respectively, the first coseismic maxima and minima. A general conclusion can be drawn from these four figures: as the fluid conductivity in the sand increases, both the coseismic and the interface response decay in amplitude, however it is the coseismic that decays faster. This observation implies the coseismic dependency on σ_f is stronger than the interface response one, i.e., coseismic wavefields are more sensitive to the fluid conductivity of the porous medium they propagate in. Conversely, the EM interface response is not only sensitive to the physical parameters of the

medium it propagates, but it also depends on contrasts of these parameters across the interface it radiates from (see the sensitivity study in Garambois and Dietrich, 2002), what justifies the behavior (with respect to σ_f) in figure 6.10. Finally, as σ_f increases in the sand, one should expect the amplitudes of the interface response to approach, or even exceed, those of the coseismic.

6.2.3 Comparing experiments and theory

In what follows the experimental data will be compared with numerical predictions using analytic and numerical solutions of the governing equations of Pride (1994). For conciseness, only the theoretical predictions in the case of a layer with 0.74 cm thickness will be presented. As in chapter 5, at first the transfer function obtained from the experiments will be contrasted with the theory. Following that, the numerical simulations and its details, will be presented to evaluate how well the theory predicts the laboratory data.

Transfer function `TF` analysis

As reviewed in section 5.6.2, to estimate the experimental TF, the z-oriented electric field is calculated from the electric potential measurements and its first maxima and minima is divided by the respective maxima and minima of the velocity data, numerically estimated from the displacement measurements. Figures 6.11a and 6.11c show the $E_z/\dot{u}_y$ values, estimated for each conductivity considered in this section. It is important, however, to stress that the focus of the present study is on the actual influence of the conductivity on seismoelectric signals, thus one should notice that differences in velocity measurements, as observed here (see figures 6.8 and 6.9), need to be corrected so the changes in the experimental TF actually translates to variations in σ_f. To perform said correction, the TF calculated when $\sigma_f = 1.31$ mS/m was taken as a reference, then the velocity data of every experiment was compared with the reference to estimate a mean amplitude ratio (considering first maxima and minima), which was finally used as a correction factor to the estimated TF; table 6.4 shows all the correction factors used. Note that due to reasons mentioned before, only z-offsets bigger or equal to 13 cm were used to estimate these values, even though it was confirmed that accounting for all z-offsets, values close to the ones in table 6.4 can be found. At last, figures 6.11b and 6.11d show the TF values after amplitude corrections.

Table 6.4: Correction factors used to adjust the values of the TF estimated from the experiments. These were calculated as the ratio between all velocity measurements and the velocity records obtained when $\sigma_f = 1.31$ mS/m. The fluid conductivity associated with each factor is also displayed for completness.

Layer thickness (cm)	Correction factors		
0.74	0.56 (3.5 mS/m)	0.5 (7.6 mS/m)	0.83 (15.3 mS/m)
1.63	0.66 (4.1 mS/m)	0.65 (7.7 mS/m)	0.82 (15.2 mS/m)

In figure 6.11, the dependency of seismoelectric signals, specifically the coseismic linked to direct P-waves, on the fluid conductivity in the medium studied is evident, being more noticeable in figures 6.11b and 6.11d, after amplitude correction. The bigger σ_f is, the lower the $E_z/\dot{u}_y$ values, following the increase in coseismic amplitudes, as expected. However, the change in values with σ_f is not linear, as described by the fact TF $\propto \frac{\zeta}{\sigma_f}$ with ζ depending on σ_f in a logarithmic manner (Pride and Morgan, 1991; Revil et al., 1999a). Moreover, from figures 6.11c and 6.11d, even though there's an apparent z-offset dependency, it is not conclusive. Notice, at last, that when $\sigma_f = 3.65$ or 4.1 mS/m there are a handful number of points with higher values than most. These are a consequence of velocity measurements with discrepant low amplitudes (see how they appear in figure 6.8a and 6.9a), due to acquisition issues.

To compare the theoretical predictions of $|E/\dot{u}|$, two models will be used for the sand. The first consider the physical parameters of Holzhauer et al. (2017), since the sand used here is essentially the same used there. Also their values of fluid conductivity are in the same range tested in the present work. However, Holzhauer et al. (2017) did not fully saturate their medium and worked with frequencies two orders of magnitude lower than the ones used here. For that reason, a direct comparison of TF values is not reasonable, but since their $|E/\dot{u}|$ values are close to the theoretical predictions, using their model parameters, adapted to the present situation (i.e., full saturation and frequencies between 100 and 300 kHz), is an alternative and meaningful way to compare and contextualize the results of this section.

The second model consists mainly of that used in chapter 5, whose parameters are listed in table 5.1, with the exception of σ_f and ζ that were adjusted for each experiment; their new values are displayed in table 6.3. Moreover, it is necessary to correct over/underestimation of numerically simulated wavefields, as a consequence of uncertainty in the physical parameters adopted and errors on the approximation used to simulate all 3D complexities inside the experiment (long electrodes, large source, reflections on the sides of the plastic box, as well as on the sand-air interface,

etc.). Therefore, when comparing experiments and simulations, fitting factors are used to adjust the TF. Because the seismic wavefields are, in practice, not affected by changes in σ_f, no matter the fluid conductivity the simulations produce the same result, which is over-predicted by a factor 3.5 (meaning numerical data need to be divided by this value to fit experiments). Regarding the electromagnetic wavefields, table 6.5 shows the factors, estimated empirically by analyzing successive numerical simulations, for each case of fluid conductivity in the sand. By multiplying the values in this table by the factor associated with velocity wavefields (i.e., 3.5), one finds

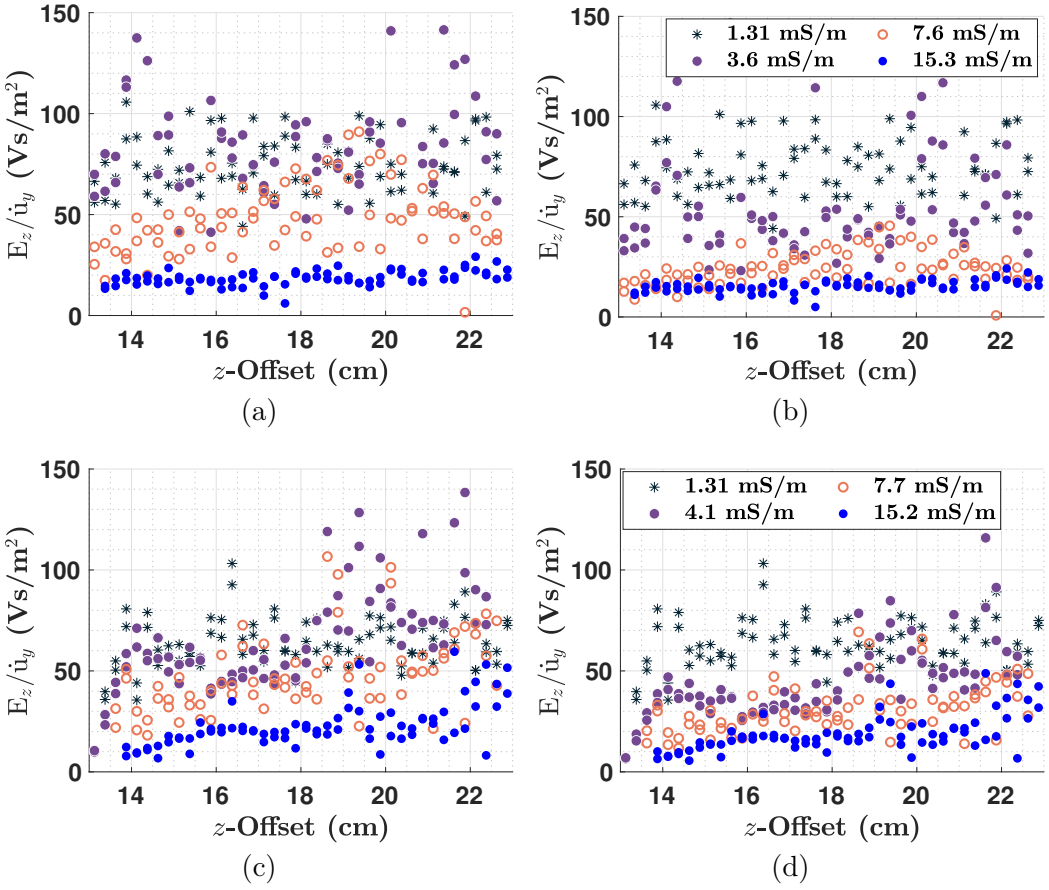

Figure 6.11: Experimental transfer function *vs* z-offset, calculated using the ratio, of first maxima and minima, between the z-oriented electric field and the velocity measurements along y. (a) and (b) represent the experiments using a 0.74 cm-thick layer, while (c) and (d) a 1.63 cm layer. The difference between (a) and (b), as well as (c) and (d), resides in a correction factor (shown in table 6.4) estimated from the velocity data, and used to ensure the changes in the TF come solely from varying σ_f, not from the mechanical parameters (linked to differences in the values of measured velocity): (b) and (d) are values after correction.

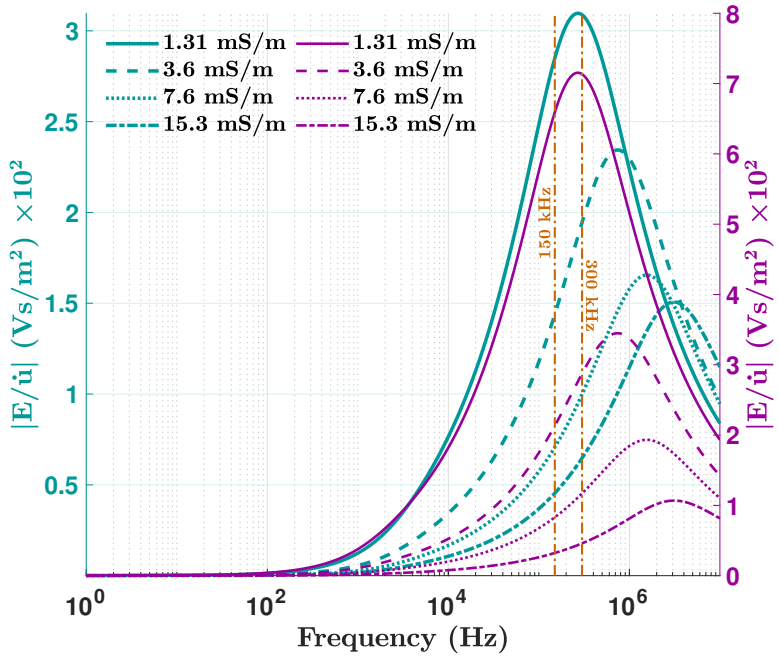

Figure 6.12: Comparison of transfer functions calculated with two theoretical models, for all conductivities studied, based on equation 2.66b. In magenta (right y-axis) the calculations used the physical parameters of Holzhauer et al. (2017) for a fully saturated medium. For the data in green (left y-axis) the values of table 5.1 were used, except for σ_f and ζ whose values are displayed in table 6.3, and the correction factors in table 6.5 were applied (see discussion in the text).

the value that multiplied by the theoretical TF adjusts it to the experimental data, and ensures numerical simulations estimate correctly the seismoelectric wavefields. Finally, the values in table 6.5 depend on the physical parameters used and need to be adjust accordingly if the model changes.

Figure 6.12 shows how the TF, calculated using the two models mentioned, with the multipliers of table 6.5 in the second model, varies with frequency for the four values of σ_f studied. The vertical lines indicate two frequencies of interest. Comparing both models one can notice the values of $|\mathrm{E}/\dot{\mathrm{u}}|$ decrease with increasing σ_f. Moreover, the maximum shifts towards higher frequencies the bigger the σ_f value, but it coincides with the same frequency in both models, what implies its position is mainly controlled by the fluid conductivity. Considering the differences, besides the discrepancies in the actual values, what is more remarkable is the fact the model of Holzhauer et al. (2017) is more sensible to σ_f, with TF values dropping faster with this parameter. Even though in the second model, contrarily to the model of Holzhauer et al. (2017), surface conductivity was taken into account, it is inde-

Table 6.5: Values used to correct the theoretical TF for each conductivity of the sand tested. These were estimated with the aid of numerical simulations and represent how close the electric field predicted by theory is to the experiments: 1 is the ideal value, higher than 1 implies underestimated fields and below 1, overestimated. 3.5 represents by how much the seismic wavefields are overestimated by theory. Therefore the actual factors, by which the TF ($|\mathbf{E}/\dot{\mathbf{u}}|$) needs to be corrected, is equal to the values in the table multiplied by 3.5.

Coductivity of sand (mS/m)	1.31	3.5	7.6	15.3
Multipliers $\times 3.5$	0.13	1.33	1.49	1.05

pendent of σ_f and therefore can not explain the difference in how TF decays with fluid conductivity. ζ is the only parameter in equation 2.66b that depends directly on σ_f and was defined differently in both models. That implies the disagreement in the σ_f-dependency between both models comes from ζ. Finally, that suggests the logarithmic rule, describing ζ as a function of σ_f, proposed by Holzhauer et al. (2017) ($\zeta = 0.044 + 0.026\log_{10}\mathtt{M_f}$) may not be adapted to the experiments.

A comparison of experimental and theoretical transfer functions *vs* fluid conductivity is shown in figure 6.13. Both the experimental TF without and with the correction factors in table 6.4 are displayed, figures 6.13a and 6.13b, respectively. For each layer and conductivity, the experimental values of the TF were averaged, with those estimated with maxima and minima treated separately, and the results plotted in figure 6.13. The calculations using the parameters of Holzhauer et al. (2017) consider three frequencies of interest here. Regarding the predictions using the second model, employed during numerical simulations, two frequencies are highlighted.

In figure 6.13, the theoretical models have higher values than the experimental ones. That is expected since in the experiments what is actually measured is $\mathrm{E_z}$ and $\dot{\mathrm{u}}_\mathrm{y}$. Recall also from chapter 4 (see figure 4.1) the fact that displacement (and consequently velocities) are measured practically in a point on top of the sand while electric potentials (and therefore electric fields) are measurements averaged along the whole electrode length. All that indicates the experimental TF can not be equal, in value, to theoretical predictions, which compare the total electric and velocity fields existing in a point in space. Nevertheless, the TF *vs* σ_f trend must be close to experimental values if the model is adapted. Evaluating, qualitatively, if predictions can describe the experiments, it can be noticed that while both coud be used, the model of Holzhauer et al. (2017) does not perform as well as the other, overpredicting values by about one order of magnitude.

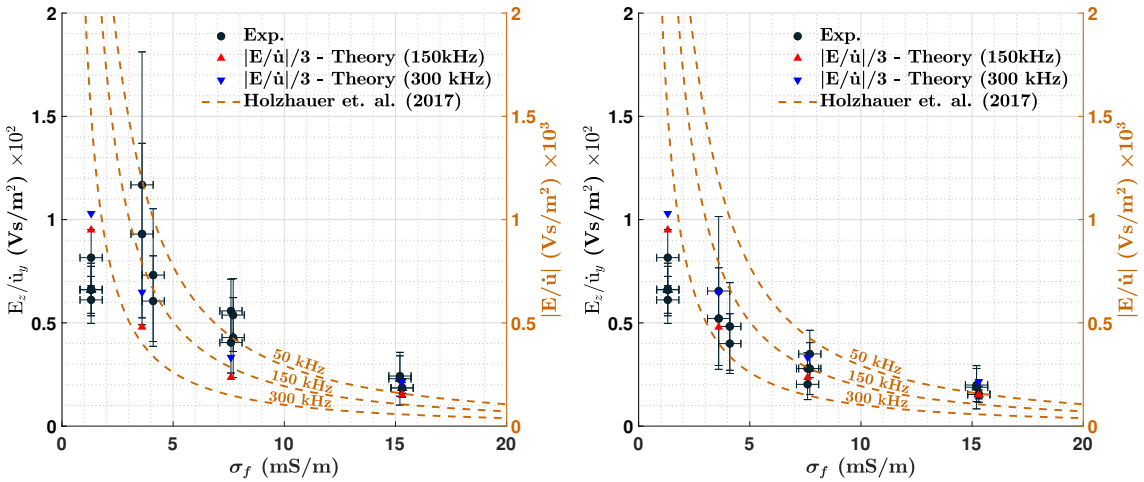

Figure 6.13: Comparison of transfer functions *vs* fluid conductivity. The experimental points are the averaged values, displayed in figure 6.11, for each layer and σ_f studied. (a) with and (b) without correction factors in table 6.4. In the average, the $E_z/\dot{u}_y$ calculated using maxima and minima are plotted separately for each case. The vertical error bars correspond to the standard deviation and the horizontal corresponds to 0.5 mS/m. The parameters of Holzhauer et al. (2017) were used to calculate equation 2.66b at three frequencies, values correspond to right y-axis. The second theoretical model is the one used in the numerical modeling and was carefully adjusted to guarantee simulations fit the experiments.

At last, as long as only coseismic and interface response wavefields are treated separately, the model of Holzhauer et al. (2017) could be adjusted for each fluid conductivity-case and results would be similar to the second model. That could be done either using multipling factors on the TF, or adjusting ζ (considering all other physical parameters are well constrained) as done by Schakel et al. (2011a). On the other side, when simulating both seismoelectric wavefields at once the task becomes more challenging, with the need for numerical simulations since there's no analytical expression describing the transfer function between P-wavefields and the interface response.

Numerical simulations

To complement the previous discussion about the TF, this subsection presents the numerical simulations, based on chapter 3 and section 5.5, seeking to compare both the experimentally measured coseismic and interface response with predictions from Pride's theory (Pride, 1994).

Regarding the physical parameters used to describe sand and sandstone, table 5.1 shows them. An exception happens for the sand, as mentioned in the previous subsection, whose ζ values are those in table 6.3, when σ_f varies, and the correction factors in table 6.5 are used to adjust the transfer function so the simulated data fits better the experiments (note that corrections associated with differences in the seismic measurements, shown in table 6.4, were not necessary in this subsection, thus they were not applied to the data). Figure 6.14 presents a superimposition of experimental and numerical data at two offsets, and figure 6.15 the comparison, of first minima and maxima, as well as the absolute maxima of the interface response maxima, between experiments and simulations.

Looking at the results of the waveform comparison in figure 6.14, there's a good agreement between the modeled data and the measurements, and that is also true for the other offsets. Both the coseismic (signals at times later than 0.09 ms) and the EM interface response (around 0.07 ms) are satisfactorily simulated, with predicted amplitudes and waveforms respecting those from experiments. Note that both the decrease in amplitudes, and the increase in the ratio between interface response and coseismic (recall figure 6.10), with increasing σ_f (in the sand), are well reproduced by the numerical simulations.

Figure 6.15 provide a global view of how the theoretically predicted amplitudes, of coseismic and interface response, compare with the measurements. Focusing first in the coseismic (6.15a), one can notice the simulations provide fair estimations of first maxima and minima, with more consistency at z-offsets bigger than 16 cm, after which the coseismic and the interface response signals do not interfere (i.e., they appear as individual events in the recorded data). Concerning the absolute maxima of the interface response (6.15b), the simulations do not agree as well as they do for the coseismic, with the best fit happening when $\sigma_f = 1.31$ mS/m. This disagreement is likely linked to the fact the amplitudes (of the interface response) are an order of magnitude smaller than the coseismic ones, thus being more prone to noise corruption and, as a consequence, to real amplitude trends becoming masked by noise. In the end, it is safe to affirm that the noise level in the experiments limits the precision, thus making it more difficult to detect the real effect of changing the fluid conductivity on the interface response, even though a variation could be detected in figure 6.10. A straightforward way to improve the SNR would be to apply a gain to ensure amplitudes are above the noise level (a gain of 10 would ensure the interface response has amplitudes in the present range of coseismic amplitudes,

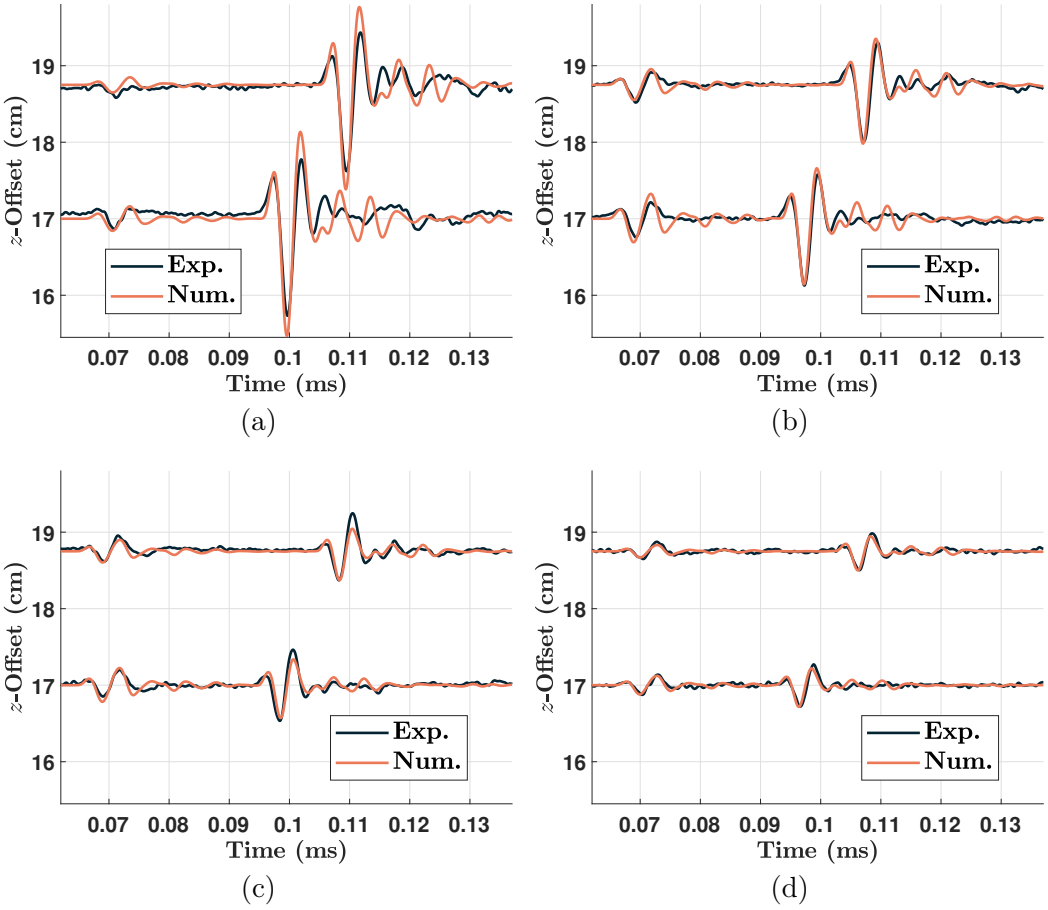

Figure 6.14: Superimposing numerical and experimental data, obtained by varying the fluid conductivity of the sand, at two z-offsets: 17 and 18.75 cm. See the text for details on the modeling. In what regards the σ_f in the sand, (a) shows the experiment with 1.31 mS/m, (b) with 3.6 mS/m, (c) 7.6 mS/m, and (d) 15.3 mS/m. Dark blue corresponds to experimental data and orange to numerical.

thus overcoming the problem of noise corruption). Post-acquisition curvelet filtering is also an alternative (Warden et al., 2012), even though it can't restore the real amplitudes.

At this point it is important to repeat that the factors in table 6.5 quantify how close the modeling is to the experimental data, 1 being the ideal value. Thus, one can notice that, in general for the range of σ_f studied, the higher the fluid conductivity of the sand, the better the theoretical predictions. Block and Harris (2006) and Schakel et al. (2011a) made the same observation when comparing Pride's theory and experiments.

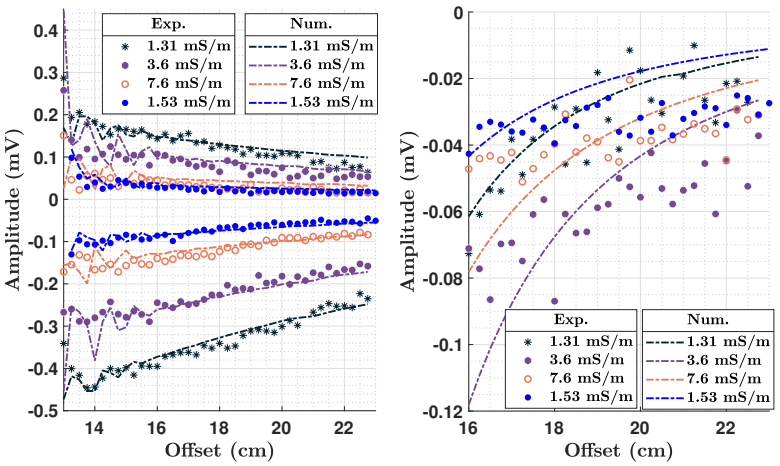

Figure 6.15: Amplitude comparison beteween numerical and experimental data, relative to experiments where the fluid conductivity of the sand was varied. (a) concerns the first maxima and minima of the coseismic signal, and (b) the absolute maxima of the EM interface response. In (b) only z-offsets bigger than 16 cm are displayed to avoid the region the coseismic and the interface response interact.

6.2.4 Sensitivity study of σ_f

Following the observations made using the experimental data, a sensitivity study focused on σ_f was carried out to aid in understanding more thoroughly if theory can predict the σ_f − dependency of the interface response, found with the experiments. Because ζ usually depends on the fluid conductivity (recall section 2.2.2), it was also adjusted. Additionally, porosity and permeability were also studied what allowed conclusions similar to those of the sensitivity tests of Garambois and Dietrich (2002). However, for brevity, and since only σ_f was effectively altered, results for these two properties are omitted.

Numerical simulations followed the same procedure as before, accounting for the length of the electrodes as well as for the PZT diameter (see section 5.5). The geometry used reproduces that of the experiments, i.e., electrodes along the z-axis, but only the results of an electrode positioned at z = 17 cm will be discussed. The physical model adopted, to simulate the seismoelectric wavefields, consisted of a 0.74 cm-thick sandstone layer, positioned between z = 11.88 cm and z = 12.62 cm, inside a water-saturated sand. As usual, table 5.1 shows the physical properties associated with each material, with the exception of σ_f and ζ which are detailed next. To access the effect of σ_f, 20 fluid molarities were tested, considering a NaCl

Table 6.6: Zeta potential (ζ) and surface conductivity (σ_n) used for sand and sandstone layers in the numerical simulations which comprise the sensitivity tests, performed by varying the fluid conductivity. The relation used to calculate ζ from the molarity $\mathtt{M_f}$, in Case-1, is the widely accepted equation of Pride and Morgan (1991). Case-2 and Case-3 use modified versions of the mentioned equations.

	Sand		Sandstone	
Physical property	ζ (mV)	σ_n (mS/m)	ζ (mV)	σ_n (mS/m)
Case-1	$8 + 26\log_{10}\mathtt{M_f}$	0	-12	0
Case-2	$1 + \log_{10}\mathtt{M_f}$	8.3E-2	-12	2
Case-3	$-10\log_{10}\mathtt{M_f}$	8.3E-2	-7	5e-6

solution: the first was 1E-5 mol/L and the other nineteen vary between 1E-4 mol/L until 1.9 mol/L, with a constant step of 1E-4 mol/L. Note that these molarities result, through equations 2.19, in fluid conductivities in the range of those used in the experiments.

Three main cases will be discussed, distinguished by the values of ζ and surface conductivity used for sand and sandstone layers, and referred hereinafter as: Case-1, Case-2, and Case-3. Table 6.6 details how ζ and σ_n were calculated in all cases explored. For the sandstone ζ was kept constant, not depending on fluid conductivity, and for the sand equation 2.23 was used in Case-1 and modified versions of it in Case-2 and Case-3. Case-1 can be considered as the unmodified, or unaltered, version of Pride's theory, because no surface conductivity was taken into account and the definition used for ζ is the same presented in Haartsen and Pride (1997). Case-2 was adapted to account for surface conductivity, and Case-3, besides considering σ_n, it also uses positive ζ values for the sand, which decrease with increasing σ_f, in analogy with all the comparisons between numerical simulations and experiments discussed previously. Moreover, for each case, at first the fluid conductivity varied only in the sand, then in the sandstone; inside the layer where the fluid conductivity did not vary, a value of 1.31 mS/m (corresponding to $\mathrm{M_f} \simeq 1.4124\mathrm{E}-4$ mol/l) was used.

Figure 6.16 summarizes the results of the sensitivity tests, showing the absolute electric potentials calculated for each case studied. The first line concerns Case-1, the middle line Case-2, and the last line Case-3. The left column shows the results of varying σ_f in the sand and the right column the results obtained by changing σ_f in the sandstone. Regarding the signals, the one around 70 μs is the EM interface response (IR) and the one around 95 μs is the coseismic due to fast P-waves.

Looking first at the situation where the fluid conductivity in the sand changes, the difference among the three cases studied are noticeable, however, in all of them,

both the IR and the coseismic amplitudes display a general decay with increasing σ_f, like observed in the experiments. The waveform of the IR varies slowly, in all cases, for fluid conductivities bigger than 5 mS/m, with the first maximum (of the waveform) becoming more prominent with respect to the second, in Case-1 and Case-2, and the inverse trend in Case-3. This suggests the signal's phase changes with σ_f. Additionally, when the fluid conductivity is smaller than 5 mS/m, in Case-1 and Case-2 (figures 6.16a and 6.16c), such change in phase affects the IR's energy, making it drop quickly towards zero, before increasing again. Notice how the shape of the IR signal for the smallest σ_f differs from the shape at the highest σ_f value: it was verified such behavior corresponds to a phase change of about 90°, leading to an apparent change in polarity. Looking at Case-3 (figure 6.16e) the change in IR shape is subtle for all fluid conductivities, even though its energy is also smaller when σ_f has the lowest value analyzed. Going back to the experimental data displayed in figures 6.6 and 6.14, one can notice the IR waveform does vary with σ_f in a similar manner to simulations for Case-3: the ratio between second-to-first maxima increases. Notice, however, that this agreement does not, necessarily, means the model in Case-3 is closer to reality, only that it was adapted to fit the experiments. Definitive conclusions about IR waveforms can only be inferred by properly constraining all the physical parameters. What is important to retain is the fact that no matter the case, numerical simulations, and therefore Pride's theory, are able to predict the amplitude and waveform trends as σ_f varies.

Regarding the coseismic, at most, but the smaller values of σ_f, and for the three cases explored, waveforms change slowly, as for the IR. To understand what happens when the fluid conductivity is too small, one should focus on the analytical solution, using the parameters in table 5.1, of the transfer function in the sand $\mathrm{TF}_{\mathrm{sand}}$, equation 5.1, which describes the coseismic behavior. In most $\sigma_f -$ situations (i.e., when $\mathtt{M_f} >\simeq 1\mathrm{E}-4$), $|L(\omega)/\tilde{\epsilon}(\omega)|$ (recall the definitions of effective electrical permittivity and electrokinetic coupling coefficient in chapter 2) increases with frequency, however, when the fluid conductivity becomes too small one finds that such dependency reverses, i.e., $|L(\omega)/\tilde{\epsilon}(\omega)| \propto 1/\omega$, what ultimately implies that the shape of the coseismic waveform will change accordingly. Comparing with the experimental records in figures 6.6 and 6.14, as with the IR, the change of coseismic waveforms predicted by theory, as σ_f increases, is consistent with the laboratory observations discussed previously.

Focusing now at the scenario where the fluid conductivity inside the sandstone changes, figures 6.16b, 6.16d, and 6.16f show the results for the three cases. The coseismic signal remains unchanged in all cases, since the simulations consider an electrode in the sand, where physical properties do not vary, and the effect of changing σ_f in the intrinsic attenuation is negligible. As for the IR, in Case-1 and Case-2 there is a general increase of its energy with σ_f, and in Case-3 the inverse behavior exists. The value of σ_f for which the IR energy is the lowest, in Case-1 and Case-2, and, conversely, highest in Case-3, corresponds to the value that is closer to the fluid conductivity in the sand. This, of course, agrees with the sensitivity tests shown in Garambois and Dietrich (2002). Again, the phase of the IR waveform is affected by σ_f, such that for the smallest value of σ_f, in Case-1 and Case-2, the phase differs by about -90°.

In order to explore further the dependency of seismoelectric wavefields on σ_f, as well as to put in evidence the previous discussion based on figure 6.16, the ratio between IR and coseismic energy is shown for each case studied in figure 6.17. Energy, as mentioned here, corresponds to the integral of the squared modulus of a signal, or conversely, the square of its Euclidean norm. To calculate it, first the IR and the coseismic waveforms, in figure 6.16, were isolated, then the squared modulus of the samples corresponding to each signal was calculated, and finally they were added. The calculations for the IR were done by constraining its waveform to the interval $[65\mu s, 80\mu s]$, and for the coseismic to the interval $[93\mu s, 102\mu s]$. Additionally, because the IR's amplitude is proportional to the contrast of physical properties across a layer (i.e., $|\mathrm{IR}| \propto |\mathtt{TF}_{\mathrm{sandstone}} - \mathtt{TF}_{\mathrm{sand}}|$, with $\mathrm{TF}_{\mathrm{sandstone}}$ the transfer function of the sandstone layer) and $\mathtt{TF}_{\mathrm{sand}}$ is proportional to the coseismic amplitudes, one can infer that

$$\left| \frac{\mathtt{TF}_{\mathrm{sandstone}} - \mathtt{TF}_{\mathrm{sand}}}{\mathtt{TF}_{\mathrm{sand}}} \right| \tag{6.1}$$

is proportional to the ratio between IR and coseismic amplitudes. This relation was analytically calculated, with the aid of equation 5.1, for frequencies between 100 and 350 kHz and figure 6.17 shows the results *vs* fluid conductivity.

Note that, since the relation 6.1, above, is a function of the electric field, and that only experimental electric potentials are analysed, a discrepancy in values when comparing it with the energy ratio of the numerically calculated IR and coseismic is expected. The fact simulations approximate the measurements made by a long electrode also play a role in the differences mentioned. Nevertheless the trend characterizing how both the energy ratio and the relation 6.1 change, with any physical

property, will be similar. The results displayed in figure 6.17 confirm the previous assertions, showing a good agreement for all three cases studied. The leftmost column, in figure 6.17, represents Case-1, the middle column Case-2, and the rightmost column Case-3; the first line concerns the simulations in which σ_f varied in the sand, and the second line simulation with σ_f varying in the sandstone.

The amplitude and waveform behavior of coseismic and IR waves in figure 6.16 is highlighted, and complemented, by figure 6.17. The top line shows that IR amplitudes decrease in a slower manner than the coseismic ones. Consequently the energy ratio increases with fluid conductivity, as is the case in the experiments (see figure 6.10), except when σ_f is too small. This dependency can be explained, with the aid of relation 6.1: in all three cases, when σ_f is very small $|\mathrm{TF}_{\mathrm{sand}}| > |\mathrm{TF}_{\mathrm{sandstone}}|$ and the energy ratio shows a decreasing trend, but as σ_f increases, $|\mathrm{TF}_{\mathrm{sand}}|$ decreases, approaching $|\mathrm{TF}_{\mathrm{sandstone}}|$ until a minimum when both transfer functions are closest in absolute value; eventually $|\mathrm{TF}_{\mathrm{sand}}|$ becomes smaller than $|\mathrm{TF}_{\mathrm{sandstone}}|$, and from this point onward the energy ratio has an increasing trend. The change in phase observed for low σ_f values in figure 6.16 is, therefore, a consequence of $|\mathrm{TF}_{\mathrm{sand}}|$ being reduced until the point it is smaller than $|\mathrm{TF}_{\mathrm{sandstone}}|$. Numerically this is equivalent to interchanging the layers in the simulations, and is the same reason the IR signals created at the two interfaces, of a thick layer inside a homogeneous material, are polarity-reversed with respect to each other, as discussed and illustrated (with numerical and experimental data) in section 6.1.

Observing the bottom line of figure 6.17, which corresponds to the simulations in the right column of figure 6.16 (fluid conductivity varies only in the sandstone), in Case-1 and Case-2 (figure 6.17d and 6.17e, respectively) there is a general increase of the energy ratio. Like the previous paragraph, the evolution of the energy ratio, for these two cases, can be explained using relation 6.1: $|\mathrm{TF}_{\mathrm{sand}}|$ is always bigger than $|\mathrm{TF}_{\mathrm{sandstone}}|$ and as the fluid conductivity increases, $|\mathrm{TF}_{\mathrm{sandstone}}|$ decreases, thus increasing the absolute value of the difference between the transfer function of both media. An exception happens in Case-2 (figure 6.17e) when σ_f has the smallest value analyzed ($\simeq 0.093$ mS/m) in the sandstone, which produces an energy ratio bigger than those associated with higher values of fluid conductivities, as a consequence of accounting for surface conductivity in the media. Note how in Case-1 (figure 6.17d), which disregards surface conductivity, the trend of energy ratios differs from Case-2 when using too low σ_f values. Regarding Case-3 (figure 6.17f) the energy ratio, contrarily to the previous cases, decrease with increasing fluid conductivity. As a

consequence of a positive ζ in the sand and a decrease of $|\mathrm{TF}_{\mathrm{sandstone}}|$ with increasing σ_f, the absolute difference in the numerator of relation 6.1 will also decrease with σ_f, thus explaining the trend in figure 6.17f. All things considered, an experiment where the fluid conductivity inside the sandstone varies would complement those discussed in this section, and it could help tackle the hypothesis of a positive ζ in the sand.

It is important to mention that relation 6.1, even though simplistic, is valid no matter the physical property studied. Therefore the amplitude and waveform behavior, of seismoelectric wavefields, created by varying σ_f will also occur when varying other physical properties. Additionally, the comparison in figure 6.17 implies that it could be used to aid in the interpretation of seismoelectric measurements, and also in adjusting numerical simulations (as done here) to ensure the correct trends between IR energy and the studied physical property can be reproduced. At last, while zeta controls the polarity of coseismic waves in the sand, the polarity of the IR is dictated by $|\mathrm{TF}_{\mathrm{sandstone}}| - |\mathrm{TF}_{\mathrm{sand}}|$, for example: given an IR signal measured in the sand when $|\mathrm{TF}_{\mathrm{sandstone}}| > |\mathrm{TF}_{\mathrm{sand}}|$, if the sand properties are adjusted to give $|\mathrm{TF}_{\mathrm{sandstone}}| < |\mathrm{TF}_{\mathrm{sand}}|$, the new IR signal will be polarity-reversed with respect to the former.

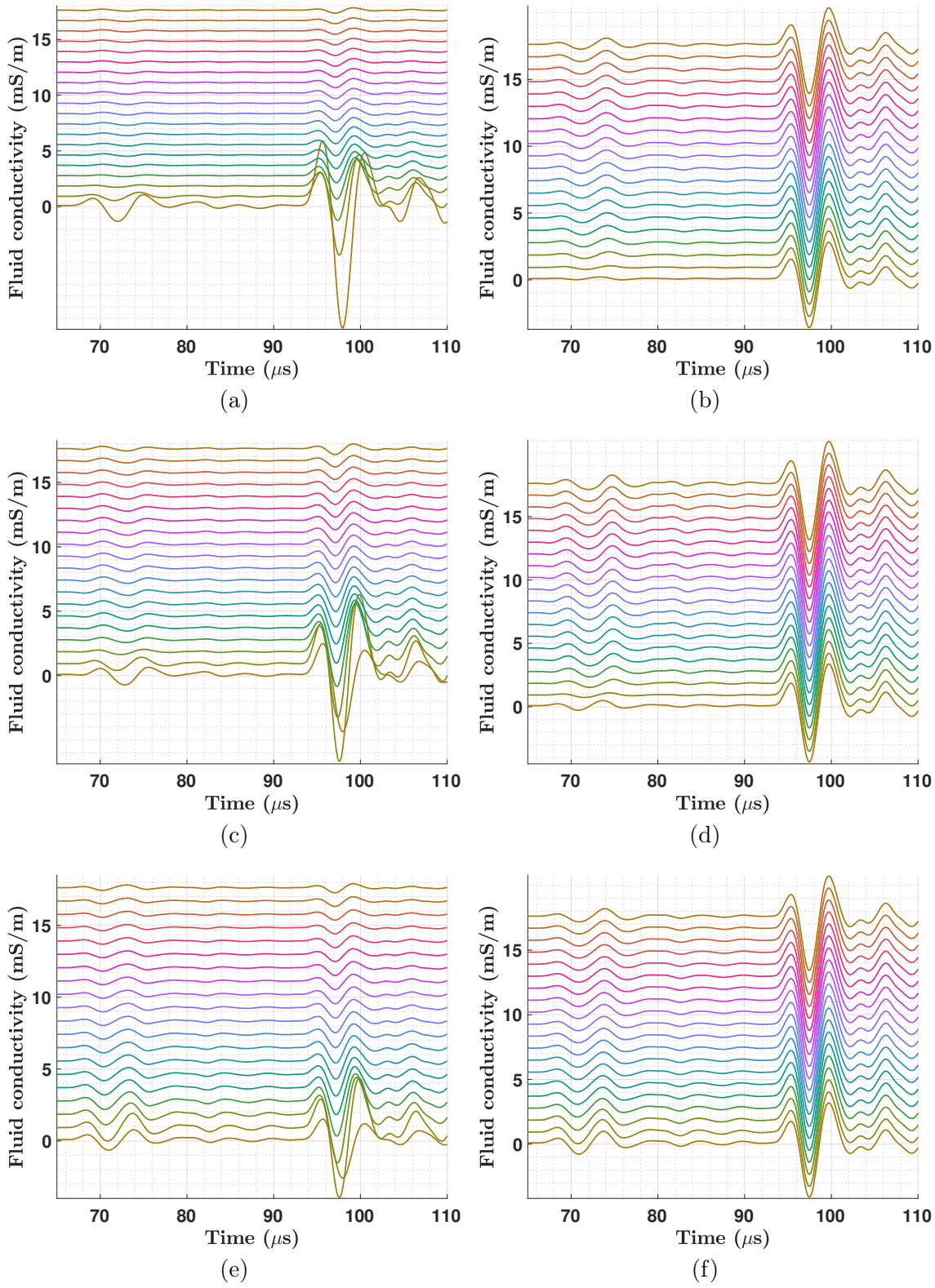

Figure 6.16: Absolute electric potentials, calculated in a model with a 0.74 cm-thick sandstone layer inside sand. The physical parameters of the porous materials are those in table 5.1, except for σ_f and those in table 6.6. Top to bottom, each line represents, respectively: Case-1, Case-2 and Case-3. Columns indicate numerical simulations where σ_f varies in the sand (left), and in the sandstone (right). The earliest event corresponds to the IR and the latest to the coseismic.

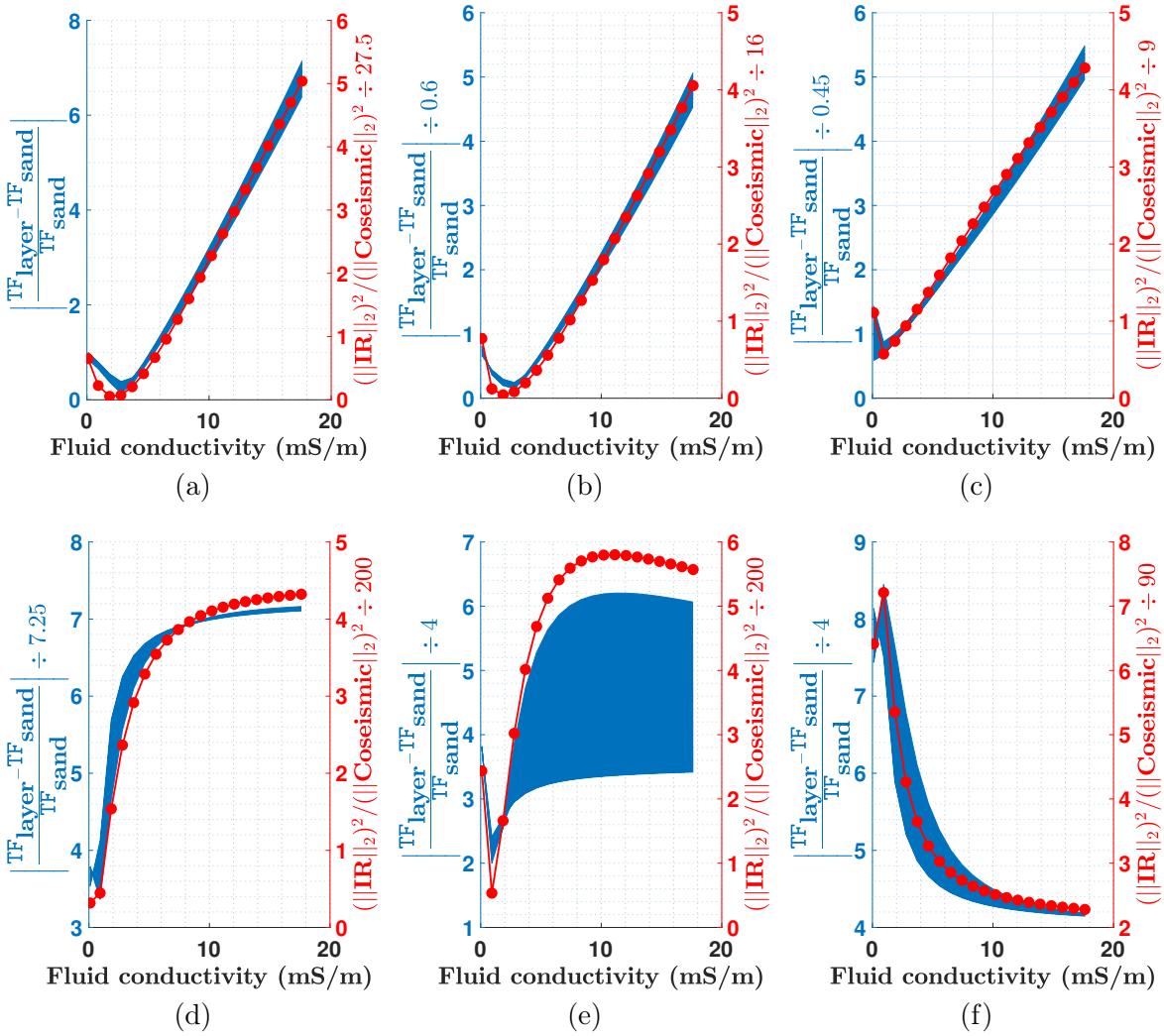

Figure 6.17: Ratio between IR and coseismic energies (in red) and analytical solution of relation 6.1 (details in the text) for frequencies ranging from 100 kHz until 350 kHz (in blue) *vs* fluid conductivity. Top line shows the results when σ_f varies in the sand; bottom line in the sandstone. Case-1 corresponds to (a) and (d), Case-2 to (b) and (e), and Case-3 to (c) and (f). The factors used to superimpose the curves are displayed in the labels of their corresponding vertical axes.

6.3 Partial conclusions

In this chapter, the effect of layer thickness and fluid conductivity across interfaces on the EM interface responses was studied with the aid of experimental and numerical data. The influence of these parameters on coseismic waves was also explored, to some extent. While exploring the influence of layer thickness, it could be noticed that the effect of layer thinning on the EM waves, created at an interface by seismoelectric phenomena, follows closely what is observed for seismic waves. Moreover, it was observed that a maximum signal enhancing, due only to the thickness, happens when a layer has a thickness equal to half the wavelength of the P-wave impinging on the layer. When studying the influence of fluid conductivity, the ability of Pride's theory to predict experimental data was evaluated, and showed to be satisfactory in terms of waveform and amplitude behavior. However, a more in-deep quantitative analysis on how well theory can predict experiments will only be possible after constraining, with precision, the physical parameters of the medium studied. Holzhauer et al. (2017) showed, for the coseismic, that theory is close enough to experimental measurements using a sand medium very similar to the one used here, but at frequencies lower than the transition frequency (see section 2.3.1). This, again, suggests that knowing the physical parameters of the sandstone, specially the electric ones, can improve a lot the previous analysis.

7 Summary, conclusions, and perspectives

7.1 Summary

In the beginning of this thesis, two objectives were put. The first was to develop an experimental set-up that allows repeatability of measurements and that is able to detect seismic and seismoelectric waves with good reliability, thus to measure signals with high signal-to-noise ratio. Eventually, the need to perform multiple electric measurements at once, and possibly automate this task, arose. Additionally, once the experiment was working, it was evident the influence of some physical properties should be explored, and in the end the parameters chosen were the layer thickness and the fluid conductivity in the sand. An experiment using a sample of Fontainebleau sandstone, described in section 4.2, was realized to study the effects of changing a rock (corresponding to a change of all physical properties, except the fluid-related ones). However, even though the interface response was properly measured, because the x and y-dimensions of the Fontainebleau sample were too small, it was decided results would not be discussed, mainly because they could not be compared with theory once the numerical code used can not model the necessary 3D effects. At last, an attemp towards multielectrode acquisitions, as done in Devi et al. (2018) and discussed in section 3.8.1, was made but, because it is incomplete, it will not be presented.

The second objective was to compare the experimental data with numerical simulations, relying on the equations of Pride (1994). To that purpose, the numerical code developed by Garambois (1999) was adapted to the experiment. Initially, the numerical methodology behind the code was thoroughly studies, then the calculation of the missing z-oriented components of the electric and magnetic fields, and also of the electric potential (after Dietrich et al. (2018)), were included. At last, the problem of modeling long electrodes/receivers and a large source (with respect to the wavelength) was addressed.

7.2 Main results and conclusions

As a product of this thesis, a laboratory experiment which allows the simultaneous measurement of seismoelectric wavefields in porous media was validated. Both the EM interface response and coseismic signals, associated with P-waves, were detected using stainless steel electrodes while particle displacement (seismic waves) was measured using a laser vibrometer. Chapter 4 details the experimental set-up as well as the media used, explaining each part of the experiment and justifying the choice of the most relevant parameters. The proposed set-up is essentially an improvement of that shown in Devi et al. (2018), working with signals in the same frequency range (hundreds of kilohertz). By using it, a good signal-to-noise ratio and repeatability could be attained, thus opening the path to laboratory studies focused on reproducing any geological setting of interest, like layers containing fluids, models in which temperature vary, partially saturated media, among others. To my knowledge, until now this laboratory experiment is the only able to, reliably and simultaneously, measure the coseismic and interface responses in a saturated and layered porous medium. Most of the previous research on this subject was focused on fluid-to-porous media interfaces (Zhu and Nafi Toksöz, 2013; Smeulders et al., 2014), and the works that investigated porous-to-porous media interfaces (Chen and Mu, 2005; Wang et al., 2021) were either not able to record both seismoelectric waves, or when they did, the interface response was corrupted by noise.

With the intent of automating electric acquisitions, an electronic card was developed to control, without human interference, which electrode was used in the measurements. Even though the goal of automation was met, as a consequence of the small amplitudes of seismoelectric signals ($\leq$ 1 mV), the noise intrinsic to the electronic card (specifically the relays) made it unfit to the present experiment. Nevertheless, it can still be used in a laboratory context where lower frequencies (and consequently higher amplitude signals) are measured, or in field acquisitions. Alternatively, adding a preamplifier before the card may enhance signals above the noise level and allow the use of this card.

In a second attempt to reduce the duration of electric acquisition, as well as human interaction with the electrodes, a preamplifier with 8-channels (able to measure 8 electrodes at once) was developed with the collaboration of E. Normadin and P. Plouraboué. Compared with the main preamplifier used during acquisitions (see section 4.7.1), the new preamplifier provided, in general, signals with almost the

same waveform but amplitudes were 6.5 times higher than expected, which could be a consequence of its higher input impedance compared to the main preamplifier. Despite the promising results, the introduction of significant artifacts, distorting to a great extent the interface response, made it unsuited. Because it is an in-house equipment, further testing will certainly help detect and solve the problems.

The experiments with varying conductivity necessitated a physical barrier to isolate sand from sandstone, ensuring they could have different fluid conductivities. For that purpose a zip-lock plastic bag was used as an envelope to isolate the sandstone, and as long as the proper lock part of this bag was not inserted in the sand, no fluid was exchanged between both media. This was proved experimentally by the fact measurements with and without the plastic led to the same results, thus confirming that both coseismic and interface response were not affected.

Regarding the comparison with numerical modeling (i.e., theoretical predictions), the only drawback of the theory so far is with respect to the amplitudes of the modeled wavefields. In most of my comparisons, experiments and simulations agree within an order of magnitude, however to conclude that ζ was adjusted because it was an unknown parameter in the experiment. My observations are similar to other works, like Schakel et al. (2011b), where the authors also attribute amplitude issues to uncertainty in ζ. Complementary, even though I tried to properly account for the effect of the large PZT source and the long electrodes, they may still contribute to the mismatch between theory and experiments. In the end, all the attempts, dealing with the interface response, to compare Pride's theory and real laboratory data, including this thesis, converge to amplitude discrepancies, which may indicate this theory is not entirely sufficient to describe real world data.

On the other side, it should be noticed that the Vosges sandstone used to study the interface response is far from a pure quartz medium and thus it may not be the best choice to evaluate quantitatively Pride's theory. A Fontainebleau sandstone may be more appropriated to use with the sand in the present experiment. The obvious conclusion here is that, to access in a quantitative manner the effectiveness of Pride's theory would be to work only with quartz-grain porous media whose physical properties are well constrained.

While experimenting different layer thicknesses, I showed that the effect of thin layers on the interface response is essentially the same observed for seismic waves and that a maximum signal enhancing, due only to layer thinning, can happen when the thickness is equal to half the P-wavelength in the layer. At last, the study of the fluid

conductivity effect on the EM interface response showed the experimental data agree with previous research on the subject, and that Pride's theory can definitely predict the general trends of amplitude *vs* fluid conductivity for coseismic and interface response wavefields, even though a mismatch in amplitude is always present.

7.3 Perspectives

7.3.1 Regarding experiments

While working on the design of the experimental setup, and also during acquisitions, a couple of ideas came up. Some were implemented, some attempted but not finished, and others can only be mentioned as future suggestions for improvement. First I point out that the electric measurements could benefit of a higher spatial precision by using electrodes with a diameter smaller than 1 mm. As discussed in section 4.7.3, the effect of diameter on measurements is small enough to disregard, thus one would only profit from using thinner electrodes. Alternatively, one could envisage using spherical small-diameter electrodes, thus providing a closer representation to punctual receivers, despite the eventual lower energy of the signals measured. When foreseeing the upscale of experimental results, such small electrodes would allow a more accurate analogy with field acquisitions.

A proper automation of electric measurements can reduce the acquisition time and, at the same time, ensure no human interaction is necessary. While the relay card mentioned in section 4.10 did not succeed, adding a high input impedance preamplifier between electrodes and this card may solve the problem, allowing acquisitions of 64 electrodes at once. Another improvement would be including motors to control the placement of the electrode comb.

The in-house 8-channel preamplifier, developed for this thesis and discussed in section 4.7.1, needs adjusting before it can be routinely applied. It consists of an effective and low-budget alternative to reduce the duration of electric acquisitions, compared with adapting the relay card mentioned above.

With the intent of comparing experiments with numerical simulations, either increasing the sandbox or sheathing the inside of the sandbox with a mechanically-isolating material, like sorbothane, would guarantee the experimental media resembles a layered and horizontally infinite media. Moreover, a laser-pulsed source could be used to have an almost punctual source, which is more convenient to reproduce numerically, as suggested and discussed by Shen (2020).

In all comparisons between experiments and theory, the lack of knowledge about the physical properties of the media used is, to a certain extent, behind the amplitude disagreement observed. Therefore, to draw proper quantitative conclusions about Pride's theory, first one should be certain about the medium used. A simpler, but effective, way would be the use of synthetic rocks, with properties known beforehand.

The experiments with varying fluid conductivity considered only the changes in the sand, thus for completeness, it would be interesting to have the reciprocal experiment, i.e., changes in the fluid conductivity inside the sandstone. Regarding the same experiments, even though the effect of the plastic bag, used to isolate sand and sandstone, was taken as insignificant, with experimental proof, a proper explanation is missing.

7.3.2 Regarding theoretical predictions

A significant improvement to numerical simulations could come from the use of a methodology that allows complex 3D models, like modelling the walls of the plastic box and the interface between sand and air. As a matter of fact, this thesis is part of the CHICkPEA (CHaracterization of Conducting Poro-elastic media using Experimental and advanced numericAl methods) project in which one of the goals was the development of a numerical code. Such feat was partially attained by Meyer (2021), but as of yet no comparison with experiments occurred. To overcome the difficulties found, in the context of the Makutu research program a PhD candidate (A. Heta) currently works on improving and extending the numerical code developed by Meyer (2021).

The formulation of analytical solutions able to describe seismic-to-electromagnetic conversion in interfaces, specially P-to-EM conversion, would be an important turning point since it would allow the direct comparison between the amplitudes of interface response and the difference of physical properties across an interface. Monachesi et al. (2018) achieved such goal, departing from Pride's equations, for SH-to-EM conversions to the case where the interface corresponds geologically to the water table.

Bibliography

Afagwu, Clement, Saad Alafnan, Mohamed A. Mahmoud, and Shirish Patil (2021). "Permeability model for shale and ultra-tight gas formations: Critical insights into the impact of dynamic adsorption". *Energy Reports* 7, pp. 3302–3316.

Aki, K., P.G. Richards, and University Science Books (2002). *Quantitative Seismology*. University Science Books. ISBN: 9780935702965.

Ali, Arfan and David K. Potter (2012). "Temperature dependence of the magnetic properties of reservoir rocks and minerals and implications for in situ borehole predictions of petrophysical parameters". *Geophysics* 77:3, WA211–WA221.

Archie, G.E. (1942). "The Electrical Resistivity Log as an Aid in Determining Some Reservoir Characteristics". *Transactions of the AIME* 146:01, pp. 54–62.

Barrière, Julien, Clarisse Bordes, Daniel Brito, Pascale Sénéchal, Julien Barrière, Clarisse Bordes, Daniel Brito, Pascale Sénéchal, Julien Barri, Clarisse Bordes, Daniel Brito, and S Pascale (2012). "Laboratory monitoring of P waves in partially saturated sand". *Geophysical Journal International* 191, pp. 1152–1170.

Bataller, Vanessa, Antonio Muñoz, Pilar Molina-Gaudó, Arturo Mediano, José Antonio Cuchí, and José Luis Villarroel (2009). "Improving Medium Access in Through-The-Earth VLF-LF Communications". *J. Commun.* 4, pp. 284–294.

Berryman, James G. (1980). "Confirmation of Biot's theory". *Applied Physics Letters* 37:4, pp. 382–384.

Bigelow, E.L. (1992). *Introduction to Wireline Log Analysis*. Western Atlas International.

Biot, M A (1956a). "Theory of Propagation of Elastic Waves in a Fluid-Saturated Porous Solid. I. Low-Frequency Range". *The Journal of the Acoustical Society of America* 28:2, pp. 168–178.

– (1962a). "Generalized Theory of Acoustic Propagation in Porous Dissipative Media". *The Journal of the Acoustical Society of America* 34:9A, pp. 1254–1264.

– (1956b). "Theory of Propagation of Elastic Waves in a Fluid-Saturated Porous Solid. II. Higher Frequency Range". *The Journal of the Acoustical Society of America* 28:2, pp. 179–191.

Biot, Maurice A (1962b). "Mechanics of Deformation and Acoustic Propagation in Porous Media". *Journal of Applied Physics* 33:4, pp. 1482–1498.

Blau, Ludwig W. and Statham Louis (1936). *Method and apparatus for seismicelectric prospecting*.

Block, Gareth I. and John G. Harris (2006). "Conductivity dependence of seismoelectric wave phenomena in fluid-saturated sediments". *Journal of Geophysical Research* 111:B1, B01304.

Bockris, John O'M. and Amulya K. N. Reddy (1970). "The Electrified Interface". In: *Volume 2 Modern Electrochemistry: An Introduction to an Interdisciplinary Area*. Springer US, Boston, MA, pp. 623–843. ISBN: 978-1-4613-4560-2.

Bodet, Ludovic, Amine Dhemaied, Roland Martin, Régis Mourgues, Fayçal Rejiba, and Vincent Tournat (2014). "Small-scale physical modeling of seismic-wave propagation using unconsolidated granular media". *Geophysics* 79:6, T323–T339.

Bordes, C, L Jouniaux, M Dietrich, J.-P. Pozzi, and S Garambois (2006). "First laboratory measurements of seismo-magnetic conversions in fluid-filled Fontainebleau sand". *Geophysical Research Letters* 33:1, n/a–n/a.

Bordes, C., Pascale Sénéchal, J. Barrière, D Brito, E Normandin, and D Jougnot (2015). "Impact of water saturation on seismoelectric transfer functions: a laboratory study of coseismic phenomenon". *Geophysical Journal International* 200:3, pp. 1317–1335.

Bordes, Clarisse (2005). "Etude expérimentale des phénomènes transitoires sismo-électromagnétiques: Mise en oeuvre au Laboratoire Souterrain de Rustrel, Pays d'Apt". PhD thesis. Université Joseph-Fourier - Grenoble I.

Bordes, Clarisse, Laurence Jouniaux, Stéphane Garambois, Michel Dietrich, Jean-pierre Pozzi, and Stéphane Gaffet (2008). "Evidence of the theoretically predicted seismo-magnetic conversion". *Geophysical Journal International* 174:2, pp. 489–504.

Bouchon, Michel (1979). "Discrete wave number representation of elastic wave fields in three-space dimensions". *Journal of Geophysical Research: Solid Earth* 84:B7, pp. 3609–3614.

– (1981). "A simple method to calculate Green's functions for elastic layered media". *Bulletin of the Seismological Society of America* 71:4, pp. 959–971.

Bourbié, Thierry, Olivier Coussy, and Bernard Zinszner (1987). *Acoustics of Porous Media*. Institut f. Editions TECHNIP, Paris, p. 334.

Brown, R. J. S. (1980). "Connection between formation factor for electrical resistivity and fluid-solid coupling factor in Biot's equations for acoustic waves in fluid-filled porous media". *Geophysics* 45:8, pp. 1269–1275.

Butler, Karl E., R. Don Russell, Anton W. Kepic, and Michael Maxwell (1996). "Measurement of the seismoelectric response from a shallow boundary". *Geophysics* 61:6, pp. 1769–1778.

Carcione, J M (2007). *Wave Fields in Real Media: Wave Propagation in Anisotropic, Anelastic, Porous and Electromagnetic Media*. Handbook of Geophysical Exploration: Seismic Exploration. Elsevier Science. ISBN: 9780080468907.

Carman, P.C. (1956). *Flow of Gases Through Porous Media*. Academic Press.

Chapman, David Leonard (1913). "LI. A contribution to the theory of electrocapillarity". *The London, Edinburgh, and Dublin Philosophical Magazine and Journal of Science* 25:148, pp. 475–481.

Charara, M., I. Zaretsky, and M. Zamora (2009). "Seismoelectric Modeling of Laboratory Experiments". In: *71st EAGE Conference and Exhibition incorporating SPE EUROPEC 2009*, pp. 8–11.

Charlaix, E., A. P. Kushnick, and J. P. Stokes (1988). "Experimental Study of Dynamic Permeability in Porous Media". *Phys. Rev. Lett.* 61, 14, pp. 1595–1598.

Chen, Benchi and Yongguang Mu (2005). "Experimental studies of seismoelectric effects in fluid-saturated porous media". *Journal of Geophysics and Engineering* 2:3, pp. 222–230.

Chen, Xiaofei (1993). "A systematic and efficient method of computing normal modes for multilayered half-space". *Geophysical Journal International* 115:2, pp. 391–409.

– (1999). "Seismogram Syntehesis in Multi-layered Half-space Part I. Theoretical Formulations". *Earthquake Research in China* 13:2.

Chin, R. C. Y., G. W. Hedstrom, and L. Thigpen (1984). "Matrix methods in synthetic seismograms". *Geophysical Journal International* 77:2, pp. 483–502.

Cui, Zhi Wen, Ke Xie Wang, Heng Shan Hu, and Jian Guo Sun (2007). "Acousto-electric well logging by eccentric source and extraction of shear wave". *Chinese Physics* 16:3, pp. 746–752.

Cui, Zhiwen, Jinxia Liu, Yujun Zhang, Kexie Wang, and Hengshan Hu (2011). "Simulation of Monopole and Multipole Seismoelectric Logging". *Advances in Acoustics and Vibration* 2011, pp. 1–10.

David, Christian, Teng-Fong Wong, Wenlu Zhu, and Jiaxiang Zhang (1994). "Laboratory measurement of compaction-induced permeability change in porous rocks: Implications for the generation and maintenance of pore pressure excess in the crust". *Pure Appl. Geophys.* 143:1-3, pp. 425–456.

Davis, J. A. and D. B. Kent (1990). "Surface Complexation Modeling in Aqueous Geochemistry". In: *Mineral-Water Interface Geochemistry*. Ed. by Michael F. Hochella and Art F. White. Mineralogical Society of America, pp. 177–260.

Day, Michael A. (1990). "The no-slip condition of fluid dynamics". *Erkenntnis* 33:3, pp. 285–296.

Devi, Maureen (2017). "Etudes expérimentales et numériques de la propagation d'ondes couplées sismiques et électromagnétiques dans des matériaux saturés non consolidés". Theses. Université Grenoble Alpes.

Devi, Maureen, S Garambois, D Brito, M Dietrich, V Poydenot, and C Bordes (2018). "A novel approach for seismoelectric measurements using multielectrode arrangements: ii—laboratory measurements". *Geophysical Gournal International* 214:3, pp. 1783–1799.

Dietrich, M., M. S. Devi, S. Garambois, D. Brito, and C. Bordes (2018). "A novel approach for seismoelectric measurements using multielectrode arrangements - I: Theory and numerical experiments". *Geophysical Journal International* 215:1, pp. 61–80.

Dukhin, A., S. Dukhin, and P. Goetz (2005). "Electrokinetics at High Ionic Strength and Hypothesis of the Double Layer with Zero Surface Charge". *Langmuir* 21:22, pp. 9990–9997.

Dupuis, Christian (2008). "Field measurements and analyses of electrokinetic seismoelectric signals generated in sedimentary environments". PhD thesis. University of New Brunswick.

Dupuis, J C, K E Butler, A W Kepic, and B D Harris (2009). "Anatomy of a seismoelectric conversion: Measurements and conceptual modeling in boreholes penetrating a sandy aquifer". *Journal of Geophysical Research* 114:B10, B10306.

Eaton, David W. S., Robert R. Stewart, and Mark P. Harrison (1991). "The Fresnel zone for P-SV waves". *GEOPHYSICS* 56:3, pp. 360–364.

Feynman, Richard Phillips, Robert B. Leighton, and Matthew Linzee Sands (1963). *Feynman lectures on physics. Volume 2: Mainly electromagnetism and matter*. Pearson/Addison-Wesley, p. 512. ISBN: 9780465040841.

Frenkel, J (1944). "On the Theory of Seismic and Seismoelectric Phenomena in a Moist Soil". *Izvestiya Akademii Nauk SSSR* 8:4, pp. 134–157.

Garambois, Stéphane (1999). "Études expérimentales et théoriques des conversions d'ondes sismoélectriques dans les milieux poreux superficiels". PhD thesis. L'Université Joseph Fourier - Grenoble I.

Garambois, Stéphane and Michel Dietrich (2001). "Seismoelectric wave conversions in porous media: Field measurements and transfer function analysis". *Geophysics* 66:5, pp. 1417–1430.

– (2002). "Full waveform numerical simulations of seismoelectromagnetic wave conversions in fluid-saturated stratified porous media". *Journal of Geophysical Research: Solid Earth* 107:B7, ESE 5–1–ESE 5–18.

Gassmann, Fritz (1951). "Uber die elastizitat poroser medien". *Vierteljahrsschrift der Naturforschenden Gesellschaft in Zurich* 96, pp. 1–23.

– (2013). "On Elasticity of Porous Media by F. Gassmann, Zürich, 1951". In: *Classics of Elastic Wave Theory*. Ed. by Michael A. Pelissier, Henning Hoeber, Norbert van de Coevering, and Ian F. Jones. Society of Exploration Geophysics. Chap. 3p, pp. 389–408.

Glover, Paul W.J. and Matthew D. Jackson (2010). "Borehole electrokinetics". *The Leading Edge* 29:6, pp. 724–728.

Gonçalves, Sérgio Pereira (2019). "Modelagem matemática e numérica do acoplamento poroelástico-eletromagnético em meios estratificadosS". PhD thesis. Universidade Estadual do Norte Fluminense.

Gouy, M. (1910). "Sur la constitution de la charge électrique à la surface d'un électrolyte". *Journal de Physique Théorique et Appliquée* 9:1, pp. 457–468.

Grahame, David C. (1947). "The Electrical Double Layer and the Theory of Electrocapillarity." *Chemical Reviews* 41:3, pp. 441–501.

Griffiths, David J. (1999). *Introduction to Electrodynamics*. 3rd ed. Prentice Hall, New Jersey. ISBN: 9780138053260.

Grobbe, N. (2016). "Coupled Poroelastic Waves and Electromagnetic Fields in Layered Media". PhD thesis. Delft University of Technology, p. 352. ISBN: 9789462954984.

Grobbe, N., A. Revil, Z. Zhu, and E. Slob (2020). *Seismoelectric Exploration: Theory, Experiments, and Applications*. Geophysical Monograph Series. Wiley. ISBN: 9781119127376.

Grobbe, N. and E. C. Slob (2016). "Seismo-electromagnetic thin-bed responses: Natural signal enhancements?" *Journal of Geophysical Research: Solid Earth* 121:4, pp. 2460–2479.

Grobbe, N., E. C. Slob, and J. W. Thorbecke (2016). "Comparison of eigenvectors for coupled seismo-electromagnetic layered-Earth modelling". *Geophysical Journal International* 206:1, pp. 152–190.

Grobbe, Niels (2015). "Towards Seismoelectric Inversion: Sensitivity Analysis using Resolution Functions". *Japan Geoscience Union Annual Meeting*, SCG15–P01.

Guan, Wei and Hengshan Hu (2008). "Finite-difference modeling of the electroseismic logging in a fluid-saturated porous formation". *Journal of Computational Physics* 227:11, pp. 5633–5648.

Gubkin, AN, AD Vinogradova, and EA Rudenchik (1986). "Determination of the relaxation function in a quartz single crystal". *Soviet Physics Journal* 29:10, pp. 840–844.

Guichet, Xavier, Laurence Jouniaux, and Nicole Catel (2006). "Modification of streaming potential by precipitation of calcite in a sand-water system: laboratory measurements pH range from 4 to 12". *Geophysical Journal International* 166, pp. 445–460.

Guichet, Xavier, Laurence Jouniaux, and Jean-Pierre Pozzi (2003). "Streaming potential of a sand column in partial saturation conditions". *Journal of Geophysical Research: Solid Earth* 108:B3.

Haartsen, Matthijs W. (1995). "Coupled Electromagnetic and Acoustic Wavefield Modeling in Poro-Elastic Media and its Applications in Geophysical Exploration". PhD thesis. Massachusetts Institute of Technology, p. 325.

Haartsen, Matthijs W. and R. S. Pride (1994). "Modeling of coupled electroseismic wave propagation from point sources in layered media". In: *SEG Technical Program Expanded Abstracts 1994*. Society of Exploration Geophysicists, pp. 1155–1158.

Haartsen, Matthijs W. and Steven R. Pride (1997). "Electroseismic waves from point sources in layered media". *Journal of Geophysical Research: Solid Earth* 102:B11, pp. 24745–24769.

Haartsen, Matthijs W., Zhenya Zhu, and M. Nafi Toksöz (1995). "Seismoelectric experimental data and modeling in porous layer models at ultrasonic frequencies". In: *SEG Technical Program Expanded Abstracts 1995*. Society of Exploration Geophysicists, pp. 696–699.

Haines, Seth S. and Steven R. Pride (2006). "Seismoelectric numerical modeling on a grid". *Geophysics* 71:6.

Hao, Jin-Qi, Lynn M. Hastie, and Frank D. Stacey (1982). "Theory of the seismomagnetic effect: a reassessment". *Physics of the Earth and Planetary Interiors* 28:2, pp. 129–140.

Hasanian, Mostafa and Cliff J Lissenden (2017). "Assessment of coating layers on the accuracy of displacement measurement in laser Doppler vibrometry". In: *AIP Conference Proceedings*. Vol. 1806. 1. AIP Publishing LLC, p. 050006.

Haskell, N A (1953). "The dispersion of surface waves on multilayered media". *Bulletin of the Seismological Society of America* 43:1, pp. 17–34.

Holzhauer, J (2015). "Seismic and seismoelectric monitoring of an unconsolidated porous medium". PhD thesis. Universit´e de Pau et des Pays de l'Adour.

Holzhauer, J., D. Brito, C. Bordes, Y. Brun, and B. Guatarbes (2017). "Experimental quantification of the seismoelectric transfer function and its dependence on conductivity and saturation in loose sand". *Geophysical Prospecting* 65:4, pp. 1097–1120.

Holzhauer, J. and U. Yaramanci (2011). "Improvements in Seismoelectric Acquisitions at Field and Lab Scales and Records Interpretation". In: *Near Surface 2011 - 17th EAGE European Meeting of Environmental and Engineering Geophysics*, pp. 12–14.

Hu, H and K Wang (2000). "Simulation of an acoustically induced electromagnetic field in a borehole embedded in a porous formation". *Borehole Acoustics and Logging Reservoir Delineation consortis, Annual Report*, pp. 13–20.

Hu, Hengshan, Wei Guan, and Jerry M. Harris (2007). "Theoretical simulation of electroacoustic borehole logging in a fluid-saturated porous formation". *The Journal of the Acoustical Society of America* 122:1, pp. 135–145.

Hu, Hengshan and Jiaqi Liu (2002). "Simulation of the converted electric field during acoustoelectric logging". *SEG Technical Program Expanded Abstracts* 21:1, pp. 348–351.

Hudson, J. A. (1969). "A Quantitative Evaluation of Seismic Signals at Teleseismic Distances—I Radiation from Point Sources". *Geophysical Journal of the Royal Astronomical Society* 18:3, pp. 233–249.

Ingeman-Nielsen, Thomas, Soňa Tomaškovičová, and Torleif Dahlin (2016). "Effect of electrode shape on grounding resistances — Part 1: The focus-one protocol". *Geophysics* 81:1, WA159–WA167.

Ishido, Tsuneo and Hitoshi Mizutani (1981). "Experimental and theoretical basis of electrokinetic phenomena in rock-water systems and its applications to geophysics". *Journal of Geophysical Research: Solid Earth* 86:B3, pp. 1763–1775.

Ivanov, A.G. (1939). "Effect of electrization of earth layers by elastic waves passing through them". *Proceedings of the USSR Academy of Sciences (Dokl. Akad. Nauk SSSR)* 24:1, pp. 42–45.

– (1940). "Seismoelectric effect of second kind". *Izvd. Akad. Nauk SSSR, Ser. Geogr. i Geofiz.* 5, pp. 699–726.

Jackson, P. D., D. Taylor Smith, and P. N. Stanford (1978). "Resistivity-porosity-particle shape relationships for marine sands". *GEOPHYSICS* 43:6, pp. 1250–1268.

Jardani, A. and A. Revil (2015). "Seismoelectric couplings in a poroelastic material containing two immiscible fluid phases". *Geophysical Journal International* 202:2, pp. 850–870.

Ji, Yanju, Li Han, Xingguo Huang, Xuejiao Zhao, Kristian Jensen, and Yibing Yu (2022). "A high-order finite-difference scheme for time-domain modeling of time-varying seismoelectric waves". *Geophysics* 87:2, T135–T146.

Johnson, David Linton, Joel Koplik, and Roger Dashen (1987). "Theory of dynamic permeability and tortuosity in fluid saturated porous media". *Journal of Fluid Mechanics* 176:1987, pp. 379–402.

Johnson, David Linton, Joel Koplik, and Lawrence M. Schwartz (1986). "New Pore-Size Parameter Characterizing Transport in Porous Media". *Phys. Rev. Lett.* 57, 20, pp. 2564–2567.

Johnson, David Linton, T. J. Plona, C. Scala, F. Pasierb, and H. Kojima (1982). "Tortuosity and Acoustic Slow Waves". *Phys. Rev. Lett.* 49, 25, pp. 1840–1844.

Johnston, M.J.S. (2002). "38 Electromagnetic fields generated by earthquakes". In: *International Geophysics*. Vol. 81. PART A, pp. 621–635.

Jouniaux, L and T Ishido (2012). "Electrokinetics in Earth Sciences: A Tutorial". *International Journal of Geophysics* 2012, pp. 1–16.

Jouniaux, L. and F. Zyserman (2016). "A review on electrokinetically induced seismo-electrics, electro-seismics, and seismo-magnetics for Earth sciences". *Solid Earth* 7:1, pp. 249–284.

Jouniaux, Laurence, Marie Lise Bernard, Maria Zamora, and Jean Pierre Pozzi (2000). "Streaming potential in volcanic rocks from Mount Pelée". *Journal of Geophysical Research: Solid Earth* 105:B4, pp. 8391–8401.

Jouniaux, Laurence and Jean-Pierre Pozzi (1995). "Streaming potential and permeability of saturated sandstones under triaxial stress: Consequences for electrotelluric anomalies prior to earthquakes". *Journal of Geophysical Research: Solid Earth* 100:B6, pp. 10197–10209.

Katz, A. J. and A. H. Thompson (1986). "Quantitative prediction of permeability in porous rock". *Phys. Rev. B* 34, 11, pp. 8179–8181.

Kennett, B. L. N. and N. J. Kerry (1979). "Seismic waves in a stratified half space". *Geophysical Journal International* 57:3, pp. 557–583.

Kepic, A. and K. Butler (2002). "The Art of Measuring Very Low Amplitude Seismoelectric Signals".

Kosten, C.
W. and C Zwikker (1941). "Extended theory of the absorption of sound by compressible wall-coverings". *Physica* 8:9, pp. 968–978.

Kurashige, M. (1989). "A thermoelastic theory of fluid-filled porous materials". *International Journal of Solids and Structures* 25:9, pp. 1039–1052.

Lebedev, Maxim, Andrej Bóna, Roman Pevzner, and Boris Gurevich (2011). "Elastic anisotropy estimation from laboratory measurements of velocity and polarization of quasi-P-waves using laser interferometry". *Geophysics* 76:3, WA83–WA89.

Leclaire, P., L. Kelders, W. Lauriks, C. Glorieux, and J. Thoen (1996). "Determination of the viscous characteristic length in air-filled porous materials by ultrasonic attenuation measurements". *The Journal of the Acoustical Society of America* 99:4, pp. 1944–1948.

Leroy, P. and A. Revil (2004). "A triple-layer model of the surface electrochemical properties of clay minerals". *Journal of Colloid and Interface Science* 270:2, pp. 371–380.

Li, Shuai, Harry Collini, and Matthew D. Jackson (2018). "Anomalous Zeta Potential Trends in Natural Sandstones". *Geophysical Research Letters* 45:20, pp. 11, 068–11, 073.

Liu, Yukai, David Smeulders, Yuanda Su, and Xiaoming Tang (2018). "Seismoelectric interface electromagnetic wave characteristics for the finite offset Vertical Seismoelectric Profiling configuration: Theoretical modeling and experiment verification". *The Journal of the Acoustical Society of America* 143:1, EL13–EL18.

Liu, Zhengping, Lei Yuan, Xin Zhang, Zhihui Liu, and Haiyan Wu (2008). "A laboratory seismoelectric measurement for the permafrost model with a frozen-unfrozen interface". *Geophysical Research Letters* 35:21, pp. 1–4.

Lorne, Benoit, Frédéric Perrier, and Jean-Philippe Avouac (1999a). "Streaming potential measurements: 1. Properties of the electrical double layer from crushed rock samples". *Journal of Geophysical Research : Solid Earth* 104:B8, pp. 17857–17877.

– (1999b). "Streaming potential measurements: 2. Relationship between electrical and hydraulic flow patterns from rock samples during deformation". *Journal of Geophysical Research: Solid Earth* 104:B8, pp. 17879–17896.

Meyer, Rose-Cloé (2021). "Mathematical modeling and simulation of waves in conducting poroelastic media using HDG method". Theses. Université de Pau et des Pays de l'Adour.

Mikhailenko, B.G. and O.N. Soboleva (1996). "Method for geophysical exploration based on the interaction of waves with the Earth's magnetic field". *Bulletin of the Novosibirsk Computing Center* 2:Mathematical Modeling in Geophysics, pp. 63–70.

– (1997). "Mathematical modeling of seismomagnetic effects arising in the seismic wave motion in the Earth's constant magnetic field". *Applied Mathematics Letters* 10:3, pp. 47–51.

Mikhailenko, Boris G (1991). "Numerical modeling of seismomagnetic effects in an elastic medium and their application in geophysical exploration". In: *SEG Technical Program Expanded Abstracts 1991*. Society of Exploration Geophysicists, pp. 428–431.

Monachesi, L B, F I Zyserman, and L Jouniaux (2018). "An analytical solution to assess the SH seismoelectric response of the vadose zone". *Geophysical Journal International* 213:3, pp. 1999–2019.

Morency, Christina, Eric Matzel, Niels Grobbe, Daniel Brito, Clarisse Bordes, Mathieu Bellanger, Mathieu Auxiètre, Kirsti Midttømme, Walter Wheeler, Hélène Barucq, Julien Diaz, and Bjarte Fageråas (2021). "Seismoelectric effects for geothermal resources assessment and monitoring". In: *IMAGE 2021 - Society of Exploration Geophysicists Annual Meeting and Exposition*. Denver, United States.

Morgan, F. D., E. R. Williams, and T. R. Madden (1989). "Streaming potential properties of westerly granite with applications". *Journal of Geophysical Research: Solid Earth* 94:B9, pp. 12449–12461.

Neev, J. and F. R. Yeatts (1989). "Electrokinetic effects in fluid-saturated poroelastic media". *Physical Review B* 40:13, pp. 9135–9141.

Onsager, Lars (1931a). "Reciprocal Relations in Irreversible Processes. I." *Phys. Rev.* 37, 4, pp. 405–426.

– (1931b). "Reciprocal Relations in Irreversible Processes. II." *Phys. Rev.* 38, 12, pp. 2265–2279.

Overbeek, J. TH. G. (1952). "Electrokinetic phenomena". In: *Colloid Science: Irreversible systems*. Ed. by H. R. Kruyt. Vol. 1. Colloid Science. Elsevier. Chap. 5, pp. 194–244.

Pape, Hansgeorg, Christoph Clauser, and Joachim Iffland (1999). "Permeability prediction based on fractal pore-space geometry". *GEOPHYSICS* 64:5, pp. 1447–1460.

Parkhomenko, Eleonora I. (1971). *Electrification Phenomena in Rocks*. Springer US, Boston, MA. ISBN: 978-1-4757-5069-0.

Peng, Rong, B. Di, J. Wei, P. Glover, P. Lorinczi, P. Ding, and Z. Liu (2018a). "The Seismoelectric Coupling in Shale". In: *80th EAGE Conference & Exhibition 2018*, Th K 13.

Peng, Rong, Bangrang Di, Paul Glover, Jianxin Wei, Piroska Lorinczi, Pinbo Ding, Zichun Liu, Yuangui Zhang, and Mansheng Wu (2019). "The effect of rock permeability and porosity on seismoelectric conversion: experiment and analytical modelling". *Geophysical Journal International*.

Peng, Rong, Bangrang Di, Paul W J Glover, Jianxin Wei, Piroska Lorinczi, Zichun Liu, and Huafei Li (2020). "Seismo-electric conversion in shale: experiment and analytical modelling". *Geophysical Journal International* 223:2, pp. 725–745.

Peng, Rong, Bangrang Di, Jianxin Wei, Pinbo Ding, Zichun Liu, Bingyan Guan, and Shiqi Huang (2018b). "Signal characteristics of electroseismic conversion". *Journal of Geophysics and Engineering* 15:2, pp. 377–385.

Peng, Rong, Bangrang Di, Jianxin Wei, Pinbo Ding, Jianguo Zhao, Xiao Pan, and Zichun Liu (2017). "Experimental study of the seismoelectric interface response in wedge and cavity models". *Geophysical Journal International* 210:3, pp. 1703–1720.

Peng, Rong, Bangrang Di, Jianxin Wei, Tao Hu, and Zichun Liu (2016a). "Seismoelectric effects: seismoelectric response of single interface". In: *SPG/SEG 2016 International Geophysical Conference, Beijing, China, 20-22 April 2016*. Society of Exploration Geophysicists and Society of Petroleum Geophysicists, pp. 658–661.

Peng, Rong, P. Glover, B. Di, J. Wei, Piroska Lorinczi, Pinbo Ding, and Z. Liu (2018c). "The Effect of Rock Permeability and Porosity on Seismoelectric Conversion". In: *80th EAGE Conference & Exhibition 2018*, We P2 02.

Peng, Rong, Jian-Xing Wei, Bang-Rang Di, Pin-Bo Ding, and Zi-Chun Liu (2016b). "Experimental research on seismoelectric effects in sandstone". *Applied Geophysics* 13:3, pp. 425–436.

Polytec (2016). *Datasheet OFV-5000 Vibrometer Controller*.

– (2017). *Datasheet OFV-505 Sensor Head*.

Pride, S. R. and F. D. Morgan (1991). "Electrokinetic dissipation induced by seismic waves". *GEOPHYSICS* 56:7, pp. 914–925.

Pride, Steve (1994). "Governing equations for the coupled electromagnetics and acoustics of porous media". *Physical Review B* 50:21, pp. 15678–15696.

Pride, Steven R. (2005). "Relationships between Seismic and Hydrological Properties". In: *Hydrogeophysics*. Ed. by Yoram Rubin and Susan S. Hubbard. Springer Netherlands, Dordrecht, pp. 253–290.

Pride, Steven R., Anthony F. Gangi, and F. Dale Morgan (1992). "Deriving the equations of motion for porous isotropic media". *The Journal of the Acoustical Society of America* 92:6, pp. 3278–3290.

Pride, Steven R. and Stephane Garambois (2005). "Electroseismic Wave Theory of Frenkel and More Recent Developments". *Journal of Engineering Mechanics* 131:9, pp. 898–907.

Pride, Steven R. and Matthijs W. Haartsen (1996). "Electroseismic wave properties". *The Journal of the Acoustical Society of America* 100:3, pp. 1301–1315.

Pride, Steven R., Frank Dale Morgan, and Anthony F. Gangi (1993). "Drag forces of porous-medium acoustics". *Physical Review B* 47:9, pp. 4964–4978.

Ranada Shaw, A. (2005). "The seismo-electric method and its sensitivity to subsurface contrasts". PhD thesis. Technische Universiteit Delft, p. 149. ISBN: 9789090201061.

Ranada Shaw, A., E. C. Slob, and C. P. A. Wapenaar (2006). "Wellbore Measurement Simulations for the Seismo-Electric Effect". In: *Society of Petroleum Engineers, 68th European Association of Geoscientists and Engineers Conference and Exhibition, incorporating SPE EUROPEC 2006, EAGE 2006: Opportunities in Mature Areas*. Vol. 6. June 2006, pp. 3029–3033.

Ren, Hengxin, Xiaofei Chen, and Qinghua Huang (2012). "Numerical simulation of coseismic electromagnetic fields associated with seismic waves due to finite faulting in porous media". *Geophysical Journal International* 188:3, pp. 925–944.

Ren, Hengxin, Qinghua Huang, and Xiaofei Chen (2010). "A new numerical technique for simulating the coupled seismic and electromagnetic waves in layered porous media". *Earthquake Science* 23:2, pp. 167–176.

– (2016a). "Existence of evanescent electromagnetic waves resulting from seismoelectric conversion at a solid-porous interface". *Geophysical Journal International* 204:1, pp. 147–166.

– (2016b). "Numerical simulation of seismo-electromagnetic fields associated with a fault in a porous medium". *Geophysical Journal International* 206:1, pp. 205–220.

– (2018). "Quantitative Understanding on the Amplitude Decay Characteristic of the Evanescent Electromagnetic Waves Generated by Seismoelectric Conversion". *Pure and Applied Geophysics* 175:8, pp. 2853–2879.

Revil, A. and N. Florsch (2010). "Determination of permeability from spectral induced polarization in granular media". *Geophysical Journal International* 181:3, pp. 1480–1498.

Revil, A. and P. W. J. Glover (1998). "Nature of surface electrical conductivity in natural sands, sandstones, and clays". *Geophysical Research Letters* 25:5, pp. 691–694.

Revil, A., A. Jardani, P. Sava, and A. Haas (2015). *The Seismoelectric Method: Theory and Applications*. Analytical Methods in Earth and Environmental Science. Wiley. ISBN: 9781118660300.

Revil, A. and H. Mahardika (2013). "Coupled hydromechanical and electromagnetic disturbances in unsaturated porous materials". *Water Resources Research* 49:2, pp. 744–766.

Revil, A., P. A. Pezard, and P. W. J. Glover (1999a). "Streaming potential in porous media: 1. Theory of the zeta potential". *Journal of Geophysical Research: Solid Earth* 104:B9, pp. 20021–20031.

Revil, A., H. Schwaeger, L. M. Cathles III, and P. D. Manhardt (1999b). "Streaming potential in porous media: 2. Theory and application to geothermal systems". *Journal of Geophysical Research: Solid Earth* 104:B9, pp. 20033–20048.

Scales, John A and Alison E Malcolm (2003). "Laser characterization of ultrasonic wave propagation in random media". *Physical Review E* 67:4, p. 046618.

Schakel, M D, D M J Smeulders, E C Slob, and H K J Heller (2011a). "Seismoelectric interface response: Experimental results and forward model". *GEOPHYSICS* 76:4, N29–N36.

– (2012). "Seismoelectric Fluid/Porous-Medium Interface Response Model and Measurements". *Transport in Porous Media* 93:2, pp. 271–282.

– (2011b). "Laboratory measurements and theoretical modeling of seismoelectric interface response and coseismic wave fields". *Journal of Applied Physics* 109:7, p. 074903.

Schakel, M. D. and D. M.J. Smeulders (2008). "Electrokinetic reflection and transmission at a fluid/porous-medium interface". *70th European Association of Geoscientists and Engineers Conference and Exhibition 2008: Leveraging Technology. Incorporating SPE EUROPEC 2008* 5:June 2008, pp. 3067–3071.

– (2009). "Seismoelectric interface response: Experiment and theory". In: *SEG Technical Program Expanded Abstracts 2009*. Society of Exploration Geophysicists, pp. 1970–1974.

– (2010a). "Seismoelectric prospecting: forward model and experimental results". In: *SEG Technical Program Expanded Abstracts 2010*. Society of Exploration Geophysicists, pp. 811–815.

Schakel, Menne and David Smeulders (2010b). "Seismoelectric reflection and transmission at a fluid/porous-medium interface". *The Journal of the Acoustical Society of America* 127:1, pp. 13–21.

Schakel, Menne D. (2011). "Coupled seismic and electromagnetic wave propagation". PhD thesis. Technische Universiteit Delft.

Schakel, Menne D., Zhenya Zhu, and Evert C. Slob (2011c). "Full-waveform model and measurements of electromagnetic to seismic conversion". In: *SEG Technical Program Expanded Abstracts 2011*. Vol. 107. Society of Exploration Geophysicists, pp. 745–749.

Schmitt, Denis P. and Michel Bouchon (1985). "Full-wave acoustic logging: synthetic microseismograms and frequency-wavenumber analysis". *GEOPHYSICS* 50:11, pp. 1756–1778.

Schön, Jürgen H (2015). *Physical properties of rocks: Fundamentals and principles of petrophysics*. Vol. 65. Elsevier.

Sen, Pabitra N. and Peter A. Goode (1992). "Influence of temperature on electrical conductivity on shaly sands". *Geophysics* 57:1, pp. 89–96.

Shen, Chengyi (2020). "Experimental and numerical studies of seismic wave propagation in carbonate rocks at the laboratory scale". Thesis. Université de Pau et des Pays de l'Adour.

Shen, Chengyi, Daniel Brito, Julien Diaz, Federico Sanjuan, Clarisse Bordes, and Stéphane Garambois (2022). "Pulsed-laser source characterization in laboratory seismic experiments". *Geomechanics and Geophysics for Geo-Energy and Geo-Resources* 8:1, pp. 1–26.

Sheng, Ping and Min-Yau Zhou (1988). "Dynamic Permeability in Porous Media". *Phys. Rev. Lett.* 61, 14, pp. 1591–1594.

Skempton, A. W. (1954). "The Pore-Pressure Coefficients A and B". *Géotechnique* 4:4, pp. 143–147.

Slattery, John C. (1967). "Flow of viscoelastic fluids through porous media". *AIChE Journal* 13:6, pp. 1066–1071.

Smeulders, D.M.J., Niels Grobbe, H.K.J. Heller, and M.D. Schakel (2014). "Seismoelectric Conversion for the Detection of Porous Medium Interfaces between Wetting and Nonwetting Fluids Seismoelectric Conversion for the Detection of Porous Medium Interfaces between Wetting and Nonwetting Fluids". *Vadose Zone Journal* 13:5.

Stacey, Frank D. (1964). "The seismomagnetic effect". *Pure and Applied Geophysics PAGEOPH* 58:1, pp. 5–22.

Stern, Otto (1924). "ZUR THEORIE DER ELEKTROLYTISCHEN DOPPELSCHICHT". *Zeitschrift für Elektrochemie und angewandte physikalische Chemie* 30:21-22, pp. 508–516.

Stoll, Robert D. and George M. Bryan (1970). "Wave Attenuation in Saturated Sediments". *The Journal of the Acoustical Society of America* 47:5B, pp. 1440–1447.

Stuart, Malcolm R. (1955). "Dielectric Constant of Quartz as a Function of Frequency and Temperature". *Journal of Applied Physics* 26:12, pp. 1399–1404.

Tatalovic, R., J.A. McDonald, and G.H.F. Gardner (1988). "Modelling study of tuning effects for the calculation of the thickness and areal extent of thin beds". *First Break* 6:12, pp. 395–404.

Thompson, A. H. and G A Gist (1993). "Geophysical applications of electrokinetic conversion". *The Leading Edge* 12:12, pp. 1169–1173.

Thompson, R. R. (1936). "The Seismic Electric Effect". *GEOPHYSICS* 1:3, pp. 327–335.

Thomsen, Leon (1986). "Weak elastic anisotropy". *GEOPHYSICS* 51:10, pp. 1954–1966.

Thomson, William T. (1950). "Transmission of Elastic Waves through a Stratified Solid Medium". *Journal of Applied Physics* 21:2, pp. 89–93.

Tiab, Djebbar and Erle C Donaldson (2015). *Petrophysics: theory and practice of measuring reservoir rock and fluid transport properties*. Gulf professional publishing.

"To: "Influence of temperature on electrical conductivity of shaly sands" by P. N. Sen and P. A. Goode (January 1992 GEOPHYSICS, p. 89–96)" (1992). *Geophysics* 57:12, pp. 1658–1658.

Ursin, Bjørn (1983). "Review of elastic and electromagnetic wave propagation in horizontally layered media". *GEOPHYSICS* 48:8, pp. 1063–1081.

Venzeler, Francisco and Viatcheslav Priimenko (2009). "Modelagem do efeito sismoelétrico em meios 2D". *Brazilian Journal of Geophysics* 27:1, pp. 63–80.

Vinogradov, J., M. Z. Jaafar, and M. D. Jackson (2010). "Measurement of streaming potential coupling coefficient in sandstones saturated with natural and artificial brines at high salinity". *Journal of Geophysical Research: Solid Earth* 115:B12.

Vinogradov, Jan, Matthew D. Jackson, and Manuel Chamerois (2018). "Zeta potential in sandpacks: Effect of temperature, electrolyte pH, ionic strength and divalent cations". *Colloids and Surfaces A: Physicochemical and Engineering Aspects* 553, pp. 259–271.

Wachter, Armin and Henning Hoeber (2006). *Compendium of Theoretical Physics*. Springer-Verlag, New York. ISBN: 0-387-25799-3.

Walker, E and PWJ Glover (2018). "Measurements of the relationship between microstructure, pH, and the streaming and zeta potentials of sandstones". *Transport in porous media* 121:1, pp. 183–206.

Walton, K. (1987). "The effective elastic moduli of a random packing of spheres". *Journal of the Mechanics and Physics of Solids* 35:2, pp. 213–226.

Wang, Dongdong, Yongxin Gao, Ping Tong, Jun Wang, Cheng Yao, and Baozhen Wang (2021). "Electroseismic and seismoelectric responses at irregular interfaces: Possible application to reservoir exploration". *Journal of Petroleum Science and Engineering* 202, p. 108513.

Wang, Jun, Zhenya Zhu, Yongxin Gao, Frank Dale Morgan, and Hengshan Hu (2020). "Measurements of the seismoelectric responses in a synthetic porous rock". *Geophysical Journal International* 222:1, pp. 436–448.

Warden, S, S Garambois, P Sailhac, L Jouniaux, and M Bano (2012). "Curvelet-based seismoelectric data processing". *Geophysical Journal International* 190:3, pp. 1533–1550.

Warden, S., S. Garambois, L. Jouniaux, D. Brito, P. Sailhac, and C. Bordes (2013). "Seismoelectric wave propagation numerical modelling in partially saturated materials". *Geophysical Journal International* 194:3, pp. 1498–1513.

Whitaker, Stephen (1969). "ADVANCES IN THEORY OF FLUID MOTION IN POROUS MEDIA". *Industrial & Engineering Chemistry* 61:12, pp. 14–28.

White, Benjamin S. and Minyao Zhou (2006). "Electroseismic prospecting in layered media". *SIAM Journal on Applied Mathematics* 67:1, pp. 69–98.

Widess, M. B. (1973). "How thin is a thin bed?" *Geophysics* 38:6, pp. 1176–1180.

Wyllie, M.R.J. and Walter D. Rose (1950). "Some Theoretical Considerations Related To The Quantitative Evaluation Of The Physical Characteristics Of Reservoir Rock From Electrical Log Data". *Journal of Petroleum Technology* 2:04, pp. 105–118.

Zhang, Hai-Ming, Xiao-Fei Chen, and Shyhong CHANG (2001). "Peak-Trough Averaging Method and its Applications to Calculation of Synthetic Seismograms with Sallow Focuses". *Chinese Journal of Geophysics* 44:6, pp. 791–799.

Zheng, Xu-Zhen, Hengxin Ren, Karl E. Butler, Haiming Zhang, Yao-Chong Sun, Wei Zhang, Qinghua Huang, and Xiaofei Chen (2021). "Seismoelectric and Electroseismic Modeling in Stratified Porous Media With a Shallow or Ground Surface Source". *Journal of Geophysical Research: Solid Earth* 126:9.

Zhu, Z. and M.N. Toksöz (2014). "Seismoelectric Measurements in an Artificial Porous Sample with Anisotropic Permeability". In: *Proceedings 76th EAGE Conference and Exhibition 2014*, pp. 16–19.

Zhu, Zhenya, Chuen H Cheng, and M. Nafi Toksö (1994). "Electrokinetic conversion in a fluid-saturated porous rock sample". In: *SEG Technical Program Expanded Abstracts 1994*. Society of Exploration Geophysicists, pp. 1057–1060.

Zhu, Zhenya, Matthijs W Haartsen, and M. N. Toksöz (2000). "Experimental studies of seismoelectric conversions in fluid-saturated porous media". *Journal of Geophysical Research: Solid Earth* 105:B12, pp. 28055–28064.

Zhu, Zhenya, Matthijs W Haartsen, and M. Nafi Toksöz (1999). "Experimental studies of electrokinetic conversions in fluid-saturated borehole models". *GEOPHYSICS* 64:5, pp. 1349–1356.

Zhu, Zhenya and M. Nafi Toksöz (2013). "Experimental measurements of the streaming potential and seismoelectric conversion in Berea sandstone". *Geophysical Prospecting* 61:3, pp. 688–700.

Zhu, Zhenya and M. N. Toksöz (1996). "Experimental studies of electrokinetic conversions in fluid-saturated porous medium". In: *SEG Technical Program Expanded Abstracts 1996*. Society of Exploration Geophysicists, pp. 1699–1702.

Zhu, Zhenya and M. Nafi Toksöz (2003a). "Crosshole seismoelectric measurements in borehole models with fractures". *GEOPHYSICS* 68:5, pp. 1519–1524.

– (2003b). *Effects of Saturant Conductivity on Seismoelectric Conversion*. Tech. rep. Massachusetts Institute of Technology. Earth Resources Laboratory.

– (2005). "Seismoelectric and seismomagnetic measurements in fractured borehole models". *GEOPHYSICS* 70:4, F45–F51.

Zhu, Zhenya, M. Nafi Toksöz, and Daniel R Burns (2008). "Electroseismic and seismoelectric measurements of rock samples in a water tank". *GEOPHYSICS* 73:5, E153–E164.

Zhu, Zhenya, M.N. Toksöz, and Xin Zhan (2016). "Seismoelectric measurements in a porous quartz-sand sample with anisotropic permeability". *Geophysical Prospecting* 64:3, pp. 700–713.

Zonge, Kenneth L. and Larry J. Hughes (1985). "Effect of electrode contact resistance on electric field measurements". In: *SEG Technical Program Expanded Abstracts 1985*, pp. 231–234.

Zyserman, Fabio, Patricia Gauzellino, and Laurence Jouniaux (2020). "Finite Element Modeling of Electroseismics and Seismoelectrics". In: *Seismoelectric Exploration*. American Geophysical Union (AGU). Chap. 18, pp. 245–267. ISBN: 9781119127383.

Zyserman, Fabio I., Patricia M. Gauzellino, and Juan E. Santos (2010). "Finite element modeling of SHTE and PSVTM electroseismics". *Journal of Applied Geophysics* 72:2, pp. 79–91.

Appendices

A Calculation of plane wave slowness

The detailed development that allows one to find the plane wave slownesses s_{P}, s_{B}, s_{S}, and s_{EM}, discussed in section 2.3.1, will be presented.

A.1 Longitudinal waves

For this case the determinant of the matrix in equation 2.63 will be set to zero:

$$\begin{vmatrix} -H\mathrm{s}(\omega)^2 + \rho_{\mathrm{B}} & \rho_{\mathrm{f}} - \mathrm{s}(\omega)^2 C & 0 \\ -\rho_{\mathrm{f}} + \mathrm{s}(\omega)^2 C & -\tilde{\rho} + \mathrm{s}(\omega)^2 M & \imath\frac{\tilde{\rho}}{\omega} L(\omega) \\ 0 & \imath\omega\mu L(\omega)\tilde{\rho} & -\mu\tilde{\epsilon} \end{vmatrix} = 0.$$

This gives:

$$(-Hs^2 + \rho_{\mathrm{B}})[\tilde{\rho}\tilde{\epsilon}\mu - M\mu\tilde{\epsilon}s^2 + \tilde{\rho}\mu L^2] - (\rho_{\mathrm{f}} - Cs^2)[\rho_{\mathrm{f}}\mu\tilde{\epsilon} - C\mu\tilde{\epsilon}s^2] = 0,$$

where I abbreviated $s = s(\omega)$ and $L = L(\omega)$, for convenience. Expanding the previous equation, one finds a biquadratic relation on s:

$$\begin{aligned} s^4(HM\mu\tilde{\epsilon} - C^2\mu\tilde{\epsilon}) + s^2(-H\tilde{\rho}\tilde{\epsilon}\mu - H\tilde{\rho}^2\mu L^2 - M\mu\rho_{\mathrm{B}}\tilde{\epsilon} + 2\rho_{\mathrm{f}}C\mu\tilde{\epsilon}) \\ + \rho_{\mathrm{B}}\tilde{\rho}\tilde{\epsilon}\mu + \rho_{\mathrm{B}}\tilde{\rho}^2\mu L^2 - \rho_{\mathrm{f}}^2\mu\tilde{\epsilon} = 0. \end{aligned} \tag{A.1}$$

The equation above is quadratic on s^2, thus the following subtitutions can be used to rewrite it in a quadratic form:

$$\mathfrak{s} = s_{\mathrm{P,B}}^2, \tag{A.2a}$$

$$B_1 = (HM\mu\tilde{\epsilon} - C^2\mu\tilde{\epsilon}), \tag{A.2b}$$

$$B_2 = (-H\tilde{\rho}\tilde{\epsilon}\mu - H\tilde{\rho}^2\mu L^2 - M\mu\rho_{\mathrm{B}}\tilde{\epsilon} + 2\rho_{\mathrm{f}}C\mu\tilde{\epsilon}), \tag{A.2c}$$

$$B_3 = \rho_{\mathrm{B}}\tilde{\rho}\tilde{\epsilon}\mu + \rho_{\mathrm{B}}\tilde{\rho}^2\mu L^2 - \rho_{\mathrm{f}}^2\mu\tilde{\epsilon}. \tag{A.2d}$$

These lead to:

$$B_1\mathfrak{s}^2 + B_2\mathfrak{s} + B_3 = 0, \tag{A.3}$$

which can be solved using Bhaskara's formula. The roots are:

$$2\mathfrak{s} = -\frac{B_2}{B_1} \pm \sqrt{\left(\frac{B_2}{B_1}\right)^2 - 4\left(\frac{B_3}{B_1}\right)}, \tag{A.4}$$

and depend only on the two fractions: $\frac{B_2}{B_1}$ and $\frac{B_3}{B_1}$. Using A.2 these fractions are:

$$\frac{B_2}{B_1} = \frac{-H\tilde{\rho} - \frac{H\tilde{\rho}^2}{\tilde{\epsilon}}L^2 - M\rho_{\mathrm{B}} + 2\rho_{\mathrm{f}}C}{(HM - C^2)}, \tag{A.5a}$$

$$\frac{B_3}{B_1} = \frac{\rho_{\mathrm{B}}\tilde{\rho} + \frac{\rho_{\mathrm{B}}\tilde{\rho}^2L^2}{\tilde{\epsilon}} - \rho_{\mathrm{f}}^2}{(HM - C^2)} = \frac{\rho_{\mathrm{B}}\tilde{\rho}(1 + \frac{\tilde{\rho}L^2}{\tilde{\epsilon}}) - \rho_{\mathrm{f}}^2}{(HM - C^2)}. \tag{A.5b}$$

It is important to note that equation A.5a was introduced in section 2.3.1 as the parameter γ. Finally, to find the slownesses of longitudinal plane waves (P and B) the relations A.5 will be introduced in A.4:

$$2\mathfrak{s} = -\gamma \pm \sqrt{\gamma^2 - 4\left(\frac{\rho_{\mathrm{B}}\tilde{\rho}(1 + \frac{\tilde{\rho}L^2}{\tilde{\epsilon}}) - \rho_{\mathrm{f}}^2}{(HM - C^2)}\right)}. \tag{A.6}$$

A.2 Transversal wave

In the case of transversal (S and EM) plane waves, the determinant of the matrix in equation 2.3.1 will be set to zero:

$$\begin{vmatrix} \rho_{\mathrm{B}} - G\mathrm{s}(\omega)^2 & \rho_{\mathrm{f}} & 0 \\ -\rho_{\mathrm{f}} & -\tilde{\rho} & \imath\frac{\tilde{\rho}}{\omega}L(\omega) \\ 0 & \imath\omega\mu L(\omega)\tilde{\rho} & \mathrm{s}(\omega)^2 - \mu\tilde{\epsilon} \end{vmatrix} = 0.$$

Developing the resulting equation a biquadratic relation can be found:

$$
\begin{aligned}
&(\rho_{\mathrm{B}} - Gs^2)[-\tilde{\rho}(s^2 - \tilde{\epsilon}\mu) - (\imath\tfrac{\tilde{\rho}}{\omega}L)(\imath\omega\mu\tilde{\rho}L)] - \rho_{\mathrm{f}}[-\rho_{\mathrm{f}}(s^2 - \tilde{\epsilon}\mu)] = 0, && \text{expand}\\
&(\rho_{\mathrm{B}} - Gs^2)[-\tilde{\rho}s^2 + \tilde{\rho}\tilde{\epsilon}\mu + \tilde{\rho}^2\mu L^2)] + \rho_{\mathrm{f}}^2 s^2 - \rho_{\mathrm{f}}^2\tilde{\epsilon}\mu = 0, && \text{divide by } \tilde{\rho}\\
&(\rho_{\mathrm{B}} - Gs^2)[-s^2 + \tilde{\epsilon}\mu + \tilde{\rho}\mu L^2)] + \tfrac{\rho_{\mathrm{f}}^2}{\tilde{\rho}}s^2 - \tfrac{\rho_{\mathrm{f}}^2}{\tilde{\rho}}\tilde{\epsilon}\mu = 0, && \text{isolate powers}\\
&Gs^4 + [-\rho_{\mathrm{B}} - G\mu(\tilde{\epsilon} + \tilde{\rho}L^2) + \tfrac{\rho_{\mathrm{f}}^2}{\tilde{\rho}}]s^2 + \tilde{\epsilon}\mu(\rho_{\mathrm{B}} - \tfrac{\rho_{\mathrm{f}}^2}{\tilde{\rho}}) + \rho_{\mathrm{B}}\tilde{\rho}\mu L^2 = 0. && \text{of } s
\end{aligned}
$$

Using the following substitutions:

$$\mathfrak{s} = s^2_{\xi=\mathrm{S,EM}}, \tag{A.7a}$$

$$B_1 = G, \tag{A.7b}$$

$$B_2 = -\rho_{\mathrm{B}} - G\mu(\tilde{\epsilon} + \tilde{\rho}L^2) + \frac{\rho_{\mathrm{f}}^2}{\tilde{\rho}}, \tag{A.7c}$$

$$B_3 = \tilde{\epsilon}\mu(\rho_{\mathrm{B}} - \frac{\rho_{\mathrm{f}}^2}{\tilde{\rho}}) + \rho_{\mathrm{B}}\tilde{\rho}\mu L^2, \tag{A.7d}$$

will allow one to re-express the previous biquadratic equation into a quadratic form, equivalent to A.3. Therefore the solution will arise from equation A.4.

$$
\begin{aligned}
2\mathfrak{s} = \frac{\rho_{\mathrm{B}} - \frac{\rho_{\mathrm{f}}^2}{\tilde{\rho}}}{G} + \mu\tilde{\epsilon}\left(1 + \frac{\tilde{\rho}L^2}{\tilde{\epsilon}}\right)\\
\pm\sqrt{\left[\frac{\rho_{\mathrm{B}} - \frac{\rho_{\mathrm{f}}^2}{\tilde{\rho}}}{G} + \mu\tilde{\epsilon}\left(1 + \frac{\tilde{\rho}L^2}{\tilde{\epsilon}}\right)\right]^2 - 4\frac{\mu}{G}\left(\tilde{\epsilon}(\rho_{\mathrm{B}} - \frac{\rho_{\mathrm{f}}^2}{\tilde{\rho}}) + \rho_{\mathrm{B}}\tilde{\rho}L^2\right)}.
\end{aligned}
\tag{A.8}
$$

If the complex density (equation 2.69) is used, the equation above will correspond exactly to equation 2.68.

B Deriving the system of equations used by Garambois (1999)

This appendix details how to arrive at the PSVTM and SHTE systems of equations (3.1 and 3.2), used as a departing point in the numerical code adopted here, from the original governing equations (2.53i).

As a first step I will expand equations 2.53i by explicitly writting all Cartesian components.

$$\partial_y E_z - \partial_z E_y = \imath\omega\mu H_x - M_x, \tag{B.9}$$

$$\partial_z E_x - \partial_x E_z = \imath\omega\mu H_y - M_y, \tag{B.10}$$

$$\partial_x E_y - \partial_y E_x = \imath\omega\mu H_z - M_z, \tag{B.11}$$

$$\partial_y H_z - \partial_z H_y = -\imath\omega\epsilon E_x + J_x + C_x, \tag{B.12}$$

$$\partial_z H_x - \partial_x H_z = -\imath\omega\epsilon E_y + J_y + C_y, \tag{B.13}$$

$$\partial_x H_y - \partial_y H_x = -\imath\omega\epsilon E_z + J_z + C_z, \tag{B.14}$$

$$J_x = L(\omega)[-\partial_x p + \omega^2 \rho_f u_x + f_x] + \sigma(\omega) E_x, \tag{B.15}$$

$$J_y = L(\omega)[-\partial_y p + \omega^2 \rho_f u_y + f_y] + \sigma(\omega) E_y, \tag{B.16}$$

$$J_z = L(\omega)[-\partial_z p + \omega^2 \rho_f u_z + f_z] + \sigma(\omega) E_z, \tag{B.17}$$

$$-\imath\omega w_x = \frac{k(\omega)}{\eta}[-\partial_x p + \omega^2 \rho_f u_x + f_x] + L(\omega) E_x, \tag{B.18}$$

$$-\imath\omega w_y = \frac{k(\omega)}{\eta}[-\partial_y p + \omega^2 \rho_f u_y + f_y] + L(\omega) E_y, \tag{B.19}$$

$$-\imath\omega w_z = \frac{k(\omega)}{\eta}[-\partial_z p + \omega^2 \rho_f u_z + f_z] + L(\omega) E_z, \tag{B.20}$$

$$-p = C[\partial_x u_x + \partial_y u_y + \partial_z u_z] + M[\partial_x w_x + \partial_y w_y + \partial_z w_z], \tag{B.21}$$

$$\begin{aligned} \tau_{xx} = {} & K_G(\partial_x u_x + \partial_y u_y + \partial_z u_z) + C(\partial_x w_x + \partial_y w_y + \partial_z w_z) \\ & + 2G\partial_x u_x - \frac{2}{3} G(\partial_x u_x + \partial_y u_y + \partial_z u_z), \end{aligned} \tag{B.22}$$

$$\begin{aligned} \tau_{yy} = {} & K_G(\partial_x u_x + \partial_y u_y + \partial_z u_z) + C(\partial_x w_x + \partial_y w_y + \partial_z w_z) \\ & + 2G\partial_y u_y - \frac{2}{3} G(\partial_x u_x + \partial_y u_y + \partial_z u_z), \end{aligned} \tag{B.23}$$

$$\begin{aligned} \tau_{zz} = {} & K_G(\partial_x u_x + \partial_y u_y + \partial_z u_z) + C(\partial_x w_x + \partial_y w_y + \partial_z w_z) \\ & + 2G\partial_z u_z - \frac{2}{3} G(\partial_x u_x + \partial_y u_y + \partial_z u_z), \end{aligned} \tag{B.24}$$

$$\tau_{xy} = G(\partial_x u_y + \partial_y u_x), \tag{B.25}$$

$$\tau_{xz} = G(\partial_x u_z + \partial_z u_x), \tag{B.26}$$
$$\tau_{yz} = G(\partial_y u_z + \partial_z u_y), \tag{B.27}$$
$$\partial_x \tau_{xx} + \partial_y \tau_{yx} + \partial_z \tau_{zx} = -\omega^2[\rho_B u_x + \rho_f w_x] - F_x, \tag{B.28}$$
$$\partial_x \tau_{xy} + \partial_y \tau_{yy} + \partial_z \tau_{zy} = -\omega^2[\rho_B u_y + \rho_f w_y] - F_y, \tag{B.29}$$
$$\partial_x \tau_{xz} + \partial_y \tau_{yz} + \partial_z \tau_{zz} = -\omega^2[\rho_B u_z + \rho_f w_z] - F_z. \tag{B.30}$$

From here onwards, the definitions below will be valid for every $\mathfrak{w}$ wavefield, except the pressure p:

$$\mathfrak{w}_V = \partial_x \mathfrak{w}_x + \partial_y \mathfrak{w}_y \tag{B.31}$$
$$\mathfrak{w}_H = \partial_x \mathfrak{w}_y - \partial_y \mathfrak{w}_x \tag{B.32}$$
$$\nabla_h^2 \mathfrak{w} = \partial_{xx} \mathfrak{w}_x + \partial_{yy} \mathfrak{w}_y. \tag{B.33}$$

The first two relations define new auxiliary components based on the horizontal (x and y) derivatives of the original vector fields, including the source terms, in the system of equations 2.53i. The third relation corresponds to the horizontal Laplacian. Additionally, for the stress tensors the two relations will be used:

$$\tau_V = \partial_x \tau_{xz} + \partial_y \tau_{yz} \tag{B.34}$$
$$\tau_H = \partial_x \tau_{yz} - \partial_y \tau_{xz}. \tag{B.35}$$

Using equation B.30 and the relation B.34, expression 3.1e can be found:

$$\partial_z \tau_{zz} = -\omega^2[\rho_B u_z + \rho_f w_z] - \tau_V - F_z. \tag{B.36}$$

Adding the x-derivative of B.26 with the y-derivative of B.27, and using relation B.31 to define u_V, one finds:

$$\begin{aligned} \partial_x \tau_{xz} &= G(\partial_{xx} u_z + \partial_{zx} u_x) \\ +\partial_y \tau_{yz} &= G(\partial_{yy} u_z + \partial_{zy} u_y) \\ \hline \tau_V &= G(\partial_{xx} u_z + \partial_{yy} u_z + \partial_z u_V) \end{aligned}. \tag{B.37}$$

Then, using B.33 equation 3.1a is easily retrieved:

$$\partial_z u_V = \frac{\tau_V}{G} - \nabla_h^2 u_z. \tag{B.38}$$

Next, I will rewrite equation B.21 as:

$$(\partial_x w_x + \partial_y w_y + \partial_z w_z) = \frac{-p - C(\partial_x u_x + \partial_y u_y + \partial_z u_z)}{M},$$

then insert it into B.24 to find:

$$\tau_{zz} = -p\frac{C}{M} + u_V\left[K_G - \frac{C^2}{M} - \frac{2}{3}G\right] + \partial_z u_z\left[K_G - \frac{C^2}{M} + 2G - \frac{2}{3}G\right].$$

Recalling the mechanical coefficient $\Delta = HM - C^2$, introduced during the plane wave analysis in section 2.3.1, one can finally find equation 3.1b:

$$\partial_z u_z = \left(\frac{M}{\Delta}\right)\tau_{zz} + \left(\frac{C}{\Delta}\right)p - \left[1 - 2G\frac{M}{\Delta}\right]u_V. \tag{B.39}$$

Adding equations B.18 and B.19, then using the effective density of the pore-fluid (equation 2.57), one finds:

$$w_V = \frac{1}{\omega^2\tilde{\rho}(\omega)}\nabla_h^2 p - \frac{\rho_f}{\tilde{\rho}(\omega)}u_V - \frac{1}{\omega^2\tilde{\rho}(\omega)}f_V - \frac{L(\omega)}{i\omega}E_V. \tag{B.40}$$

Now inserting B.39 in B.24, and using B.31 I find the intermediary expression

$$\frac{-C^2}{\Delta}\tau_{zz} = \frac{2GC^2}{\Delta}u_V + \frac{HC}{\Delta}p + Cw_V + C\partial_z u_z,$$

which, in the end, becomes equation 3.1c with the help of equation B.40:

$$\partial_z w_z = \frac{-C}{\Delta}\tau_{zz} - \left(\frac{2GC}{\Delta} - \frac{\rho_f}{\tilde{\rho}(\omega)}\right)u_V - \left(\frac{H}{\Delta} + \frac{\nabla_h^2}{\omega^2\tilde{\rho}(\omega)}\right)p + \frac{1}{\omega^2\tilde{\rho}(\omega)}f_V + \frac{L(\omega)}{i\omega}E_V. \tag{B.41}$$

By adding up the x-derivative of B.28 and the y-derivative of B.29 one finds:

$$\partial_{xx}\tau_{xx} + \partial_{yy}\tau_{yy} + 2\partial_{xy}\tau_{xy} + \partial_z\tau_V = -\omega^2[\rho_B u_V + \rho_f w_V] - F_V. \tag{B.42}$$

Analyzing the horizontal Laplacian of equation B.24, after some algebraic manipulation, one can show that: $\partial_{xx}\tau_{xx} + \partial_{yy}\tau_{yy} + 2\partial_{xy}\tau_{xy} = \nabla_h^2\tau_{zz} - 2G\nabla_h^2(\partial_z u_z) + 2G\nabla_h^2 u_V$. Therefore equation B.42 can be written as:

$$\nabla_h^2\tau_{zz} - 2G\nabla_h^2(\partial_z u_z) + 2G\nabla_h^2 u_V + \partial_z\tau_V = -\omega^2[\rho_B u_V + \rho_f w_V] - F_V. \tag{B.43}$$

Substituting B.39 and B.40 into B.43 above, equation 3.1d can finally be found:

$$\partial_z \tau_V = -\left[\omega^2\left(\rho_B - \frac{\rho_f^2}{\tilde{\rho}(\omega)}\right) + 2G\left(2 - 2G\frac{M}{\Delta}\right)\right]\nabla_h^2 u_V - \left(1 - 2G\frac{M}{\Delta}\right)\nabla_h^2 \tau_{zz} - \left(\frac{\rho_f}{\tilde{\rho}(\omega)} - 2G\frac{C}{\Delta}\right)\nabla_h^2 p - \imath\omega\rho_f L(\omega) E_V + \frac{\rho_f}{\tilde{\rho}(\omega)} f_V - F_V. \tag{B.44}$$

Multiplying B.20 by $-L(\omega)$, B.17 by $\frac{k(\omega)}{\eta}$, and adding the results, one finds:

$$J_z = \left(\sigma(\omega)\frac{k(\omega)}{\eta} - L^2(\omega)\right)E_z - \imath\omega L(\omega)\frac{\eta}{k(\omega)} w_z.$$

This result can be inserted into B.14, and with the aid of the definition of effective electrical permittivity (equation 2.59) one finds the expression for the z-oriented electric field:

$$E_z = \frac{\imath}{\omega\tilde{\epsilon}} H_H + \frac{\imath\omega\tilde{\rho}L}{\tilde{\epsilon}} w_z - \frac{\imath}{\omega\tilde{\epsilon}}\hat{C}_z. \tag{B.45}$$

Inserting this definition into equation B.20, allows equation 3.1f to be found after some manipulation:

$$\frac{\partial}{\partial z}(-p) = -\omega^2\rho_f u_z - \omega^2\tilde{\rho}\left(1 + \frac{\tilde{\rho}L^2}{\tilde{\epsilon}}\right)w_z - \frac{\tilde{\rho}L}{\tilde{\epsilon}} H_H + \frac{\tilde{\rho}L}{\tilde{\epsilon}} C_z - f_z, \tag{B.46}$$

Adding the y-derivative of B.9 with the x-derivative of B.10 gives $\partial_z E_V - \nabla_H^2 E_z = \imath\omega\mu H_H - M_H$ which combined with the definition of E_z, derived above, leads to equation 3.1h:

$$\frac{\partial}{\partial z} E_V = \imath\omega\frac{\tilde{\rho}L}{\tilde{\epsilon}}\nabla_h^2 w_z + \imath\omega\mu\left(1 + \frac{1}{\mu\tilde{\epsilon}\omega^2}\nabla_h^2\right)H_H - \frac{\imath}{\omega\tilde{\epsilon}}\nabla_h^2 C_z - M_H. \tag{B.47}$$

Following the same steps to derive equation B.47 above, I will add the y-derivative of B.10 with the x-derivative of B.9 to find:

$$-\partial_z H_H = -\imath\omega\epsilon E_V + J_V + C_V.$$

Now I will add the y-derivative of B.16 and the x-derivative of B.15 to get:

$$J_V = L(\omega)\nabla_H^2(-p) + \rho_f\omega^2 L(\omega) u_V + L(\omega) f_V + \sigma(\omega) E_V.$$

Finally, by combining both equations above and using the definition of effective electrical permittivity, equation 3.1g comes up:

$$\frac{\partial}{\partial \mathrm{z}} H_{\mathrm{H}} = -\rho_{\mathrm{f}}\omega^2 L u_{\mathrm{V}} - L\nabla_{\mathrm{h}}^2(-p) + \imath\omega\tilde{\epsilon}\left(1 + \frac{\tilde{\rho}L^2}{\tilde{\epsilon}}\right) E_{\mathrm{V}} - L f_{\mathrm{V}} - C_{\mathrm{V}}, . \quad \text{(B.48)}$$

That concludes the PSVTM system.

To start deriving the SHTE system, I will look first at B.11. With the aid of B.32 one can notice that an expression for H_{z} can be defined:

$$H_z = \frac{E_{\mathrm{H}} + M_{\mathrm{z}}}{\imath\omega\mu}. \quad \text{(B.49)}$$

Now I will add the y-derivative of B.12 with the x-derivative of B.13, and use the horizontal Laplacian of B.49 to find:

$$\partial_z H_{\mathrm{V}} - \nabla_{\mathrm{H}}^2\left(\frac{E_{\mathrm{H}} + M_{\mathrm{z}}}{\imath\omega\mu}\right) = \imath\omega\epsilon E_{\mathrm{H}} + J_{\mathrm{H}} + C_{\mathrm{H}}.$$

To find a definition for J_{H}, I will add the y-derivative of B.15 with the x-derivative of B.16, which gives:

$$J_{\mathrm{H}} = L(\omega)(\rho_f\omega^2 u_{\mathrm{H}} + f_{\mathrm{H}}) + \sigma(\omega)E_{\mathrm{H}}.$$

By combining the two relations above, equation 3.2c is found:

$$\frac{\partial}{\partial \mathrm{z}} H_{\mathrm{V}} = \rho_{\mathrm{f}}\omega^2 L u_{\mathrm{H}} - \imath\omega\tilde{\epsilon}\left(1 + \frac{\tilde{\rho}L^2}{\tilde{\epsilon}} + \frac{1}{\mu\tilde{\epsilon}\omega^2}\nabla_{\mathrm{h}}^2\right) E_{\mathrm{H}} + L f_{\mathrm{H}} + C_{\mathrm{H}} + \frac{1}{\imath\mu\omega}\nabla_{\mathrm{h}}^2 M_{\mathrm{z}}. \quad \text{(B.50)}$$

Now, deriving B.9 with respect to x, B.10 with respect to y, and adding the results one can easily check that equation 3.2d comes up:

$$\frac{\partial}{\partial \mathrm{z}} E_{\mathrm{H}} = -\imath\mu\omega H_{\mathrm{V}} + M_{\mathrm{V}}. \quad \text{(B.51)}$$

Next, by adding the y-derivative of B.26 with the x-derivative of B.27, and using definitions B.32 and B.35, equation 3.2a can be found:

$$\frac{\partial}{\partial z} u_H = \frac{\tau_H}{G}. \tag{B.52}$$

To derive the last equation, I will start by subtracting the x-derivative of B.29 from the y-derivative of B.28. Using relations B.32 and B.35, again, the intermediary expression is found:

$$\partial_z \tau_H + G\nabla_H^2 u_H = -\omega^2 \rho_B - \omega^2 \rho_f w_H - F_H.$$

In order to go on, I will seek a formula for w_H by subtracting the y-derivative of B.18 from the x-derivative of B.19:

$$w_H = -\frac{1}{\tilde{\rho}\omega^2}(\rho_f \omega^2 u_H + f_H) - \frac{L(\omega)}{\imath\omega} E_H.$$

Finally, combining both equations above, I find the missing equation (3.2b):

$$\frac{\partial}{\partial z}\tau_H = -\left[\omega^2\left(\rho_B - \frac{\rho_f^2}{\tilde{\rho}}\right) + G\nabla_h^2\right] u_H - \imath\omega\rho_f L E_H - F_H + \frac{\rho_f}{\tilde{\rho}} f_H. \tag{B.53}$$

That concludes the derivation of the SHTE system.

C Example of python routine used to control acquisition

This appendix shows an example of a python routine used to control both the oscilloscope and the function generator during acquisiton.

```
#!python3
# ********************************************************
# This program was based on the Keysight Infiniium
# oscilloscopes programmer's guide.
# ********************************************************
# Import modules.
# --------------------------------------------------------
import visa
import string
import numpy as np
```

```
import matplotlib.pyplot as plt
import struct
import sys
from datetime import datetime
import time
import os
import winsound
# Global variables (booleans:0=False, 1 = True).
# ------------------------------------------------------------
debug = 1
# ============================================================
# Initialize:
# ============================================================
def initialize():
    # Clear all status and error registers.
    do_command("*CLS")
    # Get and display the device's *IDN? string.
    idn_string = do_query_string("*IDN?")
    print("Identification string: '%s'" % idn_string)
    qresult = do_query_string(":STOP;*OPC?")
    print("Stopping oscilloscope to configure it. %s" % qresult)
    #----------
    #SETTING UP
    #----------
    # Activate Channel N and set its input parameters
    # :CHANnel<N>:DISPlay {{ON | 1} | {OFF | 0}}
    # :CHANnel<N>:INPut <parameter> ... "Here using DC 1Mohm"
    do_command(":CHANnel1:DISPlay ON")if CHANNELS[0] \
                                  else do_command(":CHANnel1:DISPlay OFF")
    do_command(":CHANnel1:INPut DC")
    do_command(":CHANnel2:DISPlay ON") if CHANNELS[1] \
                                  else do_command(":CHANnel2:DISPlay OFF")
    do_command(":CHANnel2:INPut DC")
    do_command(":CHANnel3:DISPlay ON") if CHANNELS[2] \
                                  else do_command(":CHANnel3:DISPlay OFF")
```

```
do_command(":CHANnel3:INPut DC")
do_command(":CHANnel4:DISPlay ON") if CHANNELS[3] \
                                else do_command(":CHANnel4:DISPlay OFF")
do_command(":CHANnel4:INPut DC")
#---------------
if CHANNELS[0]: do_command(":CHANnel1:OFFSet 0.0")
if CHANNELS[1]: do_command(":CHANnel2:OFFSet 0.0")
if CHANNELS[2]: do_command(":CHANnel3:OFFSet 0.0")
if CHANNELS[3]: do_command(":CHANnel4:OFFSet 0.0")
#---------------
# Set-up trigger
# Trigger mode will usually be the same throughout the experiments
# thus no need to change it.
do_command(":TRIGger:SWEep TRIGgered") # Triggered to a channel
qresult = do_query_string(":TRIGger:SWEep?")
print("Trigger sweep: %s" % qresult)
do_command(":TRIGger:MODE EDGE")
qresult = do_query_string(":TRIGger:MODE?")
print("Trigger mode: %s" % qresult)
# Set EDGE trigger parameters.
cmd_s = ":TRIGger:EDGE:SOURce "
cmd_s = cmd_s+str(TRIGGER_CHAN)
do_command(cmd_s)
do_command(":TRIGger:EDGE:SLOPe POSitive")
# Set trigger level
cmd_s = ":TRIGger:LEVel "
cmd_s = cmd_s+str(TRIGGER_CHAN)
cmd_s = cmd_s+","+str(TLEVEL)
do_command(cmd_s)
#----------------
# Set Sample Rate
cmd_s = ":ACQuire:SRATe:ANALog "
cmd_s = cmd_s+str(FS)
do_command(cmd_s)
qresult = do_query_string(":ACQuire:SRATe:ANALog?")
```

```
    print("Analog sample rate: %s" % qresult)
    #------------------------
    # Save Oscilloscope setup
    sSetup = do_query_ieee_block(":SYSTem:SETup?")
    f = open("setup.stp","+wb")
    f.write(sSetup)
    f.close
    print("Setup bytes saved: %d" % len(sSetup))
    # Set sampling:acquisition mode to Real Time Normal (single trigger event)
    do_command(":ACQuire:MODE RTIMe")
    qresult = do_query_string(":ACQuire:MODE?")
    print("Acquire mode: %s" % qresult)
#============================================================
# Waveform generator
def rigol_initialize():
    # Clear all status and error registers.
    rigol_command("*CLS")
    # To load file -> :MMEMory:LOAD:STATe filename
    # Get and display the device's *IDN? string.
    rigol_idn_string = rigol_query_string("*IDN?")
    print("Identification rigol: '%s'" % rigol_idn_string)
#----------
#SETTING UP RIGOL waveform generator
#----------
def set_rigol():
    # Set Channel 1
    rigol_command(":OUTP1 OFF")
    #
    cmd_s = ":SOUR1:APPL:SIN "
    cmd_s = cmd_s+str(FREQ_S); cmd_s = cmd_s+","
    cmd_s = cmd_s+str(VOLT_S); cmd_s = cmd_s+",0,0"
    rigol_command(cmd_s)
    #
    rigol_command("SOUR1:BURS ON")
    rigol_command("SOUR1:BURS:MODE TRIG")
```

```
    rigol_command("SOUR1:BURS:NCYC 1")
    #
    cmd_s = "SOUR1:BURS:INT:PER "
    cmd_s = cmd_s+str(T_S)
    rigol_command(cmd_s)
    rigol_command("SOUR1:BURS:TRIG:SOUR INT")
    rigol_command("SOUR1:BURS ON")
    #
    time.sleep(1)
    rigol_command(":OUTP1 ON")
# ============================================================
# Capture data (blocking method):
# ============================================================
def capture():
    Infiniium.timeout = SCOPE_ACQUISITION_TIME_OUT
    # Time in miliseconds to wait for the oscilloscope to arm,
    # trigger, finish acquisition and any processing.
    #---------------------------------------
    # Control average and set average number
    do_command(":ACQuire:AVERage ON") if AVERAGE_MODE_STATE \
                                  else do_command(":ACQuire:AVERage OFF")
    do_command(":ACQuire:COMPlete 100") # Always requests full acquisition
    cmd_s = ":ACQuire:COUNt "
    cmd_s = cmd_s + str(N_AVERAGES)
    if AVERAGE_MODE_STATE : do_command(cmd_s)
    print("Acquiring signals...\n")
    try:
        qresult = do_query_string(":RUN;*OPC?")
        do_command(":CDISplay") # Reinitialize the display
        while True:
            time.sleep(WAIT_A_BIT)
            Numavg = do_query_number(":WAVeform:COUNt?")
            print("Averaging: %s" % str(Numavg))
            if Numavg == float(N_AVERAGES):
                break
```

```
#
        qresult = do_query_string(":STOP;*OPC?")
        #qresult = do_query_string(":DIGitize;*OPC?")
        #print("Signal acquired.\n %s" % qresult)
    except Exception:
        print("The acquisition timed out, most likely due to no " \
              "trigger or improper setup causing no trigger. " \
              "Properly closing the oscilloscope connection and "\
              "exiting script.\n")
        Infiniium.clear()
        Infiniium.close()
        sys.exit("ErrorHandling.py")
#
    Infiniium.timeout = GLOBAL_TOUT
# ========================================================
# Analyze and save data
# ========================================================
def analyze():
   # Save Measurements.
   #--------------------------------------------------------
    # Save the screen image for quality control.
    # --------------------------------------------------------
    cmd = ":DISK:SAVE:IMAGe "+fname
    do_command(cmd)
    # Select relevant channel part to be saved
    do_command(":WAVeform:VIEW ALL")
    x_display = do_query_number(":WAVeform:XDISplay?")
    print(x_display)
    x_increment = do_query_number(":WAVeform:XINCrement?")
    print(x_increment)
    x_origin = do_query_number(":WAVeform:XORigin?")
    print(x_origin)
    x_fin = do_query_number("WAVeform:XRANge?")
    print(x_fin)
    x_ref = do_query_number("WAVeform:XREFerence?")
```

```
    print(x_ref)
    y_display = do_query_number(":WAVeform:YDISplay?")
    print(y_display)
    y_increment = do_query_number(":WAVeform:YINCrement?")
    print(y_increment)
    y_origin = do_query_number(":WAVeform:YORigin?")
    print(y_origin)
    y_fin = do_query_number("WAVeform:YRANge?")
    print(y_fin)
    y_ref = do_query_number("WAVeform:YREFerence?")
    print(y_ref)
    #Get percent of complete time buckets.
    qresult = do_query_string(":WAVeform:COMPlete?")
    print("Waveform complete: %s" % qresult)
    #Saving all waveforms to .h5 file
    print("Saving file: %s" % fname)
    cmd = ":DISK:SAVE:WAVeform ALL,"+fname
    cmd = cmd+",H5INt,ON"
    do_command(cmd)
# ============================================================
# Send a command and check for errors
# ============================================================
def do_command(command, hide_params=False):
    if hide_params:
        (header, data) = command.split(" ", 1)
        if debug:
            print("\nCmd = '%s'" % header)
    else:
        if debug:
            print("\nCmd = '%s'" % command)
#
    Infiniium.write("%s" % command)
    if hide_params:
        check_instrument_errors(header)
    else:
```

```
        check_instrument_errors(command)
#
#============================================================
def rigol_command(command, hide_params=False):
    if hide_params:
        (header, data) = command.split(" ", 1)
        if debug:
            print("\nCmd = '%s'" % header)
    else:
        if debug:
            print("\nCmd = '%s'" % command)

    rigol.write("%s" % command)
    if hide_params:
        rigol_check_instrument_errors(header)
    else:
        rigol_check_instrument_errors(command)
#
# ============================================================
# Send a command and a binary value and check for errors:
# ============================================================
def do_command_ieee_block(command,values):
    if debug:
        print("Cmb = '%s'" % command)
    Infiniium.write_binary_values("%s " % command, values, datatype='B')
    check_instrument_errors(command)
#
# ============================================================
# Send a query, check for errors, return string:
# ============================================================
def do_query_string(query):
    if debug:
        print("Qys = '%s'" % query)
    result = Infiniium.query("%s" % query)
    check_instrument_errors(query)
```

```
    return result
#
#============================================================
def rigol_query_string(query):
    if debug:
        print("Qys = '%s'" % query)
    result = rigol.query("%s" % query)
    rigol_check_instrument_errors(query)
    return result
#
# ============================================================
# Send a query, check for errors, return floating-point value:
# ============================================================
def do_query_number(query):
    if debug:
        print("Qyn = '%s'" % query)
    results = Infiniium.query("%s" % query)
    check_instrument_errors(query)
    return float(results)
#
#============================================================
def rigol_query_number(query):
    if debug:
        print("Qyn = '%s'" % query)
    results = rigol.query("%s" % query)
    rigol_check_instrument_errors(query)
    return float(results)
#
# ============================================================
# Send a query, check for errors, return binary values:
# ============================================================
def do_query_ieee_block(query):
    if debug:
        print("Qyb = '%s'" % query)
    result = Infiniium.query_binary_values("%s" % query, datatype='s')
```

```
    check_instrument_errors(query)
    return result[0]
#
# ============================================================
# Check for instrument errors:
# ============================================================
def check_instrument_errors(command):
    while True:
       error_string = Infiniium.query(":SYSTem:ERRor? STRing")
       if error_string:   # If there is an error string value.
          if error_string.find("0,", 0, 2) == -1:   # Not "No error".
             print("ERROR: %s, command: '%s'" % (error_string, command))
             print("Exited because of error.")
             sys.exit(1)
          else:   # "No error"
             break
       else:   # :SYSTem:ERRor? STRing should always return string.
          print("ERROR: :SYSTem:ERRor? STRing returned nothing, command: '%s'"% command)
          print("Exited because of error.")
          sys.exit(1)
#
#============================================================
def rigol_check_instrument_errors(command):
    while True:
       error_string = rigol.query(":SYSTem:ERRor?")
       if error_string:   # If there is an error string value.
          if error_string.find("0,", 0, 2) == -1:   # Not "No error".
             print("ERROR: %s, command: '%s'" % (error_string, command))
             print("Exited because of error.")
             sys.exit(1)
          else:   # "No error"
             break
       else:   # :SYSTem:ERRor? STRing should always return string.
          print("ERROR: :SYSTem:ERRor? STRing returned nothing, command: '%s'"% command)
          print("Exited because of error.")
```

```
          sys.exit(1)
#
# ============================================================
# Main program:
# ============================================================
startT = time.perf_counter()
#------------------------------------------------
# Creating logfile to follow up program execution
#   in the local machine
old_stdout = sys.stdout
tmp_log = datetime.now()
log_tmp = tmp_log.strftime("D%d-%m-%y_T%H-%M-%S")
log_tmp = "LOGFILE_" + log_tmp
log_tmp = log_tmp + ".log"
log_file = open(log_tmp,'w')
sys.stdout = log_file
print("__LOG FILE FOR SEISMOELECTRIC ACQUISITION__")
print("Date : %s \n" % datetime.now())
print("Victor Martins Gomes")
print("_____________________________________________")
print("Debug mode is on" if debug else "Debug mode is off")
LIB_VISA = "C:\\Windows\\System32\\agvisa32.dll" # Point to NI-VISA shared library
VISA_ADDRESS = "USB0::0x2A8D::0x904A::No Serial::INSTR" #Instrument's VISA address. You can use rm.list_
VISA_ADDRESS2 = "USB0::0x1AB1::0x0641::DG4E215002697::0::INSTR" # Rigol DG4102
GLOBAL_TOUT = 50000 # IO timeout in milliseconds
#------------------------------------------------
# Create a connection (session) to the Oscilloscope
try:
    rm = visa.ResourceManager(LIB_VISA)
    Infiniium = rm.open_resource(VISA_ADDRESS)
except visa.Error as ex:
    print('Couldn\'t connect to \'%s\', exiting now...' % VISA_ADDRESS)
    sys.exit()
#
print('Connected to \'%s\'' % VISA_ADDRESS)
```

```
Infiniium.timeout = GLOBAL_TOUT
Infiniium.clear()
# Rigol
try:
    rigol = rm.open_resource(VISA_ADDRESS2)
except visa.Error as ex:
    print('Couldn\'t connect to \'%s\', exiting now...' % VISA_ADDRESS2)
    sys.exit()
#
print('Connected to \'%s\'' % VISA_ADDRESS2)
rigol.timeout = GLOBAL_TOUT
rigol.clear()
#-----------------
# Set up Global variables - Oscilloscope
# Trigger channel
# CHANnel<N> | DIGital<M> | AUX | LINE
# N: integer, 1-4
# M: 0-15
TRIGGER_CHAN = 'AUX'
# Trigger level
TLEVEL = 1.25 # In volts (from the prog. guide, should be set to half the max)
# Channels ON
CHANNELS = [1,0,0,0] # I don't know why but we need channel 1 on.
# Time until first trigger event
TIME_TO_TRIGGER = 10 # Time in seconds
# Trigger period
TIME_BETWEEN_TRIGGERS = 10E-3 # Time in seconds
# Additional time to perform any processing like FFT, statistics, etc.
PROCESSING_TIME = 0 # Time in seconds
# Set Average mode if desired
AVERAGE_MODE_STATE = 1 # True or False
N_AVERAGES = 3000 # Num. of averages
if AVERAGE_MODE_STATE : print("Num. of averages: %s" % N_AVERAGES)
# Sampling frequency
FS = 500.0E6
```

```
#------------------------------
# Make sure the result of :DISK:PWD? isn't empty
do_command(":DISK:CDIRectory \"C:\\Users\\Public\\Documents\\Infiniium\"")
qresult = do_query_string(":DISK:PWD?")
print("PWD is: %s" % qresult)
# Now we move to the wanted output folder
print("Default DIR, moving to Victor")
defdir = "\"Victor\""
cmd = ":DISK:CDIRectory "+defdir
do_command("%s" % cmd)
qresult = do_query_string(":DISK:PWD?")
print("New PWD is: %s" % qresult)
# Create new folder for output and go inside
str_now = datetime.now()
defdir = str_now.strftime("\"D%d-%m-%y_T%H-%M-%S\"")
cmd = ":DISK:MDIRectory "+defdir
do_command("%s" % cmd)
cmd = ":DISK:CDIRectory "+defdir
do_command("%s" % cmd)
#-----------------------------
print("----INITIALIZING OSCILLOSCOPE----")
initialize()
# Get holdoff time: amount of time the oscilloscope
# waits before enabling the trigger again.
HO = do_query_number(":TRIGger:HOLDoff?")
N_SAMPLES = do_query_number(":ACQuire:POINts?")
T_RANGE = N_SAMPLES / FS
T_POSITION = do_query_number(":TIMebase:POSition?")
# Timeout for blocking synchronization
SCOPE_ACQUISITION_TIME_OUT = (1.1*float(TIME_TO_TRIGGER) +
                              1.2*float(PROCESSING_TIME) +
                              (1.1*float(TIME_BETWEEN_TRIGGERS) +
                               T_RANGE*2.0 + abs(T_POSITION)*2.0 +
                               HO*1.1)*N_AVERAGES)#*1.0E3
                               # in miliseconds
```

```
WAIT_A_BIT = float(TIME_TO_TRIGGER) #1.1*float(N_AVERAGES) # in seconds
# A time to see the average happening. If it is too small
# one will think nothing is going on. Experimentally determined.
#-----------------------------------------
#-------------------
# Set up Rigol variables
FREQ_S = 250000 # Frequency in Hertz
VOLT_S = 16 # Vpp
T_S = TIME_BETWEEN_TRIGGERS # Period in seconds
#-----------------------------------------
print("----ACQUISITION STARTS HERE----")
qresult = do_query_string(":STOP;*OPC?")
dict_fontT = {'fontsize' : 18, 'fontweight' : 'bold'}
dict_fontXZ = {'fontsize' : 16, 'fontweight' : 'bold'}
Xcoord = np.arange(1,2)
Zcoord = np.arange(77,81)
fig = plt.figure()
fig.show()
plt.axis([Xcoord[0]-1,Xcoord[-1]+1,Zcoord[0]-1,Zcoord[-1]+1])
plt.gca().invert_yaxis()
plt.title('Measuring points',dict_fontT)
plt.xlabel('X',dict_fontXZ); plt.ylabel('Z',dict_fontXZ)
plt.grid(True)
siginvX = 1 # Plot order control
for iterx in Xcoord:
    for iterz in Zcoord:
#----------------
        fname = "Point_X"+str(iterx)
        fname = fname+"Z"+str(iterz)
#----------------
        set_rigol()
        time.sleep(1)
#
        fname = "\""+fname
        fname = fname+"\""
```

```
#
# Plot current point
        plt.plot(iterx,iterz,'bo',markersize=2)
#
        plt.savefig("Current_point.png")
#
        capture()
        analyze()
#
        winsound.Beep(5000,1000) # Beep to indicate end of trace acquisition
        plt.plot(iterx,iterz,'r+',markersize=4)
#
        plt.savefig("Current_point.png")
        time.sleep(WAIT_A_BIT)
        input("Press enter to continue...")
#
        qresult = do_query_string(":RUN;*OPC?")
#
#-----------------------------
# Go back to Default Directory
do_command(":DISK:CDIRectory \"C:\\Users\\Public\\Documents\\Infiniium\"")
qresult = do_query_string(":DISK:PWD?")
print("PWD is: %s" % qresult)
#--------------------
# Closing and exiting
rigol_command(":OUTP1 OFF")
rigol.clear()
rigol.close()
Infiniium.clear()
Infiniium.close()
print("End of program")
endT = time.perf_counter()
print("Total approx. elapsed time: %f " % (endT-startT))
winsound.Beep(5000,1000) # Beep to indicate end of acquisition
sys.stdout = old_stdout
```

```
log_file.close()
sys.exit()
```

D Interpreting the interface response using a dipole-based model

We consider a spherical P-wave generated by a point-source at O, in the surface, and propagating along the z-direction, as sketched in fig. 1 (a). According to Thompson and Gist (1993), when the wave reaches the interface at depth z_i the maximum amplitude of the EM interface response (created by P-to -EM conversions) happens when the first half-wavelength of the P-wave crosses this interface, such that the total region affected by the wave, on the x-y plane, is the first Fresnel zone. The conceptual model dealt with here, as discussed in Garambois (1999), seeks to physically explain the interface response maxima using electric dipoles, distributed in an equally spaced manner, inside a circular region with radius r_{FZ} at the interface, which corresponds to the first Fresnel zone. In what follows we detail how r_{FZ} can be obtained, how we distribute the dipoles, and how we accounted for the contribution of each individual dipole.

In order to compute the radius of the first Fresnel zone associated with P-to-EM conversions at the interface (r_{FZ}), we follow the procedure described in Garambois and Dietrich (2002): it relies on the adaptation of the equations in Eaton et al. (1991) by replacing S-wave velocities with the EM-wave velocities, such that the corrected equations represent P-to-EM conversions at the interface. Moreover, while in P-to-SV conversions, Fresnel zones are usually ellipses whose inline (in the source-receiver plane) and crossline (out of the source-receiver plane) radii are not the same (Eaton et al., 1991), in the case of P-to-EM conversions, Garambois and Dietrich (2002) show that Fresnel zones are necessarily circular. We write, accordingly, the relationship that defines the first Fresnel zone for P-EM conversions:

$$\frac{1}{2f_{peak}} = \frac{\sqrt{(x_p \pm r_{FZ})^2 + z_i^2} - \sqrt{(x_p^2 + z^2)}}{v_P} + \frac{\sqrt{(x - x_p \mp r_{FZ})^2 + z^2} - \sqrt{(x - x_p)^2 + z_i^2}}{v_{EM}}; \tag{D.54}$$

where x_p is the x-coordinate of the point where P-to-EM wave conversion occurs which, as observed by Garambois and Dietrich (2002), will always coincide with the

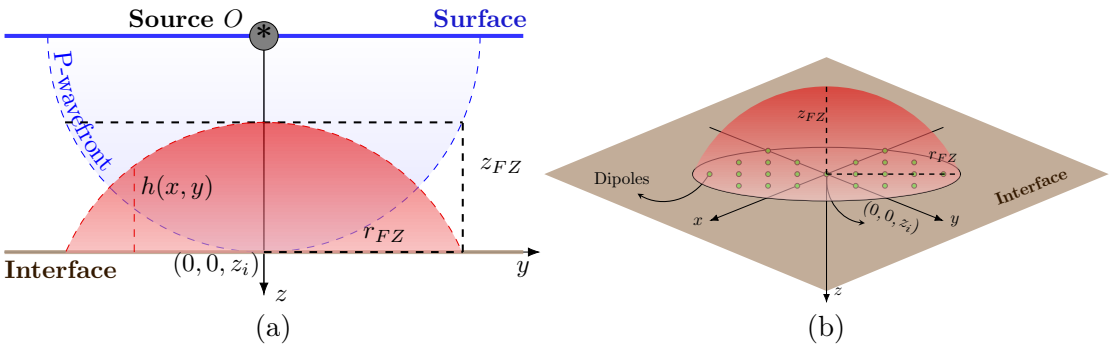

Figure 1: (a) schema 2D of a spherical P-wave (in blue) emerging from a point source at O and hitting an interface at point $(0, 0, z_i)$; the wavefront of the P-wave, with radius z_i, is illustrated by a dashed blue line. The spherical lens, bounded by the red dashed arc, is analogous to the region of the P-wave that already passed through the interface when the first Fresnel zone froms. The radius r_{FZ} of the first Fresnel zone was computed using eq. D.54 such that the maximum height z_{FZ} corresponds to the half-wavelength of the P-wave. The height $h(x, y)$, used in eq. D.56, is highlighted with a dashed red line. (b) 3D view of the Fresnel zone and lens, described in (a). The dipoles (green points) are distributed over the whole interface within the disk of radius r_{FZ}.

source's x-position, thus in the present case $x_p = 0$. Knowing the P and EM-wave velocities in the medium, as well as the dominant (peak) frequency, eq. D.54 will be solved numerically for r_{FZ}. Finally, using parameters based on the experiment with a layer (section 5.7) and on table 5.1, $f_{peak} = 250$ kHz, $z_i = 11.88$ cm, $v_P = 1783$ m/s and $v_{EM} = 5.4\text{E}7$ m/s, we obtain $r_{FZ} \simeq 2.9$ cm.

To distribute the electric dipoles over the circular region given by the radius r_{FZ}, one dipole is fixed in the center while the others are uniformly distributed, with nearly equidistant spacing, along cocentric circles of varying radii, including radius r_{FZ}. Defining N_c as the total number of circles inside the Fresnel zone, $n_l = \left\lfloor \pi / \sin^{-1}\left(\frac{1}{2l}\right) \right\rceil$, where $\lfloor\rceil$ indicates rounding to the nearest integer number, gives the number of points in each circle, with $1 \leq l \leq N_c$. It follows that the radii of the circles are given by $c_l = l r_{FZ}/N_c$ and, eventually, the position of each dipole in the Fresnel zone can be found with:

$$x_j = c_l \cos(\varphi_j) \quad \text{and} \quad y_j = c_l \sin(\varphi_j); \tag{D.55}$$

where φ_j is a set of n_l angles equally spaced in the domain $[0, 2\pi]$. Fig. 2 shows a sketch of this distribution of electric dipoles when $N_c = 4$.

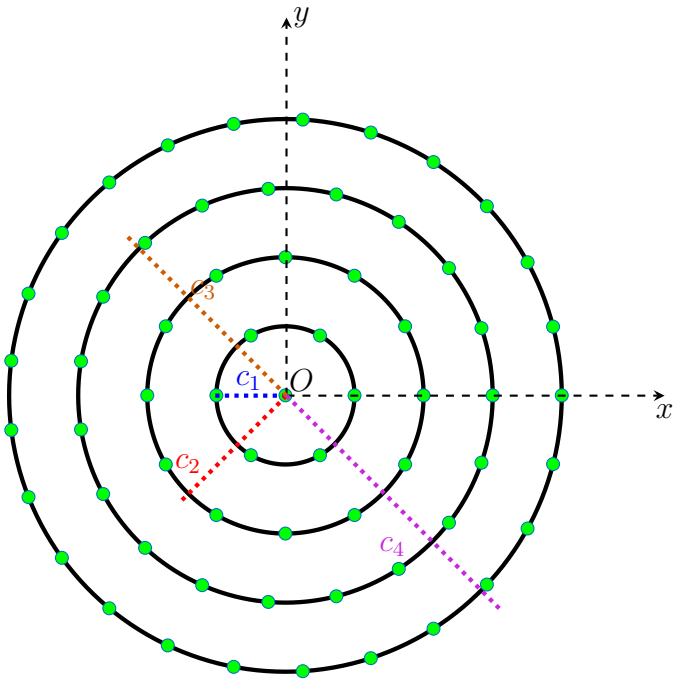

Figure 2: Example of how dipoles (green points) are distributed inside the circular region of radius r_{FZ} that defines the first Fresnel zone. For convenience, only four radii ($N_c = 4$) were considered.

Having defined the position of every dipole at the interface, now we show how to compute their individual contributions to the amplitude of the EM interface response. The main idea is to explore the relation between the wavefront of the P-wave passing through the interface and the moment of each dipole. It follows that, when the first Fresnel zone forms (i.e., half of the P-wavelength has traversed the interface), the moment of an electric dipole at a specific (x, y, z_i) position will be proportional to the magnitude of the z-component of the displacement u_z in this point. Effectively, to account for this proportionality, we used the height $h(x, y)$ of the spherical lens, sketched in figs. 1 (a) and (b), as a spatially-dependent factor to correct the moment of each dipole. This lens is geometrically equivalent to the region of the P-wavefront that crossed the interface when the first Fresnel zone takes shape, therefore it has a radius r_{FZ} in the interface plane and a maximum height z_{FZ} relative to the interface (which physically represents the half-wavelength of the P-wave), as shown in fig. 2 (a) and (b). Notice that a 2.9 cm Fresnel zone radius results in $z_{FZ} \simeq 3.6$ mm, and therefore a very thin lens.

For convenience, the analytical expression used here for the lens' height at every (x, y) position in the interface gives normalized values, varying between 0 and 1:

$$h(x,y) = 1 + \frac{-z_i + \sqrt{z_i^2 - (x^2+y^2)}}{z_{FZ}}. \tag{D.56}$$

Eventually, eq. D.56 physically describes the intensity-normalized distribution of the u_z displacement over the first Fresnel zone. When calculating the total electric potential due to all dipoles, this equation acts as a weight or a multiplication coefficient applied to the electric dipole moments (m_d). That way the electric potential at any (x, y, z) point in space due to a dipole created in the Fresnel zone will be:

$$V_{dip-FZ}(x,y,z) = h(x,y)V_{dip}(x,y,z), \tag{D.57}$$

where V_{dip} is the potential of a single dipole computed using the short electric dipole approximation:

$$V_{dip}(x,y,z) = \frac{1}{4\pi\epsilon}\frac{m_d(z-z_i)}{[\sqrt{(x-x_j)^2+(y-y_j)^2+(z-z_i)^2}]^3}. \tag{D.58}$$

It follows that the total electric potential at any point in space, due to all short dipoles in the first Fresnel zone, will be given by the equation:

$$V_{dip-total}(x,y,z) = \frac{m_d(z-z_i)}{4\pi\epsilon}\left\{\frac{1}{[\sqrt{x^2+y^2+(z-z_i)^2}]^3} + \sum_{l=1}^{N_c}\sum_{j=1}^{n_l} h(x_j,y_j)\frac{1}{[\sqrt{(x-x_j)^2+(y-y_j)^2+(z-z_i)^2}]^3}\right\}; \tag{D.59}$$

where the first term corresponds to the dipole in the centre and the second term to all other dipoles distributed along concentric circles. We have used this expression, with x=*0* and $y = 1.9$ cm, to compare three dipole-based models to the EM interface response decay *vs* z-offset obtained from experimental and numerical data in section 5.7.3, fig. 5.23 (b).

The first dipole-based model, case A, considers a single dipole, with moment $m_d = 8.8\text{E} - 13$ Cm, in the centre of the Fresnel zone, thus only the first term of eq. D.59. The second and third models, cases B and C respectively, use the parameters in table 1 to calculate the maximum amplitude of the EM interface response through eq. D.59. Case B considers dipoles distributed inside a Fresnel

Table 1: Parameters used to study cases B and, C discussed in the text.

Case	N_c	Total number of points	m_d [Cm]	r_{FZ} [m]	z_{FZ} [m]
B	68	14313	1.2E-16	2.9E-2	3.6E-3
C	102	33653	7.7E-17	4.8E-2	1.01E-2

zone with a 2.9 cm radius, as a consequence of a 250 kHz point source located at $x = 0$, $y = 1.9$ and $z = 0$ cm, which is equivalent to the centre of the PZT source used in the experiments. Case C deals with an extended source, where the PZT radius was added to the r_{FZ} of a point source. It is important to note that, while in B the value of z_{FZ} is equal to the half-wavelength of a 250 kHz P-wave, propagating with a 1783 m/s velocity, in C z_{FZ} has a different meaning, since increasing r_{FZ} and z_{FZ} implies a change in frequency that does not happen. It follows that z_{FZ} in C is the value that ensures $h(0, 0) = 1$ in eq. D.56, i.e., the maximum of $h(x, y)$ is in centre of the Fresnel zone.

Regarding the comparison with experimental and numerical data, the models used in these three cases (A,B, and C) perform well for z-offsets from the interface bigger than 4 cm (see fig. 5.23 (b)), however it is model C that shows the best agreement to both data types.

For completness we have also studied the effect of increasing the number of dipoles, which is the same as increasing N_c in eq. D.59, keeping r_{FZ} constant. By doing so we concluded that m_d decreases with an increase in the number of dipoles, but the trend of $V_{dip-total}$ *vs* z-offset remains unchanged. Finally, we have also adressed the influence of the second interface, such that when accounting for dipoles (of inverse polarity) at $z = 12.62$ cm the results diverge more from the experimental data than in case A, what indicates that the second interface plays no role at all in the maximum amplitude of the EM interface response.